

Quantum Chemical Investigation of Coinage Metal Complexes with Regard to their Application in OLEDs



INAUGURAL-DISSERTATION

zur

Erlangung des Doktorgrades der
Mathematisch-Naturwissenschaftlichen Fakultät
der Heinrich-Heine-Universität Düsseldorf

vorgelegt von

JELENA FÖLLER

aus Herdecke

Düsseldorf, August 2018

aus dem Institut für Theoretische Chemie und Computerchemie
der Heinrich-Heine-Universität Düsseldorf

Gedruckt mit der Genehmigung der
Mathematisch-Naturwissenschaftlichen Fakultät der
Heinrich-Heine-Universität Düsseldorf

Berichterstatter:

1. Univ.-Prof. Dr. Christel M. Marian
2. PD Dr. Oliver Weingart

Tag der mündlichen Prüfung:

Eidesstattliche Erklärung

Ich versichere an Eides Statt, dass die Dissertation von mir selbständig und ohne unzulässige fremde Hilfe unter Beachtung der „Grundsätze zur Sicherung guter wissenschaftlicher Praxis an der Heinrich-Heine-Universität Düsseldorf“ erstellt worden ist. Die Dissertation wurde noch bei keiner anderen Fakultät vorgelegt. Ich habe keine vorherigen Promotionsversuche unternommen.

Düsseldorf, 24. August 2018

*“Dass ich erkenne, was die Welt
im Innersten zusammen hält.”*

Goethes Faust

Summary

One of the most interesting applications of luminescent Cu(I) and Au(I) transition metal complexes is as emitter materials in organic light emitting diodes (OLEDs). Commercial applications of OLEDs comprise their use in mobile phone displays or television screens as well as in innovative lighting technology. Advantages of OLEDs over liquid crystal displays (with inorganic LEDs as backlight) include self-luminescence and higher device flexibilities. One of the major drawbacks of OLEDs is their lower operational lifetime, especially of blue light emitters. The reason why Cu(I) and Au(I) transition metal complexes gained increasing interest in the OLED research area is that they are cheaper alternatives to Ir or Pt complexes, while also being able to achieve internal quantum efficiencies of up to 100%. Cu(I) and Au(I) complexes are either phosphorescence emitters, or, if the singlet–triplet gap lies within the range of several $k_B T$ and thus can be overcome by thermal energy, they may be thermally activated delayed fluorescence (TADF) emitters. Their emission behavior therefore depends on the singlet–triplet gap as well as on the intersystem crossing (ISC) and radiative rate constants of the involved states.

In this thesis, I examine how ligand torsion, solvent environment and the introduction of different substituents affect the emission properties of several linear and trigonal Cu(I) and Au(I) complexes. To this end, high-level quantum chemical methods were employed. Density functional theory (DFT) was used for the optimization of the ground state geometries and time-dependent DFT for the relevant excited state geometries. The combined DFT/MRCI approach was applied to determine the electronic structure and properties. Where appropriate, spin–orbit coupling effects were taken into account. Solvation effects were included by means of implicit continuum solvation models.

The effect of the ligand torsion is seen to depend on the orbitals involved in the excitation and the resulting density overlap. Maximizing the density overlap — and thus the singlet–triplet gap — leads to phosphorescent complexes, whereas minimizing the overlap does not necessarily result in efficient TADF, since electronic decoupling of the donor and acceptor moieties induced by ligand torsion does not only decrease the energy gap, but also the fluorescence rate constant. Ligand torsion may also affect spin–orbit coupling between the states and thereby also influence the ISC rate constants.

Besides, it could be shown that for complexes where the dipole vector significantly changes in magnitude and direction between the ground and the excited state, (un)hindered solvent reorientation can explain sizable shifts of the emission wavelength.

Starting from a set of linear NHC-Cu(I)-pyridine complexes that are only very weakly luminescent in the solid state, modifications on the ligands were computationally investigated that led to complexes which are predicted to show efficient blue to green TADF. In addition, it could be confirmed that — in agreement with experimental findings — the corresponding trigonal complexes, where one additional pyridine binds to the copper, should be excellent emitters, too.

Zusammenfassung

Zu den interessantesten Anwendungen für lumineszente Cu(I) und Au(I) Komplexe gehört ihr Einsatz als Emittter in organischen Leuchtdioden (OLEDs). Kommerzielle Verwendung finden OLEDs z.B. in Handydisplays, Fernsehbildschirmen oder auch in der Beleuchtungstechnik. Zu den Vorteilen von OLEDs gegenüber Flüssigkristallbildschirmen (mit anorganischen LEDs als Hintergrundbeleuchtung) zählen, dass sie selbstleuchtend und mechanisch deutlich flexibler sind. Einer der Hauptnachteile ist ihre geringere Betriebslebensdauer, was insbesondere für blaue Emittter gilt. Der Grund, weswegen gerade Cu(I) und Au(I) Komplexe zunehmend im Hinblick auf ihre Eignung als Emitttermoleküle in OLEDs untersucht werden, ist, dass sie nicht nur kostengünstigere Alternativen zu Ir oder Pt Komplexen darstellen, sondern wie jene auch interne Quantenausbeuten von bis zu 100% erreichen. Cu(I) und Au(I) Komplexe können phosphoreszent sein, oder, falls die Aufspaltung zwischen Singulett- und Triplettzustand klein genug ist, um thermisch überwunden zu werden, können sie auch thermisch aktivierte, verzögerte Fluoreszenz (TADF) zeigen. Ihr Emissionsverhalten hängt somit sowohl von der Singulett-Triplett-Aufspaltung als auch von den Interkombinations- (ISC) und Strahlungsratenkonstanten ab.

Diese Arbeit beschäftigt sich mit den Effekten, die Ligandentorsion, Lösungsmittelumgebung und unterschiedliche Substituenten auf die Emissionseigenschaften von mehreren linearen und trigonalen Cu(I) und Au(I) Komplexen haben. Zu diesem Zweck wurden aufwendige quantenchemische Untersuchungen durchgeführt. Die Optimierung der Grundzustandsgeometrien erfolgte mithilfe der Dichtefunktionaltheorie (DFT) und die der angeregten Zustandsgeometrien mithilfe der zeitabhängigen DFT. Zur Bestimmung der elektronischen Struktur sowie der Eigenschaften wurde der kombinierte DFT/MRCI Ansatz gewählt und wo nötig Spin-Bahn-Kopplungseffekte mit berücksichtigt. Lösungsmittelleffekte wurden anhand von impliziten Kontinuumsmodellen miteinbezogen.

Wie sich erwiesen hat, hängt der Einfluss der Ligandentorsion von den Orbitalen, die an den Anregungen beteiligt sind, und von dem daraus resultierenden Dichteüberlapp ab. Wird der Dichteüberlapp – und somit auch die Singulett-Triplett-Aufspaltung – maximiert, führt dies zu phosphoreszenten Komplexen, wohingegen eine Minimierung des Überlapps nicht notwendigerweise effiziente TADF zur Folge hat. Dies ist darauf zurückzuführen, dass die elektronische Entkopplung der Donor- und Akzeptoreinheiten, die durch die Torsion herbeigeführt wird, nicht nur zu einer Verringerung der Singulett-Triplett-Aufspaltung, sondern auch zu kleineren Fluoreszenzratenkonstanten führt. Zudem kann die Ligandentorsion auch die Spin-Bahn-Kopplung zwischen den Zuständen und somit die ISC-Ratenkonstanten beeinflussen.

Desweiteren konnte gezeigt werden, dass sich eine starke Verschiebung des Emissionsmaximums bei Komplexen, bei denen sich die Länge und die Richtung des Dipolvektors zwischen dem Grundzustand und dem angeregten Zustand stark verändert, durch eine entsprechende (un)gehinderte Lösungsmittelumorientierung erklären lässt.

Ausgehend von einer Reihe von linearen NHC-Cu(I)-Pyridin-Komplexen, deren Kristalle nur schwache Lumineszenz zeigen, konnten mithilfe von quantenchemischen Rechnungen wohl durchdachte Modifikationen an den Liganden vorgeschlagen werden, die voraussichtlich zu Komplexen mit effizienter blauer oder grüner Emission führen. Zusätzlich konnte – im Einklang mit experimentellen Befunden – bestätigt werden, dass die trigonalen Komplexe, bei denen ein weiterer Pyridin-Ligand ans Kupfer bindet, ebenfalls exzellente Emittler darstellen.

Danksagung

Mein größter Dank gilt meiner Doktormutter Christel M. Marian für das spannende Thema und ihr stetes Engagement, mit dem sie nicht nur das Voranschreiten meiner Arbeit verfolgt, sondern sich auch für meine Finanzierung eingesetzt hat. Ich danke ihr zudem für das Vertrauen, das sie in mich und meine Fähigkeiten hatte und dafür, dass sie mir meine Freiheiten gelassen hat und doch stets da war, wenn ich Hilfe brauchte.

Ich danke PD Dr. Oliver Weingart für die Übernahme des Zweitgutachtens.

Zudem danke ich Prof. Christian Ganter dafür, dass er sich bereit erklärt hat, mein Mentor zu sein. Auch danke ich ihm und PD Dr. Andreas Steffen für die gute und interessante, wenn auch manchmal frustrierende Zusammenarbeit. Wer hätte auch ahnen können, dass das so kompliziert ist mit den linearen NHC-Komplexen!

Ich danke dem gesamten Arbeitskreis der TC für die nette, produktive Atmosphäre, in der ich arbeiten durfte. Ich habe von vielen Leuten vieles gelernt und hoffe, ich konnte auch ein bisschen Wissen weitergeben! Besonders bedanken möchte ich mich an dieser Stelle auch bei Irina Dokukina, Oliver Schillinger und Gudrun Brauwers; es war eine schöne Zeit zusammen.

Und nicht zuletzt danke ich natürlich meiner Familie und meinem Freund Maximilian Mühle dafür, dass sie immer für mich da waren und glaubhaft so getan haben, als interessiere sie das Thema meiner Doktorarbeit.

List of publications included in this thesis

Paper I

Phosphorescence or thermally activated delayed fluorescence? Intersystem crossing and radiative rate constants of a three-coordinate Copper(I)-complex determined by quantum chemical methods.

JELENA FÖLLER, Martin Kleinschmidt and Christel M. Marian,

Inorg. Chem. **2016**, *55*, 7508–7516.

OWN CONTRIBUTION: all calculations, first draft / major parts of the final paper

Paper II

Rotationally assisted spin-state inversion in carbene-metal-amides is an artifact.

JELENA FÖLLER and Christel M. Marian,

J. Phys. Chem. Lett. **2017**, *8*, 5643–5647.

OWN CONTRIBUTION: all calculations, first draft of the paper, all figures, Supporting Information

Paper III

Computer-Aided Design of Luminescent Linear NHC Cu(I) Pyridine Complexes.

JELENA FÖLLER and Christel M. Marian,

unsubmitted manuscript (held back to give the experimentalists time to finish the syntheses and measurements)

OWN CONTRIBUTION: calculations on the IPr-Cu(I)-pyridine complexes, all text concerning the IPr-Cu(I)-pyridine complexes, all figures

Book Chapter

Intersystem crossing processes in TADF emitters.

Christel M. Marian, JELENA FÖLLER, Martin Kleinschmidt and Mihajlo Etinski,

in: Yersin (Ed.), *Highly Efficient OLEDs, Materials Based on Thermally Activated Delayed Fluorescence*. Wiley-VCH (2018) ISBN: 978-3-527-33900-6

OWN CONTRIBUTION: calculations on the Cu(I)-NHC-Phenanthroline complex (see also Paper I), parts of the introduction

Contents

Summary	vii
Zusammenfassung	ix
Danksagung	xi
1 Introduction	1
1.1 Applications - OLEDs	1
1.2 TADF	3
1.3 Heavy atom effect	5
1.4 State of the art	6
1.4.1 Luminescent copper and gold complexes	6
1.4.2 NHC and CAAC ligands	9
2 Theory and methods	11
2.1 Determining the nuclear structure	11
2.1.1 Density functional theory methods	11
2.1.2 Time-dependent DFT and Tamm–Dancoff approximation	14
2.1.3 Scalar–relativistic effects	16
2.2 The electronic structure and properties	17
2.2.1 DFT/MRCI	17
2.2.2 Spin–orbit coupling	21
2.2.3 Spin-free and spin–orbit properties	24
2.3 Solvation effects	26
2.3.1 Continuum solvation models	27
2.3.2 The corrected linear response approximation	28
3 Results	31
3.1 Trigonal NHC-Cu(I)-Phenan complex (Paper I and Book Chapter)	31
3.1.1 Ground state and absorption spectrum	31
3.1.2 Excited states	34
3.2 Linear NHC-Cu(I)-Py complexes (Paper III)	38
3.2.1 Absorption spectra	39
3.2.2 Optimized excited state geometries	42

3.2.3	Effects of the crystal environment	46
3.2.4	Excitation spectra and LIPs	47
3.2.5	Emission	54
3.2.6	Summary and conclusions	58
3.3	Design principles for linear NHC complexes (Paper III)	60
3.3.1	Modification of the NHC substituents	60
3.3.2	Modification of the NHC backbone	61
3.3.3	Introducing $-M$ substituents in the pyridine ligand	63
3.3.4	Combining the $+I$ and $-M$ effects	63
3.3.5	Summary and conclusions	64
3.4	Trigonal NHC-Cu(I)-bis-Py complex (unpublished)	65
3.4.1	Ground state	65
3.4.2	Excited states	66
3.4.3	Radiative and (R)ISC rate constants	67
3.4.4	Linear Py <i>versus</i> trigonal bis-Py	69
3.5	Linear CAAC-Au(I)-Cz and CAAC-Cu(I)-Cz complexes (Paper II)	70
3.5.1	General considerations based on the calculations <i>in vacuo</i>	70
3.5.2	Environmental and structural effects on the absorption and emission properties	71
3.5.3	Prompt fluorescence versus TADF	76
3.5.4	Summary and conclusions	78
4	Conclusions	81
	Bibliography	85
	Appendices	95

List of figures

1.1	Schematic diagram showing the different layers of an OLED.	2
1.2	Schematic overview over the main photophysical processes in three generations of OLED emitters: Fluorescence, phosphorescence and TADF emitters.	3
1.3	Schematic orbital and state energy diagram of two singlet–triplet pairs that are governed by a $d_\sigma \rightarrow \pi^*$ or a $d_\pi \rightarrow \pi^*$ excitation.	5
1.4	Schematic example structures for tetrahedral, trigonal and linear Cu(I) complexes that can be either cationic or neutral.	7
1.5	General structure of NHCs or CAACs. Colored areas indicate positions for substitutions.	9
3.1	Molecular structure with atom numbers	33
3.2	Ground-state scan of the torsion angle between the NHC and phenanthroline ligands. The DFT/MRCI ground-state energies include Grimme D3 dispersion corrections.	33
3.3	Absorption spectra calculated with a) DFT/MRCI and b) TDDFT. The experimental spectrum was recorded in CH_2Cl_2	34
3.4	Ground-state scan of the torsion angle between the NHC and phenanthroline ligand. The DFT/MRCI excitation energies of T_1 , T_2 , and S_1 are given relative to the S_0 energy at the 0° S_0 geometry.	34
3.5	Franck-Condon profiles for the emission of the coplanar T_1 and S_1 structures calculated at 77 K compared to the experimental emission spectrum measured at 77 K in 2-MeTHF.	35
3.6	Fluorescence, phosphorescence and ISC rate constants at the global T_1 minimum.	36
3.7	Chemical structures of the linear NHC complexes with (A) 2-phenyl-pyridine, (B) 2-methyl-pyridine and (C) pyridine as second ligand.	38
3.8	Schematic structures of the linear and trigonal complexes and the crystals of both crystallized from THF solution. As can be seen, crystals of the trigonal complexes display bright luminescence.	38
3.9	Experimental absorption spectra in CH_2Cl_2 (black) [121] and calculated absorption spectra <i>in vacuo</i> (red), <i>in vacuo</i> with spin–orbit coupling effects (orange), for the COSMO (green) and the PCM (blue) CH_2Cl_2 solvation.	40

3.10	Experimental absorption spectra in CH_2Cl_2 (black) [121] and calculated absorption spectra <i>in vacuo</i> with different dihedral angles between the ligands: coplanar (red) and 70° (olive).	40
3.11	DFT/MRCI energies of the most relevant states at all optimized geometries. The energies are given relative to the S_0 energy at the S_0 geometry.	42
3.12	DFT/MRCI difference densities for the T_1 to T_4 at the Phpy S_0 geometry <i>in vacuo</i>	43
3.13	DFT/MRCI difference densities for the TDDFT optimized T_1 and T_2 and the TDA optimized T_1 and T_2 states of the Phpy complex.	43
3.14	DFT/MRCI difference densities for the T_1 to T_4 at the Mepy S_0 geometry <i>in vacuo</i>	44
3.15	DFT/MRCI difference densities for the optimized triplet states of the Mepy complex.	44
3.16	DFT/MRCI difference densities for the T_1 to T_4 at the Py S_0 geometry <i>in vacuo</i>	45
3.17	DFT/MRCI difference densities for the optimized triplet states of the Py complex.	45
3.18	(A) TDDFT energies for the geometry optimization of the $T_{\text{LC/MLCT}}$ geometry after distortion along the imaginary frequency. (B) Distorted geometry at optimization cycle 35.	45
3.19	Calculated absorption spectra for the optimized S_0 geometry <i>in vacuo</i> (red) and the unoptimized crystal structure without (cyan) and with the counterion BF_4^- (brown).	46
3.20	Experimental excitation spectra of the crystal and in neat films for the (A) Phpy, (B) Mepy and (C) Py complex and calculated vertical absorption and 0-0 transitions (<i>in vacuo</i>).	48
3.21	LIPs between the S_0 and S_{MLCT} state calculated <i>in vacuo</i>	50
3.22	LIPs calculated for the Phpy complex between a) the S_{MLCT} (RC=0.0) and the $T_{\text{LC,Phpy}}$ (RC=1.0) minimum and b) the S_{MLCT} (RC=0.0) and the T_{MLCT} (RC=1.0) minimum <i>in vacuo</i>	52
3.23	LIPs for (A) the Mepy and (B) the Py complex between a) the optimized geometry of the S_{MLCT} (RC=0.0) and the $T_{\text{LC,DIPP}}$ (RC=1.0) and b) the optimized geometry of the S_{MLCT} (RC=0.0) and the $T_{\text{LC/MLCT}}$ or the $T_{\text{MLCT/LC}}$ (RC=1.0) plotted with DFT/MRCI energies.	53
3.24	Experimental emission of the crystalline samples and in neat films for the Phpy (A), Mepy (B) and Py (C) complex and calculated vertical absorption and 0-0 transitions (<i>in vacuo</i>).	55
3.25	Calculated Franck-Condon profiles of the emission, vertical emission and 0-0 transitions for (A) the $T_{\text{LC+d,Phpy}}$ of the Phpy complex, (B) the $T_{\text{LC/MLCT}}$ of the Mepy complex and (C) the $T_{\text{MLCT/LC}}$ of the Py complex.	56

3.26	LIP calculated for the Phpy complex between the S_{MLCT} (RC=0.0) and the T_{MLCT} (RC=1.0) minimum <i>in vacuo</i> . The geometry changes that occur between the S_{MLCT} and the T_{MLCT} minimum affect the S_0 energy a lot stronger than the energies of the excited states.	57
3.27	Structures of the linear IPr-Cu(I)-pyridine complexes and their modifications.	60
3.28	Influence of the <i>+I</i> and <i>-M</i> substituents on the adiabatic energies of the S_{MLCT} , T_{MLCT} and $T_{IL/MLCT/LC}$ minima of compounds 6 , 8 and 9 compared to the unsubstituted compound 5	61
3.29	Radiative rates and rates for ISC and RISC between the S_{MLCT} and the $T_{IL/MLCT/LC}$ minimum for compounds 5 and 8	62
3.30	Calculated absorption spectrum of the bis-Py complex. The experimental spectrum is the one which was ascribed to the linear Py complex.	66
3.31	BH-LYP orbitals of (A) the S_0 and (B) the S_1 structure. The S_0 HOMO has strong d_{xz} and the HOMO-1 d_{z^2} character, while the spatial symmetry of the S_1 HOMO seems to be inbetween the two.	66
3.32	Most important geometry changes between (A) the S_0 and (B) the S_1 state: The asymmetric T-shaped distortion in the excited state can be understood by looking at the N-Cu-N bond angles.	67
3.33	Radiative and (R)ISC rate constants for the bis-Py complex.	68
3.34	Vertical S_1 emission for the S_1 structures with a coplanar or perpendicular arrangement of the ligands for (A) the CMA1 and (B) the CMA2 complex calculated with DFT/MRCI in different environment.	72
3.35	Schematic diagram of the dipoles moments of CMA1 and CMA2 in (a) the ground and (b) the excited state and (c) the reorganization of the solvent molecules according to the excited state.	73
3.36	Radiative and (R)ISC rate constants for the coplanar S_1 and T_1 structures of CMA1 and CMA2 in solution (cLR).	77

List of tables

3.1	Experimental copper bond lengths of the crystal structure and calculated bond lengths of the ground state minimum for four DFT functionals with varying HF exchange percentage.	32
3.2	Experimental copper bond lengths of the crystal structure and calculated bond lengths of the ground state minimum for a variation of the copper basis set cc-pVNZ with N=2 (DZ), N=3 (TZ) and N=4 (QZ).	32
3.3	Comparison of the absorption wavelength λ and the oscillator strength $f(L)$ for the states at the S_0 minima with a coplanar arrangement of the ligands and the corresponding states at the S_0 geometry with an interligand dihedral angle of 70°	41
3.4	Vertical transition energies in [nm] of the lowest singlet and the triplet states below the S_1 at the S_0 geometry <i>in vacuo</i> and in CH_2Cl_2 and of the corresponding states for the unoptimized crystal structure without and with point charges (BF_4^-).	47
3.5	Radiative rate constants for the singlet and triplets at their minima and ISC rate constants between the S_{MLCT} and the respective triplet minimum. . . .	51
3.6	Experimental emission onsets and maxima λ_{max} of the crystalline samples and in neat films. Calculated 0-0 and vertical transitions of the relevant optimized triplets.	54
3.7	Rate constants k (s^{-1}) for radiative decay of the singlet and triplets of compounds 5 , 6 , 8 and 9 at their minima and rate constants for ISC and RISC between the S_{MLCT} and the respective triplet minimum.	62
3.8	Emission wavelengths λ_{max} (nm) of the singlet and triplets of compounds 5 , 6 , 8 and 9 at their minima.	63
3.9	Vertical DFT/MRCI energies and characterization of the lowest lying singlet and triplet states at the optimized S_0 geometry.	65
3.10	SOCMEs between the S_1 and the triplets below the S_1 at the S_0 geometry. .	65
3.11	SOCMEs between the S_1 / S_2 and the T_1 / T_2 state at the optimized S_1 and T_1 minima.	68
3.12	TDDFT and DFT/MRCI adiabatic energies of the S_1 or T_1 geometries with a coplanar (plan.) and a perpendicular (perp.) arrangement of the ligands optimized <i>in vacuo</i>	71

3.13 Radiative rate constants for CMA1 and CMA2 in chlorobenzene with either PCM or cLR solvation. The fluorescence rate constant k_F and the phosphorescence rate constant k_P were computed at the respective S_1 or T_1 structures with a coplanar (plan.) and a perpendicular (perp.) arrangement of the ligands.	75
3.14 Spin-orbit coupling matrix elements computed at the coplanar T_1 and S_1 geometries of CMA1 and non-radiative rate constants (ISC from S_1 to T_1 and RISC from T_1 to S_1) calculated at 298 K and 77 K.	75
3.15 Spin-orbit coupling matrix elements computed at the coplanar T_1 and S_1 geometries of CMA2 and non-radiative rate constants (ISC from S_1 to T_1 and RISC from T_1 to S_1) calculated at 298 K.	76

Chapter 1

Introduction

The introduction aims to give the reader an overview over the possible applications of luminescent Cu(I) and Au(I) transition metal complexes, the current state of scientific research and the unresolved issues that I address in this thesis. The reader gets a first insight into the photophysics of coinage metal complexes and the influence of the molecular structure as well as environmental effects on the emission behavior. Thereby, I establish the context and the motivation for my research on several Cu(I) complexes and one Au(I) complex.

1.1 Applications - OLEDs

Among the variety of possible applications for transition metal complexes, I will focus on their use in organic light emitting diodes (OLEDs), since it was the aim of my research to achieve a better understanding of the underlying photophysics and thereby to enable a systematic improvement of the luminescence properties of the investigated complexes.

OLEDs can be used as light sources in displays such as mobile phone displays or television screens, in lamps or even as large window-like panes that are transparent during daytime, but emit light when it gets dark. Compared to inorganic LEDs, OLEDs are supposed to be easier and cheaper to produce and to have other useful properties such as a higher mechanical flexibility of the devices [1-5].

Figure 1.1 shows a schematic multi-layer structure of an OLED. If voltage is applied, charge carriers, i.e. electrons and holes, start to move from the cathode and anode towards each other. The injection layers facilitate the carrier injection from the conductor to the organic layer. The electrons and holes migrate through the transport layers and recombine in the emission layer that consists of a host doped with the dye molecules [4, 6, 7]. Recombination of the electrons and holes leads to exciton formation — according to spin-statistics 25% of singlet and 75% of triplet excitons are formed [8, 9]. One of the typical performance metrics of an OLED is the external quantum efficiency (η_{EQE} or EQE) which includes the fraction of electrons and holes that actually recombine (γ), the fraction of generated singlet or triplet excitons ($\eta_{s/t}$), the photoluminescence (PL) quantum yield

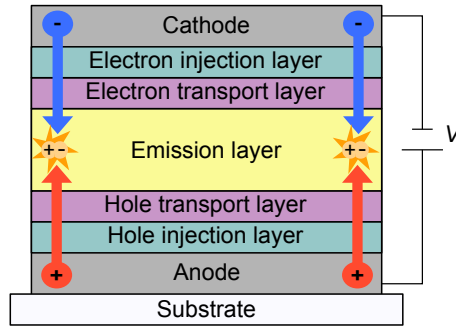


FIGURE 1.1: Schematic diagram showing the different layers of an OLED.

of the emitter material (Φ_{PL}) and the light outcoupling efficiency (η_{out}), i.e. the fraction of generated photons that eventually escape the device (and is not e.g. reabsorbed) [10]:

$$\eta_{EQE} = \gamma \times \eta_{s/t} \times \Phi_{PL} \times \eta_{out} \quad (1.1)$$

For modern multilayer devices one can assume that γ is close to one [10]. The photoluminescence (PL) quantum yield is defined as:

$$\Phi_{PL} = \frac{k_r}{k_r + \sum_i k_{nr,i}} \quad (1.2)$$

where k_r is the radiative rate constant and $\sum_i k_{nr}$ is sum over all non-radiative rate constants. The product $\eta_{s/t} \times \Phi_{PL}$ is also referred to as internal quantum efficiency (IQE) and solely depends on the emitter material. Since this thesis only treats dye molecules, further discussion will concentrate on this quantity, assuming that increasing the IQE is tantamount to enhancing the EQE of the OLED.

In the next three paragraphs, the performance of three generations of OLED emitters shall be reviewed, including other performance metrics such as brightness, operational lifetime / stability (of the device) and color quality.

The first generation of OLED dyes were small fluorescent molecules. For these molecules, the triplet excitons could not be harvested, because emission lifetimes of the involved triplets were long and therefore radiationless triplet deactivation prevailed (see also Fig. 1.2, left). Therefore $\eta_{s/t} = 0.25$ and an IQE of only $\leq 25\%$ can be achieved. Nevertheless, fluorescence emitters have several advantages, such as short emission lifetimes, high operational stabilities and clear colors due to narrow emission bands [11].

The main shortcoming — the low IQE — of fluorescence emitters is overcome in the second generation of OLED emitters, where phosphorescent emitters were employed. Here, the emitter molecules are typically transition metal complexes and the excited singlet states can undergo fast intersystem crossing (ISC) to the triplet states. Because now the phosphorescence can compete with the non-radiative processes, in principle all excitons can be harvested ($\eta_{s/t} = 1$), resulting in internal efficiencies of up to 100% [12]. Although the higher IQEs of the second generation can be seen as an advantage, it comes at the cost of

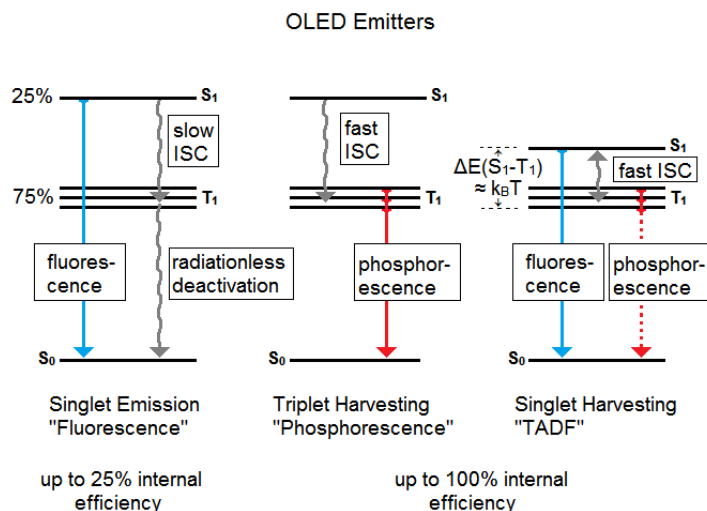


FIGURE 1.2: Schematic overview over the main photophysical processes in three generations of OLED emitters: Fluorescence, phosphorescence and TADF emitters.

longer emission lifetimes (microsecond regime) and therefore lower operational stabilities compared to the first generation. Besides, Ir and Pt, which belong to the most commonly used transition metals used for the second generation, are rather costly.

The third generation consists of organic donor–acceptor molecules and transition metal complexes of cheaper metals, such as Cu, that exhibit small singlet–triplet gaps. The gap energy lies within the range of several $k_B T$ and thus can be overcome by thermal energy at room temperature (see also Fig. 1.2, right). In other words, for these molecules not only ISC, but also reverse ISC (RISC) is possible. As consequence, the triplet excitons are converted to singlet excitons and a delayed fluorescence — called thermally activated fluorescence (TADF) — can be observed [13]. In this way, IQEs of up to 100% can be obtained for this class of OLED emitters, too. Small singlet–triplet gaps are commonly realized for excitations with strong charge transfer (CT) character. CT character yet again implies comparably low radiative rate constants ($10^6 - 10^7 \text{ s}^{-1}$) and additionally broad emission bands, which is detrimental to the desired clear colors [11]. Nevertheless, one might exploit the ability of the TADF emitters to convert triplet to singlet excitons by using them as assistant dopants. Adachi and coworkers did so, employing organic TADF dopants that transfer their excitation energy via Förster resonant energy transfer (FRET) to a fluorescence emitter [14].

1.2 TADF

As mentioned before, one of the main prerequisites for efficient TADF is a sufficiently small singlet–triplet gap that can be overcome by thermal energy at RT. The singlet–triplet gap

is in general small for excitations with a small density overlap, i.e. CT transitions, since the energy splitting between a singlet–triplet pair depends on the exchange integral. In addition, ISC and RISC should be fast and the radiative rate constant should be high, in order to outcompete non-radiative deactivation processes and to achieve high quantum yields.

Let us assume for the moment that no other states are involved and that the Condon approximation applies, i.e. that the electronic and the vibration part of the wavefunction can be separated. That means, that the ISC and RISC rate constants depend on the one hand on the vibrational overlap and on the other hand on the spin–orbit coupling matrix elements (SOCMEs) (for more details see Section 2.2.3).

Concerning the vibrational overlap, two limiting cases can be distinguished [15, 16]. In the weak coupling limit, where the coordinate displacement between the normal modes of the two involved states is small, the vibrational overlap and therefore the transition probability is maximized, if the adiabatic energy gap is minimized (energy gap law). For large coordinate displacements, which is called the strong coupling limit, an inverted dependence might be observed, in other words the transition probability might increase if the gap is increased [17]. Since we might anticipate a small coordinate displacement of the singlet and the triplet due to the similar electronic structures of the two states, the small singlet triplet gap should be favorable for the vibrational overlap.

For the SOCMEs, however, the fact the two wavefunctions mainly consist of the same configurations is disadvantageous. The spin–orbit operator that is needed in order to couple the singlet to the triplet (or vice versa) does not only change the spin, but also the orbital angular momentum, since the total angular momentum has to be conserved. In case of a copper complex, the first excited singlet and triplet wavefunction might e.g. be governed by a d_{σ} to π^* excitation. Since both the singlet and triplet have the same spatial symmetry (no change of the orbital angular momentum), the SOCMEs for the singlet–triplet transition would be small.

The radiative rate constants depend on the square of the electric dipole and the cube of the energy difference between the excited and the ground state. For the fluorescence rate constant we may assume spin–free wavefunctions. While fluorescence rate constant of local excitations lie within the range of $10^8 - 10^9 \text{ s}^{-1}$, the rate constants of CT states, where the density overlap is small, are of the order of $10^5 - 10^6 \text{ s}^{-1}$ [18]. For the spin–forbidden T_1 to S_0 transition, spin–mixed wavefunctions have to be employed. In terms of first order perturbation theory, the transition dipole moment for the T_1 to S_0 transition can be seen as a with spin–orbit coefficients weighted sum of transition dipole moments of spin–allowed transitions. The factors that influence the phosphorescence rate constant are therefore the magnitude of the dipole moments of spin–allowed transition, as well as the SOCME between the triplet and the singlets and their energy differences (see also Section 2.2.3).

All in all, that means that it is difficult within this first approximation we made (no

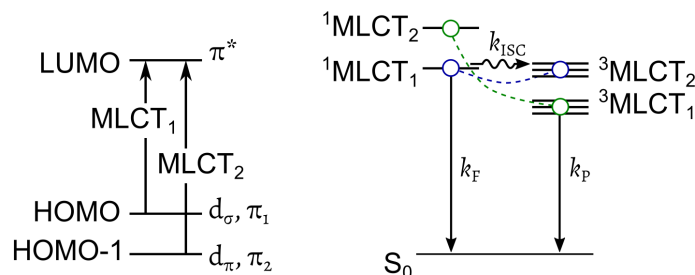


FIGURE 1.3: Schematic orbital and state energy diagram of two singlet–triplet pairs that are governed by a $d_\sigma \rightarrow \pi^*$ or a $d_\pi \rightarrow \pi^*$ excitation. The colored arrows indicate large spin–orbit coupling between the states with a change of the angular momentum ($d_\sigma \leftrightarrow d_\pi$).

other states involved, Condon approximation) to simultaneously achieve sufficiently small singlet–triplet gaps as well as high (R)ISC and radiative rate constants. If, however, another singlet–triplet pair lies close by that couples strongly with the S_1 and T_1 state, this can enhance the ISC either directly or indirectly. An indirect enhancement can be obtained, if the additional singlet–triplet pair mixes in through spin–orbit coupling, but does not participate directly [19]. If the additional triplet lies about isoenergetic or below the S_1 , it is also possible that the ISC occurs between the S_1 and the additional triplet with subsequent internal conversion to the T_1 . More specifically, for our example of a copper complex with a $^1(d_\sigma\pi^*)$ state a $^3(d_\pi\pi^*)$ might lie close by which, due to the change in the angular momentum ($d_\sigma \leftrightarrow d_\pi$), exhibits large SOCMEs with the $^1(d_\sigma\pi^*)$ state (see Fig. 1.3). Especially in case of purely organic TADF molecules, another important effect that can enhance ISC is vibronic coupling.

1.3 Heavy atom effect

In literature, the explanation of the different photophysical properties of Cu(I) and Au(I) complexes is sometimes based on the internal heavy atom and external heavy atom effect. These terms might be confusing since both Cu(I) and Au(I) complexes obviously contain a fairly heavy atom. Originally, the external heavy atom effect was experimentally observed and theoretically investigated [20, 21] for organic molecules for which the $T_1 \rightarrow S_0$ transition is significantly enhanced by additional organohalides or halide anions. This enhancement can be rationalized by the configuration interaction wavefunction of the mainly local T_1 state which has CT contributions involving the lone pairs of the halides:

$${}^3\Psi_1 = \langle T_1^{local} | + c \langle {}^3CT | \quad (1.3)$$

In a similar fashion, the S_0 wave function might also have contributions from lone pairs with a different spatial symmetry than those contributing to the T_1 state, leading to non-negligible SOCMEs between T_1 and S_0 . In case of Cu(I) and Au(I) complexes, the

observed ISC and phosphorescence of Cu(I) complexes are often equally or even more efficient than for Au(I) complexes, although one might expect the SOC in Au(I) complexes to be a lot larger due to the larger effective nuclear charge of Au. However, in Cu(I) complexes the leading configuration of the T_1 state often has significant metal-to-ligand charge transfer (MLCT) character while in many Au(I) complexes the leading configuration has mainly $\pi \rightarrow \pi^*$ character [22]. So one might argue that the Au(I) complexes 'rely' on the larger effective nuclear charge of Au that comes in through some additional contributions (external heavy atom effect), while the Cu(I) complexes profit from the larger amount of MLCT contributions (internal heavy atom effect). I am, however, not really convinced by this distinction (i.e. internal and external), since we need in any case some amount of MLCT contributions to the excited wavefunction, be it Cu(I) or Au(I). For two Cu(I) and Au(I) complexes with the same ligands studied in this thesis, it is actually the leading configuration of the first excited singlet and triplet of the Au(I) complex that has some small metal $5d$ contributions, while for the Cu(I) complex metal $3d$ contributions are only found in additional configurations and not in the leading one. In other words, one can argue that in this case we have an internal heavy atom effect for the Au(I) complex. In the end, the main question is what the total amount of metal d contributions is, and not whether it comes in through the leading or through other configurations.

1.4 State of the art

1.4.1 Luminescent copper and gold complexes

The majority of complexes investigated for this thesis are mononuclear copper complexes and I will therefore concentrate on the research done in this field and outline the insights already gained on the influence of the molecular structure as well as environmental effects on the emission behavior.

Coordination number

The coordination number of the group 11 d^{10} ions varies between two and four. In 2004, Carvajal et al. found that, looking at the structures published in the Cambridge Structural Database, about 5/8 of the Cu(I) complexes are tetracoordinate, about 1/4 tri- and about 1/8 are dicoordinate, while for Au(I) the vast majority is dicoordinate [23]. The Ag(I) complexes show tendencies closer to that Cu(I) with about 1/2 tetracoordinate, about 1/4 tri- and about 1/4 are dicoordinate complexes. The authors tried to rationalize this behavior by model calculations on $[MX_mL_n]^{(1-m)}$ (with $M = \text{Cu/Ag/Au}$, $L = \text{NH}_3/\text{PH}_3$, $X = \text{Cl/Br/I}$, $m + n = 2 - 4$), where they started with the dicoordinate complexes and in two steps inserted the additional ligands. Carvajal et al. divided the formation energy into parts that account for the geometry distortions necessary to insert the new ligand and a part that accounts for the (stabilizing) interaction of the previous complex and the entering ligand. From their DFT calculations they conclude that the much higher

deformation energies necessary in case of Au(I) compared to Ag(I) and Cu(I), lead to the trend that Au(I) usually only forms dicoordinate complexes. Concerning the ligands they found that phosphine is more stabilizing than ammonia and for the halides that $\text{Cl} > \text{Br} > \text{I}$.

Tetrahedral Cu(I) complexes

The tendency of Cu(I) to form tetracoordinate complexes is also reflected in the number of publications concerning luminescent Cu(I) complexes. Most of the tetracoordinate complexes fall into the following groups: $[\text{Cu}(\text{N}^{\wedge}\text{N})_2]^+$ [24–26], $[(\text{P}^{\wedge}\text{P})\text{Cu}(\text{N}^{\wedge}\text{N})]^+$ or $(\text{P}^{\wedge}\text{P})\text{Cu}(\text{N}^{\wedge}\text{N})$ [22, 27–39] and $(\text{P},\text{P})_2\text{CuX}(\text{N})$ or $(\text{P})\text{CuX}(\text{N}^{\wedge}\text{N})$ [40–44] with N or $\text{N}^{\wedge}\text{N}$ representing mono- or bidentate imine or deprotonated amine ligands, P or $\text{P}^{\wedge}\text{P}$ representing mono- or bidentate phosphine ligands and $\text{X} = \text{Cl}, \text{Br}$ or I . Figure 1.4 shows some example structures of Cu(I) complexes with coordination numbers 2–4.

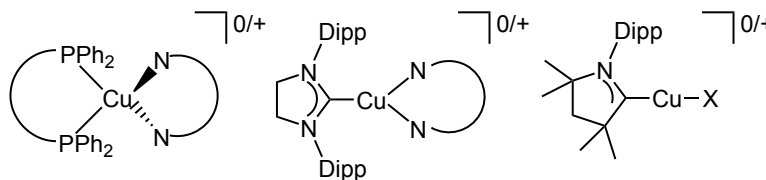


FIGURE 1.4: Schematic example structures for tetrahedral, trigonal and linear Cu(I) complexes that can be either cationic or neutral.

For solids of complexes measured at 77 K where phenantroline or bipyridine is the chromophore ligand the emission colors range between about 560–700 nm (yellow-green to red) and for those complexes with mono- or bidentate pyridine and substituted pyridine ligands being the chromophore ligand emission colors range between about 460–550 nm (blue to yellow-green). For complexes where POP is the chromophore ligand, solids measured at 1.6 K gave emission energies between about 450–470 nm (blue), while films of complexes with dppb measured at 77 K gave emission energies between about 510–560 nm (green to yellow-green). At temperatures of 77 K and below, the emission is most likely phosphorescence, independent of whether the complex shows TADF at room temperature (RT) or not, since at temperatures that low, there is not enough thermal energy to repopulate the singlet. Indeed, many of the tetrahedral complexes show temperature dependent emission shifts as well as shifts that depend on the environment. Shifts that occur between solution and solids or between films and solids, are ascribed to flattenings of the complexes in the excited state [22, 29, 32, 34, 36]. For complexes with phenantroline or bipyridine ligands that have methyl groups at the 2- and 9-, or 6- and 6'-position, respectively, smaller shifts are reported, due to a higher rigidity of the complexes [32, 34]. Increasing the rigidity of the environment, either by going from solution to films to solids or by inserting substituents, leads to a blue-shift of the emission. Besides, a larger rigidity leads to increased quantum efficiencies, since it reduces the emission quenching due to the flattening motion. The

blue-shift that is observed for many of the complexes when the temperature is increased from ≤ 77 K to RT is assigned to TADF [27, 29–33, 35–37, 42, 43].

Another effect in solution that was discussed in connection with the flattening of the complexes is that of exciplex formation. Since for the majority of the complexes the lowest excited singlet or triplet is an MLCT state, the Cu(I) is at least partially oxidized to Cu(II) and undergoes Jahn-Teller distortion. The flattening, on the other hand, is supposed to 'open' a fifth coordination side, such that donor solvents like acetonitrile could coordinate to the complex in the excited state, leading to quenching and lifetime shortenings in donor solvents [25, 45]. In 2015, however, Capano et al. could show that the lifetime shortening is not due to exciplex formation [46]. For a variety of bisphenantroline complexes they carried out MD simulations which led to the conclusion that the solute-solvent interactions responsible for the lifetime shortening are already present in the ground state and are only of transient nature.

Trigonal Cu(I) complexes

One of the most widely used ligand families employed for tricoordinate Cu(I) complexes is that of the N-heterocyclic carbenes (NHCs). The majority of luminescent NHC Cu(I) complexes reported in literature are of the type $[(\text{NHC})\text{Cu}(\text{N}^{\wedge}\text{N})]^+$ or $(\text{NHC})\text{Cu}(\text{N}^{\wedge}\text{N})$ [47–52], where $\text{N}^{\wedge}\text{N}$ is again a bidentate imine or deprotonated amine ligand and the NHC is in most of the cases $\text{IPr} = 1,3\text{-bis}(2,6\text{-diisopropylphenyl})\text{imidazol-2-ylidene}$. The interligand dihedral angle is for most of the complexes either close to 0° or about $70\text{--}90^\circ$. A new carbene ligand class that is also employed for the trigonal complexes is that of the cyclic alkyl(amino)carbenes (CAAC) [53, 54]. Properties of the NHC and CAAC ligands will be discussed in some detail in Section 1.4.2. In addition, phosphines are another group of ligands sometimes chosen for tricoordinate Cu(I) complexes. This group comprises $(\text{P}^{\wedge}\text{P})\text{CuX}$ and $(\text{P},\text{P})\text{Cu}(\text{N})$ [55–57], where $\text{P}^{\wedge}\text{P}$ represents a bidentate and P,P a mono- or bidentate phosphine ligand and $\text{X} = \text{Cl}, \text{Br}, \text{I}$.

Due to the different coordination geometry, the tricoordinate complexes do not undergo flattening distortions in the excited state, however, still many of the complexes exhibit only small quantum yields ($\lesssim 0.2$) in solution [47–50]. Another excited state distortion discussed for the trigonal complexes is a Y- or T-shaped distortion [47].

For most of the complexes, the imine or deprotonated amine is the chromophore ligand. One exception are complexes with a monodentate NHC ligand and a bidentate di(2-pyridyl)dimethylborate ligand (where two pyridine rings are bridged by a dimethylborate) investigated by Krylova et al. [49] and Leitl et al. [50]. For these complexes, also the NHC ligand participates to a varying extent in the excitation. The authors therefore find that the interligand dihedral between the NHC and the di(2-pyridyl)dimethylborate ligand has a large impact on the emission properties of the investigated complexes. Depending on the dihedral angle they either observed phosphorescence or TADF. In Section 3.1 these

findings will be discussed in some more detail and contrasted to the results obtained for an NHC-Cu(I)-phenantroline complex.

Linear Cu(I) and Au(I) complexes

Only very recently, linear copper complexes that show luminescence could be synthesized — until then they were believed to be non-emissive. Five articles were published in the course of the last two years, reporting luminescent linear copper complexes where one or two of the ligands are either CAACs or diamido carbenes (DACs) [53, 58–61]. Some of the publications also include linear Au(I) complexes [58–60]. For several of the copper complexes red-shifts in coordinating solvents were again assigned to exciplex formation [58, 60]. The corresponding gold complexes did not show this behavior.

The Au(I) and Cu(I) complexes with a CAAC and a carbazolate ligand investigated by Di et al. exhibit outstandingly fast ISC in the picosecond regime and EQEs of up to 27% [59]. According to the authors, the fast intersystem crossing can be explained by an intersection of the S_1 and T_1 potential surfaces that occurs upon rotation of the carbazolate ligand. For less rigid environments they observed a red-shift of the emission from blue to green, supporting their assumption of a 'spin-state inversion'. In less rigid environments the ligand can rotate freely leading to the an inverted singlet–triplet gap, while for more rigid environments ligand rotation is hindered. Their studies and conclusions will be further scrutinized in Section 3.5, where I will demonstrate that no spin-state inversion occurs and that the energy shifts can be traced back to (hindered) solvent reorganization. Two other theoretical articles that, in agreement with my results, also undermine the hypothesis of a spin-state inversion will be discussed, too [62, 63].

1.4.2 NHC and CAAC ligands

The electronic structure of NHCs and CAACs as well as their steric demand make them viable ligands for the stabilization of trigonal and linear copper complexes.

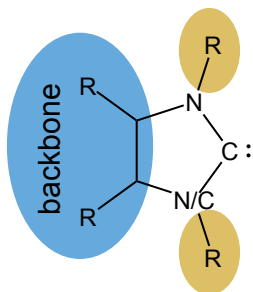


FIGURE 1.5: General structure of NHCs or CAACs. Colored areas indicate positions for substitutions.

π donating quaternary carbon [65, 66]. The electronic and steric properties of the NHC

The lone pair of the divalent carbon is assumed to be stabilized by the electron-withdrawing properties of nitrogen, while the nitrogen p_π electrons are supposed to stabilize the empty p_π^* orbital of the carbon atom [64]. The carbene metal bond is often described by a σ donation of the carbene lone pair into an empty metal d_σ orbital and a π backdonation of an occupied metal d_π into the empty p_π^* of the carbene carbon [64]. While NHC ligands are already seen as good σ donors, CAACs are supposed to be even better σ donors but also π acceptors, since one of the nitrogens is replaced by a σ donating but not π donating quaternary carbon [65, 66]. The electronic and steric properties of the NHC

and CAAC ligands can be tuned by substitutions at the backbone and at the nitrogen or quaternary carbon atoms (see Fig. 1.5). Section 3.3 covers some design principles for copper complexes with NHC ligands derived from quantum chemical investigations.

Chapter 2

Theory and methods

This chapter is divided into several sections dealing with the different levels of an accurate quantum chemical description of the nuclear and electronic structure of transition metal complexes. The first section is dedicated to the methods mainly used for the nuclear structure, that is for the retrieval of equilibrium geometries. Herein, I describe the density functional theory methods employed for the optimization of ground and excited states as well as the inclusion of scalar-relativistic effects through ECPs. The second section deals with the methods employed for an accurate treatment of the electronic structure. The benefits of the combined density functional theory and multi-reference configuration interaction method as well as the inclusion of spin-orbit coupling effects are detailed in this section. As some of the studied molecules exhibit large changes of their dipole moments upon excitation, environmental effects on their structures and properties need to be included. The last section therefore addresses the treatment of solvation effects.

2.1 Determining the nuclear structure

2.1.1 Density functional theory methods

Density functional theory (DFT) offers the possibility to include the correlation energy that is missing in Hartree-Fock (HF) theory while being comparable to HF calculations concerning the computational costs.

The basic idea of DFT is that all information about the system can be derived from the electron density. All observables of the system can be expressed as functionals of the electron density.

The relation between the electronic wave function and the electron density can be rationalized by looking at the probability density. The probability of finding electron 1 of an N-electronic wavefunction $\Psi(x_1, x_2, \dots, x_N)$ in the volume element dr_1 and finding the other electrons anywhere in the considered spatial area can be determined by integration over the spin coordinate ds_1 of electron 1 and the space-spin coordinates of all the other electrons [67]:

$$dr_1 \int \dots \int |\Psi(x_1, x_2, \dots, x_N)|^2 ds_1 dx_2 \dots dx_N \quad (2.1)$$

Multiplying by N gives the probability of finding any of the N electrons in dr_1 . Division through dr_1 eventually gives the corresponding probability density, which is the electron density $\rho(dr_1)$:

$$\rho(dr_1) = N \int \dots \int |\Psi(x_1, x_2, \dots, x_N)|^2 ds_1 dx_2 \dots dx_N \quad (2.2)$$

Since all we need for the electronic Hamiltonian

$$\hat{H} = \hat{T} + \hat{V}_{ne} + \hat{V}_{ee} = - \sum_i^N \frac{1}{2} \nabla_i^2 - \sum_i^N \sum_A \frac{Z_A}{r_{Ai}} + \sum_{i < j}^N \frac{1}{r_{ij}} \quad (2.3)$$

is the number of electrons and the external potential \hat{V}_{ne} , it is easily understood that the electron density $\rho(r)$ determines the Hamiltonian (Bright Wilson observation [68]). The number of electrons N can be obtained by integration of the density. The positions and charges of the nuclei, which are required for \hat{V}_{ne} , correspond to cusps of the electron density at the positions of the nuclei and the slopes of these cusps.

The formal proof that the electronic ground state energy can be expressed as a functional of the ground state electron density was offered by Hohenberg and Kohn in 1964 [69]. The proof is a *reductio ad absurdum*, showing that there *cannot* be two external potentials $v_1(r)$ and $v_2(r)$ that differ by more than a constant and that each give the same density $\rho(r)$. Conversely, this means that there is a one-to-one mapping between the external potential and the electron density, which is why the electronic energy can be written as a functional of the electronic density:

$$E_0 = E[\rho_0] = T[\rho_0] + V_{ne}[\rho_0] + V_{ee}[\rho_0] \quad (2.4)$$

The second Hohenberg–Kohn theorem states that the ground state energy $E[\rho_0]$ could in principle be determined in a variational manner analogous to the variation principle for wavefunctions. For a test density $\tilde{\rho}$ and its test wavefunction $\tilde{\Psi}$ one could therefore write:

$$\langle \tilde{\Psi} | \hat{H} | \tilde{\Psi} \rangle = \int \tilde{\rho}(r) v(r) dr + T[\tilde{\rho}] + V_{ee}[\tilde{\rho}] = E[\tilde{\rho}] \geq E[\rho_0] \quad (2.5)$$

In order to obtain the density, the energy has to be minimized with respect to density variations, subject to the constraint that

$$\int \rho(r) dr = N. \quad (2.6)$$

Using this constraint in a Lagrange minimization, one can write

$$\frac{\delta}{\delta \rho(r)} \left(E[\rho] - \mu \left[\int \rho(r) dr - N \right] \right) = 0 \quad (2.7)$$

for the minimization of a functional $E[\rho]$ [67]. From this equation one eventually obtains the Euler-Lagrange equation

$$\mu = v(r) + \frac{\delta T[\rho]}{\delta \rho(r)} + \frac{\delta V_{ee}[\rho]}{\delta \rho(r)} \quad (2.8)$$

which can be solved in order to get the exact density. However, this is only true if we know the exact form of the functionals. Unfortunately, the exact form of the functionals is unknown, which is the major problem of DFT.

A practical approach to this problem was introduced by Kohn and Sham [70]. The basic idea was to introduce orbitals and to rewrite the expression for the exact energy in such a way, that all terms but one can be written as exact functionals. The one remaining term should be small and contain the 'unknown' part of the functional. That means rewriting

$$E[\rho] = T[\rho] + V_{ne}[\rho] + V_{ee}[\rho] \quad (2.9)$$

as

$$E[\rho] = T_s[\rho] + J[\rho] + E_{XC}[\rho] \quad (2.10)$$

where $J[\rho]$ is the classic Coulomb repulsion, $T_s[\rho]$ is the kinetic energy of a system of non-interacting electrons and $E_{XC}[\rho]$ is the exchange-correlation functional that contains the 'unknown' part of the energy functional. It can be written as the difference between the true kinetic energy and $T_s[\rho]$ and the true electron-electron interaction $V_{ee}[\rho]$ and $J[\rho]$

$$E_{XC}[\rho] = (T[\rho] - T_s[\rho]) + (V_{ee}[\rho] - J[\rho]). \quad (2.11)$$

The corresponding Euler–Langrange equation is

$$\mu = v_{eff}(r) + \frac{\delta T_s[\rho]}{\delta \rho(r)} \quad (2.12)$$

where the non-interacting electrons move in an external potential [67, 70]

$$v_{eff}(r) = v(r) + \frac{\delta J[\rho]}{\delta \rho(r)} + \frac{\delta E_{XC}[\rho]}{\delta \rho(r)}. \quad (2.13)$$

Since no approximations were made, this equation still yields the exact density of the real system. The Hamiltonian of a system of non-interacting electrons is separable and the electron density can therefore be obtained from the solution of N single orbital equations (Kohn–Sham equations) [70]:

$$\left(-\frac{1}{2}\nabla_i^2 + v_{eff}(r) \right) \varphi_i(r) = \epsilon_i \varphi_i(r) \quad (2.14)$$

and

$$\rho(r) = \sum_i^N \varphi_i^2(r) \quad (2.15)$$

Since the electron density is unknown at the beginning of a calculation and $v_{eff}(\mathbf{r})$ depends on the density, the Kohn–Sham equations have to be solved in an iterative manner. A first guess for the electron density could be a superposition of atomic density functions. This initial guess can be used to calculate v_{eff} and thus solve the Kohn–Sham equations. The orbitals achieved in this way can be used to construct a new, improved density, which again gives a new $v_{eff}(\mathbf{r})$ and so on, until convergence is reached.

Kohn–Sham theory is still exact — if the exact $E_{XC}[\rho]$ was known, the Kohn–Sham equations would give the exact density and properties of the real system. Since the exact functional is unknown, different approximations were developed in the course of time for the exchange–correlation functional. The most simple ones are the Local Density Approximation (LDA) where the energy is a functional of just the density and its extension the Local Spin Density Approximation (LSDA) where alpha and beta electrons are placed in different Kohn–Sham orbitals. The next level is the Generalized Gradient Approximation (GGA) where the energy is not only a functional of the density, but also of the gradient of the density. Inclusion of higher derivatives of the density leads to the Meta-GGAs. The most widely used functionals are the so called hybrid functionals where $E_{XC}[\rho]$ is a weighted sum of DFT exchange correlation and the exact Hartree–Fock (HF) exchange. For this thesis two hybrid functionals were employed — the PBE0 functional with 25% HF exchange [71, 72] for the geometry optimization and the BH-LYP with 50% HF exchange [73, 74] for the DFT/MRCI calculations.

2.1.2 Time-dependent DFT and Tamm–Dancoff approximation

Time-independent DFT is only applicable for electronic ground states. For excited states, however, time-dependent DFT can be employed. Runge and Gross could show that — in analogy to the first Hohenberg–Kohn theorem — the time-dependent density determines the time-dependent wavefunction up to a time-dependent phase factor [75]. In a time-dependent approach the energy is no longer a conservative quantity. Therefore, it is no longer the energy, but the so called action integral which is subject to the variational procedure of TDDFT. The action integral is a functional of the time dependent density $\rho(r, t)$

$$A[\rho] = \int_{t_0}^{t_1} dt \left\langle \Psi[\rho](r, t) \left| i \frac{\delta}{\delta t} - \hat{H}(r, t) \right| \Psi[\rho](r, t) \right\rangle \quad (2.16)$$

and the time-dependent wavefunction is a stationary point of the action integral [76]. The corresponding Euler equation is

$$\frac{\delta A[\rho]}{\delta \rho(r, t)} = 0. \quad (2.17)$$

As for the time-independent Kohn–Sham formalism, the time-dependent density of a non-interacting system equals the real time-dependent density and can be obtained from the single-electron orbitals $\varphi_i(\mathbf{r}, t)$:

$$\rho(r, t) = \sum_i^N \varphi_i^2(r, t) \quad (2.18)$$

The time-dependent Kohn–Sham equations are

$$\left(-\frac{1}{2}\nabla_i^2 + v(r, t) + \frac{\delta J[\rho]}{\delta \rho(r, t)} + \frac{\delta A_{XC}[\rho]}{\delta \rho(r, t)} \right) \varphi_i(r, t) = i \frac{\delta}{\delta t} \varphi_i(r, t) \quad (2.19)$$

or

$$\hat{F}^{KS} \varphi_i(r, t) = i \frac{\delta}{\delta t} \varphi_i(r, t) \quad (2.20)$$

where A_{xc} is the exchange-correlation part of the action integral. Since the exact time-dependent exchange-correlation action functional (xc kernel) is unknown, the approximation is made that the density varies only slowly with time (adiabatic local density approximation, ALDA), which is why a time-independent local instead of a non-local (in time) time-dependent xc kernel can be used. This approximation allows for the use of standard ground state functionals in the TDDFT framework [76].

Starting from the time-dependent Kohn–Sham equations a non-Hermitian eigenvalue problem can be derived — either from a density-matrix linear response approach or from the poles of dynamic polarizability [76–78] — from which the excitation energies and transition amplitudes can be obtained:

$$\begin{pmatrix} \mathbf{A} & \mathbf{B} \\ \mathbf{B}^* & \mathbf{A}^* \end{pmatrix} \begin{pmatrix} \mathbf{X} \\ \mathbf{Y} \end{pmatrix} = \omega \begin{pmatrix} 1 & 0 \\ 0 & -1 \end{pmatrix} \begin{pmatrix} \mathbf{X} \\ \mathbf{Y} \end{pmatrix} \quad (2.21)$$

ω is the diagonal matrix of the excitation energies and \mathbf{X} and \mathbf{Y} contain the transition amplitudes. For a hybrid functional the elements of matrices \mathbf{A} and \mathbf{B} are given as

$$A_{ia,jb} = \delta_{ij} \delta_{ab} (\epsilon_a - \epsilon_i) + (ia|jb) - c_{HF} (ij|ab) + (1 - c_{HF}) (ia|f_{xc}|jb) \quad (2.22)$$

and

$$B_{ia,jb} = (ia|bj) - c_{HF} (ib|aj) + (1 - c_{HF}) (ia|f_{xc}|bj) \quad (2.23)$$

where i and j correspond to occupied and a and b to unoccupied orbitals, ϵ to the orbital energy and f_{xc} to the exchange-correlation kernel [76]. The two-electron integrals are given in Mulliken notation. The factor c_{HF} inserts the HF exchange of a given hybrid functional. Consequently, for $c_{HF} = 1$ the corresponding TDHF and for $c_{HF} = 0$ the non-hybrid TDDFT equations are obtained.

Neglecting the matrix \mathbf{B} in Equation 2.21 leads to the TDDFT Tamm–Dancoff approximation (TDA) [79]. The — in this case — Hermitian equation reads as follows:

$$\mathbf{A}\mathbf{X} = \omega\mathbf{X} \quad (2.24)$$

The matrix elements of matrix \mathbf{A} are the same as in equation 2.22. The Y amplitudes and the elements of \mathbf{B} , which are usually seen as a measure for correlation effects in the ground state, are in general small. Consequently, the Tamm–Dancoff approximation is usually seen as a good approximation to TDDFT [76, 80].

2.1.3 Scalar–relativistic effects

In order to include relativistic effects into the geometry optimizations, a scalar relativistic pseudopotential was employed for the copper and the gold ions. A pseudopotential allows for the inclusion of relativistic effects into an otherwise non-relativistic calculation, while also reducing the computational costs, since all core electrons and their interactions with the valence electrons do not have to be treated explicitly, but can be represented through a static potential. Relativistic effects play an important role especially for electrons close to the nucleus where for heavy elements they can reach velocities nigh on the speed of light. The result is a contraction of the s orbitals that concomitantly leads to an expansion of the orbitals with an orbital quantum number $l \geq 0$.

Since later on I also want to include spin–orbit coupling effects into my calculations, the pseudopotential for the copper and gold should be one for which a spin–free scalar–relativistic and a spin–orbit formulation can be derived. Such pseudopotentials can be obtained from spin–dependent equations (e.g. the Dirac-Hartree-Fock or the Wood-Boring equation) [81]. A pseudopotential of the general form

$$V^{PP} = U(r) + \sum_{l,j} U_{l,j}(r) \sum_{m_j} |ljm_j\rangle \langle ljm_j| \quad (2.25)$$

where $|ljm_j\rangle \langle ljm_j|$ is a projection operator, can be divided into a spin–free and a spin–orbit potential by taking appropriate averages and differences. Dropping the local potential $U(r)$, the pseudopotential then reads

$$\begin{aligned} V^{PP} &= V^{PP,sf} + V^{PP,SO} \\ &= V^{PP,sf} + \hat{H}_{SO} \\ &= \sum_l U_l^{sf}(r) \sum_{m_l} |lm_l\rangle \langle lm_l| \\ &\quad + \sum_l U_l^{SO}(r) \sum_{m_l, m_{l'}} |lm_l\rangle \langle lm_l| \mathbf{L} \cdot \mathbf{S} |lm_{l'}\rangle \langle lm_{l'}| \end{aligned} \quad (2.26)$$

where

$$U_l^{sf}(r) = \frac{1}{2l+1} [lU_{l,l-1/2} + (l+1)U_{l,l+1}] \quad (2.27)$$

and

$$U_l^{so}(r) = \frac{2}{2l+1} [U_{l,l+1/2} + U_{l,l-1}]. \quad (2.28)$$

$U_l^{sf}(r)$ can be seen as the weighted average of two potentials for two spin-orbit split levels [81].

The operator defined as the second sum in Equation 2.26 will be used as the spin-orbit operator for Cu or Au in the calculation of the spin-orbit integrals (see Section. 2.2.2). For the pseudopotentials used in this thesis (def2-ECP for Au [82] and Stuttgart-Koeln MCDHF RSC ECP [83] for Cu), the potential $U_{l,j}(r)$ was represented in terms of Gaussians

$$U_{l,j}(r) = \sum_k B_{l,j,k} \exp(-\beta_{l,j,k} r^2) \quad (2.29)$$

where the parameters $B_{l,j,k}$ and $\beta_{l,j,k}$ were adjusted to all-electron calculations in such a way that the difference between the energies calculated with the all-electron method and the energies calculated with the pseudopotentials was minimized.

2.2 The electronic structure and properties

2.2.1 DFT/MRCI

As mentioned in Section 2.1.2, the combined DFT/MRCI method was used to calculate energies and other properties (e.g. dipole moments) of the optimized geometries. The idea is to use Kohn-Sham orbitals obtained from a previous DFT calculation as a starting point to build the configuration space for a multi-reference configuration interaction (MRCI) ansatz and thus to combine the benefits from a DFT calculation (good description of dynamical correlation) with the benefits of a MRCI calculation (good description of static correlation).

In a normal, i.e. single-reference, CI ansatz, the wave function is constructed from excitations relative to a single configuration, usually the ground state Φ_0

$$|\Psi_{CI}\rangle = c_0 |\Phi_0\rangle + \sum_{i,a} c_{ia} |\Phi_{ia}\rangle + \sum_{i>j} \sum_{a>b} c_{ijab} |\Phi_{ijab}\rangle + \dots \quad (2.30)$$

Indices i and j correspond to orbitals that are occupied and a and b to orbitals that are unoccupied in the ground state. The second term of Equation 2.30 corresponds to single excitation and the third term to double excitations. If all excitations from all occupied to all unoccupied orbitals were allowed, that would correspond to a full CI expansion. Since full CI is only feasible for small basis sets and small molecules, the expansion is usually truncated after the third term (CI with singles and doubles, CISD). A possible way to improve the CISD approach is to include more reference states into the expansion

$$|\Psi_{MRCI}\rangle = \sum_I (c_I |\Phi_I\rangle + \sum_{i,a} c_{I,ia} |\Phi_{I,ia}\rangle + \sum_{i>j} \sum_{a>b} c_{I,ijab} |\Phi_{I,ijab}\rangle) \quad (2.31)$$

where Φ_I is a set of chosen reference configurations. Choosing Φ to be orthonormal configuration state functions (CSFs), one can write — according to the variational principle — for the energy

$$E = \langle \Psi | \hat{H} | \Psi \rangle = \sum_{IJ} c_I^* c_J \langle \Phi_I | \hat{H} | \Phi_J \rangle = \sum_{IJ} c_I^* c_J H_{IJ}. \quad (2.32)$$

As matrix equation we may therefore write

$$\mathbf{H}\mathbf{c} = E\mathbf{S}\mathbf{c} = E\mathbf{c} \quad (2.33)$$

where the expansion coefficients c_I are collected in the vector \mathbf{c} . Diagonalization of \mathbf{H} yields the eigenvectors \mathbf{c} and the energy eigenvalues.

Starting from the CI Hamiltonian written in second quantization and in terms of the SCF energy and Fock matrix elements (as first proposed by Wetmore and Segal [84]),

$$\begin{aligned} \hat{H} = & E_{SCF} - \sum_i F_{ii} \bar{n}_i + \frac{1}{2} \sum_{ij} \left(V_{iijj} - \frac{1}{2} V_{ijji} \right) \bar{n}_i \bar{n}_j \\ & + \sum_{ij} F_{ij} \hat{\epsilon}_i^j - \sum_{ijk} \left(V_{ijkk} - \frac{1}{2} V_{ikkj} \right) \bar{n}_k \hat{\epsilon}_i^j \\ & + \frac{1}{2} \sum_{ijkl} V_{ijkl} \left(\hat{\epsilon}_i^j \hat{\epsilon}_k^l - \delta_{jk} \hat{\epsilon}_i^l \right) \end{aligned} \quad (2.34)$$

with the SCF energy E_{SCF} and Fock matrix elements F_{ij} for a given reference occupation vector $|n\rangle$

$$E_{SCF} = \sum_i F_{ii} \bar{n}_i - \frac{1}{2} \sum_{ij} \left(V_{iijj} - \frac{1}{2} V_{ijji} \right) \bar{n}_i \bar{n}_j \quad (2.35)$$

$$F_{ij} = h_{ij} + \sum_{ijk} \left(V_{ijkk} - \frac{1}{2} V_{ikkj} \right) \bar{n}_k \quad (2.36)$$

S. Grimme and M. Waletzke developed a DFT/MRCI approach, where the matrix elements are divided into four classes (1. same space / same spin, 2. same space / different spin, 3. one-electron difference in space and 4. two-electron difference in space) and build up from the exact CI operator and corrections from DFT [85].

The first class (same space / same spin) are diagonal matrix elements given as

$$\begin{aligned}
\langle \mathbf{n}, \omega \mid \hat{H}^{DFT} - E^{DFT} \mid \mathbf{n}, \omega \rangle &= \langle \mathbf{n}, \omega \mid \hat{H} - E^{HF} \mid \mathbf{n}, \omega \rangle - \sum_{i \in c}^{n_{exc}} (F_{ii}^{HF} - F_{ii}^{KS}) \\
&+ \sum_{i \in a}^{n_{exc}} (F_{ii}^{HF} - F_{ii}^{KS}) + \Delta E_{coul} - \Delta E_{exch}
\end{aligned} \tag{2.37}$$

where \mathbf{n} stands for a spatial occupation vector, ω for a spin-coupling pattern, n_{exc} is the excitation class and a and c refer to annihilated or created electrons, respectively [85, 86]. Here, E^{HF} and F_{ii}^{HF} do not stand for the actual Hartree–Fock energy or orbital energy. The superscripts rather indicate the Hartree–Fock-like manner in which these energies are obtained [86]. The two-electron contributions ΔE_{coul} and ΔE_{exch} need to be scaled, since the orbital energy gaps between occupied and unoccupied molecular orbitals is usually a lot smaller in KS than in HF theories [86]. In the original formulation by Grimme and Waletzke, the (spin-independent) Coulomb interaction is scaled with a parameter p_J , while the exchange integral correction ${}^m p[N_0]$ depends on the multiplicity (i.e. $m = 1$ for singlets and $m = 3$ for triplets) and the number of open shells N_0 . A redesigned Hamiltonian by I. Lyskov et al. [87] also employs a scaling factor p_J for the Coulomb integrals, whereas the exchange integrals are, in this case, scaled with a multiplicity independent parameter p_X (for the spin-dependent part) or $p_X/2$ (for the spin-independent part). The reason for the reformulation of the Hamiltonian was that calculations with the original Hamiltonian led to wrong energies and singlet–triplet splittings for photoexcited dimers where two triplet-excited monomers form a singlet-coupled triplet pair [86–88]. The failure of the original Hamiltonian relates to the original exchange integral correction which underestimates the interaction energy between four active orbitals involved in the configuration and to the aforementioned different scaling of singlet and triplet states. The Coulomb and exchange corrections in the two formulations read as follows

$$\Delta E_{coul}^{orig} - \Delta E_{exch}^{orig} = \frac{1}{n_{exc}} \sum_{i \in c}^{n_{exc}} \sum_{i \in a}^{n_{exc}} (p_J V_{ijij} - {}^m p[N_0] V_{ijji}) \tag{2.38}$$

and

$$\begin{aligned}
\Delta E_{coul}^{red} - \Delta E_{exch}^{red} &= p_J \left(- \sum_{\substack{i,j \in c \\ i > j}}^{n_{exc}} V_{ijij} - \sum_{\substack{i,j \in a \\ i > j}}^{n_{exc}} V_{ijij} \sum_{i \in c}^{n_{exc}} \sum_{i \in a}^{n_{exc}} V_{ijij} \right) \\
&- p_X \left(\frac{1}{2} \sum_{i \in c}^{n_{exc}} \sum_{i \in a}^{n_{exc}} V_{ijji} + \sum_{\substack{i,j \in o \\ i > j}}^{n_{exc}} V_{ijji} \eta_{ij}^j \right).
\end{aligned} \tag{2.39}$$

Herein, a and c are defined as before, o refers to open shells in the occupation vector \mathbf{n} and η_{ij}^{ji} is a spin-coupling coefficient.

The second kind of matrix elements (same space / different spin) are unscaled in case of the original formulation, whereas in the reformulation they are scaled with $(1 - p_X)$, in order to maintain a consistent energy splitting [86, 87]:

$$\langle \mathbf{n}, \omega | \hat{H}^{DFT} | \mathbf{n}, \omega \rangle = \langle \mathbf{n}, \omega | \hat{H}^{CI} | \mathbf{n}, \omega \rangle \quad (2.40)$$

or

$$\langle \mathbf{n}, \omega | \hat{H}^{DFT} | \mathbf{n}, \omega \rangle = \langle \mathbf{n}, \omega | (1 - p_X) \hat{H}^{CI} | \mathbf{n}, \omega \rangle \quad (2.41)$$

Since the dynamic correlation is already covered in the diagonal elements, a damping function is introduced for the off-diagonal elements (one-electron and two-electron difference in space) that damps the interaction between CSFs that would also account for dynamical correlation, while it allows those interactions that account for static correlation [85]. For the same reason, it is not necessary to include a very large number of CSFs (which would be required, if the dynamical correlation was to be covered by the MRCI approach) and some energy criteria were introduced that allow for inclusion of only the most important CSFs. In the original parameterization, a damping function was chosen that depends exponentially on the configuration energy difference $\Delta E_{nn'}$:

$$\langle \mathbf{n}, \omega | \hat{H}^{DFT} | \mathbf{n}, \omega \rangle = \langle \mathbf{n}, \omega | \hat{H}^{CI} | \mathbf{n}, \omega \rangle p_1 e^{-p_2 \Delta E_{nn'}^4} \quad (2.42)$$

In the redesigned Hamiltonian, an arctangent is employed instead [87]:

$$\langle \mathbf{n}, \omega | \hat{H}^{DFT} | \mathbf{n}, \omega \rangle = \langle \mathbf{n}, \omega | \hat{H}^{CI} | \mathbf{n}, \omega \rangle \frac{p_1}{1 + (p_2 \Delta E_{nn'})^5 \arctan(p_2 \Delta E_{nn'})^5} \quad (2.43)$$

Since the damping functions fall off to almost 0 at $\Delta E_{nn'} \approx 1 E_h$, it seemed reasonable to introduce an additional energy threshold ($t_{sel} = e_{sel} + E_{max}^{ref} - E^{DFT}$) that selects configurations that should be included in the CI space or discarded [85, 86]. Grimme and Waletzke found that converged results can be obtained with $e_{sel} = 1 E_h$ and parameterized their Hamiltonian according to this threshold [85]. This e_{sel} threshold is added to the energy of the highest requested root E_{max}^{ref} . If the energy of a configuration (which is approximated by summing up the energies of created and annihilated orbitals) lies above $e_{sel} + E_{max}^{ref}$ the configuration is discarded. Lyskov et al. optimized two sets of parameters, one for $e_{sel} = 1 E_h$ and one for threshold of $e_{sel} = 0.8 E_h$. As it turned out, the steeper decay of the damping function of the redesigned Hamiltonian (Eq. 2.41) in combination with $e_{sel} = 0.8 E_h$ is less well suited for transition metal complexes than for organic molecules, though. A new damping function was therefore introduced by A. Heil et al. [89] that was especially designed for a better agreement with energies of transition

metal complexes. However, these are too recent insights and developments to enter my work. DFT/MRCI calculations for the complexes in Sections 3.1, 3.2, 3.3 and 3.4 were therefore done with the original parameter set of S. Grimme and M. Waletzke and a final threshold of $esel = 1 E_h$, while for the complexes in Section 3.5 the new parameterization by I. Lyskov with the steeper damping and a final threshold of $esel = 0.8 E_h$ was chosen.

2.2.2 Spin-orbit coupling

While scalar-relativistic effects were already accounted for via the scalar-relativistic pseudopotential used in the geometry optimizations and in the generation of the DFT/MRCI one-particle basis, another important relativistic effect — the spin-orbit coupling effect — still needs to be included into the calculations. Spin-orbit coupling is a relativistic effect that couples the spin momentum \mathbf{s} of an electron to its orbital angular momentum \mathbf{l} . As a result, the spin and the orbital quantum numbers are no longer good quantum numbers. Instead, the sum of both $\mathbf{s} + \mathbf{l} = \mathbf{j}$, where \mathbf{j} is the total angular momentum, is the conserved quantity. The same is true for the total spin \mathbf{S} and the total orbital angular momentum \mathbf{L} . Consequently, the spin multiplicities as we know them from non-relativistic theory and the associated spin-forbiddance for transitions between states of different multiplicities are less meaningful for molecules where spin-orbit coupling effects are strong. Hence, spin-orbit calculations were carried out for the determination of spin-orbit coupling matrix elements (SOCMEs) based on the spin-free wave functions. Besides, energies and properties were obtained either by SOC quasi-degenerate perturbation theory (SOC-QDPT) or by multireference spin-orbit configuration interaction (MRSOCI) [90–92].

In a fully relativistic four-component approach, spin and spin-orbit coupling arise naturally. However, neither has a fully relativistic many-electron Hamiltonian been devised yet, nor would any four-component approach be feasible for larger molecules. It is therefore more advisable to use a two-component Hamiltonian which can be divided into spin-free and spin-dependent parts, such as the Breit–Pauli-Hamiltonian [93]. The resulting spin-orbit Breit–Pauli Hamiltonian reads as follows [94]:

$$\begin{aligned}
 \hat{H}_{SO}^{BP} = & \frac{e^2 \hbar}{2m_e^2 c^2} \sum_i \left(-\nabla_i \left(\sum_I \frac{Z_I}{\hat{r}_{iI}} \right) \times \hat{\mathbf{p}}_i \right) \cdot \hat{\mathbf{s}}_i \\
 & + \frac{e^2 \hbar}{2m_e^2 c^2} \left\{ \sum_i \sum_{j \neq i} \left(\nabla_i \left(\frac{1}{\hat{r}_{ij}} \right) \times \hat{\mathbf{p}}_i \right) \cdot \hat{\mathbf{s}}_i \right. \\
 & + \sum_i \sum_{j \neq i} \left(\nabla_j \left(\frac{1}{\hat{r}_{ij}} \right) \times \hat{\mathbf{p}}_j \right) \cdot \hat{\mathbf{s}}_i \\
 & \left. + \sum_i \sum_{j \neq i} \left(\nabla_i \left(\frac{1}{\hat{r}_{ij}} \right) \times \hat{\mathbf{p}}_i \right) \cdot \hat{\mathbf{s}}_j \right\}
 \end{aligned} \tag{2.44}$$

The first term is a one-electron term that couples the spin of electron i to the orbital angular momentum induced by the nucleus I . The second term is a two-electron term that corresponds to the first term, since spin and orbit part stem from the same electron i , but where the field of nucleus I is replaced by the field of electron j . The last two terms couple the spin of electron i to the orbital angular momentum of electron j and vice versa. In order to further reduce the computational costs, several approximations can be made for the two-electron terms [94]. Four-index two-electron integrals can be neglected entirely, since their contribution to the total spin-orbit coupling matrix element between two CI wavefunctions is small. Three-index two-electron integrals, however, have to be included. In a mean-field approximation (that can be seen as an extension of the frozen-core approximation), where the summation runs not only over the core but also the valence space and an averaged occupation number n_k is introduced, a matrix element of the effective one-electron spin-orbit mean-field Hamiltonian reads

$$\begin{aligned} \langle i(1) | \hat{H}_{SO}^{mf} | j(1) \rangle &= \langle i(1) | \hat{h}_{SO} | j(1) \rangle \\ &+ \frac{1}{2} \sum_k n_k \left\{ 2 \langle i(1)k(2) | \hat{H}_{SO}(1,2) | j(1)k(2) \rangle \right. \\ &- 3 \langle k(1)i(2) | \hat{H}_{SO}(1,2) | j(1)k(2) \rangle \\ &\left. - 3 \langle i(1)k(2) | \hat{H}_{SO}(1,2) | k(1)j(2) \rangle \right\} \end{aligned} \quad (2.45)$$

when integration over the spin of electron 2 was already carried out [94].

Rewriting the mean-field Hamiltonian in terms of second quantization, any of its Cartesian components ζ can be expressed as

$$\hat{h}(\zeta) = \sum_{s,t} l_{st}(\zeta) \left(\sum_{\sigma,\tau} s_{\sigma\tau}(\zeta) \hat{a}_{s\sigma}^\dagger \hat{a}_{t\tau} \right) \quad (2.46)$$

where l_{st} is the spin-orbit integral over the ζ component of the spin-orbit operator acting on orbitals s and t , $s_{\sigma\tau}$ is a matrix element of the spin-operator \hat{s}_ζ over the spins σ and τ and $\hat{a}_{s\sigma}^\dagger$ and $\hat{a}_{t\tau}$ are creation and annihilation operators [90]. Apart from the aforementioned approximations, one additional approximation, which is made for the calculation of the spin-orbit integrals, is that all multicenter spin-orbit integrals can be neglected, which is justified by the $1/r^3$ dependence of the spin-orbit operator. Thus, the molecular mean field is replaced by a sum of atomic mean-fields, which has the convenient side effect that atomic spherical symmetry can be used to further reduce the computational costs. The spin-orbit integrals are calculated with the atomic mean-field integral program AMFI [95]. While for all non-metal atoms the atomic mean-field approximation of the Breit-Pauli spin-orbit operator is used, the SOC-ECP mentioned in Section 2.1.3 is employed for copper and gold.

As for the DFT/MRCI calculations, the spin-orbit calculation are carried out in a basis of CSFs [90–92]. A matrix element of the Hamiltonian as defined in Equation 2.46 between two CSFs $|S, \omega, \mathbf{n}\rangle$ and $\langle S', \omega', \mathbf{n}'|$ that differ by a single excitation $b \rightarrow a$ (diagonal elements are zero due to symmetry reasons and higher excitations cannot be coupled by the effective one-electron operator) can be written as

$$\begin{aligned}
 & \left\langle S', \omega', \mathbf{n}' \left| \sum_{s,t} l_{st}(\zeta) \sum_{\sigma,\tau} s_{\sigma\tau}(\zeta) \hat{a}_{s\sigma}^\dagger \hat{a}_{t\tau} \right| S, \omega, \mathbf{n} \right\rangle \\
 &= l_{ab} \left\langle S', \omega', \mathbf{n}' \left| \sum_{\sigma,\tau} s_{\sigma\tau}(\zeta) \hat{a}_{s\sigma}^\dagger \hat{a}_{t\tau} \right| S, \omega, \mathbf{n} \right\rangle \\
 &=: l_{ab} \cdot \eta(S, S', \omega, \omega', \mathbf{n}, \mathbf{n}')
 \end{aligned} \tag{2.47}$$

where S is the multiplicity, ω labels the CSF, \mathbf{n} stands for an orbital occupation, l_{ab} is a spin-orbit (spatial) integral and η is a spin-coupling coefficient [91, 92]. Since the M_S value was set to be $M_S = S$, the \hat{s}_0 , \hat{s}_+ and \hat{s}_- ladder operators (in spherical tensor representation) can be used for the calculation of the $s_{\sigma\tau}$ integrals. Thus, e.g. a singlet with $M_S = 0$ can be coupled to a triplet with $M_S = 1$ by the \hat{s}_+ operator. However, the problem may occur that the symmetry of the spin part does not match the symmetry of the (Cartesian) space part. A transformation of the 'wrong' spin operator to the one that matches the space part is obtained by 'scaled 3j-symbols' by McWeeny [90, 92, 96]. The scaled 3j-symbols make use of the Wigner-Eckart theorem and thus do not only match the symmetries of the spin and the space parts, but also generate matrix elements for all the other M_S quantum numbers.

The spin-orbit integrals can be obtained, as mentioned before, by the AMFI program. The spin-coupling coefficients can be determined in analogy to a procedure developed by Wetmore and Segal for spin-free CI calculations [84, 90–92, 97]. Since the coupling coefficients only depend on the singly and variably occupied orbitals, all doubly occupied orbitals can be excluded from further considerations. For the singly and variably occupied orbitals of two coupling states, a limited number of excitation classes or patterns can be identified for which the same coupling coefficients result.

For the calculation of spin-orbit coupled states and properties by means of SOC-QDPT the spin-orbit Hamilton matrix is build from LS coupled states and then diagonalized. For the MRSOCI calculations, the eigenvectors obtained by diagonalization of the Hamilton matrix in the SOC-QDPT step yields start vectors for the variational determination of the MRSOCI spin-orbit coupled states [92]. Whereas in SOC-QDPT, spin-orbit coupling is introduced only as small perturbation (leaving the spin-free electron interaction unaffected), in the MRSOCI approach spin-orbit coupling and electron correlation are calculated simultaneously, which means that spin-orbit influences the electronic structure and therefore the electron correlation.

2.2.3 Spin-free and spin-orbit properties

Properties of spin-free and spin-orbit MRCI wavefunctions can be obtained by means of (transition) density matrices. Since most the properties of interest (e.g. dipole moments) are expectation values of (spin-free) one-electron operators and since the transition density matrix may be seen as a generalization of the density matrix, the expectation value (for two states Φ and Ψ) may be written as follows

$$\langle \Phi | \hat{F} | \Psi \rangle = \sum_{ij} f_{ij} \langle \Phi | \hat{E}_{ij} | \Psi \rangle = \sum_{ij} f_{ij} \rho_{ij}^{[\Phi\Psi]} = \text{tr} \left\{ \mathbf{f} \boldsymbol{\rho}^{[\Phi\Psi]} \right\} \quad (2.48)$$

where \hat{F} is a one-electron operator and $\boldsymbol{\rho}^{[\Phi\Psi]}$ is the one-electron transition density [98]. For the spin-free MRCI wavefunctions the two states Φ and Ψ are linear combinations of CSFs and the one-electron transition density can be rewritten as

$$\begin{aligned} \rho_{ij}^{[\Phi\Psi]} &= \sum_{\substack{\{\mathbf{n}\} \\ \{\mathbf{n}'\}}} \sum_{\substack{\omega(\mathbf{n}) \\ \omega'(\mathbf{n}')}} a_{\mathbf{n},\omega(\mathbf{n})}^* b_{\mathbf{n}',\omega'(\mathbf{n}')} \left\langle S, M_s = S, \omega, \mathbf{n} \left| \hat{E}_{ij} \right| S, M_s = S, \omega', \mathbf{n}' \right\rangle \\ &= \sum_{\substack{\{\mathbf{n}\} \\ \{\mathbf{n}'\}}} \sum_{\substack{\omega(\mathbf{n}) \\ \omega'(\mathbf{n}')}} a_{\mathbf{n},\omega(\mathbf{n})}^* b_{\mathbf{n}',\omega'(\mathbf{n}')} \eta(S, \omega, \mathbf{n}, \omega'(\mathbf{n}')) \end{aligned} \quad (2.49)$$

where $a_{\mathbf{n},\omega(\mathbf{n})}^*$ and $b_{\mathbf{n}',\omega'(\mathbf{n}')}$ are CSF coefficients and η is again the spin-coupling coefficient. For the spin-orbit coupled wavefunctions, a similar equation can be derived, the main difference being additional sums over the S and M_S quantum numbers [98].

Radiative and intersystem crossing rate constants

Choosing the one-electron operator to be the electric dipole operator, one can calculate transition dipole moments for transitions between spin-mixed states obtained by MRSOCI.

The phosphorescence rate constant depends on the cube of energy difference between the T_1 state (or actually the triplet substates) and the S_0 state and the square of the electric transition dipole moment:

$$k_{T_1} = \frac{4e^2}{3c^3\hbar^4} (\Delta E_{S_0 \leftarrow T_1})^3 |\boldsymbol{\mu}_{el}(S_0 \leftarrow T_1)|^2 \quad (2.50)$$

The spin-forbidden $T_1 \rightarrow S_0$ transition gains allowedness by borrowing of intensity from spin-allowed $S_n \rightarrow S_0$ and $T_n \rightarrow T_1$ transitions and a direct term which involves the difference of the static dipole moments of the S_0 and T_1 states and their mutual SOC. Intensity borrowing can most easily be illustrated by defining the matrix element of the electric transition dipole moment $\boldsymbol{\mu}_{el}$ in terms of first-order perturbation theory as [94]:

$$\boldsymbol{\mu}_{el}(S_0 \leftarrow T_1) = \langle S_0^{(0)} + S_0^{(1)} | \hat{\boldsymbol{\mu}}_{el} | T_1^{(0)} + T_1^{(1)} \rangle \quad (2.51)$$

The first-order perturbation of the triplet wavefunction $|T_1^{(1)}\rangle$ can be written as a weighted sum of singlet state functions $|S_n\rangle$ (leaving out contributions from other triplet as well as from quintet functions):

$$|T_1^{(1)}\rangle = \sum_n^{\text{triplets}} \frac{\langle S_n | \hat{H}_{\text{SO}} | T_1 \rangle}{E(T_1) - E(S_n)} |S_n\rangle \quad (2.52)$$

The ground state perturbation function $\langle S_0^{(1)} |$ can be defined correspondingly:

$$\langle S_0^{(1)} | = \sum_n^{\text{singlets}} \frac{\langle T_n | \hat{H}_{\text{SO}} | S_0 \rangle}{E(S_0) - E(T_n)} \langle T_n | \quad (2.53)$$

Since we left out higher triplet (and quintet) terms in Equation 2.52, Equation 2.51 reduces to

$$\boldsymbol{\mu}_{el}(S_0 \leftarrow T_1) = \langle S_0^{(0)} | \hat{\boldsymbol{\mu}}_{el} | T_1^{(1)} \rangle + \langle S_0^{(1)} | \hat{\boldsymbol{\mu}}_{el} | T_1^{(0)} \rangle. \quad (2.54)$$

Inserting Equations 2.52 and 2.53 into Equation 2.54 yields a sum of transition dipole moments of spin-allowed transitions which are weighted with spin-orbit coefficients:

$$\begin{aligned} \boldsymbol{\mu}_{el}(S_0 \leftarrow T_1) &= \sum_n^{\text{triplets}} \frac{\langle S_n | \hat{H}_{\text{SO}} | T_1 \rangle}{E(T_1) - E(S_n)} \langle S_0 | \hat{\boldsymbol{\mu}}_{el} | S_n \rangle \\ &+ \sum_n^{\text{singlets}} \frac{\langle T_n | \hat{H}_{\text{SO}} | S_0 \rangle}{E(S_0) - E(T_n)} \langle T_n | \hat{\boldsymbol{\mu}}_{el} | T_1 \rangle \end{aligned} \quad (2.55)$$

Since the spin-orbit coefficients may be positive or negative, the spin-forbidden transition may actually not only gain but also (partly) loose allowedness through spin-allowed transitions [94].

Intersystem crossing (ISC) rate constants were calculated within the Condon approximation of Fermi's golden rule, i.e. assuming that the transition from an initial state into a set of final states is brought about by a (small) perturbation and that the electronic and the vibrational degrees of freedom can be separated. In the zero-temperature limit, the ISC rate constant in Condon approximation between a singlet S_a and a triplet T_b^α manifold can be expressed as [99, 100]

$$k_{\text{ISC}}^{\text{FC}} = \frac{2\pi}{\hbar} \sum_\alpha \left| \langle T_b^\alpha | \hat{H}_{\text{SO}} | S_a \rangle \right|_{q_0}^2 \sum_k | \langle v_{aj} | v_{bk} \rangle |^2 \delta(E_{aj} - E_{bk}). \quad (2.56)$$

Herein, α denotes a fine-structure level of the triplet and j and k label the vibrational states of the singlet and triplet state. The subscript q_0 stems from a Taylor expansion of the matrix elements that was truncated after the first term and where the reference point q_0 is chosen to be the equilibrium structure of the initial state. For large molecules with many vibrational degrees of freedom, explicit summation over the vibrational states

is not advisable. Instead a time-dependent approach was developed by M. Etinski et al. [100] where the delta function is replaced by its Fourier transform in the time regime. The potential surfaces of the singlet and the triplet state are approximated by the harmonic oscillator model with vibrational frequencies Ω_S and Ω_T . While the electronic part, i.e. the SOCMEs, can be calculated as detailed in Section 2.2.2, the vibrational frequencies can be obtained employing the SNF program [101] — a program which determines vibrational frequencies by numerical differentiation. Final and initial normal coordinates \mathbf{Q}_T and \mathbf{Q}_S are connected by a Duschinsky transformation [102]

$$\mathbf{Q}_T = \mathbf{J}\mathbf{Q}_S + \mathbf{D} \quad (2.57)$$

where \mathbf{J} is a Duschinsky rotation matrix and \mathbf{D} a displacement vector. The expression for ISC rate constant now reads

$$k_{\text{ISC}}^{\text{corr}} = \frac{2\pi}{\hbar} \sum_{\alpha} \left| \langle T_b^{\alpha} | \hat{H}_{\text{SO}} | S_a \rangle \right|_{q_0}^2 \int_{-\infty}^{\infty} dt G(t) e^{it(\Delta E_{ST}^0 + \frac{1}{2} \text{Tr} \Omega_S)} \quad (2.58)$$

where ΔE_{ST}^0 is the adiabatic energy difference between singlet and triplet and $G(f)$ is a generating function that contains matrices of the vibrational frequencies as well as the Duschinsky rotation matrix \mathbf{J} and the displacement vector \mathbf{D} . The exact form of $G(f)$ can be found in Ref. [100] and Ref. [103].

The temperature dependence of especially the reverse process (the reverse ISC from triplet to singlet) can be included via a Boltzmann distribution of the vibrational population of the initial state [103], i.e.

$$k_{\text{ISC}}^{\text{FC,T}} = \frac{2\pi}{\hbar Z} \sum_{\alpha} \left| \langle T_b^{\alpha} | \hat{H}_{\text{SO}} | S_a \rangle \right|_{q_0}^2 \sum_{kj} e^{(-E_{aj}/k_B T)} | \langle v_{aj} | v_{bk} \rangle |^2 \delta(E_{aj} - E_{bk}) \quad (2.59)$$

and

$$k_{\text{RISC}}^{\text{FC,T}} = \frac{2\pi}{3\hbar Z} \sum_{\alpha} \left| \langle S_b | \hat{H}_{\text{SO}} | T_a^{\alpha} \rangle \right|_{q_0}^2 \sum_{kj} e^{(-E_{aj}/k_B T)} | \langle v_{aj} | v_{bk} \rangle |^2 \delta(E_{aj} - E_{bk}) \quad (2.60)$$

with Z being the partition function

$$Z = \sum_j e^{(-E_{aj}/k_B T)}. \quad (2.61)$$

2.3 Solvation effects

Solvent molecules can interact with solute molecules in various ways. Depending on the polarity of the solvent and the solute, ground and excited states may be stabilized or

destabilized to different extents. This effect may be observed experimentally in absorption and emission spectra. A measure for the polarity of the solute is the dielectric constant, while for the solute one usually looks at the static dipole moment of the solute molecule or rather the change of the dipole moment between ground and excited state. Of course, a molecule with a large dipole moment in the ground state will be stabilized by a polar solvent, but if the excited state has a dipole moment that is similar in magnitude and direction to that of the ground state, it will be stabilized by about the same amount and no net effect on the absorption or emission spectra will be seen. If the interaction between a solute and solvent is mainly governed by electrostatic interactions (and no explicit solute solvent interactions as e.g. H-bonds have to be taken into account) it is sufficient to use implicit solvation models such as continuum solvation models.

2.3.1 Continuum solvation models

Both solvation models employed in this thesis, that is the integral equation formalism for the polarizable continuum model (IEFPCM) [104, 105] of the Gaussian program suite and the conductor-like screening model (COSMO) [106] of the TURBOMOLE program package, are closely related continuum solvation models that make use of the apparent surface charge (ASC) method.

The basic assumption made for continuum solvation models is that the solute charge density is spread inside a cavity that is on the one hand defined by an interlocked superposition of the solute atom radii and on the other hand by a solvent probe that rolls along the shape predefined by the aforementioned radii [107]. Where the solvent probe touches the solute radii, an area called solvent excluded surface (SES) is obtained, while the center of the probe yields an area called solvent accessible surface (SAS). The definition of the solute atom radii and the solute probe differs between the implementations in different program packages. Original estimates of the solute atom radii were based on van der Waals radii [106, 108], however, nowadays there are optimized radii available based on e.g. united force field (UFF) or DFT calculations [109, 110]. The cavity surface thus defined can be divided into discrete elements (tesserae). Outside of the cavity the solvent is described as a dielectric continuum — in the original formulation of the PCM method [108] with a relative permittivity ϵ corresponding to that of the solute and in the COSMO with a permittivity $\epsilon \sim \infty$, i.e. that of a conductor, which is later scaled with a factor in order to obtain the interaction with the actual solvent [106]. The electrostatic interaction between the solute and the solvent, where the charge distribution of the solute polarizes the dielectric continuum, which then again polarizes the solute charge distribution and so on, can be expressed as a so called reaction potential \hat{V}_σ , such that the free energy functional that has to be minimized reads [111]

$$G[|\Psi\rangle] = \langle \Psi | \hat{H}^0 + \hat{V}_\sigma | \Psi \rangle - \frac{1}{2} \langle \Psi | \hat{V}_\sigma | \Psi \rangle \quad (2.62)$$

where an apparent surface charge $\sigma(\mathbf{s})$ is introduced that spreads on the cavity surface Γ and \hat{V}_σ can be written as

$$\hat{V}_\sigma(\mathbf{r}) = \int_\Gamma \frac{\sigma(\mathbf{s})}{|\mathbf{r} - \mathbf{s}|} d^2s. \quad (2.63)$$

If one assumes that the aforementioned tesserae are small enough that $\sigma(\mathbf{s})$ can be considered constant within each tessera, $\sigma(\mathbf{s})$ may be replaced by a set of point charges $q(k)$ placed at the center of the tessera area A_k [107, 111]:

$$\hat{V}_\sigma(\mathbf{r}) \simeq \sum_k \frac{\sigma(\mathbf{s}_k) A_k}{|\mathbf{r} - \mathbf{s}_k|} = \sum_k \frac{q_k}{|\mathbf{r} - \mathbf{s}_k|}. \quad (2.64)$$

For the ground-state (GS) free energy, one may now write [111]

$$G_{GS} = E^{GS} - \frac{1}{2} \sum_i V_{GS}(s_i) q_{GS}(s_i). \quad (2.65)$$

In case of equilibrium solvation, i.e. where the dynamic and inertial contributions of \hat{V}_σ are adapted to the excited state K , the corresponding equation for the excited state energy is

$$G_K^{eq} = E_{GS}^K - \frac{1}{2} \sum_i V_{GS}(s_i) q_{GS}(s_i) + \frac{1}{2} \sum_i V(s_i, \mathbf{P}_\Delta) q_\Delta(s_i, \mathbf{P}_\Delta) \quad (2.66)$$

with \mathbf{P}_Δ being a relaxation term of the solute density matrix that was divided into a GS and a relaxation term [111] and q_Δ being the corresponding charges. Dynamic and inertial contributions relate to, in simple terms, the response of the solvent electrons (dynamic) and the the nuclear degrees of freedom of the solvent (inertial) [107].

In the next section, I will detail the first-order approach developed by Caricato et al. to solve Equation 2.66 and explain the reasons to employ this approach for the calculation of emission energies.

2.3.2 The corrected linear response approximation

For the excitation into an excited solute state (absorption), subsequent geometry relaxation and eventual deexcitation (emission) in the presence of a solvent, the following steps can be identified [111]:

- 1. In the ground state the solvent molecules are fully adapted to the ground state density of the solute.
- 2. Vertical excitation: The solvent is still adapted to the ground state. The first change may be a partial equilibration (i.e. of the dynamic part) of the solvent molecules according to new charge distribution of the excited state.

- 3. The solvent achieves full equilibrium (dynamic + inertial parts) with the charge distribution of the excited state, which still maintains the ground state geometry.
- 4. The solute relaxes towards its minimum structure. The solvent molecules have to reorganize according to the new geometry.
- 5. Vertical emission: The solute emits and returns to its electronic ground state. The solvent is still adapted to the excited state. Again a first adjustment of the dynamic part of the solvent molecules according to the ground state charge distribution takes place.
- 6. The solvent achieves full equilibrium (dynamic + inertial parts) with the charge distribution of the solute ground state, which still maintains the excited state geometry.
- 7. The solute relaxes towards its ground state structure. The solvent molecules have to reorganize accordingly.

This is a simplification, of course, since in reality the different processes are not as decoupled as presented here and the time scales of the various processes may also differ according to e.g. the specific solute and solvent structure as well as the temperature etc. In order to describe the absorption of a solute it is sufficient to employ the 'normal' COSMO or IEFPCM formulation, i.e. assuming that the solvent remains fixed to the solute's ground state charge distribution. For a very fast emission or very viscous solvents, where geometry relaxation might be hindered, something inbetween steps 2 and 4 might apply. For the Au(I) and Cu(I) complexes investigated in this thesis, it is, however, reasonable to assume that, if geometry relaxation is not hindered, the geometry relaxation of the excited state is faster than the emission, i.e. we need the solvent to reorganize according to the excited state minimum structure. This effect can be mimicked by the corrected linear response (cLR) approach by Caricato et al. [111]. Since the calculation of the relaxed density matrix in Equation 2.66 depends on the reaction field, which itself again depends on the density, Equation 2.66 represents a non-linear problem that is not easily solved. As an approximated solution to this problem, Caricato et al. chose a first order approach within a TDDFT linear response framework. As an approximation to Equation 2.66, we may write

$$G_K^{eq} = G^{GS} + \omega_K^0 + \frac{1}{2} \sum_i V(s_i, \mathbf{P}_\Delta) q_\Delta(s_i, \mathbf{P}_\Delta) \quad (2.67)$$

where ω_K^0 is the excitation energy in the presence of the PCM reaction field kept frozen in the ground state situation, which can be obtained in a first step by solving the TDDFT equation (Equation 2.21). The results of this first step are then used to solve the TDDFT equations again. The relaxed density matrix can be calculated according to

$$\mathbf{P}_\Delta = \mathbf{T}_K + \mathbf{Z}_K \quad (2.68)$$

with \mathbf{T}_K being the unrelaxed density matrix and where \mathbf{Z}_K accounts for orbital relaxation effects [111]. The apparent charges q_Δ and with them the free energy can be calculated, once P_Δ is known.

Cammi et al. [112] could relate differences between the excitation energies obtained with linear response (LR) methods, on the one hand, and state-specific (SS) methods, on the other hand, to a solvent response that depends on either the solute transition density (in case of LR) or on the change of the solute's electron density (in case of SS). For a simplified model of a dipolar solute in a spherical cavity, Cammi et al. could also show that a solvent response that depends on the solute transition density is tantamount to a dependence on the transition dipole moment of the excited state, while a dependence on the change of the solute's electron density is equivalent to a dependence on the difference between the static dipole moments of the ground and the excited state. Based on these considerations, they could explain that the SS approach has a stronger effect on the energies of states with a static dipole moment that differs strongly from the ground state (i.e. CT states), whereas within the LR approach states with a large transition dipole moment are most strongly affected. The cLR approach employed in this thesis may at first sight seem to belong into the class of LR approaches, as the name suggests. However, Caricato et al. also termed it 'a linear response approach to a state-specific solvent response' [111]. As one can see from Equation 2.67, the reaction potential $V(s_i, \mathbf{P}_\Delta)$ in the cLR framework depends on the relaxed density, that is on the change of the density (which is obtained within a LR approach). The authors therefore state that 'the LR-SS differences in vertical excitation energies are largely reduced' within the cLR approach [111].

Inclusion of the solvation effects into the DFT/MRCI calculations

Since Turbomole is interfaced to the DFT/MRCI program, inclusion of the COSMO solvation into the DFT/MRCI calculations is straightforward. For the PCM and PCM/cLR calculations, however, a workaround was chosen, where the apparent charges obtained in the (TD)DFT PCM and PCM/cLR calculations were included as point charges into the DFT/MRCI calculations. The output of the apparent charges can be requested by setting the IOP(5/33=3) flag for the PCM and by setting the IOP(10/33=3) flag for the cLR calculations. In case of the cLR calculations, the output gives the ground state and the q_Δ charges which have to be summed up in order to obtain the charges induced by the density of the excited state.

Chapter 3

Results

3.1 Trigonal NHC-Cu(I)-Phenan complex (Paper I and Book Chapter)

The first copper complex I studied is a cationic trigonal complex with a monodentate NHC and a bidentate phenanthroline (Phenan) ligand ($[(\text{IPr})\text{Cu}(\text{Phenan})]^+$ with IPr = 1,3-bis(2,6-diisopropylphenyl)imidazol-2-ylidene). Since many trigonal copper complexes show favorable emission properties and since experimental absorption and emission data were available for this complex, it was chosen as a candidate to validate our methods. The complex shows phosphorescence in the orange to red region with rather low quantum yields [47]. Similar complexes with a monodentate NHC and a di(2-pyridyl)dimethylborate as bidentate ligand investigated by Leitl et al. [50], on the other hand exhibit large quantum yields and — depending on the interligand dihedral between the NHC and the bidentate ligand — either TADF or phosphorescence. In order to understand the photophysics of the NHC-Cu(I)-phenanthroline complex, detailed quantum chemical investigations were carried out that shed light on the absorption and emission properties of this complex. Besides, the influence of the interligand dihedral angle on the properties of the NHC-Cu(I)-phenanthroline complex were studied and contrasted to the results obtained by Leitl et al. for their NHC-Cu(I)-di(2-pyridyl)dimethylborate complexes.

3.1.1 Ground state and absorption spectrum

As mentioned before, we sought to validate our methods by comparing our calculated results with the experimental data. In order to gain some insight into the performance of different DFT functionals and basis sets, the obtained ground state geometry parameters can be compared with the experimental data of the crystal structure. To this end, the diisopropyl moieties of the NHC ligand were replaced by methyl groups to reduce the computational costs. All optimizations were done *in vacuo*. In Table 3.1 the results for four different functionals (BLYP, B3LYP, PBE0 and BH-LYP) are collected. The basis sets that were chosen for this comparison are the def-SV(P) for all nonmetal atoms and the cc-pVDZ basis set together with the corresponding Stuttgart-Koeln ECP for copper. The most important geometry parameters, i.e. the copper-nitrogen and the copper-carbon

TABLE 3.1: Experimental copper bond lengths of the crystal structure and calculated bond lengths of the ground state minimum for four DFT functionals with varying HF exchange percentage.

bond length [\AA]	crystal	BLYP	B3LYP	PBE0	BH-LYP
		0% HF	20% HF	25% HF	50% HF
Cu1-N2	2.04	2.10	2.10	2.07	2.11
Cu1-N11	2.05	2.10	2.10	2.07	2.11
Cu1-C24	1.88	1.90	1.91	1.89	1.93

TABLE 3.2: Experimental copper bond lengths of the crystal structure and calculated bond lengths of the ground state minimum for a variation of the copper basis set cc-pVNZ with N=2 (DZ), N=3 (TZ) and N=4 (QZ).

bond length [\AA]	crystal	cc-pVNZ		
		DZ	TZ	QZ
Cu1-N2	2.04	2.07	2.07	2.07
Cu1-N11	2.05	2.07	2.07	2.07
Cu1-C24	1.88	1.89	1.89	1.89

bond lengths, of the crystal structure and the corresponding calculated results are listed. As can be seen from Table 3.1, the PBE0 functional yields the closest agreement with the experimental results. In a second study, I checked whether the copper basis set with double zeta (DZ) quality is large enough. In this case the PBE0 functional was employed and again def-SV(P) for all nonmetal atoms, while for copper the basis set was cc-pVNZ with N=2 (DZ), N=3 (TZ) or N=4 (QZ) (together with the Stuttgart-Koeln ECP). Table 3.2 illustrates that for the copper bonds no improvement is achieved with the larger basis sets of triple and quadruple zeta quality and that the cc-pVDZ basis set is therefore indeed sufficient. Hence, all the following geometry optimizations were carried out with the PBE0 functional and the def-SV(P) basis set for all nonmetal atoms and the cc-pVDZ basis set together with the Stuttgart-Koeln ECP for copper. For the ground state minimum that was optimized with the diisopropyl (DIPP) moieties the Cu-C bond length does not change, while the the Cu-N bonds are slightly longer (2.08 \AA) compared to the optimization with the methyl groups. The arrangement of the ligands is almost perfectly coplanar, the interligand dihedral angles being $\text{N25-C24-Cu1-N11} = 179.6^\circ$ and $\text{N30-C24-Cu1-N2} = 177.5^\circ$ (for atom numbers see Figure 3.1).

A minimum-energy path of the electronic ground state (calculated with Grimme D3 dispersion corrections [113]), where the interligand dihedral angle was varied in steps of 30° between the coplanar arrangement (corresponds to 0° in Figure 3.2) and the perpendicular arrangement (90°) of the ligands, confirmed the coplanar configuration to be the only and therefore global minimum.

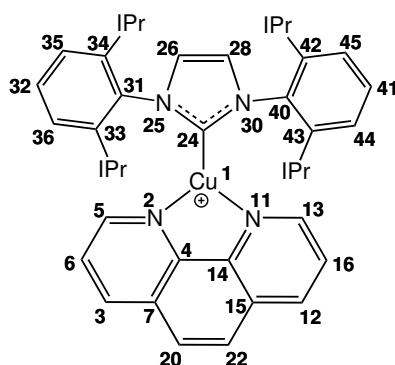


FIGURE 3.1: Molecular structure with atom numbers

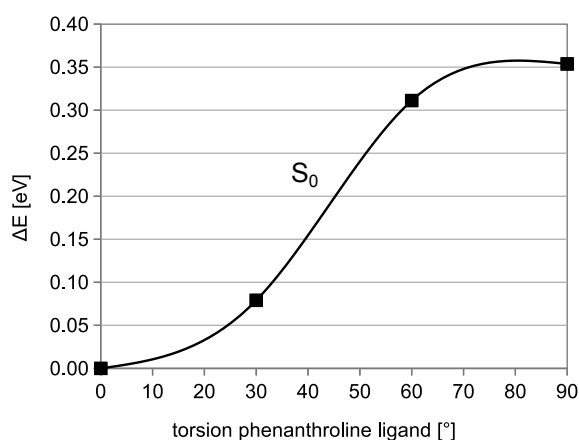


FIGURE 3.2: Ground-state scan of the torsion angle between the NHC and phenanthroline ligands. The DFT/MRCI ground-state energies include Grimme D3 dispersion corrections.

The absorption spectrum was calculated once with TDDFT and once with DFT/MRCI (without dispersion corrections). As can be seen from Figure 3.3 the absorption spectrum calculated with DFT/MRCI matches the experimental spectrum (recorded in CH_2Cl_2) almost perfectly, while the TDDFT spectrum agrees considerably less well with the experiment. Since the DFT/MRCI spectrum computed *in vacuo* already matches the experimental spectrum that well, there was no need seen to include solvation effects in the calculations. For a more detailed discussion of the absorption spectra see Ref. [114] or in Paper I in the Appendix. According to the TDDFT calculations, the S_1 and T_1 are MLCT states that stem from the same $d_\sigma \rightarrow \pi_{\text{phenan}}^*$ excitation and lie at 475 nm and 502 nm. In the DFT/MRCI calculations the corresponding states are the S_1 and the T_2 (which lie at 403 nm and 423 nm). At the coplanar ground state geometry another triplet lies below the MLCT triplet, however, a slight change of the torsion angle of about 5° is enough to reverse the order of the two triplet states (see Figure 3.4). TDDFT optimizations of the S_1 and T_1 state gave the $d_\sigma \rightarrow \pi_{\text{phenan}}^*$ MLCT states and the states were therefore renumbered according to the order of their adiabatic minima.

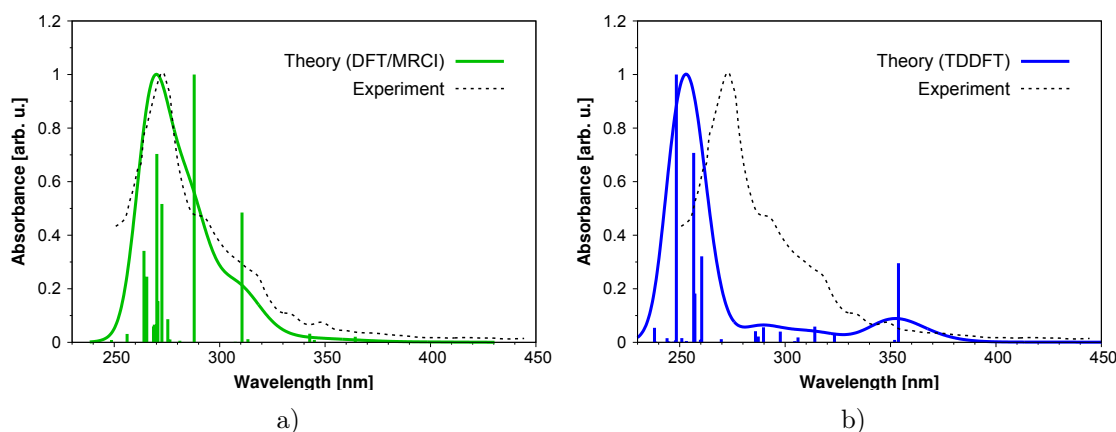


FIGURE 3.3: Absorption spectra calculated with a) DFT/MRCI and b) TDDFT. The experimental spectrum was recorded in CH_2Cl_2 . The data points of the experimental spectrum have been taken from Figure 3 of Ref. [47]

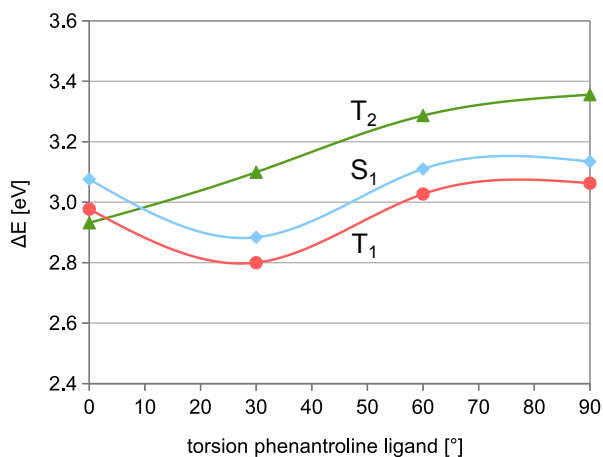


FIGURE 3.4: Ground-state scan of the torsion angle between the NHC and phenanthroline ligand. The DFT/MRCI excitation energies of T_1 , T_2 , and S_1 are given relative to the S_0 energy at the 0° S_0 geometry.

3.1.2 Excited states

Unlike for the ground state structure, a scan of the torsion angle between the NHC and the phenanthroline ligand for the T_1 geometry revealed that the perpendicular conformation constitutes a second minimum on the potential surface. For calculations without dispersion corrections the perpendicular minimum is actually the global minimum. Excited state optimizations with methyl instead of DIPP groups could even show that the bulky DIPP groups are indeed needed in order to keep the phenanthroline ligand from twisting in the excited state. If, however, dispersion effects are included (for the structures with DIPP), the coplanar conformation becomes the global minimum, albeit lying only about 0.02 eV below the perpendicular conformation. The barrier between the two minima is rather small (0.13 eV), but since the results that were obtained at the coplanar geometries agree better with the experiment, I will concentrate on these results in order to explain the experimental

findings. The results for the perpendicular geometry will be discussed in the context of the question whether the dihedral angle influences the TADF properties of this complex.

As mentioned before, the S_1 and the T_1 exhibit the same electronic structures, which is also reflected in the optimized structures, where the bond lengths differ by no more than 0.01 Å and the bond angles by no more than 0.4°. Due to the strong charge transfer character of the S_1 and the T_1 , the exchange interaction integral is small and therefore ΔE_{ST} is small, too. According to DFT/MRCI calculations ΔE_{ST} at the T_1 geometry is ≈ 0.1 eV (see also Figure 3.4). Thus ΔE_{ST} lies in the range of thermal energy at RT making TADF in principle possible. In order to further explore this assumption, phosphorescence and fluorescence as well as the ISC and RISC rate constants were investigated.

Emission properties of the coplanar conformers

The FC profiles of the emission calculated for the coplanar conformations are shown in Figure 3.5, together with the experimental spectrum measured at 77 K in 2-MeTHF. The emission maximum of the coplanar S_1 structure lies at 572 nm and that of the T_1 at 600 nm, which is both slightly blue-shifted compared to the experimental value of 630 nm. Due to the underlying harmonic oscillator approximation, the calculated spectra are somewhat broader and fall off more slowly than the experimental spectrum.

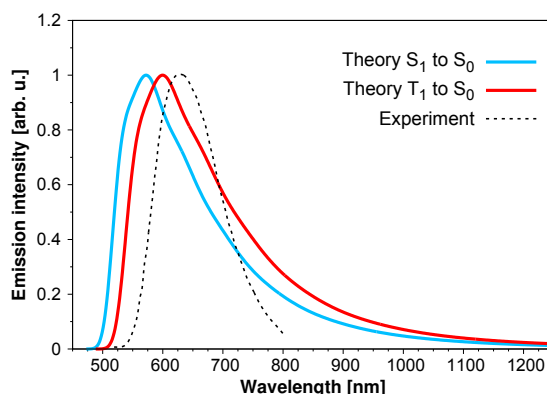


FIGURE 3.5: Franck-Condon profiles for the emission of the coplanar T_1 and S_1 structures calculated at 77 K compared to the experimental emission spectrum measured at 77 K in 2-MeTHF (data points taken from Figure 3 of Ref. [47]). The spectra were normalized to one.

Phosphorescence and fluorescence rate constants have been calculated at the S_1 and the T_1 geometries. At the T_1 geometry, the average of the three phosphorescence rate constants is $k_{P,av} = 3.75 \times 10^3 \text{ s}^{-1}$ (lifetime $\tau_P = 267 \mu\text{s}$). The calculated fluorescence rate constant is quite small. Although the fluorescence of $^1\text{MLCT}$ states is usually slow (calculated rate constants for other d^{10} complexes are of the order of $\sim 10^6 - 10^7 \text{ s}^{-1}$ [38, 115–117]) compared to that of ^1LC states, the fluorescence rate constant calculated at the S_1 geometry $k_F = 8.83 \times 10^4 \text{ s}^{-1}$ ($\tau_F = 11 \mu\text{s}$) is again 1–2 orders of magnitude smaller. At room temperature ISC proceeds with $k_{ISC} = 3.00 \times 10^7 \text{ s}^{-1}$ outcompeting prompt fluorescence by

2–3 orders of magnitude. RISC, on the other hand, proceeds with $k_{\text{RISC}} = 3.62 \times 10^5 \text{ s}^{-1}$, which is 2 orders of magnitude larger than the averaged phosphorescence rate. Since both intersystem crossing rates constants are about 2 orders of magnitude larger than the emission rate constants, one can assume that at room temperature the S_1 and the T_1 populations equilibrate before decaying radiatively. Figure 3.6 shows the energies and rate constants calculated at the T_1 geometry.

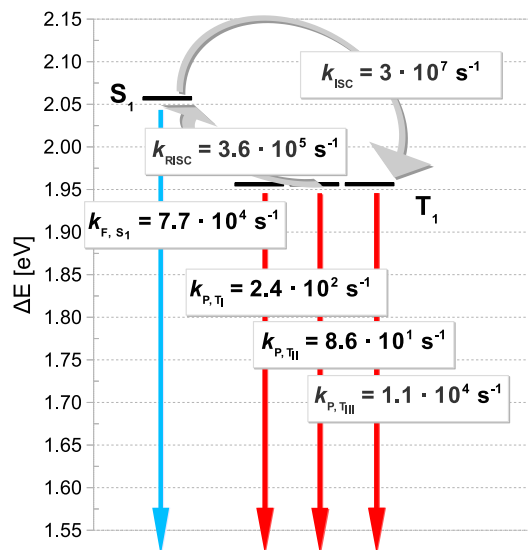


FIGURE 3.6: Fluorescence, phosphorescence and ISC rate constants at the global T_1 minimum.

When the temperature is set to 77 K, a different picture evolves. The strong temperature-dependence of the RISC rate constant leads to a decrease of the rate constant by several orders of magnitude to about 8 s^{-1} , whereas the ISC rate constant is almost unaffected. Hence, RISC at liquid-nitrogen temperatures cannot compete with the phosphorescence and the experimental emission spectrum measured at 77 K should therefore mainly stem from the T_1 emission.

While it is obvious that the low-temperature emission is dominated by phosphorescence from the T_1 , the emission at room temperature is less easily understood. Since various rate constants are involved (apart from emission and (R)ISC, also non-radiative deactivation of the S_1 and the T_1), limiting cases such as the equilibrium limit are often used by experimentalists for fitting their data. For this complex, however, only one of the conditions for the equilibrium limit, i.e. $k_{\text{ISC}} \gg k_{\text{F}}$, is fulfilled at all temperatures, while the second condition, $k_{\text{RISC}} \gg k_{\text{P}}$, is not. The respective quantum yields were therefore calculated according to the kinetic analysis of Hirata et al [118]. The results of the kinetic analysis suggest that also at room temperature, the emission is governed by phosphorescence, the quantum yield for deactivation via phosphorescence being 77.7%, while that for TADF is 22% and prompt fluorescence contributes with only 0.3%.

Influence of the torsion angle on the emission properties

The radiative rates are hardly affected by the orientation of the ligands. For the interligand dihedral of 90° the averaged phosphorescence rate constant is $k_{P,av} = 1.81 \times 10^3 \text{ s}^{-1}$ compared to $k_{P,av} = 3.75 \times 10^3 \text{ s}^{-1}$ for 0° and the fluorescence rate constant is $k_F = 1.03 \times 10^5 \text{ s}^{-1}$ compared to $k_F = 8.83 \times 10^4 \text{ s}^{-1}$. The effect on the ISC and RISC rate constants is a lot more pronounced. They increase by about two orders of magnitude from $k_{ISC} = 3.00 \times 10^7 \text{ s}^{-1}$ to $k_{ISC} = 2.87 \times 10^9 \text{ s}^{-1}$ and from $k_{RISC} = 3.62 \times 10^5 \text{ s}^{-1}$ to $k_{RISC} = 4.62 \times 10^7 \text{ s}^{-1}$. So in contrast to what Leitl et al. [50] find for their NHC-Cu(I)-di(2-pyridyl)dimethylborate complexes, the (R)ISC rate constants do not decrease, but increase. Besides, the changes are not related to the magnitude of the singlet–triplet gap. According to the TDDFT calculations by Leitl et al., the singlet–triplet gap of a NHC-Cu(I)-dipyridyldimethylborate model complex is increased from 540 cm^{-1} at 0° to 3700 cm^{-1} at 70° . They consider this increased gap to be the reason why one of their complexes with an interligand dihedral angle of about 70° is a phosphorescence emitter, while another complex with an interligand dihedral angle of about 5° shows TADF emission. The singlet–triplet splitting of the NHC-Cu(I)-phenanthroline complex, on the other hand, changes only slightly from 650 cm^{-1} at 0° to 830 cm^{-1} at 90° (calculated at the MRSOCI level of theory). The different effect of the torsion angle on the singlet–triplet gaps may be explained by the different density overlaps of the orbitals involved in the excitation. For the NHC-Cu(I)-di(2-pyridyl)dimethylborate investigated by Leitl et al., the density overlap increases significantly upon torsion of the di(2-pyridyl)dimethylborate ligand, while for the NHC-Cu(I)-phenanthroline complex the orbitals and overlaps barely change at all. The reason for the increased ISC and RISC rate constants of the NHC-Cu(I)-phenanthroline complex can instead be ascribed to a change in the electronic interaction. For the perpendicular conformers the sum of squared SOCMEs is by a factor of 20–40 larger than for the coplanar conformers. The slightly larger fluorescence rate constant and the slightly smaller phosphorescence as well as the faster ISC and RISC processes lead to a considerably larger TADF quantum yield at RT of 45.7%, while the contribution of the phosphorescence is reduced to 54.3%.

3.2 Linear NHC-Cu(I)-Py complexes (Paper III)

Reports of mononuclear, linear copper complexes that show luminescence are scarce. However, a few examples have been presented in literature in the course of the last two years where one or two of the ligands are either cyclic amino(alkyl) carbenes (CAACs) or diamido carbenes (DACs) [53, 58–61]. It seems therefore reasonable to search for luminescent linear NHC complexes as well.

In the group of Prof. Christian Ganter, three linear NHC complexes could be synthesized, where the NHC ligand is always the widely-used IPr ligand (see also Section 3.1) and the second ligand is either pyridine, 2-methyl-pyridine or 2-phenyl-pyridine (see Figure 3.7). The spectroscopic measurements were mainly done in PD Dr. Andreas Steffen's group.

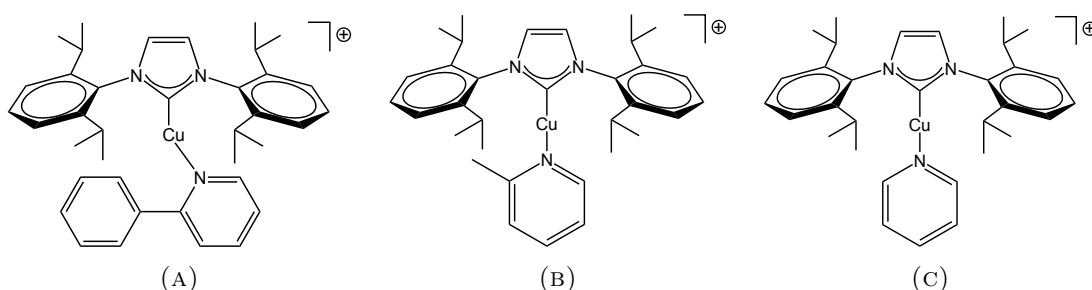


FIGURE 3.7: Chemical structures of the linear NHC complexes with (A) 2-phenyl-pyridine, (B) 2-methyl-pyridine and (C) pyridine as second ligand.

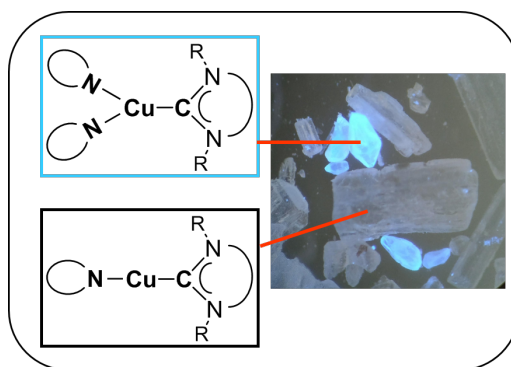


FIGURE 3.8: Schematic structures of the linear and trigonal complexes and the crystals of both crystallized from THF solution. As can be seen, crystals of the trigonal complexes display bright luminescence. In comparison, crystals of the linear complexes almost seem to be non-emissive. The figure was kindly provided by Prof. Ganter.

X-ray diffraction studies of single-crystals (obtained from CHCl_3 solutions) of all three complexes could confirm the linearity of the complexes. Crystal powders of all three complexes showed luminescence, which is why, at the beginning of my PhD research, these complexes were assumed to be promising emitter materials. However, this assumption turned out to be erroneous. My quantum chemical calculations indicated that these complexes should rather be non-emissive (see below), which seemed at odds with the experimental

findings. More recently, crystallization of the complexes from THF rather than CHCl_3 solutions gave again crystals of the linear complexes, but also crystals of the equivalent trigonal complexes with one additional pyridine ligand. Single-crystals of the linear complexes were only weakly luminescent, whereas crystals of the trigonal complexes displayed bright luminescence (see Fig. 3.8) [119]. These findings eventually led to the conclusion that the powders obtained from the linear complexes contained to some extent also the trigonal complexes. Besides, it turned out that the crystals of the linear complexes show mechanochromic luminescence after grinding [120]. This behavior is not fully understood at this point in time, however first calculations indicate that a strong interaction with the counterion (BF_4^-) could be the reason. Although this means that the linear complexes themselves cannot be considered promising emitters, the quantum chemical investigations on these complexes still give some useful insight into the photophysics of these complexes. New design principles can be deduced which may lead to highly luminescent linear NHC complexes (see also Section 3.3).

The following sections reflect the difficulties to square the quantum chemical results with the experimental results, which were erroneously ascribed solely to the linear complexes.

Initially, the cationic Phpy, Mepy and Py complexes were calculated *in vacuo* omitting the counterion. Experimental absorption spectra were measured in CH_2Cl_2 solution. Additionally, excitation and emission spectra were recorded for crystal powders, neat films and in PMMA.

3.2.1 Absorption spectra

Since the calculated absorption spectra *in vacuo* were not in particularly good agreement with the experiment, different attempts were made to improve the results. The inclusion of spin-orbit coupling effects (employing the spin-orbit coupling quasi-degenerate perturbation theory) neither changes the energy nor the intensity of the $S_0 \rightarrow S_n$ transitions (see Figure 3.9). Additional calculations with different functionals (BP-86, B3-LYP, BH-LYP and CAM-B3LYP) also did not lead to significant changes or improvements, neither with regard to the geometry parameters nor to the absorption spectra (tested for BP-86 and CAM-B3LYP).

Electrostatic effects

The influence of the solvent on the absorption was studied by means of the COSMO model (see Figure 3.9). For the DFT/MRCI calculations, all atom radii used for the construction of the solvent cavity had to be changed from the default values. The default values (i.e. the optimized values mentioned in Section 2.3.1) gave problems in the calculation of the one-electron integrals and were therefore changed to the van der Waals radii (Cu: 2.223 to 1.40 Å, N: 1.83 to 1.55 Å, C: 2.00 to 1.70 Å, H: 1.30 to 1.10 Å). For each of the complexes,

the COSMO solvation shifts the spectrum to slightly higher energies. For comparison, a PCM calculation was done for the Py and the Mepy complex. The apparent charges of the PCM calculation were used as point charges in the DFT/MRCI calculations. The difference between the calculation *in vacuo* and the PCM calculation is, if anything, even smaller than for the COSMO environment and neither of the approaches leads to a much better agreement with the experimental spectra.

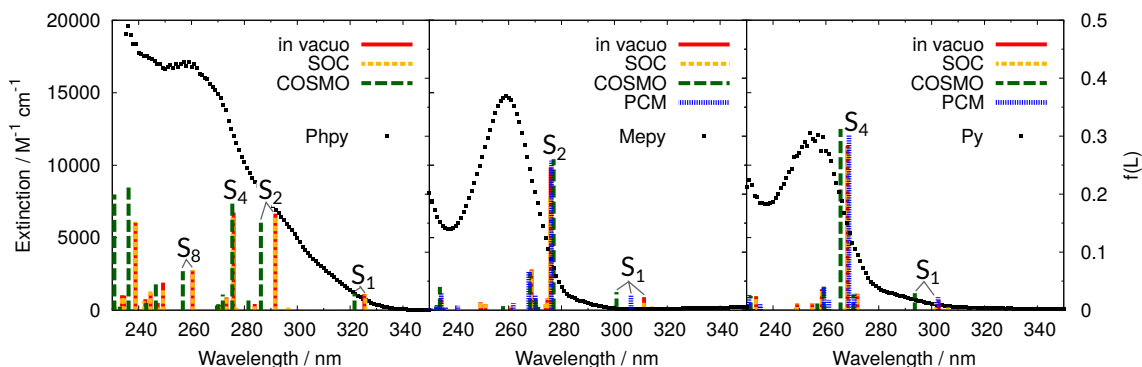


FIGURE 3.9: Experimental absorption spectra in CH_2Cl_2 (black) [121] and calculated absorption spectra *in vacuo* (red), *in vacuo* with spin-orbit coupling effects (orange), for the COSMO (green) and the PCM (blue) CH_2Cl_2 solvation.

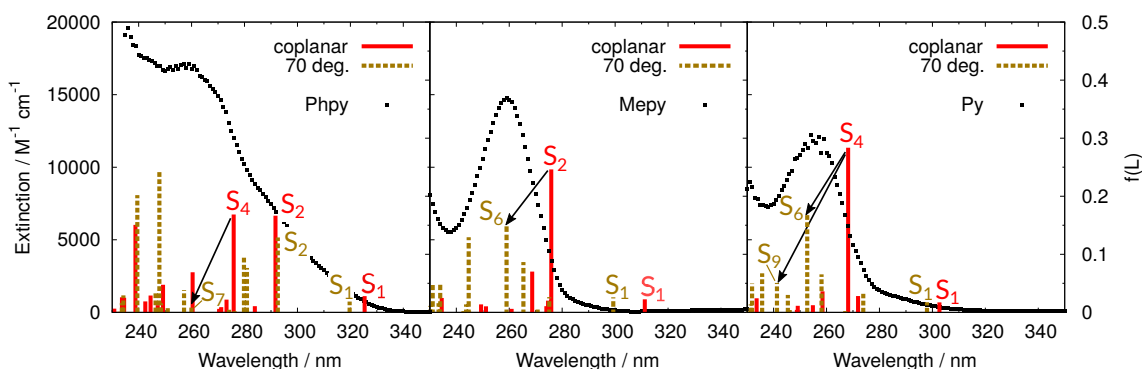


FIGURE 3.10: Experimental absorption spectra in CH_2Cl_2 (black) [121] and calculated absorption spectra *in vacuo* with different dihedral angles between the ligands: coplanar (red) and 70° (olive).

Conformational effects

Another reason for the deviations between the calculated spectra and the experimental spectra might have been that in solution different conformations of the molecules occur. The ground state geometry optimizations led to structures with a roughly coplanar interligand dihedral angle between the NHC and the pyridine ligand, but at least for TDDFT calculations *in vacuo* the torsional barrier for the rotation of the pyridine ligand is <10 kJ/mol for all three molecules. In the crystal structure, the interligand dihedral angle is 20° and 71° for Mepy and Py, respectively, which is why these angles were further investigated.

TABLE 3.3: Comparison of the absorption wavelength λ and the oscillator strength $f(L)$ for the states at the S_0 minima with a coplanar arrangement of the ligands and the corresponding states at the S_0 geometry with an interligand dihedral angle of 70° .

	at coplanar S_0			at 70° S_0		
	states	λ [nm]	$f(L)$	states	λ [nm]	$f(L)$
Phpy	S_1	325	0.028	S_1	320	0.019
	S_2	292	0.166	S_2	293	0.129
	S_3	284	0.010	S_4	280	0.095
	S_4	276	0.169	S_7	260	0.012
	S_8	260	0.069	S_8	257	0.038
	S_{12}/S_{13}	242/239	0.019/0.151	S_{11}/S_{13}	248/239	0.242/0.202
Mepy	S_1	311	0.022	S_1	299	0.026
	S_2	276	0.246	S_6	259	0.149
	S_5/S_6	269/261	0.070/0.006	S_4/S_5	271/265	0.008/0.087
	S_7/S_8	251/249	0.010/0.014	S_8	245	0.129
Py	S_1	303	0.017	S_1	298	0.017
	S_4	268	0.284	S_6/S_9	253/241	0.169/0.051
	S_5	258	0.036	S_5	258	0.065
	S_7/S_8	249/249	0.011/0.004	S_8/S_{12}	246/232	0.004/0.050
	S_{10}/S_{12}	236/229	0.000/0.000	S_{11}/S_{15}	236/225	0.067/0.057

Changing the dihedral angle to 20° only had a minor effect on the spectrum, while the influence of an angle of 70° on the absorption spectrum is considerably larger than the effect of the solvent (Figure 3.10). Interestingly, it turns out that, at least for the Mepy complex, according to the DFT/MRCI calculations the 70° conformer is a bit more favorable than the coplanar conformer — the DFT/MRCI S_0 energy of the 70° conformer lies very slightly below the DFT/MRCI S_0 energy of the coplanar conformer (by about 0.9 kJ/mol).

The excitation with the highest oscillator strength ($S_0 \rightarrow S_4$ for Phpy and Py and $S_0 \rightarrow S_2$ for Mepy), which involves charge transfer from the NHC to the pyridine ligand, experiences the strongest shift and simultaneously loses oscillator strength when the interligand dihedral angle is changed from about 0° to 70° (see Figure 3.10 and Table 3.3). In contrast to that, the $S_0 \rightarrow S_2$ transition of the Phpy complex, which is mainly located on the phenylpyridine ligand, is — unsurprisingly — almost unaffected by the torsion. Especially in case of the Mepy and Py, the agreement between the experimental spectrum and the calculated spectrum is significantly enhanced for a rotation of the pyridine ligand to 70° . Nevertheless, it remains unclear why an interligand dihedral of 70° should be favorable in solution.

3.2.2 Optimized excited state geometries

In order to explain the relaxation and emission behavior of the three complexes, the geometries of the lowest lying excited states have to be optimized. For all three complexes, there are four triplets below the S_1 state at the coplanar S_0 geometry *in vacuo*.

Phpy complex. At the S_0 geometry of the Phpy complex, there is an MLCT triplet (T_{MLCT}) which corresponds to the S_1 , where the electron density is transferred from the Cu d_{z^2} to the NHC carbon and the pyridine ring, there are two triplets, where the transition is localized on the DIPP moieties of the NHC ligand ($T_{LC,DIPP}$) and the lowest triplet, which is mainly localized on the phenylpyridine ligand ($T_{LC+d,Phpy}$) (see Figures 3.11 and 3.12). All three LC triplets have some small MLCT contributions, too.

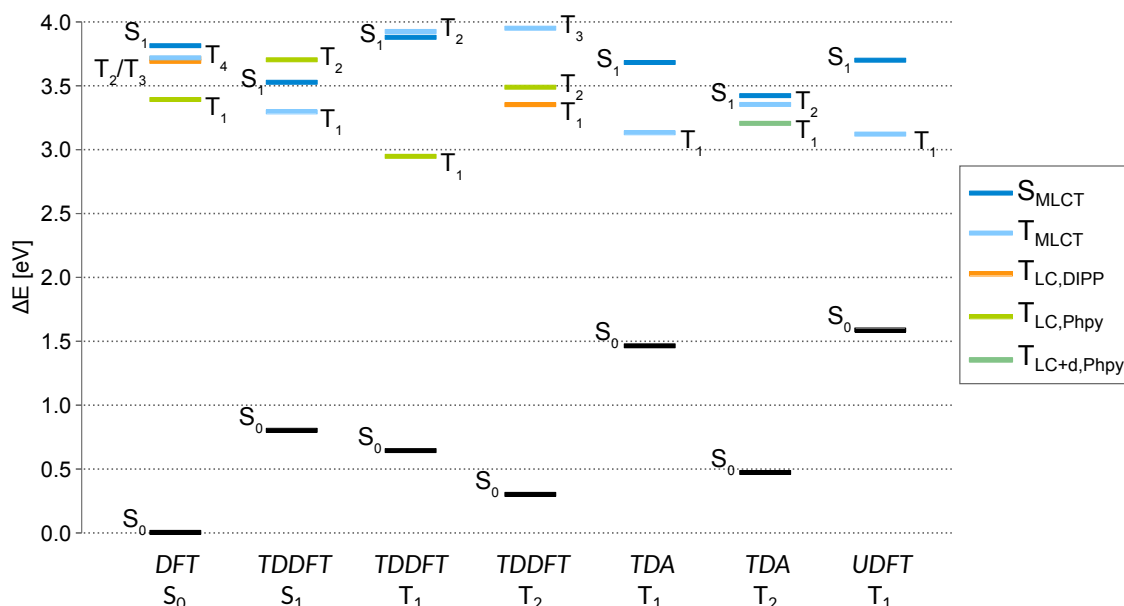


FIGURE 3.11: DFT/MRCI energies of the most relevant states at all optimized geometries. The energies are given relative to the S_0 energy at the S_0 geometry.

Different attempts were made to optimize these states. Starting from the S_0 geometry, TDDFT optimization of the T_1 state leads to a triplet minimum with an electronic structure that is equivalent to that of the T_1 state at the S_0 geometry, but with almost no copper $3d$ contributions ($T_{LC,Phpy}$). UDFT and TDDFT/TDA optimizations of the T_1 state lead to triplet minima with wavefunctions that are governed by an MLCT configuration and therefore resemble the T_{MLCT} state at the S_0 geometry, but with stronger local contributions on the phenylpyridine ligand. TDDFT/TDA optimization of the T_2 again gives a triplet minimum with a similar electronic structure as the TDDFT optimized T_1 state, but with more pronounced Cu $3d$ contributions ($T_{LC+d,Phpy}$) (see Figures 3.12 and 3.13). TDDFT optimization of the T_2 state gives one of the $T_{LC,DIPP}$ states (only identifiable by DFT/MRCI, in TDDFT there are too many small amplitudes), but only

as a saddle point. Distortion along the imaginary mode leads to a triplet geometry that resembles the TDDFT/TDA optimized T_2 . With regard to the DFT/MRCI energy the TDDFT optimized T_1 is the lowest, the UDFT and TDDFT/TDA optimized T_1 states lie about 0.18 eV above the TDDFT optimized T_1 , the TDDFT/TDA optimized T_2 state 0.26 eV and the TDDFT optimized T_1 state 0.40 eV (see also Figure 3.11). Further discussion will concentrate on the $T_{LC,Phpy}$, $T_{LC+d,Phpy}$ and the T_{MLCT} .

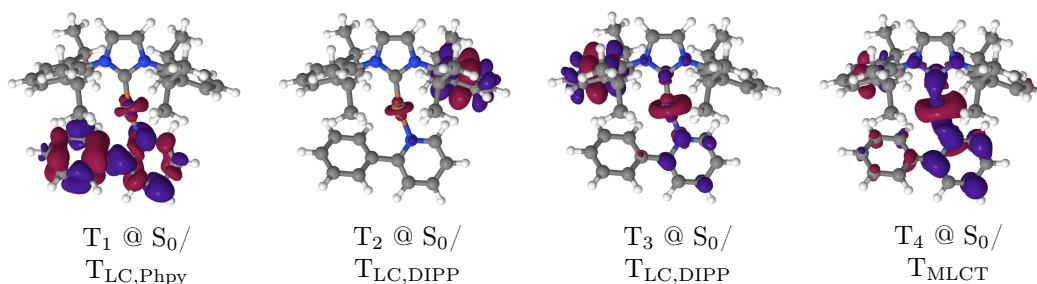


FIGURE 3.12: DFT/MRCI difference densities for the T_1 to T_4 at the Phpy S_0 geometry *in vacuo*. A loss of electron density upon electronic excitation from the ground state is depicted in magenta, a gain of electron density in violet-blue.

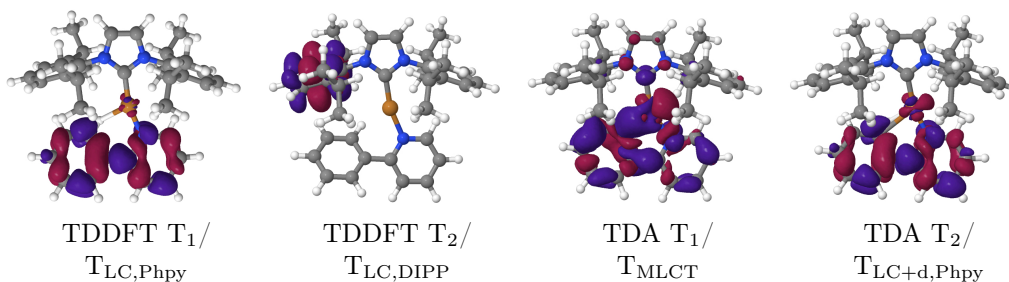


FIGURE 3.13: DFT/MRCI difference densities for the TDDFT optimized T_1 and T_2 and the TDA optimized T_1 and T_2 states of the Phpy complex. For color codes see Fig. 3.12.

Mepy and Py complexes. The lowest singlet and triplets states of the Mepy and Py complexes are quite similar. At the S_0 geometry, the T_4 state has MLCT (coming from a Cu d_π orbital) and LC (mainly localized on the pyridine ligand) contributions. In case of the Mepy complex, the LC contributions are somewhat stronger, which is why it is denominated $T_{LC/MLCT}$, while in case of the Py complex the MLCT character is more pronounced, therefore this triplet is denominated $T_{MLCT/LC}$ (see Figures 3.14 and 3.16). The T_3 state is for both complexes an MLCT state that corresponds to the T_{MLCT} of the Phpy complex and T_1 and T_2 are the $T_{LC,DIPP}$ states also present in the Phpy complex, but without copper $3d$ contributions and localized on both DIPP phenyl rings.

Starting from the S_0 geometry, for both complexes TDDFT optimization of the T_1 state gives a $T_{LC,DIPP}$ minimum where the excitation is localized on one of the DIPP phenyl rings (see Figures 3.15 and 3.17). The $T_{LC/MLCT}$ of the Mepy complex and the

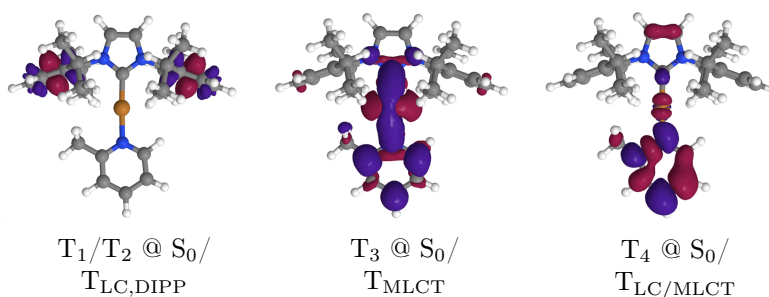


FIGURE 3.14: DFT/MRCI difference densities for the T_1 to T_4 at the Mepy S_0 geometry *in vacuo*. For color codes see Fig. 3.12.

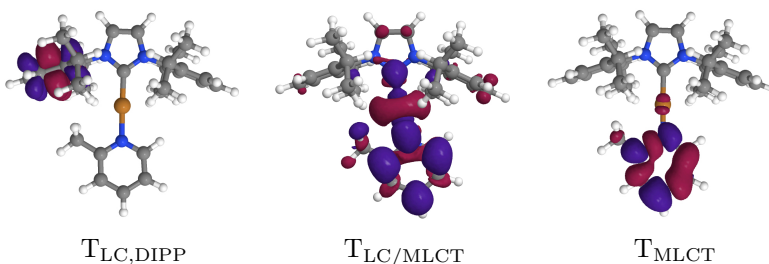


FIGURE 3.15: DFT/MRCI difference densities for the optimized triplet states of the Mepy complex. For color codes see Fig. 3.12.

$T_{MLCT/LC}$ of the Py complex could be optimized starting from the S_1 geometry, optimizing the T_1 state. Both triplets have stronger local contribution at their minimum structures. In case of the $T_{MLCT/LC}$, the Cu d_π contributions slightly decrease and the d_{z^2} contributions increase. According to the TDDFT calculations, the $T_{LC/MLCT}$ of the Mepy complex constitutes only a saddle point on the potential surface. Distortion along the imaginary frequency leads to strong out-of-plane bending of the methyl group and eventually to a conical intersection with the ground state (see Figure 3.18). For the Mepy complex, starting from the S_1 geometry, optimization of the T_2 gave the T_{MLCT} minimum. For the Py complex the optimization of the T_2 starting from the S_1 geometry fails, because the T_{MLCT} and the $T_{MLCT/LC}$ seem to cross. TDDFT/TDA optimization of the T_1 state leads for both the Mepy and the Py complex to the T_{MLCT} minimum structure. In case of the Mepy complex, the DFT/MRCI energy of the TDA optimized T_{MLCT} is almost identical to the DFT/MRCI energy of the TDDFT optimized T_{MLCT} .

In contrast to the excited state optimizations of the Phenan complex, inclusion of dispersion effects did not lead to an improvement of the calculated results for the pyridine complexes. Most optimizations indeed ended up in crossings with the ground state.

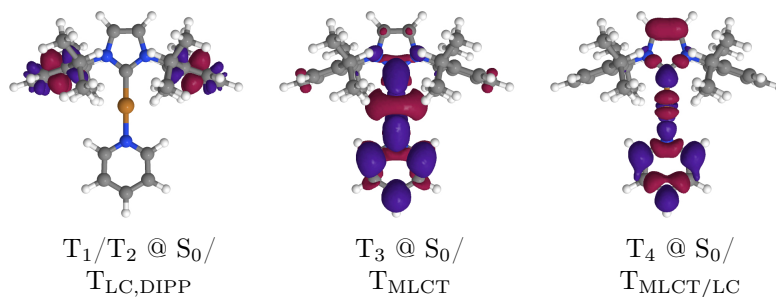


FIGURE 3.16: DFT/MRCI difference densities for the T_1 to T_4 at the Py S_0 geometry *in vacuo*. For color codes see Fig. 3.12.

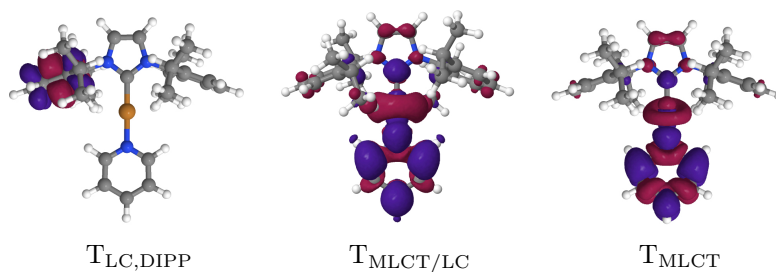


FIGURE 3.17: DFT/MRCI difference densities for the optimized triplet states of the Py complex. For color codes see Fig. 3.12.

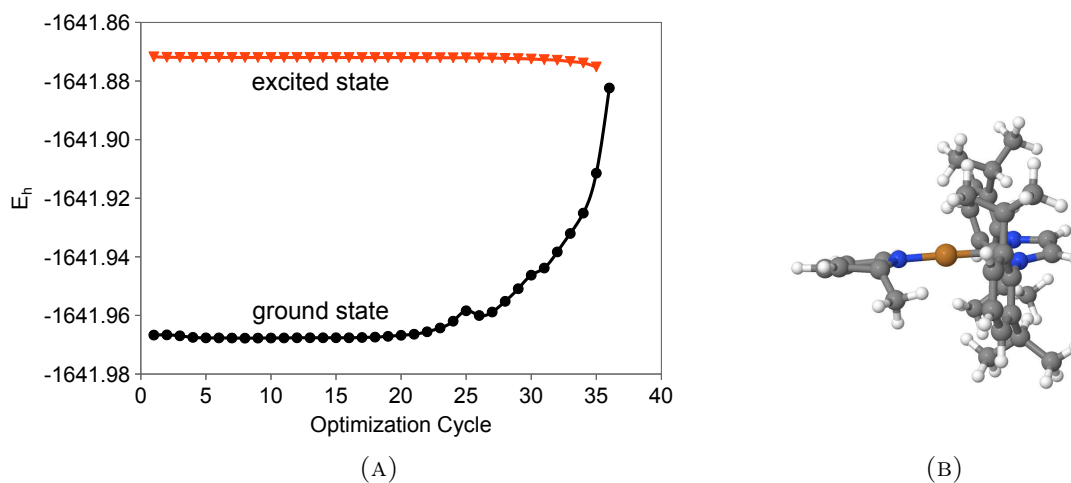


FIGURE 3.18: (A) TDDFT energies for the geometry optimization of the $T_{LC}/MLCT$ geometry after distortion along the imaginary frequency. (B) Distorted geometry at optimization cycle 35.

3.2.3 Effects of the crystal environment

Since the excitation and emission spectra were (among others) recorded for crystalline samples, where X-ray diffraction studies showed that only the Phpy exhibits a coplanar arrangement of the ligands, while for Mepy and Py the interligand dihedral angle is 20° and 71° , respectively, the influence of the crystal structure as well as the influence of the counterions, in particular on the supposedly emissive states, was further studied.

For the Phpy complex, the calculation of absorption spectrum for the unoptimized crystal structure gives similar results to the calculation for the optimized S_0 geometry *in vacuo* (see Figure 3.19). Surprisingly, the $S_0 \rightarrow S_8$ transition at about 260 nm gains oscillator strength at the crystal structure — $f(L)$ is more than 1.5 times higher than at the optimized geometry *in vacuo*. The reason for the increase of oscillator strength might be the decreased CT character of the S_8 at the crystal structures indicated by a smaller change of the dipole moment between the S_0 and the S_8 . The S_1 state is slightly stabilized and the absorption wavelength is shifted from 325 nm to 333 nm.

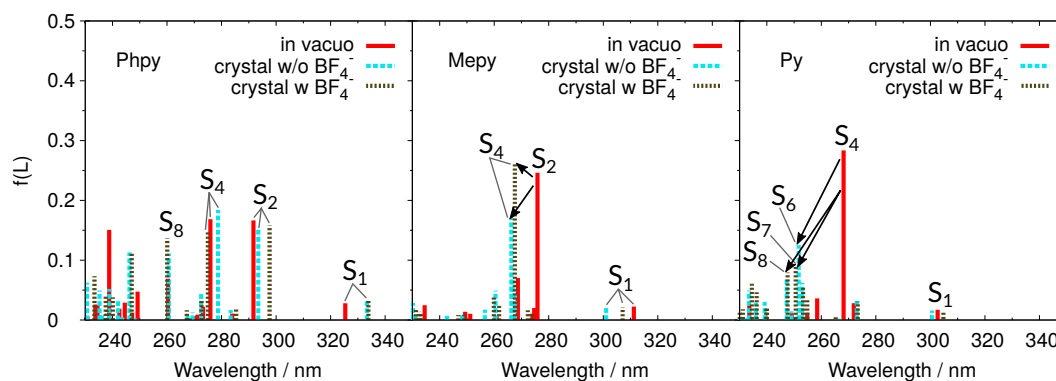


FIGURE 3.19: Calculated absorption spectra for the optimized S_0 geometry *in vacuo* (red) and the unoptimized crystal structure without (cyan) and with the counterion BF_4^- (brown).

For the Mepy and Py complex, the same trends can be observed for the $S_0 \rightarrow S_2$ transition of the Mepy and the $S_0 \rightarrow S_4$ of the Py complex as for the optimized 70° geometry, although they are less pronounced in case of the Mepy complex, since the dihedral angle in the crystal structure is only 20° . In a similar fashion the $S_0 \rightarrow S_1$ transition of the Mepy and the Py complexes are shifted to slightly smaller wavelengths (311 nm to 301 nm and 303 nm to 301 nm, see also Table 3.4).

The triplets below the S_1 state mostly experience a small destabilization. This effect is significant for the Phpy and the Py complex, where it changes the order of states. At the crystal structure, the $T_{\text{LC,DIPP}}$ states of the Phpy and the $T_{\text{MLCT/LC}}$ of the Py complex do not lie below, but above the S_1 state.

In order to study the influence of the counterion BF_4^- in a roughly balanced way, all borates within a distance of 10 \AA to the copper(I) center were included as point charges into the calculations. The charge of the BF_4^- ion was divided by the number of borates.

TABLE 3.4: Vertical transition energies in [nm] of the lowest singlet and the triplet states below the S_1 at the S_0 geometry *in vacuo* and in CH_2Cl_2 and of the corresponding states for the unoptimized crystal structure without and with point charges (BF_4^-).

Phpy	S_1	$T_{\text{LC+d,Phpy}}$	$T_{\text{LC,DIPP}}$	$T_{\text{LC,DIPP}}$	T_{MLCT}
<i>in vacuo</i>	325	365	336	334	333
CH_2Cl_2	321	358	334	329	330
crystal	333	370	329	324	336
BF_4^-	333	382	329	325	339
Mepy	S_1	$T_{\text{LC,DIPP}}$	$T_{\text{LC,DIPP}}$	T_{MLCT}	$T_{\text{LC/MLCT}}$
<i>in vacuo</i>	311	339	339	329	313
CH_2Cl_2	301	334	332	323	315
crystal	301	333	328	318	310
BF_4^-	307	338	334	323	310
Py	S_1	$T_{\text{LC,DIPP}}$	$T_{\text{LC,DIPP}}$	T_{MLCT}	$T_{\text{MLCT/LC}}$
<i>in vacuo</i>	303	332	332	316	305
CH_2Cl_2	294	332	332	312	303
crystal	301	332	331	309	294
BF_4^-	305	333	333	312	295

That means for example in case of the Phpy complex, where 6 BF_4^- ions were close to the Cu(I), each of the 6 point charges got a charge of -0.1667. The effect of the introduction of the BF_4^- point charges compared to the crystal structure without point charges is rather modest. For the S_1 and the triplet states below, the point charges seem to lead to a small stabilization of these states. The effect is strongest for the $T_{\text{LC,Phpy}}$ of the Phpy complex which is shifted from 370 nm to 382 nm.

All in all, the structural effects of the crystal and the effects of the point charges on the S_1 and the triplets below are small, however, as mentioned before, in case of the Phpy and the Py complex the order of states differs between the calculations *in vacuo* and the calculations at the crystal structure. Based on these findings, it seems reasonable to compare the results calculated for the Mepy complex *in vacuo* with the excitation and emission measured for the crystalline samples, while for the Phpy and the Py complex one has to deliberate more on the effects of the changed order of states.

3.2.4 Excitation spectra and LIPs

Excitation spectra

In order to understand the excitation and emission processes, it is necessary to find out into which states the excitation predominantly goes and which relaxation paths are possible after the excitation.

According to the absorption spectra, the strongest absorbing states lie at about 260 nm for the Mepy and Py complexes and at about 240 for the Phpy complex, whereas excitation spectra of the crystalline samples peak at about 310 nm for the Mepy and Py complexes and at about 350 nm for the Phpy complex (compare Figures 3.9 and 3.20). In other words, the excitation spectra deviate unexpectedly strongly from the absorption spectra. One should also note the odd deviations between the excitation spectra of the crystalline samples and the ones recorded in neat films. The deviations are especially strong for the Phpy complex, where the maximum is shifted from about 350 nm to about 310 nm (see Fig. 3.20).

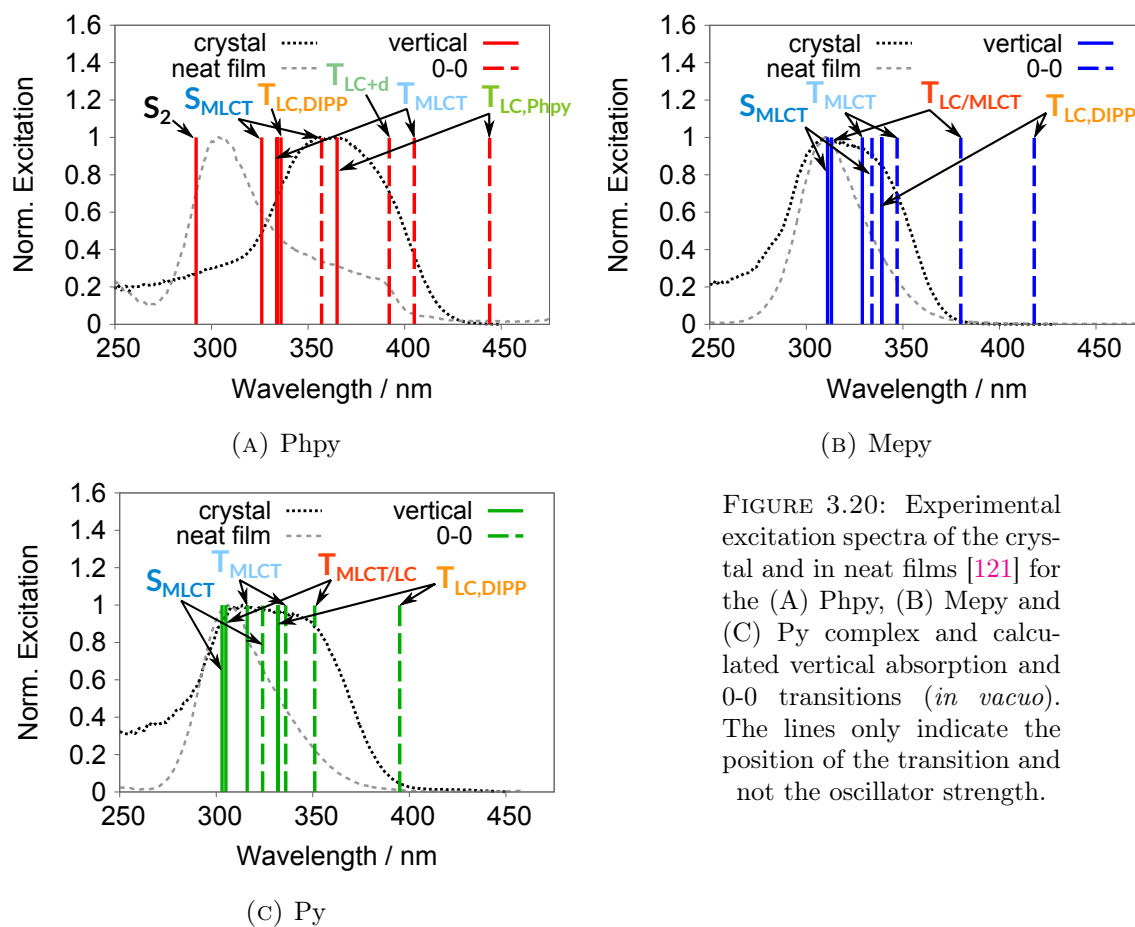


FIGURE 3.20: Experimental excitation spectra of the crystal and in neat films [121] for the (A) Phpy, (B) Mepy and (C) Py complex and calculated vertical absorption and 0-0 transitions (*in vacuo*). The lines only indicate the position of the transition and not the oscillator strength.

Although single crystals of the linear complexes show only weak emission and although it therefore remains unclear whether the excitation spectra actually stem from the linear complexes, the experimental spectra were plotted together with vertical and 0-0 transitions of the states closest in energy (Fig. 3.20).

The vertical S_1 excitation energy of the Phpy complex lies at 325 nm where the intensity of the excitation spectrum of the crystal powder is already strongly decreased, while the 0-0 transition of the S_1 state (357 nm) almost coincides with the maximum of the spectrum (Fig. 3.20). Additionally, the vertical excitation into the $T_{LC,Phpy}$ (365 nm) lies within the range of the excitation maximum. The neat film excitation spectrum peaks at about

305 nm. The next closest vertical singlet excitation is the excitation into the S_2 at 292 nm. In between the S_1 and the S_2 state lie several triplets, which were omitted in Figure 3.20 in order to keep the picture uncluttered. Anyways, one would not expect significant excitation intensity stemming from the triplets in a neat film.

For the Mepy complex the vertical S_1 energy (311 nm) and the vertical $T_{LC/MLCT}$ energy (313 nm) agree almost perfectly with the excitation maximum of the crystal powder and the neat film. In the region between about 310 nm and 380 nm the intensity of the spectrum in neat film falls off considerably steeper compared to the spectrum of the solid.

The excitation spectrum of the crystalline Py complex is even broader than the spectrum of the Mepy complex. The vertical energies of the S_1 and the $T_{MLCT/LC}$ do not agree as well with the excitation maximum as they do for the Mepy complex. It seems like the vertical excitation energies calculated *in vacuo* for the Py complex are all slightly too high in energy. However, this does not seem to be an effect of the different geometry in crystal structure. For the neat film the agreement between the S_1 vertical energy and the excitation maximum appears to be rather good. As for the Mepy complex, the intensity falls off considerably steeper compared to the crystal spectrum.

Although transitions can be found that match the excitation spectra energetically, one has to keep in mind that the oscillator strengths of these transitions are small. In spite of all the mentioned doubts, further discussion is based on the assumption that the excitation and emission spectra stem from the linear complexes.

LIPs between the S_0 and S_1 minima

Linearly interpolated paths (LIPs) between the S_0 and S_1 minimum were calculated in order to understand what happens after vertical excitation into the S_1 state (see Figure 3.21). The reaction coordinate $RC = 0.0$ corresponds to the DFT optimized S_0 and the $RC = 1.0$ to the TDDFT optimized S_1 minimum. At each of the points DFT/MRCI calculations were carried out and the energies relative to the S_0 energy at the S_0 minimum were plotted.

Phpy complex. For the Phpy complex, excitation into the maximum of the excitation spectrum at about 350 nm was assumed, as mentioned before, to be either an excitation into 0-0 transition of the S_1 state or directly into the $T_{LC,Phpy}$ state. Exciting into the 0-0 transition is equivalent to exciting into the S_1 minimum, which means that, in this case, for understanding the photophysical relaxation pathway the LIP between the S_1 and the T_1 minimum is more important to look at.

Mepy and Py complexes. For the Mepy and the Py complex on the other hand, excitation at 310 nm presumably means vertical excitation into the S_1 state. While relaxing towards the S_1 minimum, the S_1 surface (blue squares) crosses at about $RC = 0.2$ with the $T_{LC/MLCT}$ (red triangles) in case of the Mepy and with the $T_{MLCT/LC}$ (red triangles) in

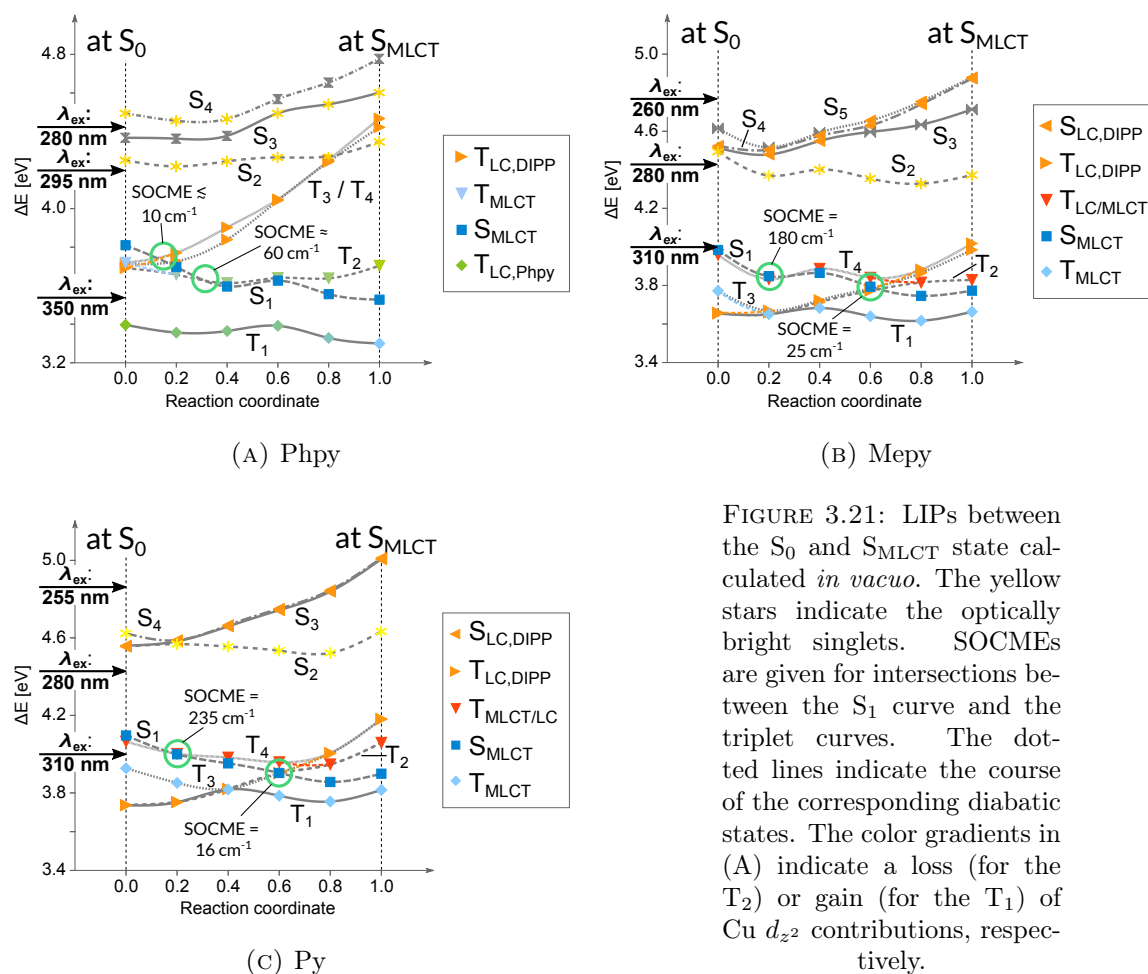


FIGURE 3.21: LIPs between the S_0 and S_{MLCT} state calculated *in vacuo*. The yellow stars indicate the optically bright singlets. SOCMEs are given for intersections between the S_1 curve and the triplet curves. The dotted lines indicate the course of the corresponding diabatic states. The color gradients in (A) indicate a loss (for the T_2) or gain (for the T_1) of Cu d_{z^2} contributions, respectively.

case of the Py complex (see Figure 3.21 (B) and (C)). In case of the Py complex, however, one has to keep in mind that at crystal structure the $T_{MLCT/LC}$ lies above the S_1 state, so it is not clear if the crossing would actually occur in the crystal. Nevertheless, it might still be possible to populate the $T_{MLCT/LC}$ upon excitation, since the Steffen group uses a Hg lamp with a filter for the excitation. The excitation pulse has a line width which is not infinitesimally small. Because the S_1 and the $T_{LC/MLCT} / T_{MLCT/LC}$ have Cu $3d$ contributions from different spatial orbitals, spin-orbit coupling between the S_1 and the $T_{LC/MLCT} / T_{MLCT/LC}$ is rather large — at $RC = 0.2$ the largest mutual $S_1 / T_{MLCT/LC}$ SOCME = 235 cm^{-1} (see Fig. 3.21). Such strong spin-orbit coupling does presumably not only enable a fast ISC process, but also the preparation of a spin-orbit mixed excited state wave package.

A second crossing occurs at $RC = 0.6$ with the $T_{LC,DIPP}$ states. Although the SOCMEs for these triplets are significantly smaller, they are large enough to enable ISC into these states, too.

Assuming that the S_1 does not lose all its population on its relaxation path, intersystem crossing rate constants at the S_1 minimum as well as the LIPs between the S_1 minimum

TABLE 3.5: Radiative rate constants for the singlet and triplets at their minima and ISC rate constants between the S_{MLCT} and the respective triplet minimum.

	singlet	k_{F} [s^{-1}]	triplet	k_{P} [s^{-1}]	τ_{P}	k_{ISC} [s^{-1}]
Phpy	S_{MLCT}	5.3×10^6	$T_{\text{LC,Phpy}}$	6.8×10^1	15 ms	6.0×10^{10}
			T_{MLCT}	2.4×10^2	4.1 ms	2.1×10^{10}
			$T_{\text{LC+d,Phpy}}$	6.1×10^3	0.16 ms	4.0×10^{10}
Mepy	S_{MLCT}	5.3×10^6	$T_{\text{LC,DIPP}}$	1.6×10^{-1}	6.2 s	1.1×10^8
			T_{MLCT}	2.0×10^5	$5.1 \mu\text{s}$	5.9×10^7
			$T_{\text{LC/MLCT}}$	2.0×10^2	5.1 ms	1.9×10^{12}
Py	S_{MLCT}	4.7×10^6	$T_{\text{LC,DIPP}}$	2.0×10^{-1}	5.1 s	1.5×10^7
			T_{MLCT}	1.5×10^5	$6.5 \mu\text{s}$	3.2×10^8
			$T_{\text{MLCT/LC}}$	4.2×10^4	$24 \mu\text{s}$	6.2×10^{10}

and the triplet minima have to be studied, too. Since the S_1 geometry and the T_{MLCT} geometry are virtually the same, no LIP was calculated between the two.

ISC and LIPs between the S_1 minimum and the triplet minima

Phpy complex. ISC rate constants were calculated for the ISC between the S_{MLCT} and the $T_{\text{LC,Phpy}}$, the $T_{\text{LC+d,Phpy}}$ and the T_{MLCT} . The ISC rate constants are all of the same order of magnitude, for the $T_{\text{LC,Phpy}}$ it is $k_{\text{ISC}} = 6.0 \times 10^{10} \text{ s}^{-1}$, for the $T_{\text{LC+d,Phpy}}$ it is $k_{\text{ISC}} = 2.1 \times 10^{10} \text{ s}^{-1}$ and for the T_{MLCT} $k_{\text{ISC}} = 4.0 \times 10^{10} \text{ s}^{-1}$. Hence, all three ISC rate constants are four orders of magnitude larger than the fluorescence rate constant $k_{\text{F}} = 5.3 \times 10^6 \text{ s}^{-1}$ and fluorescence is outcompeted by ISC into the triplets (see also Table 3.5).

LIPs connecting the S_{MLCT} minimum with two of the triplet minima — the $T_{\text{LC,Phpy}}$ and the T_{MLCT} minimum — were calculated. Both LIPs look quite similar (Fig. 3.22). Both triplet minima can be reached barrier-free. The LIP between the S_{MLCT} and the $T_{\text{LC+d,Phpy}}$ is expected to look much alike the LIP between the S_{MLCT} and the $T_{\text{LC,Phpy}}$, only flatter, since the $T_{\text{LC+d,Phpy}}$ minimum lies at 3.2 eV. In case of the LIP between the S_{MLCT} and the $T_{\text{LC,Phpy}}$ minimum, the aforementioned loss of Cu d_{z^2} contributions is indicated by a color gradient. Starting from the T_{MLCT} at the S_{MLCT} minimum relaxation into either the $T_{\text{LC,Phpy}}$ or the T_{MLCT} minimum seems almost equally probable. Since the T_1 curve of the $T_{\text{LC,Phpy}}$ LIP is a bit steeper and the ISC rate constant between the $T_{\text{LC,Phpy}}$ and the S_{MLCT} is by a factor of 1.5 larger, population of this minimum might be a bit more likely.

Mepy complex. Again all ISC processes are faster than the fluorescence which proceeds at a rate of $k_{\text{F}} = 5.3 \times 10^6 \text{ s}^{-1}$. The ISC between the S_{MLCT} and the $T_{\text{LC/MLCT}}$ is the fastest, due to the aforementioned strong spin-orbit coupling between these two states. The ISC rate constant for the $T_{\text{LC/MLCT}}$ is $k_{\text{ISC}} = 1.0 \times 10^{13} \text{ s}^{-1} / 1.9 \times 10^{12} \text{ s}^{-1}$ (calculated

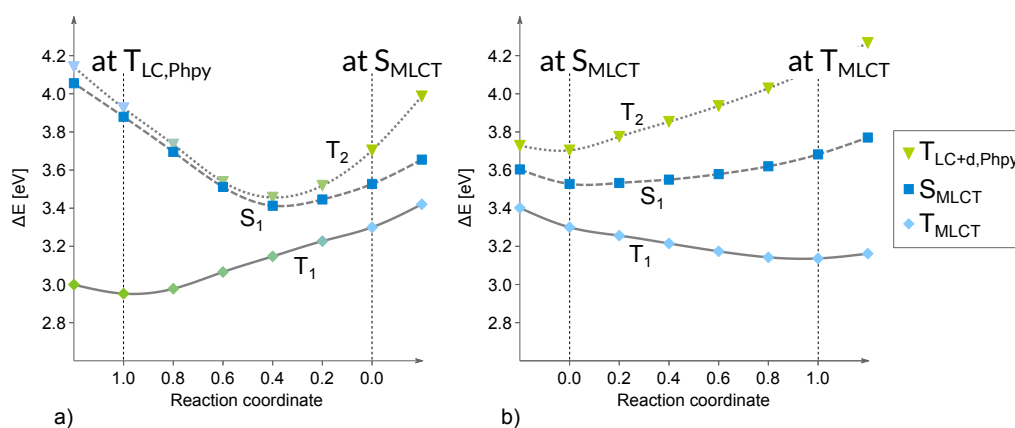


FIGURE 3.22: LIPs calculated for the Phpy complex between a) the S_{MLCT} (RC=0.0) and the $T_{LC,Phpy}$ (RC=1.0) minimum and b) the S_{MLCT} (RC=0.0) and the T_{MLCT} (RC=1.0) minimum *in vacuo*. The color gradients in a) indicate a loss (for the T_1) or gain (for the T_2) of Cu d_{z^2} contributions, respectively.

with $i26\text{ cm}^{-1}$ / $+26\text{ cm}^{-1}$) and hence several orders of magnitude larger than the rate constants for the T_{MLCT} ($k_{ISC} = 5.9 \times 10^7\text{ s}^{-1}$) and the $T_{LC,DIPP}$ ($k_{ISC} = 1.1 \times 10^8\text{ s}^{-1}$). Judging only from the ISC rate constants, population of the $T_{LC/MLCT}$ seems most likely.

The $T_{LC/MLCT}$ and the $T_{LC,DIPP}$ states both lie above the S_{MLCT} state at the S_{MLCT} geometry, but at their optimized geometries, they lie below the S_{MLCT} . In order to investigate the supposed crossings of the two triplet surfaces with the singlet surface and the barrier height for the transition of the singlet population into these states, LIPs between the S_{MLCT} and each of the triplets were calculated. The results are depicted in Figure 3.23 (A). Both LIPs suggest that there is a crossing between the S_1 and the T_2 close to or at the S_1 minimum. Population of the T_2 and subsequent internal conversion to the T_1 state is probably fast and efficient. Besides it seems like both minima, i.e. the $T_{LC/MLCT}$ and the $T_{LC,DIPP}$ minimum, can be reached from the T_{MLCT} almost barrier-free. Since the slope of the $T_{LC,DIPP}$ curve is considerably steeper than the slope of the $T_{LC/MLCT}$ curve, population of the $T_{LC,DIPP}$ seems more likely.

Py complex. Concerning the ISC rate constants and LIPs, the trends are rather similar to the results for the Mepy complex. The $S_{MLCT} \rightsquigarrow T_{MLCT/LC}$ ISC process is the fastest with $k_{ISC} = 6.2 \times 10^{10}\text{ s}^{-1}$, again because of the large SOCMEs between the S_{MLCT} and the $T_{MLCT/LC}$. For the Py complex, the rate constant for ISC between the S_{MLCT} and the T_{MLCT} is $k_{ISC} = 3.2 \times 10^8\text{ s}^{-1}$ and hence one order of magnitude larger than the rate constant for ISC between the S_{MLCT} and the $T_{LC,DIPP}$ ($k_{ISC} = 1.5 \times 10^7\text{ s}^{-1}$). ISC is again faster than the fluorescence which proceeds at a rate of $k_F = 4.7 \times 10^6\text{ s}^{-1}$.

The LIPs look quite alike the ones obtained for the Mepy complex (Figure 3.23 (B)). The potential surfaces calculated for the LIP to the $T_{MLCT/LC}$ are quite flat and the S_1 , T_1 and T_2 potentials are very close in energy. The same assumptions as for the Mepy

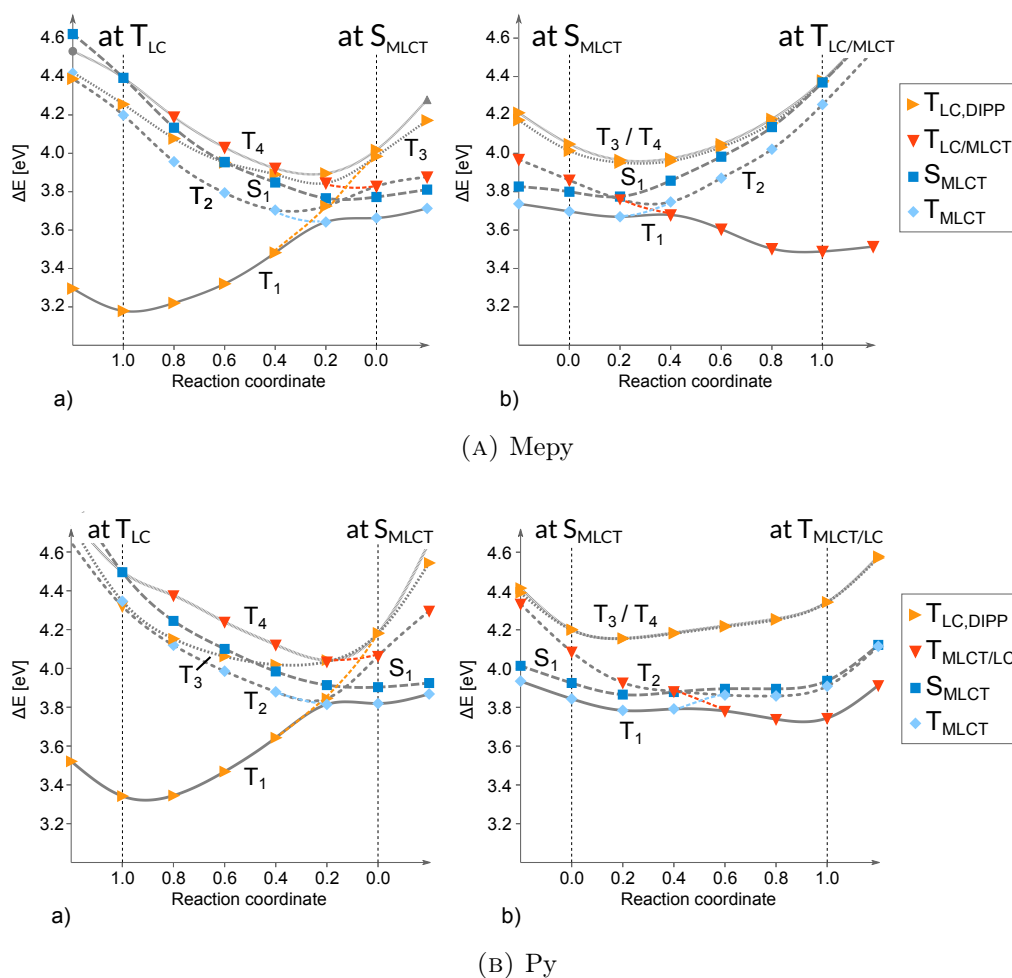


FIGURE 3.23: LIPs for (A) the Mepy and (B) the Py complex between a) the optimized geometry of the S_{MLCT} ($RC=0.0$) and the $T_{LC,DIPP}$ ($RC=1.0$) and b) the optimized geometry of the S_{MLCT} ($RC=0.0$) and the $T_{LC/MLCT}$ or the $T_{MLCT/LC}$ ($RC=1.0$) plotted with DFT/MRCI energies. The dotted lines indicate the course of the corresponding diabatic states.

complex can be made — population of the T_2 due to the crossing between the S_1 and the T_2 curve and subsequent internal conversion to the T_1 state as well as barrier-free transition from the T_{MLCT} to the $T_{MLCT/LC}$ and the $T_{LC,DIPP}$ minimum. Population of the $T_{LC,DIPP}$ seems again more probable. Besides, the $T_{MLCT/LC}$ is quite shallow, the T_1 at the $T_{MLCT/LC}$ minimum lying only 0.1 eV below the T_1 energy at S_1 minimum. Although the reaction coordinates of $T_{MLCT/LC}$ and the $T_{LC,DIPP}$ state involve different normal coordinates and hence cannot be seen as one coordinate, the S_1 minimum may still be seen as a connecting point. It can thus be suggested that if (at room temperature) the energy difference of 0.1 eV can be overcome it is possible to transfer the $T_{MLCT/LC}$ population via the T_{MLCT} to the $T_{LC,DIPP}$ minimum. The T_1 at the $T_{LC,DIPP}$, on the other hand, lies almost 0.5 eV below the T_1 at S_1 minimum and a back transfer seems unlikely in this case.

Unfortunately, the photophysics of all three complexes are quite complicated and it is therefore not possible to finally and unequivocally answer the question which states are populated after photoexcitation. The answer depends on whether one assumes a full relaxation of the S_1 state into its minimum or a depopulation of the S_1 through crossings with the triplets earlier on its relaxation pathway. Since all the involved states are quite close in energy, a lot of intersections and avoided crossings occur. All in all, there are too many factors and not all uncertainties can be resolved in this work. Molecular dynamics calculations might shed some more light onto this question, however, to include as many states into a dynamic calculation — as would be necessary in this case — would be very demanding.

3.2.5 Emission

As I elaborated in the previous section, emission of the linear complexes will most likely be quenched by locally excited triplet states with radiative lifetimes in the ms to s regime. The quantum yields of these complexes are therefore expected to be quite small. However, since at the beginning of my research on these complexes we did not know about the highly luminescent trigonal complexes, I will compare the experimental emission spectra with the results obtained for the linear complexes. For a discussion of the emission properties of the trigonal IPr-Cu(I)-Py complex see Section 3.4.3.

TABLE 3.6: Experimental emission onsets and maxima λ_{max} of the crystalline samples and in neat films. Calculated 0-0 and vertical transitions of the relevant optimized triplets.

	experimental			triplet	calculated	
	environ.	onset [nm]	λ_{max} [nm]		0-0 [nm]	vertical [nm]
Phpy	crystal	420	489	$T_{LC,Phpy}$	444	536
	neat film	410	520	T_{MLCT}	405	740
				$T_{LC+d,Phpy}$	392	452
Mepy	crystal	390	457	$T_{LC,DIPP}$	418	458
	neat film	400	489	T_{MLCT}	347	367
				$T_{LC/MLCT}$	380	446
Py	crystal	400	481	$T_{LC,DIPP}$	395	438
	neat film	400	482	T_{MLCT}	336	367
				$T_{MLCT/LC}$	351	392

Calculated 0-0 transitions correspond to the onsets of experimental spectra and calculated vertical emissions often coincide with experimental emission maxima (λ_{max}). The experimental onsets and emission maxima of the crystals and in neat films as well as the calculated 0-0 and vertical transitions of the optimized triplets are therefore listed in Table 3.6. As for the excitation spectra, the experimental spectra of the crystalline samples and of the neat films are seen to deviate. In this case, rather strong shifts of

the emission maxima (by about 30 nm) can be observed for the Phpy as well as the Mepy complex, whereas for the Py complex the spectra are almost identical (Fig. 3.24 or 3.25).

Since all calculated ISC rates constants are at least one order of magnitude larger than the fluorescence rate constants, the S_1 was excluded from further considerations. Calculated 0-0 transitions and vertical emissions of those triplet states with lifetimes \leq ms are plotted together with the experimental spectra in Figure 3.24. Additionally, Franck-Condon profiles of the emission were calculated (Fig. 3.25).

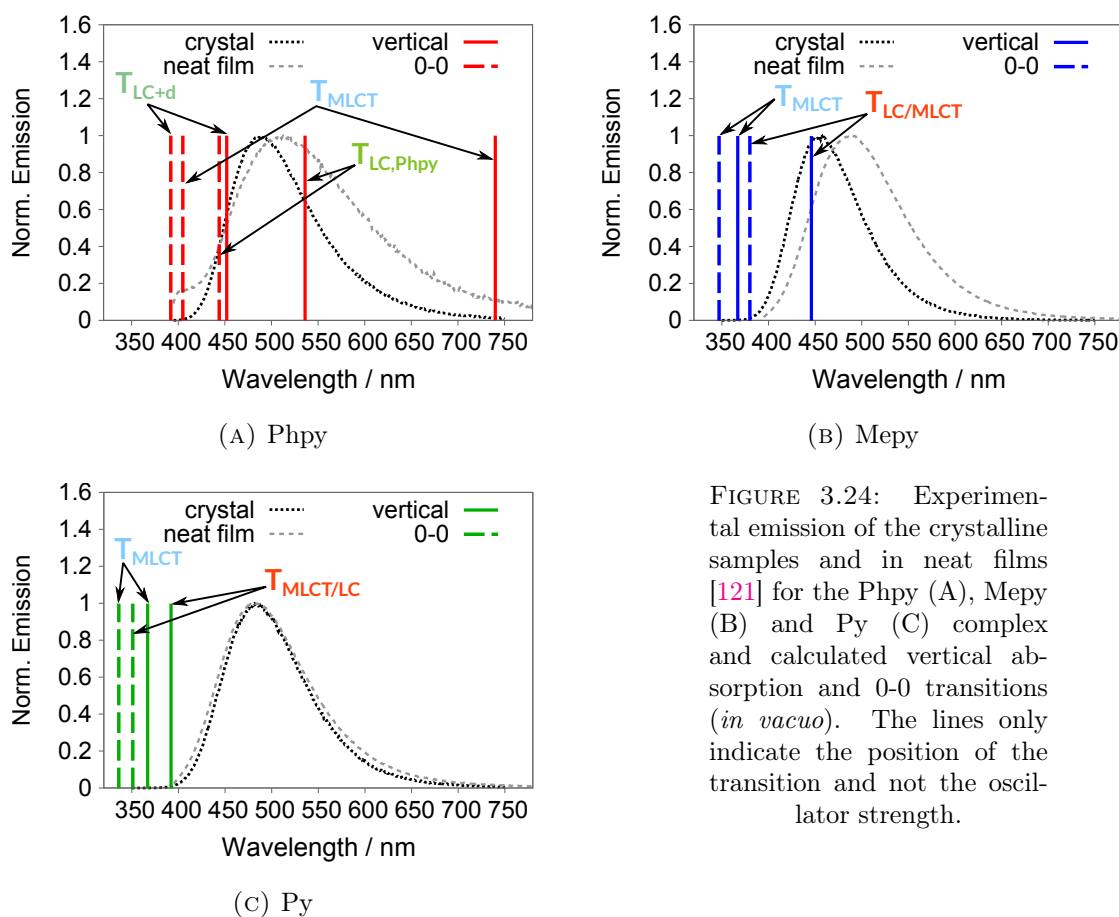


FIGURE 3.24: Experimental emission of the crystalline samples and in neat films [121] for the Phpy (A), Mepy (B) and Py (C) complex and calculated vertical absorption and 0-0 transitions (*in vacuo*). The lines only indicate the position of the transition and not the oscillator strength.

Phpy complex. For the Phpy complex, the onsets and vertical emissions of the triplets denoted $T_{LC,Phpy}$, T_{MLCT} and $T_{LC+d,Phpy}$ at least cover the range of the experimental emission. The 0-0 transition of the T_{MLCT} fairly agrees with the onsets of the emission (see Figure 3.24 and Table 3.6). The vertical emission wavelength of the T_{MLCT} , which is shifted far into the red region, might be an artifact. The short distance between the Cu1 and the C6 atom of the phenylpyridine phenyl leads to a strong destabilization of the S_0 state. At the S_1 geometry the Cu1-C6 distance is 2.34 Å and the S_0 state lies 0.8 eV above the S_0 of the optimized S_0 geometry, while at the T_{MLCT} geometry the Cu1-C6 distance is 2.07 Å and the S_0 state lies 1.5 eV above the S_0 of the optimized S_0 (see also Figure 3.11). In other words, small geometry changes can have a large impact on the emission energy,

as is also illustrated in Figure 3.26. The T_1 curve is quite flat and going from $RC=1.0$ to $RC=0.8$ corresponds to increasing the T_1 energy by only 0.006 eV, but decreasing the S_0 energy by 0.193 eV and therefore shifting the emission wavelength from 740 nm to 661 nm. Similar observations held true for the other states and complexes and we therefore have to deal with large uncertainties concerning the calculated emission maxima.

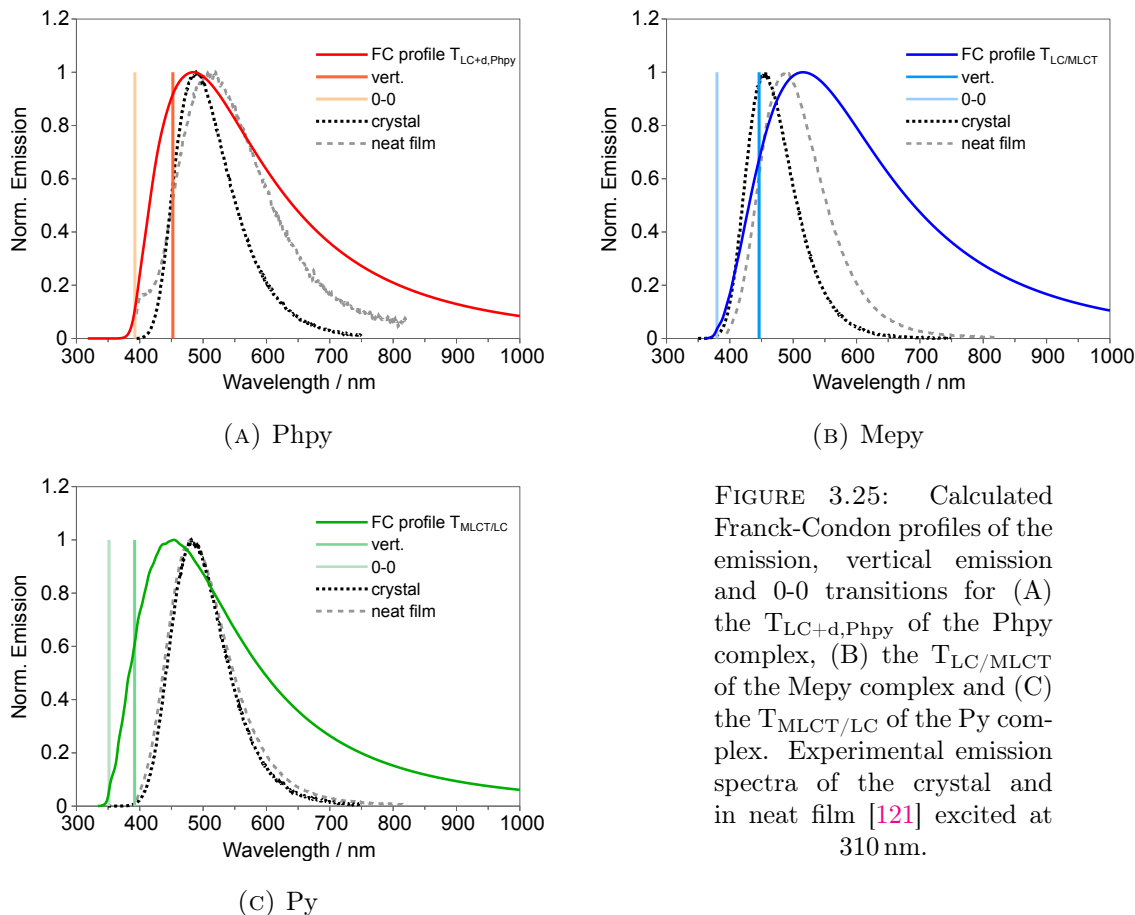


FIGURE 3.25: Calculated Franck-Condon profiles of the emission, vertical emission and 0-0 transitions for (A) the $T_{LC+d,Phpy}$ of the Phpy complex, (B) the $T_{LC/MLCT}$ of the Mepy complex and (C) the $T_{MLCT/LC}$ of the Py complex. Experimental emission spectra of the crystal and in neat film [121] excited at 310 nm.

Calculation of the Franck-Condon (FC) profiles gave only reasonable results for the $T_{LC+d,Phpy}$. The maximum of the calculated FC profile does not coincide with the calculated vertical transition, however, it matches the maximum of the emission spectrum of the crystalline sample (see Fig.3.25). On the other hand, the onset of the calculated spectrum just barely matches the experimental onsets. Besides, the FC profile is far too broad, probably because of the harmonic oscillator approximation employed in the calculations.

The phosphorescence rate constants calculated for the three minima vary over two orders of magnitude (see Table 3.5). The $T_{LC,Phpy}$ has the smallest rate constant ($k_P = 6.8 \times 10^1 \text{ s}^{-1}$) and the $T_{LC+d,Phpy}$ the largest ($k_P = 6.1 \times 10^3 \text{ s}^{-1}$), while the T_{MLCT} lies roughly in the middle ($k_P = 2.4 \times 10^2 \text{ s}^{-1}$). For the $T_{LC,MLCT}$ the energy difference $\Delta E_{S_1-T_1}$ is the smallest and the coupling to the S_1 state the strongest. The T_{MLCT} has large SOCMEs with the S_2 and S_3 state, however, these states lie more than 1.3 eV above the triplet state. The corresponding radiative lifetimes are rather long — 15 ms ($T_{LC,Phpy}$),

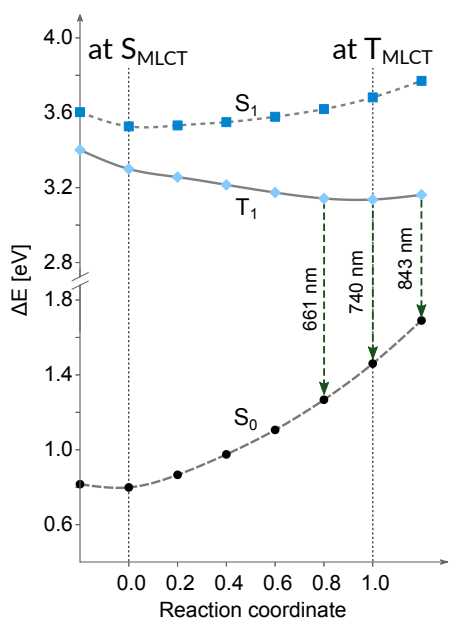


FIGURE 3.26: LIP calculated for the Phpy complex between the S_{MLCT} ($\text{RC}=0.0$) and the T_{MLCT} ($\text{RC}=1.0$) minimum *in vacuo*. The geometry changes that occur between the S_{MLCT} and the T_{MLCT} minimum affect the S_0 energy a lot stronger than the energies of the excited states. The vertical emission energies of the T_1 state given for $\text{RC} = 0.8, 1.0$ and 1.2 therefore vary between 661 and 843 nm.

4.1 ms (T_{MLCT}) and 0.16 ms ($T_{\text{LC+d,Phpy}}$). Hence, it does not seem reasonable to assume that the phosphorescence can compete with non-radiative relaxation processes (at least not at RT).

Mepy complex. For the Mepy complex, the 0-0 transition and vertical emissions of the $T_{\text{LC/MLCT}}$ and $T_{\text{LC,DIPP}}$ state match the experimental emission of the crystalline sample quite well, but the lifetime of the $T_{\text{LC,DIPP}}$ is so long ($\tau_P = 6.2$ s) that it is highly improbable to observe phosphorescence from this state (see Tables 3.6 and 3.5 and Figure 3.24). The emission from the $T_{\text{LC/MLCT}}$ state proceeds with $k_P = 2.0 \times 10^2 \text{ s}^{-1}$. The phosphorescence rate constant of the T_{MLCT} state is $2.0 \times 10^5 \text{ s}^{-1}$, yet the T_{MLCT} lies energetically above the $T_{\text{LC/MLCT}}$ and the $T_{\text{LC,DIPP}}$ states and, as we have seen in before, can be depopulated barrier-free. Since the $T_{\text{LC/MLCT}}$ is the only state geometry from which phosphorescence might be observable, it is the only state for which a Franck-Condon profile was calculated (see Figure 3.25). As for the Phpy $T_{\text{LC+d,Phpy}}$, the maximum of the calculated FC profile does not coincide with the calculated vertical transition and the whole spectrum is far too broad. As mentioned before, the 0-0 transition and vertical emissions match the experimental emission of the crystalline sample rather well, but the maximum of the FC profile is somewhat too far red-shifted to match λ_{max} of the experimental spectra. Possible effects of the solvent molecules (CHCl_3), which are incorporated into the crystal lattice, are not accounted for in the calculations.

Py complex. For the Py complex the agreement between the experimental emission spectra and the calculations seems to be very poor (Figure 3.24). The only calculated vertical emission that fits somehow to the experimental emission is the emission of the $T_{\text{LC,DIPP}}$ (see Table 3.6). However, this state is as dark as it is in the Mepy complex (see

Table 3.5). The $T_{\text{MLCT/LC}}$ phosphorescence rate constant amounts to $4.2 \times 10^4 \text{ s}^{-1}$ and that for the T_{MLCT} to $1.5 \times 10^5 \text{ s}^{-1}$, yet again the T_{MLCT} can be depopulated barrier-free. The Franck-Condon profile was therefore calculated for the $T_{\text{MLCT/LC}}$ (Fig. 3.25). The maximum of the calculated FC profile lies at higher wavenumbers than the vertical transition which leads to a somewhat better agreement with the experimental λ_{max} , but the onset does not match the experimental onsets. As for the Phpy and Mepy complex, the FC profile is a lot broader than the experimental spectra.

3.2.6 Summary and conclusions

Summing the results up:

- The agreement between the calculated and the experimental absorption spectra is not very good. Although it seems reasonable to assume that the pyridine ligands rotate freely and an interligand dihedral angle of 70° leads to a much better agreement with the experimental spectra for the Mepy and Py complex, it remains unclear why this angle should be favorable. Environmental effects only play a marginal role.
- The S_1 and the first four triplets lie quite close in energy. The high density of states makes it difficult to decide which of the states is populated after photoexcitation.
- For all three complexes the calculated ISC into the triplets is faster than the fluorescence from the S_1 state.
- For all three molecules, the triplet with the lowest absolute energy has LC character. Due to the strong LC character, the radiative lifetimes of these states are quite long. For the Phpy complex it is the $T_{\text{LC,Phpy}}$ with $\tau_P = 15 \text{ ms}$ and for the Mepy and the Py complex it is the $T_{\text{LC,DIPP}}$ with $\tau_P = 6.2 \text{ s}$ or $\tau_P = 5.1 \text{ s}$, respectively. If we assume that these states are predominantly populated, we have to conclude that the complexes should not be luminescent at room temperature.
- The vertical emission wavelength and the 0-0 transitions calculated at the vacuum minima only (if at all) agree for the Phpy and Mepy complex with the experimental emission spectra. In case of the Py complex, all the calculated transitions are too high in energy.

The described discrepancies between the calculated results and the experimental results may be explained by assuming that the experimental samples contained some mixture between the linear and the trigonal complexes. In solution, both species probably exist in equilibrium, so the absorption spectrum might be some superposition of both the absorption properties from the linear and the trigonal complexes. The emission, on the other hand, probably stems from the trigonal complexes, since the single-crystals of the linear

complexes show no luminescence, while the single-crystals of the trigonal complexes do. The photophysical properties of the trigonal Py complex will be discussed in Section 3.4.

Although the linear complexes are only weak emitters, some of their properties suggest that deliberate modifications on the ligands could lead to molecules with good emission qualities. One of the major drawbacks of metal organic TADF emitters is that in many cases the S_1 and T_1 are MLCT states where the wavefunctions consist of the same configurations. Spin-orbit coupling elements between a singlet and a triplet with the same spatial occupation are small — or strictly speaking zero — due to symmetry reasons. In other words, the electronic part of the ISC rate constants may reduce the overall rate constant. In case of the Mepy complex, all three SOCMEs between the S_{MLCT} and the T_{MLCT} are smaller than 1 cm^{-1} , reducing k_{ISC} by a factor of 0.5. If, however, a second triplet with other metal $3d$ contributions is close by, this can enhance the ISC rate constants. For example in case of the Py complex, the ISC rate constant between the S_{MLCT} and the $T_{MLCT/LC}$ is two orders of magnitude larger than the $S_{MLCT} \rightsquigarrow T_{MLCT}$ ISC rate constant. Hence, if it was possible to either remove the $T_{LC,DIPP}$ state by using aliphatic groups or to modify the aromatic groups in such a way, that the $T_{LC,DIPP}$ state is pushed to higher energies, while also preserving the favorable properties of the S_{MLCT} , T_{MLCT} and the $T_{MLCT/LC}$ states, the modified linear complexes may prove to be good emitters. The replacement of the DIPP moieties by aliphatic groups and the resulting implications will be explored in the next section (Section 3.3).

3.3 Design principles for linear NHC complexes (Paper III)

As mentioned in the previous section (Section 3.2.6), the linear Ipr-Cu(I)-pyridine complexes show some favorable properties, such as fast ISC between the S_{MLCT} and the $T_{MLCT/LC}$, due to different copper $3d$ contributions ($d_\sigma \leftrightarrow d_\pi$) and the resulting large spin-orbit coupling between the two states. In addition, the energy gaps between the S_{MLCT} and the T_{MLCT} as well as the $T_{MLCT/LC}$ are small enough that RISC and TADF might be realized for these complexes. The radiative rate constants of the S_{MLCT} , T_{MLCT} and the $T_{MLCT/LC}$ are reasonably large for efficient phosphorescence or TADF, but the emission is quenched by the long-lived $T_{LC,DIPP}$ state. By replacing the DIPP moieties with aliphatic moieties, this problem should be solved. The calculations, however, indicate that such a replacement leads to emission energies in the UV region. The next sections will therefore not only cover the substitution of the DIPP moieties, but also modifications on the NHC backbone and the pyridine ligand that enable a tuning of the emission energies back into the visible regime.

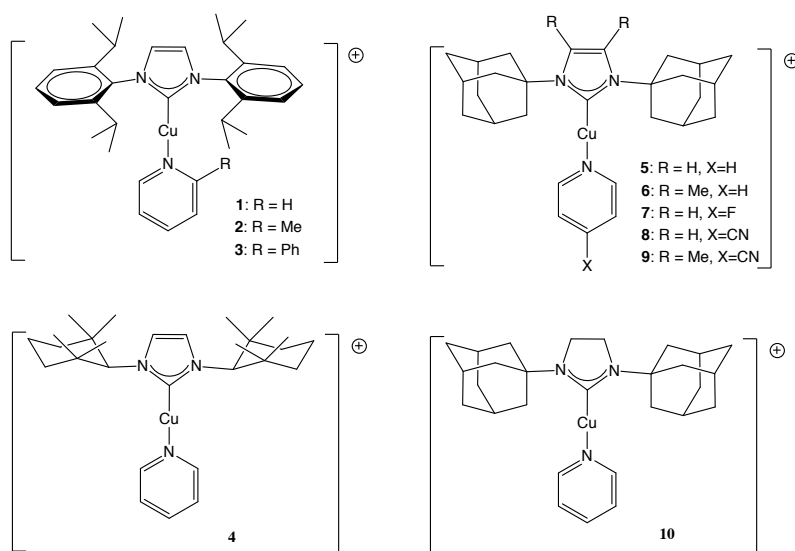


FIGURE 3.27: Structures of the linear IPr-Cu(I)-pyridine complexes and their modifications.

3.3.1 Modification of the NHC substituents

Starting from the Ipr-Cu(I)-pyridine complex, a first attempt to get rid of the $T_{LC,DIPP}$ state was made by substituting bulky cyclohexane derivatives for the DIPP moieties (Figure 3.27, compound 4). Although this substitution showed that the favorable properties of the S_{MLCT} , T_{MLCT} and the $T_{MLCT/LC}$ can be preserved, the resulting emission maximum lies too far in the UV region (345 nm for the phosphorescence) to assume that it can be tuned to the visible regime.

A more promising structural motif is achieved by replacing DIPP by 1-adamantyl (Ad) (Figure 3.27, compound **5**), since the calculated emission wavelengths are close to the visible regime (about 380 nm for the fluorescence and about 400 nm for the phosphorescence). The $T_{\text{MLCT/LC}}$ state gains interligand charge transfer contributions ($\pi_{\text{NHC}} \rightarrow \pi_{\text{Py}}$) (IL) upon geometry relaxation and is therefore renamed $T_{\text{IL/MLCT/LC}}$. It lies at 3.52 eV and constitutes the global triplet minimum (see Figure 3.28). The S_{MLCT} and T_{MLCT} states lie at 3.81 eV and 3.65 eV, respectively. Spin-orbit coupling remains large between the S_{MLCT} and the $T_{\text{IL/MLCT/LC}}$, resulting in high ISC and RISC rate constants that are of the same order of magnitude ($k_{\text{ISC}} = 2.9 \times 10^{11} \text{ s}^{-1}$ and $k_{\text{RISC}} = 1.0 \times 10^{11} \text{ s}^{-1}$). Since the computed radiative rate constant for the S_{MLCT} is $k_{\text{F}} = 2.3 \times 10^6 \text{ s}^{-1}$, while phosphorescence from the $T_{\text{IL/MLCT/LC}}$ proceeds with $k_{\text{P}} = 1.4 \times 10^4 \text{ s}^{-1}$, prompt fluorescence and phosphorescence will be outcompeted by (R)ISC and TADF should be the main emission channel (see also Table 3.7 and Fig. 3.29).

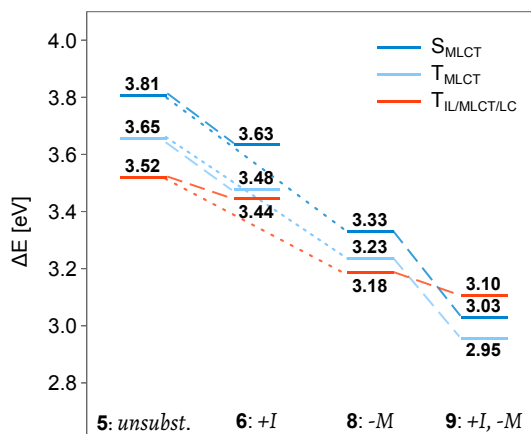


FIGURE 3.28: Influence of the $+I$ and $-M$ substituents on the adiabatic energies of the S_{MLCT} , T_{MLCT} and $T_{\text{IL/MLCT/LC}}$ minima of compounds **6**, **8** and **9** compared to the unsubstituted compound **5**.

Because the orbitals involved in the lowest singlet and triplet excitations have amplitudes on the carbon atoms of the NHC backbone as well as on the pyridine ligand, $+I$ substituents were introduced into the NHC backbone and $-M$ substituents at the *para* position of the pyridine ligand. Thereby, the electron donating properties of the NHC ligand and the electron accepting properties of the pyridine ligand were sought to be enhanced and the emissive states to be lowered in energy.

3.3.2 Modification of the NHC backbone

By introducing methyl groups in the 4- and 5-positions of the imidazol-2-ylidene (Figure 3.27, compound **6**), the adiabatic energies of the S_{MLCT} and T_{MLCT} states are lowered by about 0.17 eV while the $T_{\text{IL/MLCT/LC}}$ state is only stabilized by about 0.08 eV (see also Figure 3.28). Since the calculated emission maximum still lies in the violet, barely visible

TABLE 3.7: Rate constants k (s^{-1}) for radiative decay of the singlet and triplets of compounds **5**, **6**, **8** and **9** at their minima and rate constants for ISC and RISC between the S_{MLCT} and the respective triplet minimum.

compound	singlet	k_{F}	triplet	k_{P}	k_{ISC}	k_{RISC}
5	S_{MLCT}	2.4×10^6	T_{MLCT}	1.0×10^5	9.0×10^8	
			$T_{\text{IL/MLCT/LC}}$	1.4×10^4	2.9×10^{11}	1.0×10^{11}
6	S_{MLCT}	1.7×10^6	T_{MLCT}	4.6×10^4	not calc.	
			$T_{\text{IL/MLCT/LC}}$	2.1×10^4	not calc.	not calc.
8	S_{MLCT}	1.0×10^6	T_{MLCT}	7.8×10^4	4.1×10^8	
			$T_{\text{IL/MLCT/LC}}$	1.3×10^4	1.3×10^{11}	8.0×10^{10}
9	S_{MLCT}	8.6×10^5	T_{MLCT}	4.6×10^4	7.0×10^7	9.7×10^5
			$T_{\text{IL/MLCT/LC}}$	5.8×10^3	2.1×10^{11}	3.6×10^{11}

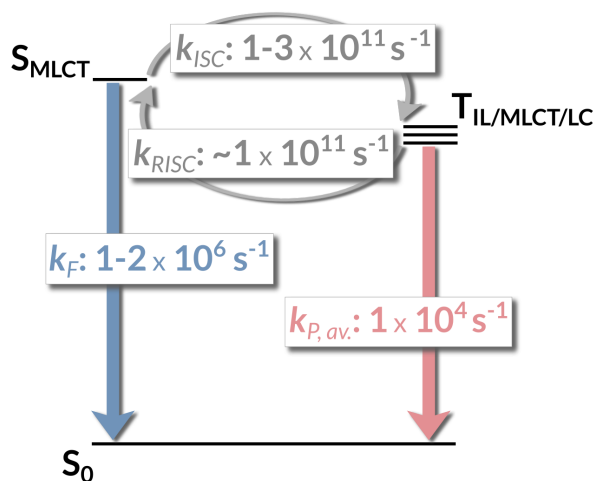


FIGURE 3.29: Radiative rates and rates for ISC and RISC between the S_{MLCT} and the $T_{\text{IL/MLCT/LC}}$ minimum for compounds **5** and **8**

spectral region ($\lambda_{\text{max}} \approx 400 \text{ nm}$), no (R)ISC rate constants were calculated for this complex. Although the $+I$ effect of the methyl groups is by itself not sufficient to tune the emission to the visible regime, it can assist the effect of the $-M$ substituent introduced in the next section.

An alternative route, where the $\text{C}=\text{C}$ double bond of the five-membered ring was hydrogenated (Figure 3.27, compound **10**), was discarded. The stabilization of the adiabatic energies of the S_{MLCT} and T_{MLCT} only amount to 0.06 eV and 0.08 eV, respectively. Besides, all attempts to optimize the $T_{\text{IL/MLCT/LC}}$ (which is in this case dominated by a mixture of $d_{\pi} \rightarrow \pi_{\text{Py}}$ and local $\pi \rightarrow \pi^*$ excitations) failed, since they all ended up in crossings with the T_{MLCT} state.

TABLE 3.8: Emission wavelengths λ_{max} (nm) of the singlet and triplets of compounds **5**, **6**, **8** and **9** at their minima.

compound	singlet	$\lambda_{\mathbf{F}}$	triplet	$\lambda_{\mathbf{P}}$
5	S _{MLCT}	378	T _{MLCT}	395
			T _{IL/MLCT/LC}	393
6	S _{MLCT}	398	T _{MLCT}	417
			T _{IL/MLCT/LC}	397
8	S _{MLCT}	452	T _{MLCT}	470
			T _{IL/MLCT/LC}	450
9	S _{MLCT}	496	T _{MLCT}	513
			T _{IL/MLCT/LC}	484

3.3.3 Introducing $-M$ substituents in the pyridine ligand

The first idea, which was to introduce fluorine at the *para* position of the pyridine ligand (Figure 3.27, compound **7**), did not lead to success. It seems like the desired ($-I$) effects caused by fluorination are outweighed by its $+M$ effects, leading to an increase instead of a decrease of the excitation energies.

Substituents with a $-M$ effect, on the other hand, seem to shift the excitation energies into the right direction, as can be shown by adding a cyano group in *para* position of the pyridine ligand (compound **8**). The adiabatic energies of the S_{MLCT} and T_{MLCT} of compound **8** are decreased by about 0.4–0.5 eV compared to the unsubstituted complex **5**. Stabilization of the T_{MLCT/LC} state amounts to 0.34 eV. The (R)ISC and radiative rate constants are very similar to those calculated for complex **5**, which means that prompt fluorescence and phosphorescence are outcompeted by (R)ISC and TADF is expected to prevail. The strong redshift induced by the $-M$ substituent leads to an emission in the blue spectral region, the calculated vertical S_{MLCT} emission energy being 452 nm.

3.3.4 Combining the $+I$ and $-M$ effects

Further tuning of the emission wavelength can be achieved by combining the $+I$ effects, brought about by the methylation of the imidazol-2-ylidene, and the $-M$ effect, induced by a CN substituent introduced at the *para* position of the pyridine ligand (Figure 3.27, compound **9**). Due to stonger effect of the $+I$ and $-M$ substituents on the adiabatic energies of the T_{MLCT} (and S_{MLCT}), the T_{MLCT} now constitutes the global triplet minimum at 2.95 eV (see also Figure 3.28). The T_{IL/MLCT/LC}, on the other hand, lies slightly above the S_{MLCT}. Spin-orbit coupling between the S_{MLCT} and T_{MLCT} is weak due to their nearly identical electronic structures. Nevertheless, their nested potentials and small energy gap lead to (R)ISC rate constants that can compete with the fluorescence and the phosphorescence. Both ISC processes between the S_{MLCT} and the T_{IL/MLCT/LC} are predicted to proceed at the picosecond time scale (Table 3.7). Taken together, the calculations suggest that the

major emission process will be blue to green TADF. The emission maxima calculated for compounds **5**, **6**, **8** and **9** are collected in Table 3.8.

3.3.5 Summary and conclusions

Summing the results up:

- It is possible to get rid of the $T_{LC,DIPP}$ states by replacing DIPP with adamantyl, while concomitantly preserving the favorable properties of the S_{MLCT} , T_{MLCT} and $T_{MLCT/LC}$ states (i.e. fast (R)ISC and sufficiently short emission lifetimes). The $T_{MLCT/LC} / T_{IL/MLCT/LC}$ state constitutes the global triplet minimum.
- Substituting adamantyl for DIPP leads to a strong blue-shift of the emission energies into the UV region.
- The emission wavelength can be tuned back into the visible spectral region by introducing $+I$ substituents in the NHC backbone and $-M$ substituents at the *para* position of the pyridine ligand.
- The $+I$ effect of methylation of the imidazol-2-ylidene is by itself not strong enough to obtain emission maxima in the visible regime.
- The $-M$ effect of CN, however, leads to a substantial stabilization of the emissive states. An emission wavelength of about 450 nm, i.e. in the blue spectral region, can be achieved.
- Combination of the $+I$ effect of methyl and the $-M$ effect of CN can be used to further shift the emission maximum into the blue-green region. Although the ordering of states changes — with the T_{MLCT} now as the lowest triplet minimum — (R)ISC is still fast enough to outcompete prompt fluorescence and phosphorescence.
- Complexes **8** and **9** are therefore predicted to be efficient blue to green TADF emitters.

3.4 Trigonal NHC-Cu(I)-bis-Py complex (unpublished)

In this section the different behavior of the linear and the trigonal complexes will be exemplified and explained with computational studies on the trigonal Ipr-Cu(I)-bis-Py complex. All calculations were carried out *in vacuo*. The same methods were used as for the linear complexes. The DFT/MRCI calculations at the excited state minima were restricted to 10 excited roots.

3.4.1 Ground state

According to DFT/MRCI calculations at the DFT optimized S_0 geometry, the two lowest lying singlets have MLCT character, where the electron density is transferred from a d_{xz} like orbital to π^* orbitals on both pyridine ligands (see also Table 3.9). The T_1 and T_2 state have mixed MLCT/LC character, the T_1 having stronger MLCT and the T_2 having stronger LC contributions. The T_3 state corresponds to the S_1 state. The T_4 state is also a MLCT state, but in this case the metal d contributions come from a d_{z^2} like orbital (the axis designation was chosen assuming that the Cu-C bond lies on the z-axis). The T_5 state corresponds to the S_2 with some additional $\pi_{\text{NHC}} \rightarrow \pi_{\text{Py}}^*$ CT contributions.

TABLE 3.9: Vertical DFT/MRCI energies and characterization of the lowest lying singlet and triplet states at the optimized S_0 geometry.

state	excitation	energy	
		[eV]	[nm]
S_1	$d_{xz} \rightarrow \pi_{\text{Py}}^*$	3.93	315.8
S_2	$d_{xz} \rightarrow \pi_{\text{Py}}^*$	4.04	306.9
T_1	$d_{xz}/\pi_{\text{DIPP}} \rightarrow \pi_{\text{DIPP}}^*$	3.76	330.1
T_2	$(d_{xz})/\pi_{\text{DIPP}} \rightarrow \pi_{\text{DIPP}}^*$	3.76	330.0
T_3	$d_{xz} \rightarrow \pi_{\text{Py}}^*$	3.77	328.9
T_4	$d_{z^2} \rightarrow \pi_{\text{Py}}^*/\pi_{\text{NHC}}^*$	3.87	320.3
T_5	$d_{xz}/\pi_{\text{NHC}} \rightarrow \pi_{\text{Py}}^*$	3.88	319.2
T_6	$d_{z^2} \rightarrow \pi_{\text{Py}}^*$	4.00	309.7

TABLE 3.10: SOCMEs between the S_1 and the triplets below the S_1 at the S_0 geometry.

state	$\langle S_1 \hat{H}_{\text{SO}} T_n \rangle$ [cm ⁻¹]		
	x	y	z
T_1	8.2	-2.8	-4.2
T_2	-35.3	18.0	11.4
T_3	-4.1	-0.7	4.7
T_4	313.8	-149.3	-105.6
T_5	-73.5	37.5	26.6

The first bright singlet is the S_3 at 296 nm for which the electronic structure resembles that of the T_4 state. The largest oscillator strength was calculated for the S_{12} , which lies at 252 nm and is dominated by local $\text{Cu}(d_\pi)$ to $\text{Cu}(4p_\pi)$ with some additional CT character. The calculated absorption spectrum is presented in Figure 3.30, together with the experimental spectrum that was assigned to the linear Py complex. As can be seen in Figure 3.30, the absorption maximum of the bis-Py complex agrees well with the experimental spectrum, supporting the idea that in solution linear and trigonal complexes exist in equilibrium.

Spin-orbit matrix elements between the S_1 and the triplets that lie below the S_1 at the S_0 geometry are listed in Table 3.10. As can be expected, the SOCMEs between the S_1 and the triplet with corresponding character, i.e. the T_3 , are rather small, while especially those with the triplet that has a different spatial d contribution, i.e. the T_4 , are quite sizable.

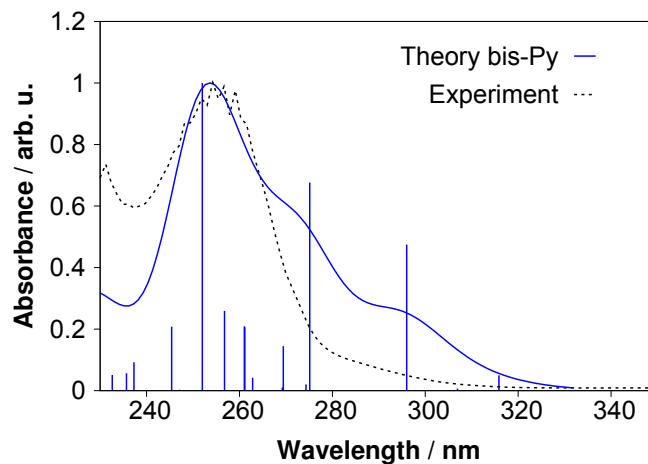


FIGURE 3.30: Calculated absorption spectrum of the bis-Py complex. The experimental spectrum is the one which was ascribed to the linear Py complex.

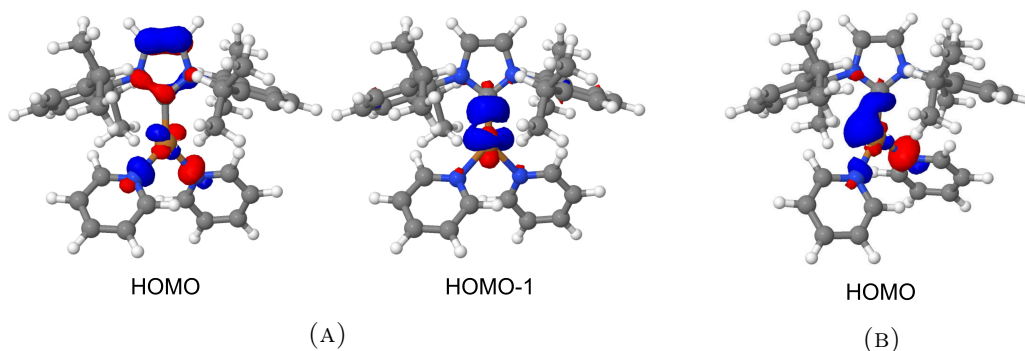


FIGURE 3.31: BH-LYP orbitals of (A) the S_0 and (B) the S_1 structure. The S_0 HOMO has strong d_{xz} and the HOMO-1 d_{z^2} character, while the spatial symmetry of the S_1 HOMO seems to be inbetween the two.

3.4.2 Excited states

In contrast to the linear Py complex, where the lowest triplet minimum corresponds to local DIPP excitations, here TDDFT optimization of the T_1 state gave a triplet minimum with mainly $d_{xz}/d_{z^2} \rightarrow \pi_{\text{Py}}^*$ character, where the π_{Py}^* is localized on only one of the pyridine ligands ($E_{\text{adia.}} = 3.48$ eV). Optimization of the S_1 yielded the corresponding singlet minimum ($E_{\text{adia.}} = 3.66$ eV). Due to the asymmetric T-shape distortion in excited state geometries, one of the C-Cu-N angles is closer to linearity than at the S_0 geometry (about

150–160° compared to about 130°) and the spatial symmetry of the involved d orbital is less obvious and seems to be inbetween d_{xz} and d_{z^2} (see also Fig. 3.31 and Fig. 3.32).

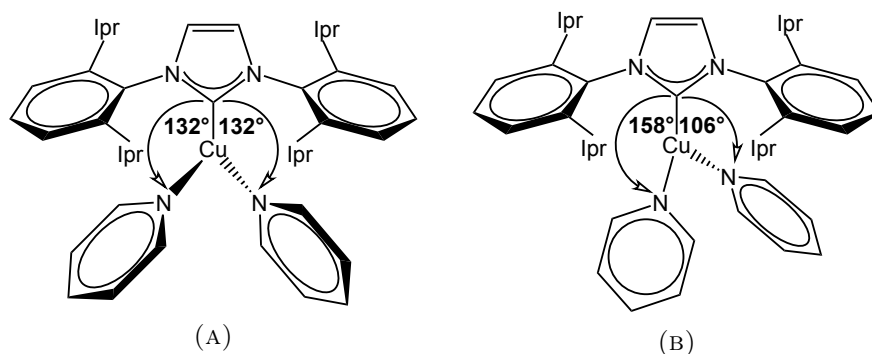


FIGURE 3.32: Most important geometry changes between (A) the S_0 and (B) the S_1 state: The asymmetric T-shaped distortion in the excited state can be understood by looking at the N-Cu-N bond angles.

According to TDDFT calculations at the ground state geometry, the $d_{z^2} \rightarrow \pi^*$ triplet is the T_3 . It was not possible to optimize this minimum, though, probably due to the aforementioned asymmetric distortions in the excited state. The optimization therefore always ends up in a crossing with the T_1 state.

The adiabatic energy of the optimized $d_{xz}/\pi_{\text{DIPP}} \rightarrow \pi_{\text{DIPP}}^*$ triplet state lies at 3.76 eV, that is to say above the S_1 minimum. The structure, however, only constitutes a saddle point on the potential surface (with an imaginary frequency of $i53.1 \text{ cm}^{-1}$).

At the optimized S_1 minimum, only the corresponding triplet state lies below the S_1 . The energy gap at the S_1 minimum amounts to 0.14 eV, while at the T_1 minimum the gap is more than two times larger (0.33 eV). In other words, the T_1 minimum structure is less favorable for the S_1 than *vice versa*. The SOCMEs between the S_1 and the T_1 computed at the two minima are listed in Table 3.11, together with their sum of squares. Judging from the non-negligible SOCMEs, the electronic structures of the S_1 and the T_1 differ strongly enough to enable substantial spin-orbit coupling. In addition, especially at the T_1 minimum, coupling between the S_1 and the T_2 as well as between the T_1 and the S_2 is strikingly strong. For the T_1 and the S_1 state, the leading configuration is the HOMO to LUMO excitation, whereas the T_2 and the S_2 states are governed by HOMO-3 to LUMO and HOMO-6 to LUMO excitations. The spatial symmetry of the $3d$ orbitals that contribute to HOMO-3 and HOMO-6 differ from that contributing to the HOMO, leading to the aforementioned large mutual SOCMEs.

3.4.3 Radiative and (R)ISC rate constants

For the calculation of the vibrational overlap it was necessary to optimize the S_1 starting from the T_1 minimum. The optimized S_1 and T_1 starting from S_0 yield different coordinates, since for the T_1 minimum the excitation goes into the one pyridine ligand and for the S_1 minimum into the other. The S_1 starting from the T_1 minimum and the S_1 starting

TABLE 3.11: SOCMEs between the S_1 / S_2 and the T_1 / T_2 state at the optimized S_1 and T_1 minima.

geometry	states	$\langle S_n \hat{H}_{SO} T_n \rangle$ [cm ⁻¹]			$\Sigma(\text{SOCMEs})^2$ [cm ⁻²]
		x	y	z	
at S_1	S_1, T_1	22.7	1.5	8.1	582
	S_1, T_2	-24.2	6.0	-6.3	661
	S_2, T_1	-4.9	-1.9	0.9	28
at T_1	S_1, T_1	-190.8	24.2	28.1	12596
	S_1, T_2	-361.8	62.6	52.3	137553
	S_2, T_1	-402.9	72.8	65.7	171945

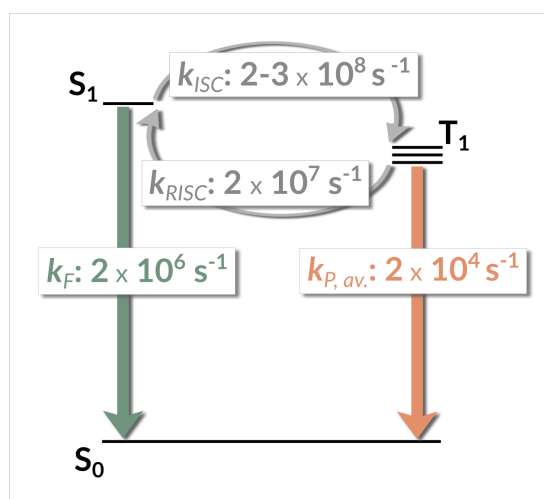


FIGURE 3.33: Radiative and (R)ISC rate constants for the bis-Py complex.

from the S_0 minimum can, however, be transferred into each other by rotation and are therefore equivalent. The calculated radiative and (R)ISC rate constants are presented in Figure 3.33. The T_1 and S_1 lifetimes lie within the normal range of ns for the S_1 and μs for the T_1 . Prompt fluorescence is outcompeted by ISC which two orders of magnitude faster than the fluorescence. Owing to the large SOCMEs between the T_1 and S_1 at the T_1 minimum, the RISC rate constant amounts to $2 \times 10^7 \text{ s}^{-1}$. The RISC rate constant is therefore three orders of magnitude larger than the mean phosphorescence rate constant and TADF should be observable for this complex. The vertical emission of the S_1 lies at 424 nm and that of the T_1 at 465 nm, i.e. the emission maximum lies in the violet to blue spectral range. With 465 nm the triplet emission of the bis-Py complex also lies closer to $\lambda_{max} = 480 \text{ nm}$ of the emission spectrum than any of the emission wavelengths calculated for the linear Py complex (see also Table 3.6). Unfortunately, since the 0-0 overlap between the excited states and the ground state is close to zero, no meaningful Franck-Condon profiles of the emission could be calculated.

3.4.4 Linear Py *versus* trigonal bis-Py

In contrast to the linear Py complex, the emission of the trigonal bis-Py complex is not quenched by a low-lying ^3LC state. Instead, the T_1 has $d_{xz}/d_{z^2} \rightarrow \pi_{\text{Py}}^*$ character and couples strongly with the S_2 state. Besides, coupling between the S_1 and T_1 is non-negligible, too. Taken together, that leads to sufficiently large (R)ISC and radiative rate constants to expect large quantum yields for this complex. This is in agreement with the experimental findings that the crystals of trigonal complexes show luminescence that is several times stronger than that of the linear complexes.

3.5 Linear CAAC-Au(I)-Cz and CAAC-Cu(I)-Cz complexes (Paper II)

For the two complexes discussed in this section — the cyclic (alkyl)(amino)-carbene (CAAC) metal carbazolate (Cz) complexes CAAC-Au-Cz (CMA1) and CAAC-Cu-Cz (CMA2) — the inclusion of solvation effects is essential in order to explain the experimental findings. The complexes presented by Di et al. show high OLED performance enabled by fast ISC [59]. The authors claim that the fast intersystem crossing is due to an intersection of the S_1 and T_1 potential surfaces that occurs upon rotation of the carbazolate ligand. They named this mechanism rotationally assisted spin-state inversion (RASI), since the S_1 state supposedly drops below the T_1 state along the torsional path. They see their claim supported by their observation that the emission wavelength varies for different environments by about 0.4 eV. For the crystalline powder, the most rigid environment, they report an emission of 2.6 eV while in solution the emission lies at 2.22 eV. Hence they conclude that in rigid environments the rotation of the ligand is hindered and consequently the spin-state inversion can not occur. They sought to further verify their assumptions by quantum chemical calculations. Indeed their optimizations of the CAAC-Au-Cz S_1 and T_1 geometries gave a S_1 geometry with an interligand dihedral angle of about 90° which lies energetically below both the T_1 with an interligand dihedral angle of about 0° and of about 90° . However, they optimized the S_1 geometries with TDDFT and the T_1 geometries with UDFT and compared the corresponding energies directly which is — at least — questionable.

Quantum chemical calculations aim at understanding and explaining or even predicting experimental results. A treatment of all involved states and geometries at the same level of theory is advisable to achieve that goal, which is why we repeated the calculations optimizing both the S_1 and the T_1 geometries at the TDDFT level of theory. Subsequent DFT/MRCI and spin-orbit coupling CI calculations were carried out in order to check the two possible reasons we could think of that can invert the singlet-triplet gap in principle — contributions of closed-shell doubly excited configurations to the singlet state and mixing of the states due to spin-orbit coupling.

3.5.1 General considerations based on the calculations *in vacuo*

First calculations were performed *in vacuo*. These results would best be compared to experimental studies in gas phase or unpolar environments. However, because the CMA1 and CMA2 both have a rather large dipole moment in the ground state, so that even the crystal environment can be considered as polar, the vacuum results do not compare very well with the experiment. Nevertheless, the vacuum results are sufficient for some general considerations that hold true for the calculations *in vacuo* as well as in solution. In both molecules the leading configuration for the T_1 and S_1 states (at both the S_0 geometry and at their optimized geometries) is the HOMO to LUMO excitation with about 80%–90%. The HOMO is located on the carbazolate, while the LUMO is mainly located on

TABLE 3.12: TDDFT and DFT/MRCI adiabatic energies of the S_1 or T_1 geometries with a coplanar (plan.) and a perpendicular (perp.) arrangement of the ligands optimized *in vacuo*.

geometry		TDDFT E [eV]			DFT/MRCI E [eV]		
		S_1	T_1	ΔE_{ST}	S_1	T_1	ΔE_{ST}
CMA1	plan.	2.27	2.01	0.26	2.45	2.35	0.10
	perp.	2.05	2.04	0.01	2.49	2.45	0.04
CMA2	plan.	2.18	1.91	0.27	2.42	2.30	0.12
	perp.	1.99	1.97	0.02	2.36	2.30	0.06

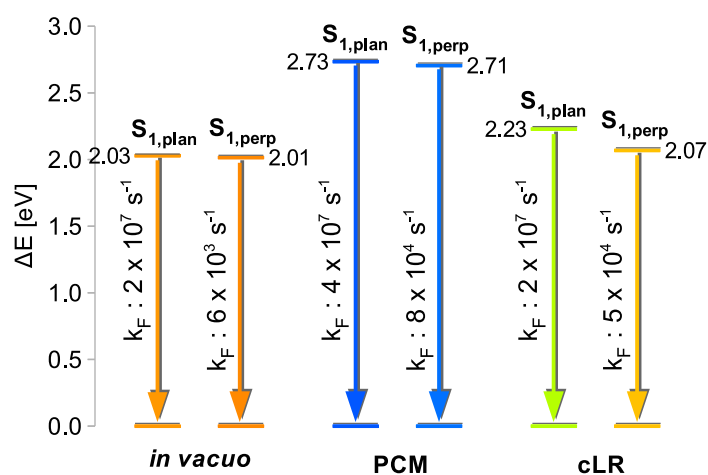
the CAAC ligand. So for both molecules, the T_1 and S_1 states have ligand-to-ligand charge transfer character. In case of the Au complex, the LUMO orbital itself has some small Au d_π contributions, while for the Cu complex the wavefunction has some additional configurations with Cu d_π contributions.

In Table 3.12 the adiabatic TDDFT and DFT/MRCI energies of the S_1 or T_1 geometries with a coplanar (plan.) and a perpendicular (perp.) arrangement of the ligands can be compared. It is apparent from this table that for both complexes the T_1 energy always lies below the S_1 energy and hence that no spin-state inversion occurs. Instead, the gap between S_1 or T_1 is significantly reduced at the perpendicular structures (at least at the TDDFT level of theory). For torsional paths of the CMA1 complex and more details concerning the solvation and spin-orbit coupling effects see the Supporting Information of Ref. [115] or Paper I in the Appendix.

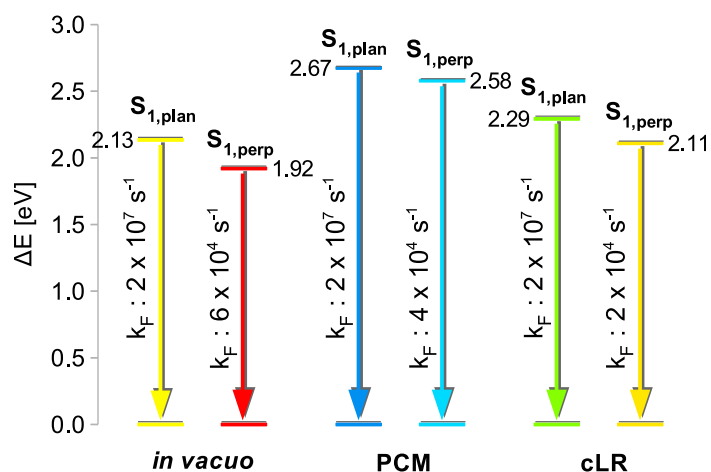
The general trends concerning the emission properties are very similar for both complexes. The *in vacuo* emission wavelength of the S_1 and the T_1 structures with a coplanar and a perpendicular arrangement of the ligands calculated with DFT/MRCI lie for both complexes between about 1.9 and 2.1 eV (for the S_1 emission energies see Figure 3.34). As mentioned before, the calculated emission wavelengths do not match the experimental λ_{max} and their shifts do not account for the observed difference of 0.4 eV between the measurements — neither the difference between crystal and solution nor the difference for time-resolved measurements in solution between small time delays (< 1 ps) and longer time delays ($\sim 2 \mu\text{s}$). Both might be explained by (hindered) solvent reorganization, as will be detailed in the following.

3.5.2 Environmental and structural effects on the absorption and emission properties

As mentioned before, both molecules have a rather large dipole moment in the ground state (about 11 D *in vacuo* and about 14 D in chlorobenzene) and the dipole vector points towards the carbazolate ligand. Upon excitation into the S_1 or the T_1 state electron density is moved from the carbazolate ligand to the CAAC ligand. Thus, the direction of the dipole



(A) CMA1



(B) CMA2

FIGURE 3.34: Vertical S_1 emission for the S_1 structures with a coplanar or perpendicular arrangement of the ligands for (A) the CMA1 and (B) the CMA2 complex calculated with DFT/MRCI in different environment. The colors of the arrows indicate the emission wavelength.

moment vector gets reversed and its magnitude reduces to about 5–6 D for the CMA1 complex and to about 3–4 D for the CMA2 complex (in chlorobenzene). This corresponds to a change of the dipole moment by about 20 D for CMA1 and by about 18 D for CMA2. Due to this large change one would expect that solvation and solvent reorganization should have a large impact on the absorption and emission properties. See also Figure 3.35 for a schematic representation of the dipole moments and the reorganization of the solvent molecules according to the excited state.

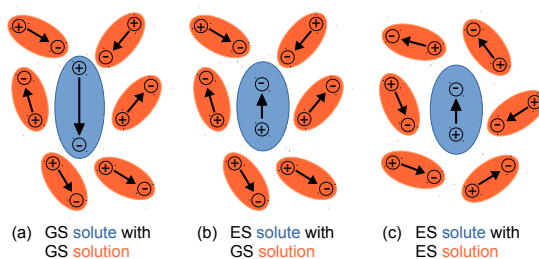


FIGURE 3.35: Schematic diagram of the dipole moments of CMA1 and CMA2 in (a) the ground and (b) the excited state and (c) the reorganization of the solvent molecules according to the excited state.

Effect on the spectra

In the experimental absorption spectrum (measured in THF), the first absorption band peaks at about 365 nm for CMA1 and at about 370 nm for CMA2. *In vacuo* the calculated $S_0 \rightarrow S_1$ transition lies at 438 nm for CMA1 and 450 nm for CMA2, which does not agree with the experimental value. In chlorobenzene, the calculated transition $S_0 \rightarrow S_1$ lies at 364 nm for CMA1 and at 370 nm for CMA2 and in THF it lies at 358 nm and at 364 nm. Compared to the results *in vacuo*, the $S_0 \rightarrow S_1$ transition experiences a strong blue shift. The blue shift arises from the strong destabilization of the S_1 state due to the polar solvent which is still adapted to the S_0 density. Since the calculated wavelengths for CMA1 and CMA2 in THF are slightly smaller than the experimental values, it seems like the effect is somewhat overestimated. Nevertheless, the calculated and the experimental values are in good agreement.

For the emission, two scenarios seem plausible, assuming that geometry relaxation of the excited state solute is fast. The first scenario would be for short time delays or in rather rigid polar environments, where the orientation of the solvent molecules is still adapted to the ground state. In the second scenario, on the other hand, for longer time delays and in less rigid environments, the solvent molecules can reorient according to the excited state density, which leads to an additional stabilization of the excited state (and a destabilization of the ground state). The first scenario can be simulated by PCM calculations, while for the second scenario corrected linear response (cLR) calculations have to be employed.

For the CMA1 complex the PCM calculations with chlorobenzene as solvent give vertical emission energies of 2.73 eV (453 nm) at the planar S_1 and 2.76 eV (449 nm) at the T_1 structure, while for CMA2 the S_1 emission energy is 2.67 eV (464 nm) and the T_1 emission energy is 2.35 eV (527 nm). In Figure 3.34 the vertical S_1 emission energies of both complexes in the different environments are depicted. The emission in PCM solvation of both complexes is again (like the absorption) blue-shifted with respect to the energies calculated *in vacuo*.

The reorganization of the solvent calculated with cLR leads to a red-shift of the emission energies, which lie at 2.23 eV (556 nm) for the planar S_1 and at 2.14 eV (580 nm) for the

planar T_1 structure of CMA1. For the CMA2 complex the planar S_1 energy lies at 2.29 eV (541 nm) and the T_1 energy at 2.18 eV (569 nm). It might be noted that the cLR energies are still a bit blue-shifted compared to the energies *in vacuo*.

The PCM S_1 energy of CMA1 may be best compared to the experimental wavelength of 470 nm measured in chlorobenzene at a time delay of 0.5 ps. It might also roughly compare with the emission of the crystal that lies at about 2.6 eV. The cLR S_1 energy of 556 nm, on the other hand, agrees well with the experimental value of 550 nm for the delayed emission in chlorobenzene. For the CMA2 complex, there are almost no emission data given in the article by Di et al. [59]. There is only one spectrum of CMA2 dispersed at 20 wt% in poly(9-vinylcarbazone) (PVK) that peaks at about 510 nm, which lies roughly in the middle between the S_1 emission wavelength calculated with PCM and the one calculated with cLR. Besides, the maximum EQE (also measured in PVK) given for CMA2 is by a factor of 3 lower than the maximum EQE of CMA1 (9.7% compared to 26.3%). A possible reason for the lower EQE of CMA2 will be given in Section 3.5.3.

Taken together, these results show that the different emission wavelengths can be explained by (hindered) solvent reorganization. The next section will focus on the influence of the solvation model and the interligand dihedral angle on the radiative and ISC rate constants.

Effect on the radiative and ISC rate constant

For the fluorescence rate constants calculated at the S_1 structures with a coplanar and a perpendicular arrangements of the ligands, the effect of the solvation model is very modest, whereas the influence of the different interligand dihedral angles is quite large (see Table 3.13). The fluorescence rate constants for the PCM model are only by a factor of < 2 larger than the rate constants for cLR. The difference between the coplanar and the perpendicular arrangements of the ligands amounts to three orders of magnitude. For the phosphorescence rate constants calculated at the T_1 structures, on the other hand, the influence of the interligand dihedral angles is negligible (factor of 4 at most) for both complexes. For CMA2, the influence of the solvation model is quite small, too. For CMA1, however, the k_P is reduced by about one order of magnitude when going from PCM to cLR solvation. The large influence of the interligand angle on the fluorescence rate constant is mainly due to the decoupling of the donor (carbazolate) and acceptor (CAAC) moieties at the perpendicular S_1 conformer which leads to a minimized density overlap and therefore to very small oscillator strengths. The T_1 , on the other hand, borrows its emission intensity mainly from a singlet state with d_σ character which is less affected by the orientation of the ligands.

The effect of the solvation on the ISC and RISC rate constants is small in case of CMA1 and more pronounced in case of CMA2. For CMA1 the ISC and RISC rate constants differ only by a factor < 3 (see Table 3.14). For CMA2, on the other hand, the PCM ISC rate constant is one order of magnitude larger, due to larger SOCMEs, and the PCM RISC

TABLE 3.13: Radiative rate constants for CMA1 and CMA2 in chlorobenzene with either PCM or cLR solvation. The fluorescence rate constant k_F and the phosphorescence rate constant k_P were computed at the respective S_1 or T_1 structures with a coplanar (plan.) and a perpendicular (perp.) arrangement of the ligands.

		CMA1		CMA2	
		k_F [s^{-1}]	k_P [s^{-1}]	k_F [s^{-1}]	k_P [s^{-1}]
PCM	plan.	4.1×10^7	2.7×10^4	2.3×10^7	2.0×10^4
	perp.	8.5×10^4	2.9×10^4	4.0×10^4	7.4×10^3
cLR	plan.	2.4×10^7	3.6×10^3	1.7×10^7	4.3×10^3
	perp.	4.9×10^4	2.8×10^3	2.2×10^4	5.0×10^3

TABLE 3.14: Spin-orbit coupling matrix elements computed at the coplanar T_1 and S_1 geometries of CMA1 and non-radiative rate constants (ISC from S_1 to T_1 and RISC from T_1 to S_1) calculated at 298 K and 77 K.

process	$\langle T_1 \hat{H}_{SO} S_1 \rangle$ [cm^{-1}]			$\Sigma(\text{SOCMEs})^2$ [cm^{-2}]	rate constant [s^{-1}]	
	x	y	z		298 K	77 K
ISC @ S_1						
PCM	2.45	0.27	-1.81	9	1.3×10^9	3.3×10^9
cLR	-1.22	-3.58	0.17	14	2.0×10^9	5.4×10^9
RISC @ T_1						
PCM	7.40	-1.95	-1.33	60	7.2×10^8	6.9×10^4
cLR	4.26	0.02	0.96	19	3.1×10^8	8.1×10^4

is almost 3 orders of magnitude smaller (see Table 3.15), mainly due to a substantially larger energy gap between T_1 and S_1 (1953 cm^{-1} for PCM compared to 851 cm^{-1} for cLR). The reason for the increased gap is that in the PCM environment the T_1 and the S_1 wavefunctions of CMA2 differ a lot more than in the cLR environment (or *in vacuo*). As mentioned before, the HOMO to LUMO excitation contributes in most cases with about 80%–90% to the wavefunction. At the coplanar structures with PCM solvation, however, the contribution of the HOMO to LUMO excitation to the triplet wavefunction is decreased to about 40–50%, while contributions from MLCT transitions are strongly increased (to about 36% for PCM compared to about 7–16% in cLR). For the S_1 wavefunction, the MLCT contributions are also increased, but considerably less so than for the T_1 wavefunction (the HOMO to LUMO excitation still contributes with about 60–70%). The strongly increased MLCT character of the T_1 wavefunction and the difference in the composition of the T_1 and the S_1 wavefunctions also lead to significantly larger SOCMEs between T_1 and S_1 at the coplanar PCM S_1 structure. Since the geometries do not change when going from PCM to cLR solvation, this is a purely electrostatic effect.

TABLE 3.15: Spin-orbit coupling matrix elements computed at the coplanar T_1 and S_1 geometries of CMA2 and non-radiative rate constants (ISC from S_1 to T_1 and RISC from T_1 to S_1) calculated at 298 K.

process	$\langle T_1 \hat{H}_{SO} S_1 \rangle$ [cm ⁻¹]			$\Sigma(\text{SOCMEs})^2$ [cm ⁻²]	rate constant [s ⁻¹]
	x	y	z		
ISC @ S_1					298 K
PCM	20.98	4.37	-2.99	468	3.8×10^{10}
cLR	5.22	0.21	-0.77	28	1.6×10^9
RISC @ T_1					298 K
PCM	-0.66	-4.99	0.36	25	8.0×10^5
cLR	8.48	-1.64	-2.09	79	3.6×10^8

3.5.3 Prompt fluorescence versus TADF

For efficient TADF to take place, several prerequisites have to be fulfilled. The ISC rate constant from the S_1 to the T_1 state has to be larger than the fluorescence rate constant and the RISC rate constant has to be larger than the phosphorescence rate constant in order to outcompete prompt fluorescence and phosphorescence. Both, the ISC and the RISC rate constants, depend on the spin-orbit coupling between the S_1 and the T_1 state, so SOCMEs between S_1 and T_1 have to be sufficiently large. Besides, the energy gap between S_1 and T_1 has to be small enough that it can be overcome by thermal energy at room temperature. Ideally, the emission and the (R)ISC are faster than any other (non-radiative) deactivation processes.

Apart from the ISC rate constant of CMA2 in PCM solvation (where $k_{\text{ISC}} = 4 \times 10^{10}$), all the ISC rate constants at RT are of the order of $1 - 2 \times 10^9 \text{ s}^{-1}$, which is two orders of magnitude smaller than the experimental value (of CMA1), that was estimated to be about $2.5 \times 10^{11} \text{ s}^{-1}$ in neat films. In a recent paper from Tom Penfold's group, quantum dynamics simulations on CMA1 were presented that gave ISC rate constants of about $1 - 2 \times 10^{10} \text{ s}^{-1}$ [63] which is in closer agreement with the experimental value than our rate calculated in the Condon approximation. Nevertheless, our ISC rate constants are about two orders of magnitude larger than the fluorescence rate constants of the coplanar conformers which is in qualitative agreement with the experimentally observed quenching of the prompt fluorescence after 4 ps (for CMA1). For CMA1 and for CMA2 with cLR solvation, the RISC rate constants at RT are four to five magnitudes larger than the phosphorescence rate constants, making TADF at RT likely for both complexes. In Figure 3.36 the (R)ISC and radiative rate constants of both complexes in cLR solvation are shown. For CMA2 in PCM solvation though, where the RISC rate constant is almost five orders of magnitude smaller than the ISC rate constant and only one to two orders of magnitude larger than the phosphorescence, the T_1 state is presumably populated to some larger extent. Since the phosphorescence lifetime is by three orders of magnitude longer than the fluorescence

lifetime (μs compared to ns regime) and therefore less able to compete with non-radiative deactivation, population of the T_1 state is probably tantamount with a larger amount of emission quenching. If we assume that the PVK host material, in which the OLED measurements were done, is rather described by PCM than by cLR environment, this might be the reason for the smaller EQEs obtained for CMA2 compared to CMA1.

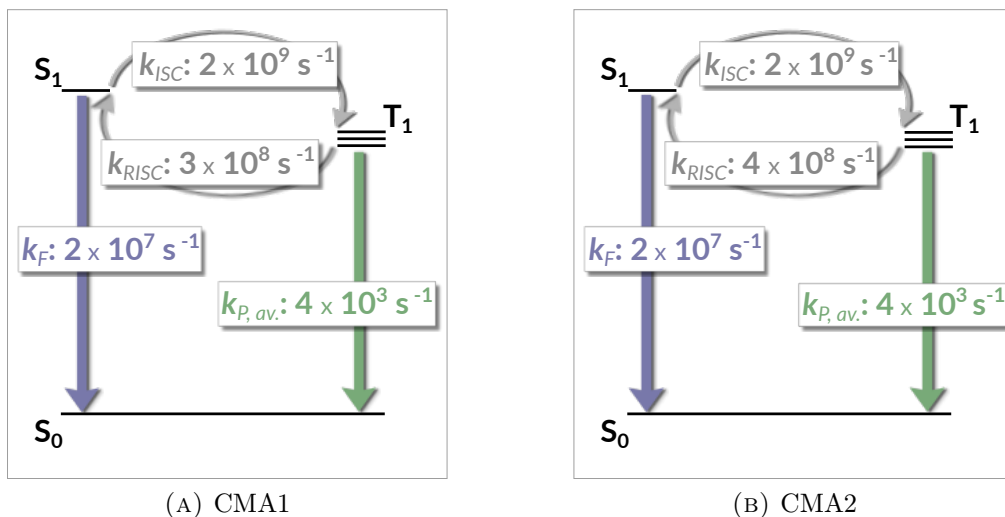


FIGURE 3.36: Radiative and (R)ISC rate constants for the coplanar S_1 and T_1 structures of CMA1 and CMA2 in solution (cLR). The rate constants are almost identical for CMA1 and CMA2.

For photoluminescence measurements of neat films, the experimental lifetime of CMA1 is reported as $\sim 10 \mu\text{s}$ for temperatures below 100 K which agrees quite well with our calculated lifetime of about $37 \mu\text{s}$ in PCM solvation. For 300 K the experimentalists report a lifetime of $\sim 350 \text{ ns}$ (which corresponds to a rate constant of $\sim 2.9 \times 10^6 \text{ s}^{-1}$). In an electroluminescence measurement at 300 K a rate constant of $3 \times 10^6 \text{ s}^{-1}$ is assigned to triplet emission. Based on our findings it seems, however, more likely that both rate constants (the PL and the EL rate constant at 300 K) correspond to a delayed fluorescence with maybe some portion of phosphorescence.

Judging only from the calculated fluorescence rate constants at the S_1 geometries with a coplanar and a perpendicular interligand dihedral angle, TADF is most efficient at the coplanar geometries, where k_F is three orders of magnitude larger than at the perpendicular geometries. But since the ISC and RISC rate constant also play a crucial role for TADF, it is worthwhile to consider their influence, too. We did not study the dependence between the interligand dihedral angle and the (R)ISC rate constants in detail. According to the quantum dynamics simulations on CMA1 from the Penfold group, ISC should be fastest at the point of degeneracy, i.e. at the perpendicular geometries. On the other hand, they also state that ISC is possible all along the torsional mode and that a degree change of about 30 is sufficient to get close to the point of degeneracy. Their dynamics simulations are based on TDDFT calculations, where our calculations *in vacuo* also predict a strong

decrease of ΔE_{ST} between the coplanar and the perpendicular conformations from 0.26 eV to 0.01 eV (see Table 3.12 in Section 3.5.1), whereas our DFT/MRCI calculations yield a more moderate decrease by about 0.06 eV. The DFT/MRCI calculations would therefore suggest a modest influence of the dihedral angle on the ISC rate constants.

In another recent publication on CMA2, the authors claim that the spin-orbit coupling is maximized at the coplanar T_1 geometry, but small at the perpendicular S_1 , wherefore they conclude that RISC should be most efficient at the coplanar T_1 geometry [62]. Their calculations were done *in vacuo*. Indeed, their observation agrees with the CMA2 SOCMEs we calculated *in vacuo*, where the SOCMEs at the perpendicular T_1 geometry are smaller than the ones at the coplanar T_1 geometry (-0.1/0.7/0.8 cm^{-1} compared to 0.6/0.4/-3 cm^{-1}). This is, however, not true for the SOCMEs calculated in PCM and cLR solvation. There, the SOCMEs at the perpendicular geometries are considerably larger, due to strong contributions from other configurations than the HOMO to LUMO excitation. For example at the perpendicular T_1 geometry in PCM solvation the SOCMEs are one to two magnitudes larger than at the coplanar geometry (12/34/-27 cm^{-1} compared to -0.7/-5/0.4 cm^{-1}). For CMA1, on the other hand, the SOCMEs at the coplanar and the perpendicular structures are rather similar, the SOCMEs at the perpendicular structures being slightly smaller. Unfortunately, there were no quantum dynamics simulations done for the RISC process.

So, although it is obvious that delayed fluorescence occurs most likely at the coplanar structure, the influence of the dihedral angle on the ISC and RISC rate constants is not definitely clarified yet and might even be different for the two complexes.

3.5.4 Summary and conclusions

Summing the results up

- The results for CMA1 and CMA2 are in general very similar.
- At most geometries, the wavefunctions of S_1 and T_1 are governed by a HOMO \rightarrow LUMO excitation which corresponds to CT from the carbazolate to the CAAC ligand.
- Consistent treatment of the S_1 and T_1 yields no intersection of S_1 and T_1 potential surfaces within the TDDFT and the DFT/MRCI framework. Only if spin-orbit coupling is included variationally, i.e. via spin-orbit CI, and only for the perpendicular geometries of CMA1 with cLR solvation the spin-orbit mixed S_1 drops slightly below the triplet manifold (the energy splitting being smaller than 0.01 eV).
- The emission energies of the isolated molecules calculated at the coplanar and perpendicular geometries do not match the experimental emission wavelengths and do not account for the time- and environment-dependent shifts of the emission.
- Taking solvation effects into account leads to a much better agreement between the calculated and the experimental emission wavelengths and shows that the shifts of

the emission wavelength can be explained by (hindered) solvent reorganization. Reorganization of the solvent molecules leads to a red-shift of the emission that can be observed after a time delay > 1 ps in liquid solutions.

- At the coplanar structures ISC at RT is about 2 orders of magnitude faster than the fluorescence and the RISC is about 5 orders of magnitude faster than the phosphorescence. The photophysics of CMA1 and CMA2 can therefore be explained by a 'normal' delayed fluorescence
- An exception is the CMA2 complex with PCM environment, where the RISC rate constant is decreased by almost 3 orders of magnitude. Assuming that PVK (used as a host in the OLED measurements) is rather described by PCM than by cLR environment and that the emission is quenched to some larger extent due to population of the longer-lived T_1 state, this could explain the smaller EQEs obtained for CMA2 compared to CMA1.
- Judging from the calculated fluorescence rate constants at the S_1 geometries with a coplanar and a perpendicular interligand dihedral angle, TADF is most efficient at the coplanar geometries.
- The torsion of the carbazolate ligand might enhance ISC, however not because of an intersection of the S_1 and T_1 potential surfaces, but because of the minimized energy gap at the perpendicular geometries.

Chapter 4

Conclusions

The aim of this thesis was to gain insight into the photophysical properties of Cu(I) and Au(I) complexes in order to rationalize their emission behavior and eventually enable systematic improvement of their emission properties. Since the emission behavior depends on the energy gaps, the (reverse) ISC and the radiative rate constants of the lowest lying states, ground and excited state geometries of several Cu(I) complexes and one Au(I) complex were optimized and non- and radiative rate constants were computationally determined. Because experimental studies on some of the complexes (or similar ones) indicated that ligand torsion and solvation affect the emission behavior of the complexes, the effects of ligand torsion and solvation on the energy gaps and rate constants were explored as well.

For the first complex investigated in this thesis, experimental and DFT studies on similar complexes exist, which could show that the emission behavior for these complexes depends on the dihedral angle between the two ligands attached to copper [50]. For a coplanar arrangement of the ligands, Leitl et al. [50] obtained a small singlet–triplet gap and therefore TADF emission was observed. Upon torsion, the singlet–triplet gap was seen to increase such that for an interligand dihedral angle of about 70° it was no longer in the range of thermal energy and the authors therefore found phosphorescence to be the main emission channel. In contrast to that, the energy splitting of the S_1 and T_1 of the complex studied in this thesis was hardly affected at all by ligand torsion. The different behavior can be traced back to the orbitals involved in the excitation. For the complex investigated in this thesis the HOMO is located on the phenanthroline ligand and the LUMO has amplitudes at the copper and the two phenanthroline nitrogen atoms, which leads to a small density overlap. Since the orbitals and therefore the density overlap does not change upon ligand torsion, the singlet–triplet splitting does not change either being equally small for all torsion angles. For the complexes studied by Leitl et al., on the other hand, the LUMO is mainly located at the NHC ligand and since the HOMO gains density distribution on the NHC by increasing the torsion angle, the density overlap and hence the singlet–triplet gap is seen to increase. In spite of its small singlet–triplet gap, the phenanthroline complex does not show efficient TADF. The electronic structure of the S_1 and T_1 are too similar and therefore their mutual spin–orbit coupling and the (R)ISC rate constants are rather small.

In addition, the fluorescence rate constants is comparably small too and the emission of the complex is governed by phosphorescence.

How the existence of another triplet with substantial copper $3d$ contributions in close energetic proximity can enhance the ISC processes could be shown in a second study on linear NHC-Cu(I)-pyridine complexes. The initial assumption that the Ipr-Cu(I)-pyridine complexes are luminescent themselves turned out to be erroneous [119, 120]. Luminescence of the crystal powders is now rather believed to stem from the trigonal complexes that were contained in the powder as by-product. Another possibility that still has to be further investigated is that the complexes show mechanochromic luminescence. The reason why the linear Ipr-Cu(I)-pyridine complexes are only weak emitters is that the emission is quenched by a long-lived T_{LC} state (ms to s regime). Nevertheless, the complexes also show some favorable properties, such as the aforementioned close proximity of another triplet with copper $3d$ contributions. In other words, apart from a singlet-triplet pair (S_{MLCT} and T_{MLCT}) with copper d_σ contributions, an additional triplet with d_π contributions lies close by ($T_{MLCT/LC}$). Due to the change in the angular momentum, spin-orbit coupling between the S_{MLCT} and $T_{MLCT/LC}$ is large and the ISC process between the two is fast. Besides, radiative rate constants of the S_{MLCT} , T_{MLCT} and the $T_{MLCT/LC}$ are large enough to achieve efficient phosphorescence or TADF. It was therefore only consequent to search for possible modifications that eliminate the possibility of low-lying T_{LC} states, but concomitantly preserve the favorable properties of the complexes. This goal was attained by replacing the DIPP moieties of the IPr ligand with adamantyl moieties. Since calculations on the first (unsubstituted) complex suggest that the complex emits in the UV range, substituents were introduced into the NHC backbone and at the *para* position of the pyridine ligand. The *+I* effect of methylation of the NHC ligand was found to be too weak (by itself) to obtain emission maxima in the visible regime. The *-M* effect of a CN substituent at the *para* position of the pyridine, on the other hand, leads to a substantial stabilization of the emissive states and emission in the blue spectral region could be achieved. Combination of the *+I* effect of methyl and the *-M* effect of CN leads to a further shift the emission maximum into the blue-green region. The ISC processes are predicted to proceed faster than prompt fluorescence and phosphorescence, so the modified complexes presumably are efficient blue to green TADF emitters. These predictions still await experimental verification.

An additional study on the trigonal Ipr-Cu(I)-pyridine complex could confirm that the trigonal complexes should be efficient emitters as well, in agreement with the experimental finding that crystals of the trigonal complexes show bright emission. The difference between the linear and the trigonal Ipr-Cu(I)-pyridine complex is that in case of the trigonal complex the T_{MLCT} state constitutes the global triplet minimum. Since spin-orbit coupling between the S_1 and the T_{MLCT} on the one hand and especially between the T_{MLCT} and S_2 state on the other hand is strong, the resulting (R)ISC and radiative rate constants

are large enough to expect large quantum yields for this complex.

The last study presented in this thesis dealt with linear CAAC complexes with either copper or gold as metal center and a carbazolate as second ligand. It could be shown that the new relaxation process proposed for these complexes — the so called rotationally assisted spin-state inversion (RASI) — is an artifact that can be traced back to an arguable application of different methods. The complexes were experimentally investigated by Di et al. [59]. OLEDs based on these complexes attain exceptionally high EQEs, especially in case of the gold complex. The fast ISC process enabling the high EQE — measured for the gold complex to lie in the ps regime — was explained to result from an intersection of the S_1 and T_1 potential. In fact, the authors supposed that the S_1 drops below the T_1 state upon ligand torsion — a mechanism which they termed RASI. This assumption was supported by their observation that the emission wavelength varies for different environments by about 0.4 eV. For the crystalline powder, the most rigid environment, the emission maximum lies at 2.6 eV, whereas in solution it lies at 2.22 eV. Hence, emission in rigid environments, where ligand torsion is hindered, was assumed to stem from the T_1 state, while emission in solution was supposed to stem from the S_1 state that could relax energetically below the T_1 . Additional quantum chemical calculations, that the authors carried out in order to further support their conclusions, were carried out employing TDDFT for the optimization of the S_1 geometries and UDFT for the optimization of the T_1 geometries. For a torsion angle between the ligands of about 90° , these optimizations did indeed yield a S_1 minimum which lies energetically below both the T_1 geometries, i.e. that with a torsion angle of about 0° and that with a torsion angle of about 90° . Comparing energies obtained with different methods seems, however, like a more than questionable approach. If instead TDDFT is employed consistently for the optimization of the S_1 as well as T_1 geometries, as I did in my studies, ligand torsion does only lead to a decrease of the singlet–triplet energy gap, but to no intersection. Even the inclusion of closed-shell doubly excited configurations, which only exist for singlet states and could in principle invert the singlet–triplet energy gap, through the DFT/MRCI ansatz, did not result in an intersection. An alternative explanation for the observed shifts, could be found by looking at the solvent reorganization. Based on calculations that can mimic either a hindered or a full solvent reorganization, I could show that the red-shift of the emission maximum that can be observed in liquid solutions can be traced back to unhindered solvent reorganization. The outstanding performance of the complexes can be explained by normal, although quite fast RISC into the S_1 state followed by comparably fast TADF.

Bibliography

- [1] B. D'Andrade, S. Forrest, "White Organic Light-Emitting Devices for Solid-State Lighting", *Adv. Mater.* **2004**, *16*, 1585.
- [2] J. W. Park, D. C. Shin, S. H. Park, "Large-area OLED lightings and their applications", *Semicond. Sci. Technol.* **2011**, *26*, 034002.
- [3] C. Murawski, K. Leo, M. C. Gather, "Efficiency Roll-Off in Organic Light-Emitting Diodes", *Adv. Mater.* **2013**, *25*, 6801.
- [4] S. Reineke, M. Thomschke, B. Lüssem, K. Leo, "White organic light-emitting diodes: Status and perspective", *Rev. Mod. Phys.* **2013**, *85*, 1245.
- [5] C. Adachi, "Third-generation organic electroluminescence materials", *Jpn. J. Appl. Phys.* **2014**, *53*, 060101.
- [6] B. Geffroy, P. le Roy, C. Prat, "Organic light-emitting diode (OLED) technology: materials, devices and display technologies", *Polym. Int.* **2006**, *55*, 572.
- [7] H.-W. Chen, J.-H. Lee, B.-Y. Lin, S. Chen, S.-T. Wu, "Liquid crystal display and organic light-emitting diode display: present status and future perspectives", *Light Sci. Appl.* **2018**, *7*, 17168.
- [8] L. J. Rothberg, A. J. Lovinger, "Status of and prospects for organic electroluminescence", *J. Mater. Res.* **1996**, *11*, 3174.
- [9] M. A. Baldo, D. F. O'Brien, M. E. Thompson, S. R. Forrest, "Excitonic singlet-triplet ratio in a semiconducting organic thin film", *Phys. Rev. B* **1999**, *60*, 14422.
- [10] S. Nowy, B. C. Krummacher, J. Frischeisen, N. A. Reinke, W. Brütting, "Light extraction and optical loss mechanisms in organic light-emitting diodes: Influence of the emitter quantum efficiency", *J. Appl. Phys.* **2008**, *104*, 123109.
- [11] C. Adachi, J. Adachi, High Performance TADF for OLEDs. Presentation at the 2015 SSL R&D WORKSHOP in San Francisco, California.
- [12] M. A. Baldo, D. F. O'Brien, Y. You, A. Shoustikov, S. Sibley, M. E. Thompson, S. R. Forrest, "Highly Efficient Phosphorescent Emission from Organic Electroluminescent Devices", *Nature* **1998**, *395*, 151.
- [13] A. Endo, M. Ogasawara, A. Takahashi, D. Yokoyama, Y. Kato, C. Adachi, "Thermally Activated Delayed Fluorescence from Sn⁴⁺-Porphyrin Complexes and Their Application to Organic Light Emitting Diodes – A Novel Mechanism for Electroluminescence", *Adv. Mater.* **2009**, *21*, 4802.

- [14] H. Nakanotani, T. Higuchi, T. Furukawa, K. Masui, K. Morimoto, M. Numata, H. Tanaka, Y. Sagara, T. Yasuda, C. Adachi, "High-efficiency organic light-emitting diodes with fluorescent emitters", *Nat. Comm.* **2014**, *5*, 4016.
- [15] R. Englman, J. Jortner, "The energy gap law for radiationless transitions in large molecules", *Mol. Phys.* **1970**, *18*, 145.
- [16] K. F. Freed, J. Jortner, "Multiphonon Processes in the Nonradiative Decay of Large Molecules", *J. Chem. Phys.* **1970**, *52*, 6272.
- [17] M. Etinski, C. M. Marian, "Overruling the energy gap law: fast triplet formation in 6-azauracil", *Phys. Chem. Chem. Phys.* **2010**, *12*, 15665.
- [18] C. M. Marian, J. Föllner, M. Kleinschmidt, M. Etinski, "Intersystem crossing processes in TADF emitters" in *Highly Efficient OLEDs, Materials Based on Thermally Activated Delayed Fluorescence*, (Ed.: H. Yersin), to appear in Nov, Wiley-VCH, Weinheim, **2018**, Chapter 8.
- [19] R. Czerwieniec, M. J. Leidl, H. H. Homeier, H. Yersin, "Cu(I) complexes – Thermally activated delayed fluorescence. Photophysical approach and material design", *Coord. Chem. Rev.* **2016**, *325*, 2.
- [20] M. Kasha, "Collisional Perturbation of Spin–Orbital Coupling and the Mechanism of Fluorescence Quenching. A Visual Demonstration of the Perturbation", *J. Chem. Phys.* **1952**, *20*, 71.
- [21] B. F. Minaev, S. Knuts, H. Ågren, "On the interpretation of the external heavy atom effect on singlet–triplet transitions", *Chem. Phys.* **1994**, *181*, 15.
- [22] C.-W. Hsu, C.-C. Lin, M.-W. Chung, Y. Chi, G.-H. Lee, P.-T. Chou, C.-H. Chang, P.-Y. Chen, "Systematic Investigation of the Metal-Structure–Photophysics Relationship of Emissive d10-Complexes of Group 11 Elements: The Prospect of Application in Organic Light Emitting Devices", *J. Am. Chem. Soc.* **2011**, *133*, 12085.
- [23] M. A. Carvajal, J. J. Novoa, S. Alvarez, "Choice of Coordination Number in d10 Complexes of Group 11 Metals", *J. Am. Chem. Soc.* **2004**, *126*, 1465.
- [24] J. R. Kirchhoff, R. E. Gamache, M. W. Blaskie, A. A. Del Paggio, R. K. Lengel, D. R. McMillin, "Temperature dependence of luminescence from $\text{Cu}(\text{NN})_2^+$ systems in fluid solution. Evidence for the participation of two excited states", *Inorg. Chem.* **1983**, *22*, 2380.
- [25] M. K. Eggleston, D. R. McMillin, K. S. Koenig, A. J. Pallenberg, "Steric Effects in the Ground and Excited States of $\text{Cu}(\text{NN})_2^+$ Systems", *Inorg. Chem.* **1997**, *36*, 172.
- [26] C. T. Cunningham, J. J. Moore, K. L. H. Cunningham, P. E. Fanwick, D. R. McMillin, "Structural and Photophysical Studies of $\text{Cu}(\text{NN})_2^+$ Systems in the Solid State. Emission at Last from Complexes with Simple 1,10-Phenanthroline Ligands", *Inorg. Chem.* **2000**, *39*, 3638.

- [27] R. Czerwieńiec, J. Yu, H. Yersin, “Blue-Light Emission of Cu(I) Complexes and Singlet Harvesting”, *Inorg. Chem.* **2011**, *50*, 8293.
- [28] L. Bergmann, J. Friedrichs, M. Mydlak, T. Baumann, M. Nieger, S. Bräse, “Outstanding luminescence from neutral copper(I) complexes with pyridyl-tetrazolate and phosphine ligands”, *Chem. Commun.* **2013**, *49*, 6501.
- [29] X.-L. Chen, R. Yu, Q.-K. Zhang, L.-J. Zhou, X.-Y. Wu, Q. Zhang, C.-Z. Lu, “Rational Design of Strongly Blue-Emitting Cuprous Complexes with Thermally Activated Delayed Fluorescence and Application in Solution-Processed OLEDs”, *Chem. Mater.* **2013**, *25*, 3910.
- [30] R. Czerwieńiec, K. Kowalski, H. Yersin, “Highly efficient thermally activated fluorescence of a new rigid Cu(I) complex $[\text{Cu}(\text{dmp})(\text{phanephos})]^+$ ”, *Dalton Trans.* **2013**, *42*, 9826.
- [31] S. Igawa, M. Hashimoto, I. Kawata, M. Yashima, M. Hoshino, M. Osawa, “Highly efficient green organic light-emitting diodes containing luminescent tetrahedral copper(I) complexes”, *J. Mater. Chem. C* **2013**, *1*, 542.
- [32] C. L. Linfoot, M. J. Leitl, P. Richardson, A. F. Rausch, O. Chepelin, F. J. White, H. Yersin, N. Robertson, “Thermally Activated Delayed Fluorescence (TADF) and Enhancing Photoluminescence Quantum Yields of $[\text{CuI}(\text{diimine})(\text{diphosphine})]^+$ Complexes—Photophysical, Structural, and Computational Studies”, *Inorg. Chem.* **2014**, *53*, 10854.
- [33] X.-L. Chen, C.-S. Lin, X.-Y. Wu, R. Yu, T. Teng, Q.-K. Zhang, Q. Zhang, W.-B. Yang, C.-Z. Lu, “Highly efficient cuprous complexes with thermally activated delayed fluorescence and simplified solution process OLEDs using the ligand as host”, *J. Mater. Chem. C* **2015**, *3*, 1187.
- [34] G. Cheng, G. K.-M. So, W.-P. To, Y. Chen, C.-C. Kwok, C. Ma, X. Guan, X. Chang, W.-M. Kwok, C.-M. Che, “Luminescent zinc(II) and copper(I) complexes for high-performance solution-processed monochromic and white organic light-emitting devices”, *Chem. Sci.* **2015**, *6*, 4623.
- [35] R. Czerwieńiec, H. Yersin, “Diversity of Copper(I) Complexes Showing Thermally Activated Delayed Fluorescence: Basic Photophysical Analysis”, *Inorg. Chem.* **2015**, *54*, 4322.
- [36] Q. Zhang, J. Chen, X.-Y. Wu, X.-L. Chen, R. Yu, C.-Z. Lu, “Outstanding blue delayed fluorescence and significant processing stability of cuprous complexes with functional pyridine-pyrazolate diimine ligands”, *Dalton Trans.* **2015**, *44*, 6706.
- [37] L. Bergmann, G. J. Hedley, T. Baumann, S. Bräse, I. D. W. Samuel, “Direct observation of intersystem crossing in a thermally activated delayed fluorescence copper complex in the solid state”, *Sci. Adv.* **2016**, *2*, e1500889.

- [38] L. Lv, K. Yuan, Y. Wang, "Theoretical studying of basic photophysical processes in a thermally activated delayed fluorescence copper(I) complex: Determination of reverse intersystem crossing and radiative rate constants", *Org. Electron.* **2017**, *51*, 207.
- [39] Z. C. Su, C. C. Zheng, G. Cheng, C.-M. Che, S. J. Xu, "Triplet harvesting in luminescent Cu(I) complexes by the thermally activated luminescence transition mechanism: impact of the molecular structure", *J. Mater. Chem. C* **2017**, *5*, 4488.
- [40] R. Starosta, M. Florek, J. Krol, M. Puchalska, A. Kochel, "Copper(I) iodide complexes containing new aliphatic aminophosphine ligands and diimines-luminescent properties and antibacterial activity", *New J. Chem.* **2010**, *34*, 1441.
- [41] R. Starosta, M. Puchalska, J. Cybinska, M. Barys, A. V. Mudring, "Structures, electronic properties and solid state luminescence of Cu(I) iodide complexes with 2,9-dimethyl-1,10-phenanthroline and aliphatic aminomethylphosphines or triphenylphosphine", *Dalton Trans.* **2011**, *40*, 2459.
- [42] H. Ohara, A. Kobayashi, M. Kato, "Simple and extremely efficient blue emitters based on mononuclear Cu(I)-halide complexes with delayed fluorescence", *Dalton Trans.* **2014**, *43*, 17317.
- [43] H. Ohara, A. Kobayashi, M. Kato, "Effects of N-heteroaromatic ligands on highly luminescent mononuclear copper(I)-halide complexes", *C. R. Chim.* **2015**, *18*, 766.
- [44] P. Liang, A. Kobayashi, T. Hasegawa, M. Yoshida, M. Kato, "Thermal and Mechanochemical Syntheses of Luminescent Mononuclear Copper(I) Complexes", *Eur. J. Inorg. Chem.* **2017**, 5134.
- [45] N. Armaroli, "Photoactive mono- and polynuclear Cu(I)-phenanthrolines. A viable alternative to Ru(II)-polypyridines?", *Chem. Soc. Rev.* **2001**, *30*, 113.
- [46] G. Capano, U. Rothlisberger, I. Tavernelli, T. J. Penfold, "Theoretical Rationalization of the Emission Properties of Prototypical Cu(I)-Phenanthroline Complexes", *J. Phys. Chem. A* **2015**, *119*, 7026.
- [47] V. A. Krylova, P. I. Djurovich, M. T. Whited, M. E. Thompson, "Synthesis and characterization of phosphorescent three-coordinate Cu(I)-NHC complexes", *Chem. Commun.* **2010**, *46*, 6696.
- [48] V. A. Krylova, P. I. Djurovich, J. W. Aronson, R. Haiges, M. T. Whited, M. E. Thompson, "Structural and Photophysical Studies of Phosphorescent Three-Coordinate Copper(I) Complexes Supported by an N-Heterocyclic Carbene Ligand", *Organometallics* **2012**, *31*, 7983.
- [49] V. A. Krylova, P. I. Djurovich, B. L. Conley, R. Haiges, M. T. Whited, T. J. Williams, M. E. Thompson, "Control of emission colour with N-heterocyclic carbene (NHC) ligands in phosphorescent three-coordinate Cu(I) complexes", *Chem. Commun.* **2014**, *50*, 7176.

- [50] M. J. Leitl, V. A. Krylova, P. I. Djurovich, M. E. Thompson, H. Yersin, "Phosphorescence versus Thermally Activated Delayed Fluorescence. Controlling Singlet–Triplet Splitting in Brightly Emitting and Sublimable Cu(I) Compounds", *J. Am. Chem. Soc.* **2014**, *136*, 16032.
- [51] R. Marion, F. Sguerra, F. D. Meo, E. Sauvageot, J.-F. Lohier, R. Daniellou, J.-L. Renaud, M. Linares, M. Hamel, S. Gaillard, "NHC Copper(I) Complexes Bearing Dipyrindylamine Ligands: Synthesis, Structural, and Photoluminescent Studies", *Inorg. Chem.* **2014**, *53*, 9181.
- [52] M. Elie, M. D. Weber, F. Di Meo, F. Sguerra, J.-F. Lohier, R. B. Pansu, J.-L. Renaud, M. Hamel, M. Linares, R. D. Costa, S. Gaillard, "Role of the Bridging Group in Bis-Pyridyl Ligands: Enhancing Both the Photo- and Electroluminescent Features of Cationic (IPr)Cu^I Complexes", *Chem. - Eur. J.* **2017**, *23*, 16328.
- [53] M. Gernert, U. Müller, M. Haehnel, J. Pflaum, A. Steffen, "A Cyclic Alkyl(amino)carbene as Two-Atom π -Chromophore Leading to the First Phosphorescent Linear Cu^I Complexes", *Chem. - Eur. J.* **2017**, *23*, 2206.
- [54] R. Hamze, R. Jazzar, M. Soleilhavoup, P. I. Djurovich, G. Bertrand, M. E. Thompson, "Phosphorescent 2-, 3- and 4-coordinate cyclic (alkyl)(amino)carbene (CAAC) Cu(I) complexes", *Chem. Commun.* **2017**, *53*, 9008.
- [55] K. J. Lotito, J. C. Peters, "Efficient luminescence from easily prepared three-coordinate copper(I) arylamidophosphines", *Chem. Commun.* **2010**, *46*, 3690.
- [56] M. Hashimoto, S. Igawa, M. Yashima, I. Kawata, M. Hoshino, M. Osawa, "Highly Efficient Green Organic Light-Emitting Diodes Containing Luminescent Three-Coordinate Copper(I) Complexes", *J. Am. Chem. Soc.* **2011**, *133*, 10348.
- [57] M. Osawa, M. Hoshino, M. Hashimoto, I. Kawata, S. Igawa, M. Yashima, "Application of three-coordinate copper(I) complexes with halide ligands in organic light-emitting diodes that exhibit delayed fluorescence", *Dalton Trans.* **2015**, *44*, 8369.
- [58] A. S. Romanov, D. Di, L. Yang, J. Fernandez-Cestau, C. R. Becker, C. E. James, B. Zhu, M. Linnolahti, D. Credgington, M. Bochmann, "Highly photoluminescent copper carbene complexes based on prompt rather than delayed fluorescence", *Chem. Commun.* **2016**, *52*. Corrected in: Romanov et al., *Chem. Commun.* **2018**, *54*, 3672, 6379.
- [59] D. Di, A. S. Romanov, L. Yang, J. M. Richter, J. P. H. Rivett, S. Jones, T. H. Thomas, M. Abdi Jalebi, R. H. Friend, M. Linnolahti, M. Bochmann, D. Credgington, "High-performance light-emitting diodes based on carbene-metal-amides", *Science* **2017**, *356*, 159.

- [60] A. S. Romanov, C. R. Becker, C. E. James, D. Di, D. Credgington, M. Linnolahti, M. Bochmann, "Copper and Gold Cyclic (Alkyl)(amino)carbene Complexes with Sub-Microsecond Photoemissions: Structure and Substituent Effects on Redox and Luminescent Properties", *Chem. - Eur. J.* **2017**, *23*, 4625.
- [61] S. Shi, L. R. Collins, M. F. Mahon, P. I. Djurovich, M. E. Thompson, M. K. Whittlesey, "Synthesis and characterization of phosphorescent two-coordinate copper(I) complexes bearing diamidocarbene ligands", *Dalton Trans.* **2017**, *46*, 745.
- [62] E. J. Taffet, Y. Olivier, F. Lam, D. Beljonne, G. D. Scholes, "Carbene-Metal-Amide Bond Deformation, Rather Than Ligand Rotation, Drives Delayed Fluorescence", *J. Phys. Chem. Lett.* **2018**, *9*, 1620.
- [63] S. Thompson, J. Eng, T. J. Penfold, "The intersystem crossing of a cyclic (alkyl)-(amino) carbene gold (I) complex", *J. Chem. Phys.* **2018**, *149*, 014304.
- [64] W. A. Herrmann, C. Köcher, "N-Heterocyclische Carbene", *Angew. Chem.* **2006**, *119*, 2256.
- [65] V. Lavallo, Y. Canac, C. Präsang, B. Donnadieu, G. Bertrand, "Stable Cyclic (Alkyl)(Amino)Carbenes as Rigid or Flexible, Bulky, Electron-Rich Ligands for Transition-Metal Catalysts: A Quaternary Carbon Atom Makes the Difference", *Angew. Chem. Int. Ed.* **2005**, *44*, 5705.
- [66] M. Soleilhavoup, G. Bertrand, "Cyclic (Alkyl)(Amino)Carbenes (CAACs): Stable Carbenes on the Rise", *Acc. Chem. Res.* **2015**, *48*, 256.
- [67] D. J. Tozer, "Density Functional Theory" in *European Summerschool in Quantum Chemistry - Book II*, (Eds.: S. Reine, T. Saue), printed by Priulla, Palermo, **2017**, Chapter 10, pp. 573–575.
- [68] N. C. Handy, "The importance of Colle–Salvetti for computational density functional theory", *Theor. Chem. Acc.* **2009**, *123*, 165.
- [69] P. Hohenberg, W. Kohn, "Inhomogeneous Electron Gas", *Phys. Rev.* **1964**, *136*, B864.
- [70] W. Kohn, L. J. Sham, "Self-Consistent Equations Including Exchange and Correlation Effects", *Phys. Rev.* **1965**, *140*, A1133.
- [71] J. P. Perdew, K. Burke, M. Ernzerhof, "Generalized Gradient Approximation Made Simple", *Phys. Rev. Lett.* **1996**, *77*, 3865.
- [72] C. Adamo, V. Barone, "Toward Reliable Density Functional Methods without Adjustable Parameters: The PBE0 Model", *J. Chem. Phys.* **1999**, *110*, 6158.
- [73] C. Lee, W. Yang, R. G. Parr, "Development of the Colle–Salvetti Correlation-Energy Formula into a Functional of the Electron Density", *Phys. Rev. B* **1988**, *37*, 785.
- [74] A. D. Becke, "A New Mixing of Hartree–Fock and Local Density-Functional Theories", *J. Chem. Phys.* **1993**, *98*, 1372.

- [75] E. Runge, E. K. U. Gross, “Density-Functional Theory for Time-Dependent Systems”, *Phys. Rev. Lett.* **1984**, *52*, 997.
- [76] A. Dreuw, M. Head-Gordon, “Single-Reference ab Initio Methods for the Calculation of Excited States of Large Molecules”, *Chem. Rev.* **2005**, *105*, 4009.
- [77] R. Bauernschmitt, R. Ahlrichs, “Treatment of Electronic Excitations within the Adiabatic Approximation of Time Dependent Density Functional Theory”, *Chem. Phys. Lett.* **1996**, *256*, 454.
- [78] R. E. Stratmann, G. E. Scuseria, M. J. Frisch, “An efficient implementation of time-dependent density-functional theory for the calculation of excitation energies of large molecules”, *J. Chem. Phys.* **1998**, *109*, 8218.
- [79] S. Hirata, M. Head-Gordon, “Time-dependent density functional theory within the Tamm–Dancoff approximation”, *Chem. Phys. Lett.* **1999**, *314*, 291.
- [80] M. J. G. Peach, M. J. Williamson, D. J. Tozer, “Influence of Triplet Instabilities in TDDFT”, *J. Chem. Theory Comput.* **2011**, *7*, 3578.
- [81] K. G. Dyall, K. Fægri, Jr., *Introduction to Relativistic Quantum Chemistry*, 1st ed., Oxford University Press, Oxford, **2007**, Chapter 20, pp. 396–426.
- [82] D. Andrae, U. Häußermann, M. Dolg, H. Stoll, H. Preuß, “Energy-adjusted ab initio pseudopotentials for the second and third row transition elements”, *Theor. Chim. Acta* **1990**, *77*, 123.
- [83] D. Figgen, G. Rauhut, M. Dolg, H. Stoll, “Energy-Consistent Pseudopotentials for Group 11 and 12 Atoms: Adjustment to Multi-Configuration Dirac–Hartree–Fock Data”, *Chem. Phys.* **2005**, *311*, 227.
- [84] R. W. Wetmore, G. A. Segal, “Efficient generation of configuration interaction matrix elements”, *Chem. Phys. Lett.* **1975**, *36*, 478.
- [85] S. Grimme, M. Waletzke, “A Combination of Kohn–Sham Density Functional Theory and Multi-Reference Configuration Interaction Methods”, *J. Chem. Phys.* **1999**, *111*, 5645.
- [86] C. Marian, A. Heil, M. Kleinschmidt, “The DFT/MRCI Method”, *WIREs Comput. Mol. Sci.* **2018**, submitted.
- [87] I. Lyskov, M. Kleinschmidt, C. M. Marian, “Redesign of the DFT/MRCI Hamiltonian”, *J. Chem. Phys.* **2016**, *144*, 034104.
- [88] J. D. Spiegel, I. Lyskov, M. Kleinschmidt, C. M. Marian, “Charge-transfer contributions to the excitonic coupling matrix element in BODIPY-based energy transfer cassettes”, *Chem. Phys.* **2017**, *482*, 265.
- [89] A. Heil, M. Kleinschmidt, C. Marian, “On the performance of DFT/MRCI Hamiltonians for electronic excitations in transition metal complexes: The role of the damping function”, *J. Chem. Phys.* **2018**, submitted.

- [90] M. Kleinschmidt, J. Tatchen, C. M. Marian, "Spin–Orbit Coupling of DFT/MRCI Wavefunctions: Method, Test Calculations, and Application to Thiophene", *J. Comput. Chem.* **2002**, *23*, 824.
- [91] M. Kleinschmidt, C. M. Marian, "Efficient Generation of Matrix Elements for One-Electron Spin–Orbit Operators", *Chem. Phys.* **2005**, *311*, 71.
- [92] M. Kleinschmidt, J. Tatchen, C. M. Marian, "SPOCK.CI: A Multireference Spin–orbit Configuration Interaction Method for Large Molecules", *J. Chem. Phys.* **2006**, *124*, 124101.
- [93] W. Pauli, "Zur Quantenmechanik des magnetischen Elektrons", *Z. Phys.* **1927**, *43*, 601.
- [94] C. M. Marian, "Spin–Orbit Coupling in Molecules" in *Reviews in Computational Chemistry*, (Eds.: B. Lipkowitz, D. B. Boyd), Wiley-Blackwell, **2001**, Chapter 3, pp. 99–204.
- [95] AMFI is an atomic spin–orbit integral program written by B. Schimmelpfennig, University of Stockholm, **1996**.
- [96] R. McWeeny, "On the Origin of Spin–Hamiltonian Parameters", *J. Chem. Phys.* **1965**, *42*, 1717.
- [97] G. A. Segal, R. W. Wetmore, K. Wolf, "Efficient methods for configuration interaction calculations", *Chem. Phys.* **1978**, *30*, 269.
- [98] J. Tatchen, "Spin-verbotene photophysikalische Prozesse in organischen Molekülen: Entwicklung quantenchemischer Methoden und Anwendung auf Psoralene", PhD thesis, Heinrich-Heine-Universität, Düsseldorf, **2006**.
- [99] J. Tatchen, N. Gilka, C. M. Marian, "Intersystem Crossing Driven by Vibronic Spin–Orbit Coupling: A Case Study on Psoralen", *Phys. Chem. Chem. Phys.* **2007**, *9*, 5209.
- [100] M. Etinski, J. Tatchen, C. M. Marian, "Time-Dependent Approaches for the Calculation of Intersystem Crossing Rates", *J. Chem. Phys.* **2011**, *134*, 154105.
- [101] T. Weymuth, M. P. Haag, K. Kiewisch, S. Lubner, S. Schenk, C. R. Jacob, C. Herrmann, J. Neugebauer, M. Reiher, "MOVIPAC: Vibrational spectroscopy with a robust meta-program for massively parallel standard and inverse calculations", *J. Comput. Chem.* **2012**, *33*, 2186–2198.
- [102] F. Duschinsky, *Acta Physicochim. USSR* **1937**, 551.
- [103] M. Etinski, J. Tatchen, C. M. Marian, "Thermal and Solvent Effects on the Triplet Formation in Cinnoline", *Phys. Chem. Chem. Phys.* **2014**, *16*, 4740.
- [104] E. Cancès, B. Mennucci, J. Tomasi, "A new integral equation formalism for the polarizable continuum model: Theoretical background and applications to isotropic and anisotropic dielectrics", *J. Chem. Phys.* **1997**, *107*, 3032.

- [105] B. Mennucci, E. Cancès, J. Tomasi, "Evaluation of Solvent Effects in Isotropic and Anisotropic Dielectrics and in Ionic Solutions with a Unified Integral Equation Method: Theoretical Bases, Computational Implementation, and Numerical Applications", *J. Phys. Chem. B* **1997**, *101*, 10506.
- [106] A. Klamt, G. Schüürmann, "COSMO: a new approach to dielectric screening in solvents with explicit expressions for the screening energy and its gradient", *J. Chem. Soc., Perkin Trans. 2* **1993**, 799.
- [107] J. Tomasi, B. Mennucci, R. Cammi, "Quantum Mechanical Continuum Solvation Models", *Chem. Rev.* **2005**, *105*, 2999.
- [108] S. Miertuš, E. Scrocco, J. Tomasi, "Electrostatic interaction of a solute with a continuum. A direct utilization of AB initio molecular potentials for the prevision of solvent effects", *Chem. Phys.* **1981**, *55*, 117.
- [109] A. K. Rappe, C. J. Casewit, K. S. Colwell, W. A. Goddard, W. M. Skiff, "UFF, a full periodic table force field for molecular mechanics and molecular dynamics simulations", *J. Am. Chem. Soc.* **1992**, *114*, 10024.
- [110] A. Klamt, V. Jonas, T. Bürger, J. C. W. Lohrenz, "Refinement and Parametrization of COSMO-RS", *J. Phys. Chem. A* **1998**, *102*, 5074.
- [111] M. Caricato, B. Mennucci, J. Tomasi, F. Ingrosso, R. Cammi, S. Corni, G. Scalmani, "Formation and relaxation of excited states in solution: A new time dependent polarizable continuum model based on time dependent density functional theory", *J. Chem. Phys.* **2006**, *124*, 124520.
- [112] R. Cammi, S. Corni, B. Mennucci, J. Tomasi, "Electronic excitation energies of molecules in solution: State specific and linear response methods for nonequilibrium continuum solvation models", *J. Chem. Phys.* **2005**, *122*, 104513.
- [113] S. Grimme, J. Antony, S. Ehrlich, H. Krieg, "A Consistent and Accurate ab Initio Parametrization of Density Functional Dispersion Correction (DFT-D) for the 94 Elements H-Pu", *J. Chem. Phys.* **2010**, *132*, 154104.
- [114] J. Föllner, M. Kleinschmidt, C. M. Marian, "Phosphorescence or Thermally Activated Delayed Fluorescence? Intersystem Crossing and Radiative Rate Constants of a Three-Coordinate Copper(I) Complex Determined by Quantum-Chemical Methods", *Inorg. Chem.* **2016**, *55*, 7508.
- [115] J. Föllner, C. M. Marian, "Rotationally Assisted Spin-State Inversion in Carbene-Metal-Amides Is an Artifact", *J. Phys. Chem. Lett.* **2017**, *8*, 5643.
- [116] A. Garnica, "Quantenchemische Charakterisierung von Cu(I)-Komplexen gemischter P,N-Liganden auf [2.2]Paracyclophanbasis: Variation der Pyridyleinheit", Bachelor's thesis, Heinrich-Heine-Universität, Düsseldorf, **2018**.

-
- [117] S. Gladt, "Quantenchemische Charakterisierung von Cu(I)-Komplexen gemischter P,N-Liganden auf [2.2]Paracyclophanbasis: Variation der Diarylphosphineinheit", Bachelor's thesis, Heinrich-Heine-Universität, Düsseldorf, **2018**.
- [118] S. Hirata, Y. Sakai, K. Masui, H. Tanaka, H. Lee, Sae Youn and Nomura, N. Nakamura, M. Yasumatsu, H. Nakanotani, Q. Zhang, K. Shizu, H. Miyazaki, C. Adachi, "Highly Efficient Blue Electroluminescence Based on Thermally Activated Delayed Fluorescence", *Nat. Mater.* **2015**, *14*, 330.
- [119] C. Ganter, private communication.
- [120] A. Steffen, private communication.
- [121] A. Steffen, private communication. Absorption, excitation and emission spectra were recorded in Andreas Steffen's group.

Appendices

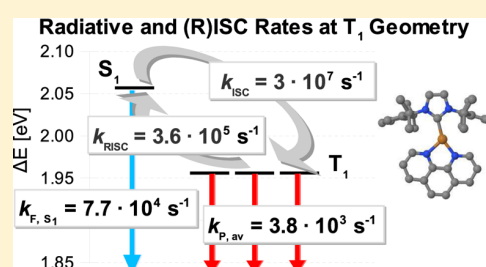
Paper I

Phosphorescence or Thermally Activated Delayed Fluorescence? Intersystem Crossing and Radiative Rate Constants of a Three-Coordinate Copper(I) Complex Determined by Quantum-Chemical Methods

Jelena Föllner, Martin Kleinschmidt, and Christel M. Marian*

Institut für Theoretische Chemie und Computerchemie, Heinrich-Heine-Universität Düsseldorf, Universitätsstrasse 1, D-40225 Düsseldorf, Germany

ABSTRACT: The photophysical properties of a cationic three-coordinate copper(I) complex with a monodentate N-heterocyclic carbene ligand and a bidentate phenanthroline ligand have been investigated by employing computational chemistry methods. The absorption spectrum, calculated with the combined density functional theory and multireference configuration interaction method, matches experimentally available data perfectly, thus corroborating the validity of our applied theoretical approach. On the basis of our calculated singlet–triplet gap of 650 cm^{-1} and the (reverse) intersystem crossing rates that are both larger than the fluorescence and phosphorescence rates at room temperature, we conclude that thermally activated delayed fluorescence should be observable for this complex in addition to phosphorescence. Torsion of the ligands has only a small impact on the singlet–triplet gap. However, the electronic coupling between the S_1 and T_1 states—and hence the probability for (reverse) intersystem crossing—is seen to increase substantially when moving from a coplanar to a perpendicular arrangement of the ligands.



INTRODUCTION

Transition-metal complexes as luminescent materials for organic light-emitting diodes (OLEDs) have been investigated for about 2 decades now.^{1–6} The first generation of small-molecule OLED emitters were fluorescent with an internal quantum yield of up to 25%.⁷ Dyes of this first generation have slow intersystem crossing (ISC) and negligible phosphorescence rates, and therefore only singlet excitons, which means only 25% of the excitons, can be harvested.²

The second generation of OLEDs employs phosphorescent dopants instead of fluorescent ones. Their excited singlet states typically undergo fast ISC to the lowest triplet state that can compete with fluorescence. Thus, in addition to the 75% of excitons that populate the lowest triplet, the 25% singlet excitons can be harvested also, leading to an internal quantum yield of up to 100%.^{2,8}

Both generations have their advantages and disadvantages.^{9,10} The advantages of the first generation are clear colors due to narrow emission bands and good stability of the dyes. The greatest disadvantage is probably the low internal quantum yield. The main disadvantage of the second-generation dyes is their comparatively long radiative lifetimes (microsecond regime), which lead to undesirable side effects, namely, quenching processes and bleaching reactions. Besides, these dyes are rather costly because of the pricey transition metals, such as iridium and platinum, that are used.

The third-generation emitters are organic molecules and transition-metal complexes with a rather small singlet–triplet

gap that lies within the range of thermal energy at room temperature.^{11–19} ISC and reverse ISC (RISC) from the lowest triplet to the lowest singlet are reasonably fast, and therefore a thermally activated delayed fluorescence (TADF) is possible. These dyes also show an internal quantum yield of up to 100%, and cheaper first-row transition metals such as copper can be used.

In the 1980s, Kirchoff et al.²⁰ found evidence for the participation of two energetically close-lying excited states in luminescence from four-coordinate $\text{Cu}(\text{NN})_2^+$ complexes. These authors tentatively assigned the lower state of the two as a triplet state and the upper one as a singlet metal-to-ligand charge transfer (MLCT) state. In 3-fold-coordinated copper(I) complexes with a sterically demanding monodentate N-heterocyclic carbene (NHC) ligand and a heterocyclic bidentate ligand, the relative orientation of the ligands seems to decide on the size of the singlet–triplet splitting and, hence, whether TADF (coplanar orientation) or phosphorescence (perpendicular orientation) is observed.^{14,21–23} In some phosphorescent complexes, conformational analysis indicates a nearly free rotation about the $\text{C}_{\text{NHC}}\text{--Cu}$ bond in solution.²²

Theory can help to achieve a better understanding of the factors that influence the emission behavior of such compounds. Optimal conditions for TADF (i.e., a small singlet–triplet gap, decent radiative rates, fast ISC, etc.) are

Received: April 5, 2016

Published: July 18, 2016

not easily satisfied simultaneously. On the one hand, a small overlap of electron and hole orbital densities—as may be found in MLCT compounds—leads to small exchange interactions and hence to small singlet–triplet gaps. On the other hand, a certain overlap of orbital densities is necessary for obtaining sizable values for transition dipole moments and spin–orbit coupling (SOC).

The NHC and phenanthroline ligands in the copper(I) complex investigated by Krylova et al.²¹ (Figure 1) were found

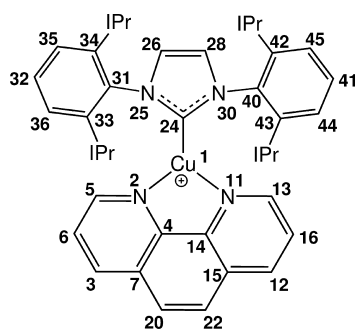


Figure 1. Molecular structure with atom numbers.

to have a coplanar orientation. Density functional theory (DFT) calculations performed by these authors indicated the lowest transition to have MLCT character. Nevertheless, the complex was reported to show only phosphorescence. In an effort to understand the reasons for this behavior and the underlying mechanisms, we became interested in the photo-physics of this compound. To our knowledge, this is the first quantum-chemical study on a three-coordinate copper(I) complex that goes beyond the determination of singlet–triplet splittings and throws light also on other factors that may influence its emission properties. The high-level quantum-chemical methods employed here have been shown to yield reliable rate constants for ISC and phosphorescence in organic as well as metal–organic compounds.^{24–30} The applicability of these methods to copper(I) complexes is corroborated in the present case by the excellent agreement of the calculated absorption spectrum with the experimental data.

METHODS AND COMPUTATIONAL DETAILS

For all calculations, the counterion (OTf) of the cationic complex was omitted. The ground-state geometry was optimized at the DFT level,³¹ whereas time-dependent DFT (TDDFT)³² was utilized for the excited-state geometries applying the *TURBOMOLE*, version 6.6, program package.³³ The PBE0 hybrid functional^{34,35} with a Hartree–Fock exchange ratio of 1:4 was used for optimization. The def-SV(P)³⁶ basis set for all nonmetal atoms and the cc-pVDZ-PP³⁷ basis set for the copper atom, together with the Stuttgart–Koeln multiconfiguration Dirac–Fock scalar relativistic effective core potential (ECP),³⁸ were chosen. All calculations were carried out in C_1 symmetry in the gas phase. The obtained geometries were verified as equilibrium geometries by employing either an analytical Hessian generated by the AOFORCE module of the *TURBOMOLE* package or finite-difference methods utilizing the NUMFORCE module.^{32,39,40}

Initially, the imidazol-2-ylidene and phenanthroline ligands were assumed to be coplanar because this arrangement corresponds to the minimum of the electronic ground state. In a second set of calculations, the geometries of the ground and low-lying excited states were optimized for a structure with perpendicular orientation of the ligands. To get a rough torsion path, constrained geometry optimizations for two intermediate points with torsion angles of 30° and 60° were performed. Dispersion corrections to the torsional

energy profiles were computed using the semiempirical Grimme D3 scheme.⁴¹

The spin-free vertical excitation spectra were calculated with the parallel version of the combined DFT and multireference configuration interaction (DFT/MRCI) method.^{42,43} This method includes the dynamic correlation from DFT as well as the static correlation from the MRCI approach. On the basis of the DFT-optimized structures, single-point calculations employing the BH-LYP functional^{44,45} (which is the only functional for which the DFT/MRCI Hamiltonian has been parametrized) were performed. The thus-received Kohn–Sham orbitals were used as the one-particle basis for MRCI expansion. In the DFT/MRCI step, orbitals 1–47 and 716–728, that is, orbitals with energies of less than -3.0 hartree and more than $+4.0$ hartree, were frozen. At all geometries, 21 singlet and 20 triplet roots were calculated. The only exception is the DFT/MRCI calculation at the twisted S_1 geometry, where calculation indicated that the singlet roots did not converge and the number of roots was therefore reduced to 18 roots.

SOC calculations were performed on top of the above-mentioned DFT/MRCI calculations. Spin–orbit matrix elements (SOMEs) of the spin-free DFT/MRCI wave functions were calculated with the SOC kit SPOCK developed in our laboratory.^{46,47} Herein, we employed SOC-ECP³⁸ on copper and an atomic mean-field approximation of the Breit–Pauli spin–orbit operator on all other centers.^{48–50} The excitation energies and transition dipole moments for the absorption spectrum including SOC were obtained with SOC quasi-degenerate perturbation theory (SOC-QDPT). For the phosphorescence and fluorescence rates or lifetimes, respectively, multireference spin–orbit configuration interaction (MRSOCI)⁵¹ wave functions were calculated. Five roots—one for the ground state, three for the three components of the first triplet, and one for the first excited singlet state—were calculated at the T_1 and S_1 geometries. The electric transition dipole moments of the received spin-mixed wave functions can be used to calculate the rates according to

$$\Gamma_{1,\zeta} = \frac{4e^2}{3c^3\hbar^4} \Delta E_{S_0 \leftarrow T_{1,\zeta}}^3 |\mu_{el}(S_0 \leftarrow T_{1,\zeta})|^2 \quad (1)$$

wherein $T_{1,\zeta}$ represents one of the three spin–orbit-coupled sublevels and $\Delta E_{S_0 \leftarrow T_{1,\zeta}}$ its vertical emission energy.

The Franck–Condon (FC) profiles of the emission from the T_1 and S_1 states to the ground state S_0 were obtained using the time-dependent branch of the *VIBES* program.^{52,53} The temperature was set to 77 K. For integration of the time correlation function, a time interval of 3 ps and a grid of 65536 points were chosen. The correlation function was damped with a Gaussian function of 1 cm^{-1} width. All spectra were normalized to one. The vibrational contributions to the ISC and RISC rates were also calculated with the *VIBES* program. The rates were obtained in the Condon approximation, which means that the vibrational and electronic contributions can be separated. This is a good approximation for molecules where the SOMEs are small compared to the adiabatic energy difference between the initial and final states and for systems where the size of the SOMEs does not change substantially upon geometry distortion. The temperature dependence, which is particularly important for the RISC, is included through a Boltzmann distribution of the vibrational population of the initial state. The ISC rate in the Condon approximation may then be expressed as

$$k_{\text{ISC}}^{\text{FC},T} = \frac{2\pi}{\hbar Z} |\langle \hat{V}_{\text{SO}}^1 \phi_a^{(0)} | \hat{V}_{\text{SO}}^1 \phi_b^{(0)} \rangle|^2 \times \sum_{j,k} e^{-(E_{bj} - E_{bo})/k_B T} |\langle \nu_{ak} | \nu_{bj} \rangle|^2 \delta(E_{bj} - E_{ak}) \quad (2)$$

with Z being the partition function defined as

$$Z = \sum_j e^{-(E_{bj} - E_{bo})/k_B T} \quad (3)$$

The ISC and RISC rates were calculated for two temperatures, 298 and 77 K. For calculation at 298 K, the time correlation function was

integrated over a time interval of 3 ps and a grid of 65536 points was chosen. The correlation function was damped in this case with a Gaussian function of 10 cm^{-1} width. For 77 K, the time interval had to be increased to 500 ps and the number of points to 262144. The width of the Gaussian function was set to 0.1 cm^{-1} .

RESULTS AND DISCUSSION

Electronic Ground State. The parameters of the ground-state equilibrium geometry are in good agreement with the experiment.²¹ The triangular copper coordination is slightly asymmetric. The Cu–N bond lengths are 2.04 Å (Cu1–N2) and 2.05 Å (Cu1–N11) in the crystal structure, while the calculated bond lengths of the isolated cation are both 2.08 Å (for atom labels, see Figure 1). The Cu–C bond to the NHC ligand is 1.88 Å in the experiment compared to a computed value of 1.89 Å. In the crystal structure, the C–Cu–N bond angles are $\text{C24–Cu1–N2} = 136.6^\circ$ and $\text{C24–Cu1–N11} = 141.5^\circ$. The corresponding calculated angles are 139.7° and 139.9° , respectively. The phenanthroline and NHC ligands are approximately coplanar. The dihedral angles in the experimental structure are $\text{N25–C24–Cu1–N11} = 175.0^\circ$ and $\text{N30–C24–Cu1–N2} = 169.1^\circ$, while the calculated dihedral angles are 179.6° and 177.5° . The somewhat larger deviations between the experiment and calculation for the dihedral angles are due to the fact that in the crystal structure the phenanthroline ligand is tilted toward the counterion.

The minimum-energy path of the electronic ground state along the torsional coordinate is shown in Figure 2. The

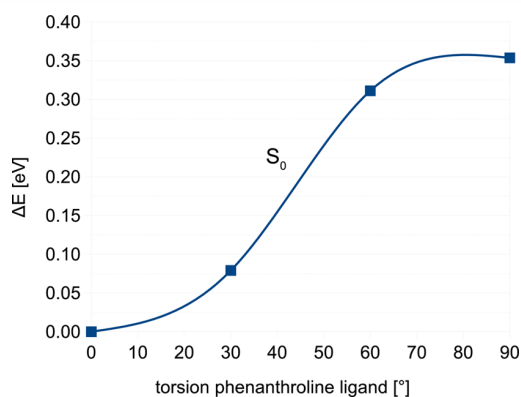


Figure 2. Ground-state scan of the torsion angle between the NHC and phenanthroline ligands. The DFT/MRCI ground-state energies include Grimme D3 dispersion corrections.

stationary point in the perpendicular arrangement of the phenanthroline and NHC ligands (torsion angle of 90°) turned out to be a saddle point with two very small ($<10i \text{ cm}^{-1}$) imaginary vibrational frequencies. Energetically, it is located approximately 0.17 eV above the minimum when no dispersion interactions are included. Dispersion corrections preferentially stabilize the coplanar orientation of the ligands and increase the barrier height in the electronic ground state to about 0.35 eV. Qualitatively, this trend is easily understood. In the coplanar nuclear arrangement, the hydrogen atoms in positions 5 and 13 of the phenanthroline ligands directly point toward the aromatic π system of the isopropylphenyl substituents of the NHC ligand, whereas these are far apart when the NHC and phenanthroline ligands are oriented in a perpendicular fashion.

Absorption Spectrum. The experimental spectrum,²¹ together with the calculated spectrum at the scalar relativistic

level and the calculated spectrum including SOC effects, is shown in Figure 3. They are seen to match perfectly. The

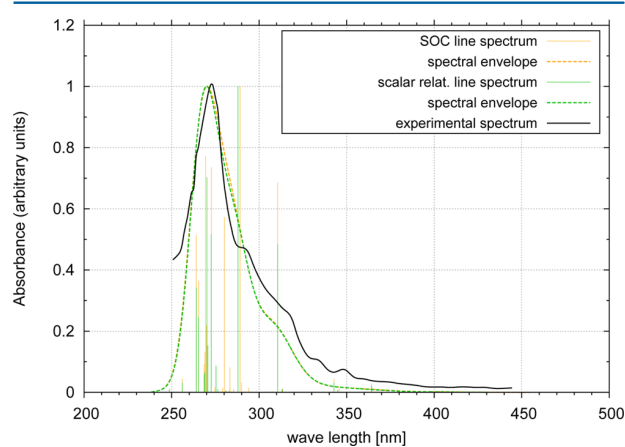


Figure 3. Absorption spectra obtained at the scalar relativistic DFT/MRCI level and including SOC effects by means of QDPT. The spectral envelope was plotted with Gaussians of 1500 cm^{-1} full width at half-maximum. The data points of the experimental spectrum have been taken from Figure 3 of ref 21.

experimental absorption spectrum has been recorded in CH_2Cl_2 . Very weak bands between 400 and 500 nm were assigned to triplet MLCT states. In the calculated spectrum, no electronic excitations with substantial oscillator strengths are found in this region. However, the S_1 , T_1 , and T_2 states lie between 400 and 420 nm, and the excitations might gain some intensity through vibronic transitions. The main configurations of these states are single excitations from HOMO–2 and HOMO–3 to LUMO for S_1 and T_2 and from HOMO–4 and HOMO–5 to LUMO+1 for T_1 . (For a molecular orbital scheme with graphical representations of the Kohn–Sham B3LYP orbital densities, see Figure 5.) HOMO–2 and HOMO–3 have d/σ character originating from a linear combination of a d_{xy} -like orbital of the copper atom with p orbitals of the phenanthroline (phenan) nitrogen atoms. HOMO–4 and HOMO–5 are d/π orbitals, where d is a d_{xz} -like orbital and the π contributions are located at the phenanthroline and imidazol-2-ylidene (NHC) ligands. LUMO and LUMO+1 are π^* (phenan) orbitals, so S_1 and T_2 have mainly MLCT character and T_1 has MLCT character mixed with some NHC to phenanthroline ligand charge-transfer contributions. In the region between 340 and 400 nm, there are some excitations with small oscillator strengths, two $d/\sigma(\text{phenan}) \rightarrow \pi^*$ (phenan) excitations and one with contributions from a $d/\pi(\text{phenan+NHC}) \rightarrow \pi^*$ and a $\pi(\text{phenan}) \rightarrow \pi^*(\text{phenan})$ configuration. The excitation at 311 nm, which is the first one with significant oscillator strength, has $d/\pi(\text{phenan+NHC}) \rightarrow \pi^*$ and $d/\pi(\text{NHC}) \rightarrow \pi^*$ contributions. The experimentalists assigned the bands between 250 and 300 nm to ligand-centered (LC) $\pi \rightarrow \pi^*$ excitations and the excitations at lower energies (explicitly 332 and 348 nm) to $d/\pi \rightarrow \pi^*$. In the calculated scalar relativistic spectrum, one can find the excitation with the strongest oscillator strength at 288 nm. This excitation is dominated by a $d \rightarrow \pi^*(\text{phenan})$ configuration. The excitation at 273 nm is a LC $\pi(\text{phenan}) \rightarrow \pi^*(\text{phenan})$ excitation. At 273 nm, there is again a $d \rightarrow \pi^*(\text{phenan})$ excitation. The two excitations with large oscillator strengths at 264 and 265 nm have marked charge-transfer $\pi(\text{phenyl}) \rightarrow \pi^*(\text{phenan})$

character. The shape of the spectrum does not change significantly when SOC effects are included. Differences can only be seen in the line spectra where many excitations gain oscillator strength due to singlet–triplet interaction. At 280 nm, there is an excitation with substantial oscillator strength that has no correspondence in the spin-free spectrum. It is a triplet $d \rightarrow \pi^*$ excitation with some singlet admixture ($d \rightarrow \pi^*$).

Because TDDFT is an often-used standard method, we also calculated and plotted an absorption spectrum with TDDFT using the PBE0 functional (see Figure 4). The match between

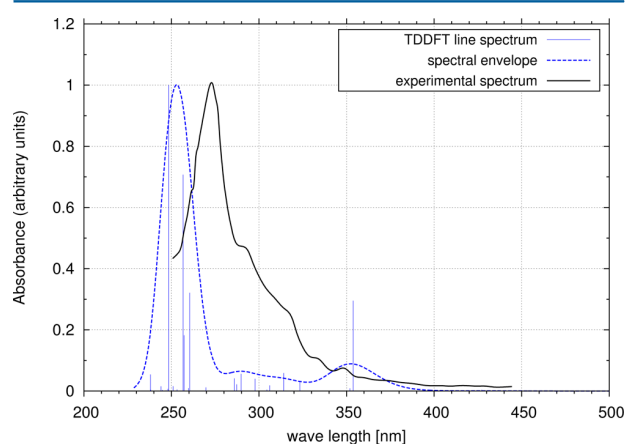


Figure 4. Scalar relativistic TDDFT/PBE0 absorption spectrum. The spectral envelope was plotted with Gaussians of 1500 cm^{-1} full width at half-maximum. The data points of the experimental spectrum have been taken from Figure 3 of ref 21.

the TDDFT and experimental spectra is not nearly as good as the match between the DFT/MRCI spectrum and the experiment. The transition at 354 nm corresponds to a $d/\pi(\text{NHC}) \rightarrow \pi^*(\text{phenan})$ excitation and is similar in character to the DFT/MRCI excitation at 311 nm. The two transitions at 260 and 257.2 nm are governed by $d/\pi(\text{NHC}) \rightarrow \pi^*(\text{phenan})$ excitations. The LC excitations at 256.6 and 248 nm have the largest oscillator strengths and are dominated by $\pi(\text{phenan}) \rightarrow \pi^*(\text{phenan})$ but have some $d/\pi(\text{phenyl}) \rightarrow \pi^*(\text{phenan})$ contributions also. Apparently, the DFT/MRCI and TDDFT results differ in the vertical excitation energies as well as in the transition dipole moments of the excitations.

Excited States. At the equilibrium geometry of the ground state, two triplets are located below the S_1 state (see Figure 6). A slight geometry distortion is, however, sufficient to reverse the order of the two triplet states. Henceforth, we renumber the states according to the order of their adiabatic minima. The main configurations of S_1 and T_1 are $d/\sigma \rightarrow \pi^*$ excitations, where the BH-LYP orbitals correspond to the PBE0 HOMO and LUMO orbitals. TDDFT optimization yielded these states as S_1 and T_1 equilibrium geometries (Figure 7). It is worth noting that the bulky isopropyl substituents of the phenyl groups keep the NHC and phenanthroline ligands from twisting in the excited state. When methyl is substituted for isopropyl, the coplanar arrangement of the NHC and phenanthroline ligands constitutes a saddle point on the excited-state potential energy surface. The excited-state minima with a torsion angle of 0° show a T-shaped distortion of the three-coordinated copper(I), as suggested by Krylova et al.²¹ The S_1 and T_1 geometries are very similar, with the largest deviation for the bond length being 0.01 \AA and that for the

bond angle being 0.4° . DFT/MRCI calculations at these states show that the S_1 and T_1 states lie close together at the T_1 geometry (ca. 0.1 eV ; Figure 8) and are rather isolated. Both the T-shaped distortion and the torsion of the phenanthroline ligand appear to be very unfavorable for the $d_\pi-\pi$ type of bonding of copper and the ligands, pushing the HOMO–4 \rightarrow LUMO+1 and HOMO–5 \rightarrow LUMO+1 configurations upward. Because the energy gap between the S_1 and T_1 states is so small, TADF might be possible and therefore phosphorescence and fluorescence as well as the ISC and RISC rates were investigated for both the coplanar (torsion angle 0°) and perpendicular (torsion angle 90°) arrangement of the ligands.

Phosphorescence and Fluorescence. The FC profiles for emission in the coplanar and perpendicular arrangements of the ligands, respectively, are shown in Figure 9, together with the experimental spectrum measured at 77 K in 2-MeTHF.²¹ For the VIBES calculation at the 90° twisted geometry, the imaginary frequencies of the ground-state vibrations were omitted. Clearly, the FC profiles for the coplanar arrangement of the ligands compare better to the experimental spectrum. Further discussion in this section will therefore concentrate on the minimum geometries with 0° torsion angle. The shapes of both FC spectra—from S_1 and T_1 —are very much alike. Both are slightly broader and fall off more slowly than the experimental spectrum. This behavior is ascribed to the harmonic oscillator approximation underlying the calculations. The maximum of the fluorescence spectrum is located at 572 nm, while the phosphorescence spectrum is found to peak at 600 nm, somewhat blue-shifted compared to the experimental maximum at 630 nm. Phosphorescence and fluorescence rates or lifetimes, respectively, have been calculated at both the S_1 and T_1 geometries. The zero-field splitting is small, the first (T_1) and second (T_{II}) triplet components are virtually degenerate, and the splitting between the T_{II} and T_{III} components amounts to about 1 cm^{-1} (see Table 1). The calculated rates at the S_1 and T_1 geometries are quite similar. At the T_1 geometry, the calculated mean for the three phosphorescence rates is $k_{p,av} = 3.75 \times 10^3 \text{ s}^{-1}$ (lifetime $\tau_p = 267 \mu\text{s}$) and the rate for the fluorescence is $k_F = 7.73 \times 10^4 \text{ s}^{-1}$ ($\tau_F = 13 \mu\text{s}$). For the S_1 geometry, we obtain values of $k_{p,av} = 3.80 \times 10^3 \text{ s}^{-1}$ ($\tau_p = 263 \mu\text{s}$) and $k_F = 8.83 \times 10^4 \text{ s}^{-1}$ ($\tau_F = 11 \mu\text{s}$) (see also Figure 10).

Because the values were computed in vacuo, they can best be compared with the experimental results obtained in a frozen matrix of 2-MeTHF at 77 K [$\tau = 1.8 \mu\text{s}$ (24%) and $4.6 \mu\text{s}$ (76%);²¹ quantum yield not measured]. Note that the experimental emission lifetimes are not pure radiative lifetimes but contain contributions from nonradiative decay processes. Other measurements from the same authors in solvent (e.g., in CH_2Cl_2 at 300 K, $\tau = 0.08 \mu\text{s}$ and quantum yield <0.001) or as a solid ($\tau = 1.2 \mu\text{s}$ at 300 K and quantum yield 0.026) show that the majority of excited states decay nonradiatively at room temperature. Because the emission quantum yield Φ_{em} is related to the radiative k_r and nonradiative k_{nr} decay rates by

$$\Phi_{em} = \frac{k_r}{k_{nr} + k_r} \quad (4)$$

pure radiative lifetimes can be estimated from knowledge of the total emission decay time and quantum yield. From eq 4 and the relationship $k_r = 1/\tau_r$, estimated experimental radiative lifetimes of $>80 \mu\text{s}$ in CH_2Cl_2 at 300 K and $\approx 46 \mu\text{s}$ in the crystalline state can be derived. These values compare better

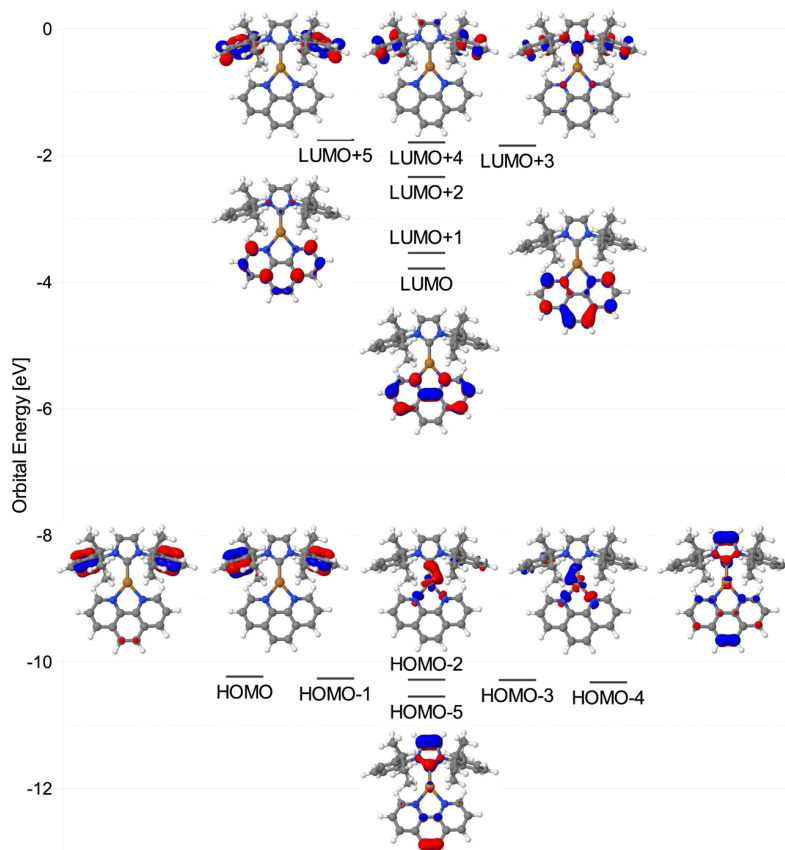


Figure 5. Ground-state BH-LYP molecular orbitals.

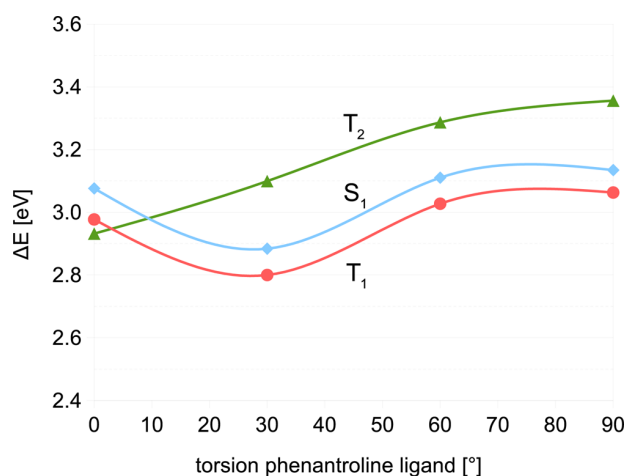


Figure 6. Ground-state scan of the torsion angle between the NHC and phenanthroline ligands. The DFT/MRCI excitation energies of T_1 , T_2 , and S_1 are given relative to the S_0 energy at the 0° S_0 geometry.

with our calculated fluorescence lifetime of $\tau_F = 11 \mu\text{s}$ than with $\tau_P = 267 \mu\text{s}$.

The radiative rates change only a little upon moving to a perpendicular orientation of the ligands. The mean phosphorescence decay at this minimum of the T_1 potential is a bit slower than that for a torsion angle of 0° . It proceeds at an average rate of $k_{P,av} = 1.81 \times 10^3 \text{ s}^{-1}$. In contrast, the fluorescence rate ($k_F = 1.03 \times 10^5 \text{ s}^{-1}$), computed at the 90°

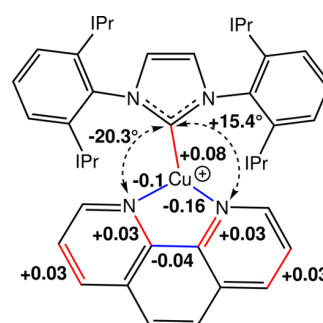


Figure 7. Important geometry changes between S_0 and T_1 . Bonds that shorten are in blue and bonds that elongate in red [for bond angles (deg) and bond lengths (Å)].

twisted S_1 minimum, is slightly larger than the one obtained for the coplanar arrangement of the ligands.

Torsion Path of the T_1 State. When no dispersion corrections are applied, the T_1 and S_1 minima with perpendicular orientations of the ligands are the global minima on these potential energy surfaces, albeit with a small energy preference of only 0.08 eV over the local minima at 0° torsion. As mentioned above, the comparison of computed and measured emission spectra indicates the reverse energetic order. Therefore, we repeated our calculations, adding semiempirical dispersion corrections. Dispersion is seen to have a small but differential effect on the torsion potential of the S_1 and T_1 states. It not only increases the barrier between the two minima on the excited-state potential energy surface

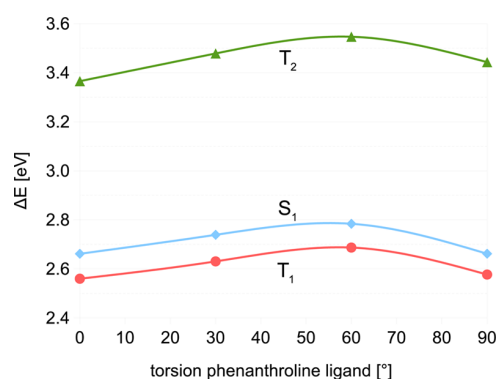


Figure 8. Scan of the torsion angle between the NHC and phenanthroline ligands for the T_1 geometry. DFT/MRCI excitation energies of the T_1 , T_2 , and S_1 states refer to the S_0 energy at the 0° S_0 geometry.

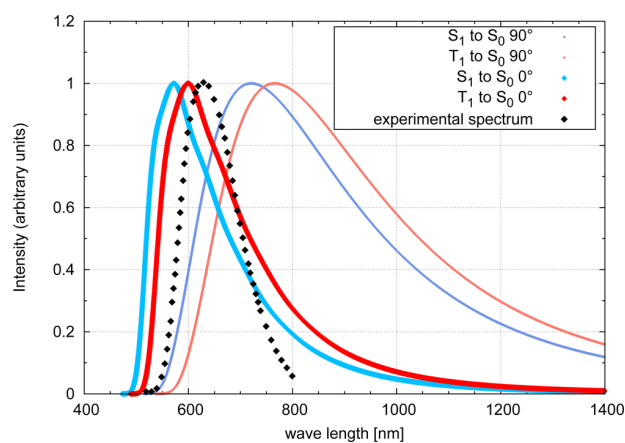


Figure 9. FC profile for the emission from T_1 and S_1 at 0° and 90° torsion compared to the experimental emission spectrum (data points taken from Figure 3 of ref 21). The spectra were normalized to one.

Table 1. Vertical Energies, Oscillator Strengths $f(L)$, Radiative Rates, and Lifetimes τ at the 0° T_1 and S_1 Minimum

state	ΔE [cm^{-1}]	$f(L)$	rate [s^{-1}]	τ [μs]
At T_1				
T_1	15776	1.50×10^{-6}	2.44×10^2	4091
T_{II}	15776	5.00×10^{-7}	6.64×10^1	11575
T_{III}	15777	6.58×10^{-5}	1.06×10^4	92
				$\tau_{av} = 267$
At S_1				
T_1	15910	1.50×10^{-6}	2.51×10^2	3988
T_{II}	15911	4.00×10^{-7}	6.30×10^1	15866
T_{III}	15911	6.57×10^{-5}	1.11×10^4	90
				$\tau_{av} = 263$
S_1	16691	4.75×10^{-4}	8.83×10^4	11

but also preferentially lowers the coplanar arrangement of the ligands such that this minimum becomes the global one. The barrier for the torsion on the T_1 potential energy surface is about 0.13 eV. A similar value (0.12 eV) is obtained for the S_1 state. Although the barrier is not high, the experimentally observed emission seems to stem from the structure with a coplanar arrangement of the ligands (Figure 9).

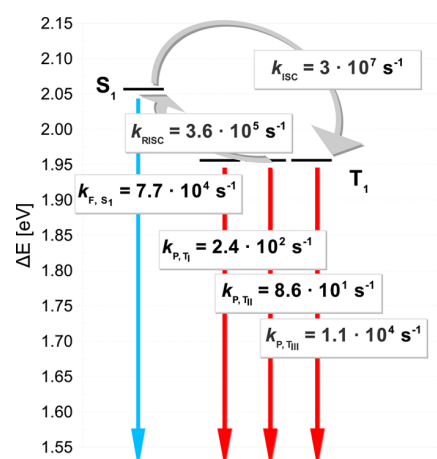


Figure 10. Fluorescence, phosphorescence, and ISC rates at the global T_1 minimum.

Regarding the contributions of the configurations to the T_1 and S_1 DFT/MRCI wave functions, there are only small changes along the torsional coordinate (see Table 2). For all

Table 2. Configurations (with Squared Coefficients) of the S_1 and T_1 States for the T_1 Geometry Torsion

S_1		T_1	
angle [deg]	configuration	angle [deg]	configuration
0	HOMO \rightarrow LUMO (79.7)	0	HOMO \rightarrow LUMO (79.9)
	HOMO-7 \rightarrow LUMO (2.2)		HOMO-7 \rightarrow LUMO (2.3)
	HOMO \rightarrow LUMO+2 (1.7)		HOMO \rightarrow LUMO+2 (2.1)
30	HOMO \rightarrow LUMO (80.5)	30	HOMO \rightarrow LUMO (80.7)
	HOMO-6 \rightarrow LUMO (1.9)		HOMO \rightarrow LUMO+2 (2.1)
	HOMO \rightarrow LUMO+2 (1.7)		HOMO-6 \rightarrow LUMO (1.9)
60	HOMO \rightarrow LUMO (79.6)	60	HOMO \rightarrow LUMO (80.1)
	HOMO \rightarrow LUMO+2 (1.7)		HOMO \rightarrow LUMO+2 (2.1)
	HOMO-5 \rightarrow LUMO (1.6)		HOMO-5 \rightarrow LUMO (1.5)
90	HOMO \rightarrow LUMO (78.8)	90	HOMO \rightarrow LUMO (79.4)
	HOMO-3 \rightarrow LUMO (1.9)		HOMO \rightarrow LUMO+2 (2.2)
	HOMO \rightarrow LUMO+2 (1.8)		HOMO-3 \rightarrow LUMO (1.7)

four angles, the main contribution with a weight of about 80% stems from the HOMO-to-LUMO excitation. As to the electron density distribution of the orbitals, one can observe an increase of the density at the NHC ligand from almost no density at 0° to small contributions at all five ring atoms for the 90° distorted geometry (Figure 11).

The singlet-triplet splitting changes only slightly along the path, namely, from 650 cm^{-1} at 0° to 830 cm^{-1} at 90° , in contrast to the observations of Leitl et al.¹⁴ in a related Cu^I-NHC-dipyridyldimethylborate complex. These authors report an increase from 540 cm^{-1} at 0° to 3700 cm^{-1} at 70° torsion

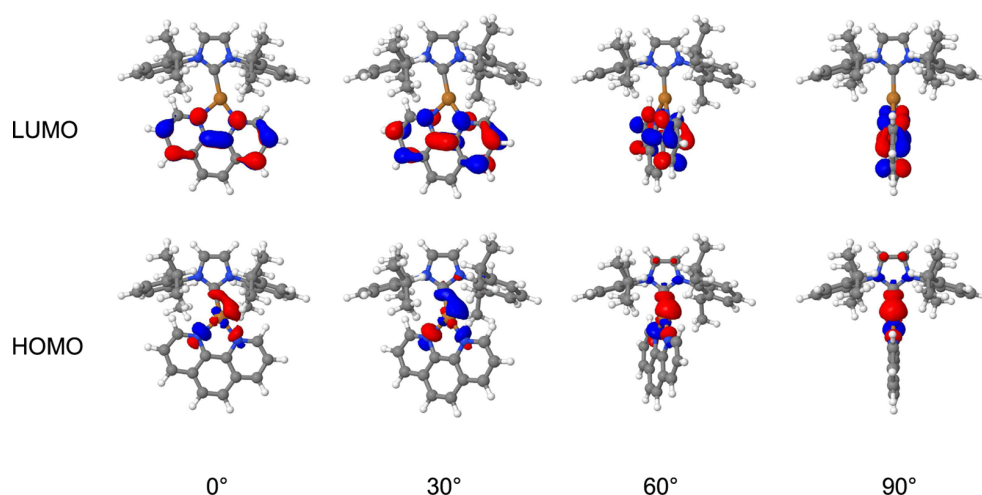


Figure 11. Electron density distributions of the ground-state BH-LYP frontier molecular orbitals for a twist of the T_1 molecular structure.

angle. The different behavior of the two complexes can be explained by the different electron density distributions of the frontier orbitals. In our case, the density of the HOMO is mainly located at copper and that of the LUMO at the phenanthroline ligand, which does not change so much during the torsion. Correspondingly, we find only a small increase of the energy gap. In contrast, the orbital overlaps of the Cu^I-NHC–dipyridyldimethylborate investigated by Leilt et al.¹⁴ increase considerably upon torsion. In their case, the LUMO is located at the NHC ligand and the HOMO of the 90° geometry has (like in our case, but even more pronounced) additional density at the NHC ligand.

ISC and RISC. Owing to the small difference between the adiabatic DFT/MRSOCI energies of the S_1 and T_1 minima, TADF should, in principle, be possible. In order to actually take place, S_1 has to be repopulated. That means that the RISC rate has to be larger than the rates of radiative and nonradiative decay of T_1 to the electronic ground state. Because the S_1 and T_1 states arise from the same orbital excitation, their mutual spin–orbit interaction is rather small (see Table 3) and

Table 3. SOMEs [cm^{-1}] Computed at the 0° and 90° T_1 and S_1 Minima and Rates (RISC from T_1 to S_1 and ISC from S_1 to T_1)

angle [deg]	$\langle T_1 \hat{H}_{SO} S_1 \rangle$			$\sum(\text{SOMEs})^2$	rate [s^{-1}]
	x	y	z		
	At T_1				RISC
0	0.204	−0.200	−0.643	0.495	3.62×10^5
90	−0.882	−4.44	0.213	20.6	4.26×10^7
	At S_1				ISC
0	−0.107	0.150	0.912	0.866	3.00×10^7
90	−0.844	−4.43	0.183	20.4	2.87×10^9

vibronic effects may have to be taken into account.⁵⁴ Here, we compute the ISC and RISC rate constants in the Condon approximation. To this end, the SOMEs between the three Cartesian triplet components and S_1 have been squared and summed up because we are not interested in the individual crossing rates between each of the triplet sublevels and the singlet but in the overall rate. According to eq 2, this sum is

multiplied by the FC-weighted density of states to yield the (R)ISC rate.

In the coplanar arrangement of the ligands, RISC proceeds at a rate of $k_{\text{RISC}} = 3.62 \times 10^5 \text{ s}^{-1}$ at 298 K, which is 2 orders of magnitude larger than the mean phosphorescence rate. This implies that the S_1 state can be populated from the T_1 state. However, the ISC rate $k_{\text{ISC}} = 3.0 \times 10^7 \text{ s}^{-1}$ is again about 2–3 orders of magnitude larger than the fluorescence rate. We therefore conclude that at room temperature the S_1 and T_1 populations quickly equilibrate before decaying radiatively. The situation changes when the temperature is set to 77 K. Because the RISC rate is particularly temperature-dependent, the RISC rate becomes very small, about 8 s^{-1} , while the ISC rate decreases only slightly from $k_{\text{ISC}} = 3.0 \times 10^7 \text{ s}^{-1}$ to $k_{\text{ISC}} = 2.5 \times 10^7 \text{ s}^{-1}$. That means that the RISC cannot compete with the phosphorescence at liquid-nitrogen temperatures and that TADF should not be observable.

Kirchhoff et al.²⁰ carefully analyzed the kinetics of a three-level system relating to TADF. The scheme is sketched in Figure 12, where we have changed the nomenclature for an easier identification of the kinetic constants. Kirchhoff et al. concluded that the steady-state emission properties of the three-level system depend upon the relative values of the various rate constants as well as the relative energies of the levels and considered two limiting cases, the kinetic and

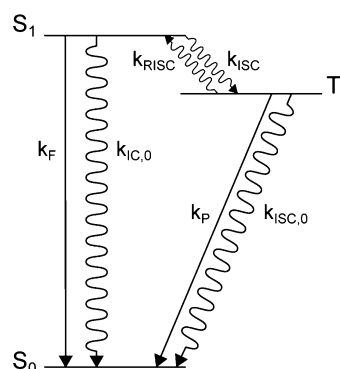


Figure 12. Kinetic scheme of a three-level system according to Kirchhoff et al.²⁰

equilibrium limits. The basic assumption in the kinetic-limit case is that the S_1 state achieves a steady-state concentration that is negligibly affected by the RISC process. Most of the photons would then appear from prompt fluorescence or phosphorescence. The calculated rate constants at 77 K, where k_{RISC} is several orders of magnitude smaller than k_{F} and k_{ISC} , shows that their ratio reaches a level close to this kinetic-limit case. In contrast, the equilibrium-limit case, where the steady-state populations of the S_1 and T_1 states are determined by Boltzmann statistics, appears to be more appropriate at room temperature. For this limit case to be adequate, $k_{\text{ISC}} \gg k_{\text{F}} + k_{\text{IC}_0}$ and $k_{\text{RISC}} \gg k_{\text{P}} + k_{\text{ISC}_0}$. We have not calculated the rate constants for the internal conversion of S_1 to S_0 (k_{IC_0}) and for ISC from T_1 to S_0 (k_{ISC_0}). Because of the substantial energy gap between the S_1 and T_1 states, on the one hand, and the electronic ground state, on the other hand, these processes are assumed to be much slower than the radiative decay rates and will be neglected in the following. The first condition for the equilibrium limit, namely, $k_{\text{ISC}} \gg k_{\text{F}}$, is certainly fulfilled at all temperatures, but the second condition, $k_{\text{RISC}} \gg k_{\text{P}}$, is not. In the present case, the formula used by many experimentalists to fit the energy gap between the S_1 and T_1 states, $\Delta E(S_1 - T_1)$, and the decay times of the individual states from the temperature dependence of the emission decay time of the TADF compound¹⁸

$$\tau(T) = \frac{3 + \exp[-\Delta E(S_1 - T_1)/k_{\text{B}}T]}{\frac{3}{\tau(T_1)} + \frac{1}{\tau(S_1)} \exp[-\Delta E(S_1 - T_1)/k_{\text{B}}T]} \quad (5)$$

is therefore not valid at low temperatures.

The respective quantum yields were calculated instead following the kinetic analysis of Hirata et al.⁵⁵ In deriving their expression for the TADF quantum yield Φ_{TADF} in relation to the triplet quantum yield Φ_{T} , the authors assumed that the internal conversion from the S_1 state to the electronic ground state S_0 can be neglected and that the ISC from S_1 to T_1 is much faster than the reverse process. Neglecting the non-radiative deactivation of the T_1 sublevels but taking into account their phosphorescence decay through the averaged high-temperature limit of the individual rate constants, one arrives at

$$\frac{\Phi_{\text{TADF}}}{\Phi_{\text{P}}} = \frac{1}{\frac{k_{\text{P,av}}}{k_{\text{RISC}}\Phi_{\text{PF}}} + 1} \quad (6)$$

For 298 K, our calculated quantum yield of prompt fluorescence Φ_{PF} is quite small, only 0.3%. The quantum yield for deactivation via phosphorescence is 77.7%, and the remaining 22% is the quantum yield for TADF.

The ISC and RISC rates are seen to change dramatically along the torsional coordinate. Their increase by about 2 orders of magnitude, with the RISC rate being $k_{\text{RISC}} = 4.26 \times 10^7 \text{ s}^{-1}$ and the ISC rate $k_{\text{ISC}} = 2.87 \times 10^9 \text{ s}^{-1}$ in the perpendicular arrangement of the ligands, is not related to the magnitude of the singlet–triplet gap. As discussed before, ΔE_{ST} grows slightly from 650 cm^{-1} at 0° to 830 cm^{-1} at 90° , implicating a slowdown of the RISC process. The energetic aspect is overcompensated, however, by the electronic interaction that becomes much stronger, as may be seen in Table 3, where the SOMEs at both the T_1 and S_1 minima are listed. The smaller mean phosphorescence rate as well as the increased fluorescence and (R)ISC rates lead to a larger quantum yield for TADF, that

is, 45.7%, in the perpendicular arrangement, while the quantum yield for phosphorescence is decreased to 54.3%.

CONCLUSIONS

This work computationally investigated the geometries and photophysical properties of a Cu^{I} -NHC–phenanthroline complex. The calculations conveyed that the coplanar orientation of the ligands yields the global minimum on the ground-state potential energy surface, whereas the perpendicular orientation corresponds to a saddle point. The absorption spectrum obtained with the DFT/MRCI approach is in excellent agreement with the experimental data. Because TDDFT is an often-used standard method, we also calculated an absorption spectrum with this method for comparison by employing the PBE0 functional. The match between the TDDFT and experimental spectra is not nearly as good as for DFT/MRCI. Therefore, all electronic excitation energies and properties reported in this work refer to DFT/MRCI values.

Dispersion interactions are found to favor a coplanar arrangement of the ligands in the excited states also, with the local minima corresponding to a perpendicular arrangement lying only marginally higher. Comparison of the calculated FC emission profiles with the experimental emission spectrum, nevertheless, indicates that the emission stems from a coplanar arrangement of the ligands, although the torsional barrier is rather low (ca. 0.13 eV) in the excited states. The small singlet–triplet gap of $\Delta E_{\text{ST}} = 650 \text{ cm}^{-1}$ suggests that TADF should be possible. From the magnitude of the computed radiative and nonradiative rate constants, we infer that, after a fast equilibration of the singlet and triplet populations, radiation will be emitted from both the S_1 and T_1 states. This would fit to the experimentally measured lifetimes of $>80 \mu\text{s}$ in CH_2Cl_2 at 300 K and $\approx 46 \mu\text{s}$ in the crystalline state, which lie between our calculated mean phosphorescence lifetime of $\tau_{\text{P}} = 267 \mu\text{s}$ and the fluorescence lifetime of $\tau_{\text{F}} = 11 \mu\text{s}$.

The torsion of the phenanthroline ligand in the excited states has only a small influence on the singlet–triplet gap. Neither the configurations nor the orbitals that are involved in the excitations change significantly during the torsion. This is why we find only a slight increase of the singlet–triplet gap, in contrast to the observations of Leitl et al.¹⁴ for a related Cu^{I} -NHC–dipyridyldimethylborate complex. However, we observe a pronounced effect on the nonradiative rates. The RISC and ISC rates both increase by about 2 orders of magnitude compared to their values in the coplanar arrangement of the ligands. In contrast, the radiative rates are only moderately affected by the torsion of the phenanthroline ligand. In the perpendicular arrangement, the mean phosphorescence rate is reduced to half of its value at 0° , whereas the fluorescence rate is about 1.33 times faster than that at 0° . This leads to a much larger TADF quantum yield at the perpendicular arrangement of the ligands (45.7%) compared to the coplanar structure (22%). The only remaining problem is the broad vibrational profile of the emission. The results of our quantum-chemical analysis suggest that a perpendicular arrangement of the ligands in a three-coordinate NHC– Cu^{I} -N $^{\wedge}$ N complex is not a hindrance per se for observing TADF (in addition to phosphorescence), provided that the electron is transferred to the N $^{\wedge}$ N ligand in the MLCT transition.

AUTHOR INFORMATION

Corresponding Author

*E-mail: Christel.Marian@hhu.de.

Notes

The authors declare no competing financial interest.

ACKNOWLEDGMENTS

The authors thank Prof. Christian Ganter (Düsseldorf) for helpful discussions. Funds (INST 208/704-1 FUGG) provided by the Deutsche Forschungsgemeinschaft to purchase the hybrid compute cluster used in this study are gratefully acknowledged.

REFERENCES

- (1) Ma, Y.; Zhang, H.; Shen, J.; Che, C. *Synth. Met.* **1998**, *94*, 245–248.
- (2) Forrest, S. R.; Baldo, M. A.; O'Brien, D. F.; You, Y.; Shoustikov, A.; Sibley, S.; Thompson, M. E. *Nature* **1998**, *395*, 151–154.
- (3) Yersin, H.; Rausch, A. F.; Czerwiec, R.; Hofbeck, T.; Fischer, T. *Coord. Chem. Rev.* **2011**, *255*, 2622–2652.
- (4) Murawski, C.; Leo, K.; Gather, M. C. *Adv. Mater.* **2013**, *25*, 6801–6827.
- (5) Choy, W. C. H.; Chan, W. K.; Yuan, Y. *Adv. Mater.* **2014**, *26*, 5368–5399.
- (6) Cariati, E.; Lucenti, E.; Botta, C.; Giovanella, U.; Marinotto, D.; Righetto, S. *Coord. Chem. Rev.* **2016**, *306*, 566–614.
- (7) Tang, C. W.; VanSlyke, S. A. *Appl. Phys. Lett.* **1987**, *51*, 913–915.
- (8) Baldo, M. A.; Lamansky, S.; Burrows, P. E.; Thompson, M. E.; Forrest, S. R. *Appl. Phys. Lett.* **1999**, *75*, 4–6.
- (9) Adachi, C. *Jpn. J. Appl. Phys.* **2014**, *53*, 060101.
- (10) Adachi, C.; Adachi, J. High Performance TADF for OLEDs. Presentation at the 2015 SSL R&D Workshop in San Francisco, CA, http://www.energy.gov/sites/prod/files/2015/02/f19/adachi_oled-tadf_sanfrancisco2015.pdf.
- (11) Uoyama, H.; Goushi, K.; Shizu, K.; Nomura, H.; Adachi, C. *Nature* **2012**, *492*, 234–238.
- (12) Dias, F. B.; Bourdakos, K. N.; Jankus, V.; Moss, K. C.; Kamtekar, K. T.; Bhalla, V.; Santos, J.; Bryce, M. R.; Monkman, A. P. *Adv. Mater.* **2013**, *25*, 3707–3714.
- (13) Zhang, Q.; Li, B.; Huang, S.; Nomura, H.; Tanaka, H.; Adachi, C. *Nat. Photonics* **2014**, *8*, 326–332.
- (14) Leidl, M. J.; Krylova, V. A.; Djurovich, P. I.; Thompson, M. E.; Yersin, H. *J. Am. Chem. Soc.* **2014**, *136*, 16032–16038.
- (15) Osawa, M.; Kawata, I.; Ishii, R.; Igawa, S.; Hashimoto, M.; Hoshino, M. *J. Mater. Chem. C* **2013**, *1*, 4375–4383.
- (16) Chen, X.-L.; Yu, R.; Zhang, Q.-K.; Zhou, L.-J.; Wu, X.-Y.; Zhang, Q.; Lu, C.-Z. *Chem. Mater.* **2013**, *25*, 3910–3920.
- (17) Linfoot, C. L.; Leidl, M. J.; Richardson, P.; Rausch, A. F.; Chepelin, O.; White, F. J.; Yersin, H.; Robertson, N. *Inorg. Chem.* **2014**, *53*, 10854–10861.
- (18) Czerwiec, R.; Yersin, H. *Inorg. Chem.* **2015**, *54*, 4322–4327.
- (19) Zhang, Q.; Chen, J.; Wu, X.-Y.; Chen, X.-L.; Yu, R.; Lu, C.-Z. *Dalton Trans.* **2015**, *44*, 6706–6710.
- (20) Kirchhoff, J. R.; Gamache, R. E., Jr.; Blaskie, M. W.; Del Paggio, A. A.; Lengel, R. K.; McMillin, D. R. *Inorg. Chem.* **1983**, *22*, 2380–2384.
- (21) Krylova, V. A.; Djurovich, P. I.; Whited, M. T.; Thompson, M. E. *Chem. Commun.* **2010**, *46*, 6696–6698.
- (22) Krylova, V. A.; Djurovich, P. I.; Aronson, J. W.; Haiges, R.; Whited, M. T.; Thompson, M. E. *Organometallics* **2012**, *31*, 7983–7993.
- (23) Krylova, V. A.; Djurovich, P. I.; Conley, B. L.; Haiges, R.; Whited, M. T.; Williams, T. J.; Thompson, M. E. *Chem. Commun.* **2014**, *50*, 7176–7179.
- (24) Rai-Constapel, V.; Etinski, M.; Marian, C. M. *J. Phys. Chem. A* **2013**, *117*, 3935–3944.
- (25) Rai-Constapel, V.; Villnow, T.; Ryseck, G.; Gilch, P.; Marian, C. M. *J. Phys. Chem. A* **2014**, *118*, 11708–11717.
- (26) Villnow, T.; Ryseck, G.; Rai-Constapel, V.; Marian, C. M.; Gilch, P. *J. Phys. Chem. A* **2014**, *118*, 11696–11707.
- (27) Mundt, R.; Villnow, T.; Ziegenbein, C. T.; Gilch, P.; Marian, C. M.; Rai-Constapel, V. *Phys. Chem. Chem. Phys.* **2016**, *18*, 6637–6647.
- (28) Lobsiger, S.; Etinski, M.; Blaser, S.; Frey, H.-M.; Marian, C.; Leutwyler, S. *J. Chem. Phys.* **2015**, *143*, 234301.
- (29) Kleinschmidt, M.; van Wüllen, C.; Marian, C. M. *J. Chem. Phys.* **2015**, *142*, 094301.
- (30) Heil, A.; Gollnisch, K.; Kleinschmidt, M.; Marian, C. M. *Mol. Phys.* **2016**, *114*, 407–422.
- (31) Von Arnim, M.; Ahlrichs, R. *J. Comput. Chem.* **1998**, *19*, 1746–1757.
- (32) Furche, F.; Ahlrichs, R. *J. Chem. Phys.* **2002**, *117*, 7433–7447.
- (33) TURBOMOLE V6.6 2014, a development of University of Karlsruhe and Forschungszentrum Karlsruhe GmbH, 1989–2007; TURBOMOLE GmbH, since 2007; available from <http://www.turbomole.com>.
- (34) Perdew, J. P.; Burke, K.; Ernzerhof, M. *Phys. Rev. Lett.* **1996**, *77*, 3865–3868.
- (35) Adamo, C.; Barone, V. *J. Chem. Phys.* **1999**, *110*, 6158–6170.
- (36) Schäfer, A.; Horn, H.; Ahlrichs, R. *J. Chem. Phys.* **1992**, *97*, 2571–2577.
- (37) Peterson, K. A.; Puzzarini, C. *Theor. Chem. Acc.* **2005**, *114*, 283–296.
- (38) Figgen, D.; Rauhut, G.; Dolg, M.; Stoll, H. *Chem. Phys.* **2005**, *311*, 227–244.
- (39) Deglmann, P.; Furche, F.; Ahlrichs, R. *Chem. Phys. Lett.* **2002**, *362*, 511–518.
- (40) Deglmann, P.; Furche, F. *J. Chem. Phys.* **2002**, *117*, 9535–9538.
- (41) Grimme, S.; Antony, J.; Ehrlich, S.; Krieg, H. *J. Chem. Phys.* **2010**, *132*, 154104.
- (42) Grimme, S.; Waletzke, M. *J. Chem. Phys.* **1999**, *111*, 5645–5655.
- (43) Kleinschmidt, M.; Marian, C. M.; Waletzke, M.; Grimme, S. *J. Chem. Phys.* **2009**, *130*, 044708.
- (44) Lee, C.; Yang, W.; Parr, R. G. *Phys. Rev. B: Condens. Matter Phys.* **1988**, *37*, 785–789.
- (45) Becke, A. D. *J. Chem. Phys.* **1993**, *98*, 1372–1377.
- (46) Kleinschmidt, M.; Tatchen, J.; Marian, C. M. *J. Comput. Chem.* **2002**, *23*, 824–833.
- (47) Kleinschmidt, M.; Marian, C. M. *Chem. Phys.* **2005**, *311*, 71–79.
- (48) Mitin, A. V.; van Wüllen, C. *J. Chem. Phys.* **2006**, *124*, 064305.
- (49) Hess, B. A.; Marian, C. M.; Wahlgren, U.; Gropen, O. *Chem. Phys. Lett.* **1996**, *251*, 365–371.
- (50) Schimmelpfennig, B. *AMFI, an atomic spin-orbit integral program*; University of Stockholm: Stockholm, Sweden, 1996.
- (51) Kleinschmidt, M.; Tatchen, J.; Marian, C. M. *J. Chem. Phys.* **2006**, *124*, 124101.
- (52) Etinski, M.; Tatchen, J.; Marian, C. M. *J. Chem. Phys.* **2011**, *134*, 154105.
- (53) Etinski, M.; Tatchen, J.; Marian, C. M. *Phys. Chem. Chem. Phys.* **2014**, *16*, 4740–4751.
- (54) Tatchen, J.; Gilka, N.; Marian, C. M. *Phys. Chem. Chem. Phys.* **2007**, *9*, 5209–5221.
- (55) Hirata, S.; Sakai, Y.; Masui, K.; Tanaka, H.; Lee, S. Y.; Nomura, H.; Nakamura, N.; Yasumatsu, M.; Nakanotani, H.; Zhang, Q.; Shizu, K.; Miyazaki, H.; Adachi, C. *Nat. Mater.* **2014**, *14*, 330–336.

Paper II

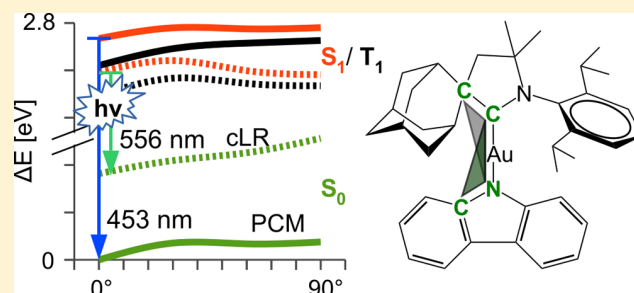
Rotationally Assisted Spin-State Inversion in Carbene–Metal–Amides Is an Artifact

Jelena Föller and Christel M. Marian*^{ib}

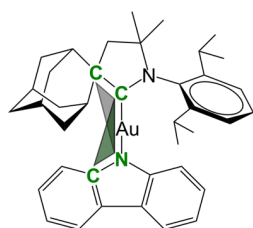
Institute of Theoretical and Computational Chemistry, Heinrich Heine University Düsseldorf, Universitätsstr. 1, D-40225 Düsseldorf, Germany

Supporting Information

ABSTRACT: High-level quantum chemical calculations, presented in this Letter, show that the unusual luminescence properties of the high-performance thermally activated delayed fluorescence emitter CMA1, observed recently by Di et al. [*Science* 2017, 356, 159–163], can be explained without resorting to the rotationally assisted spin-state inversion mechanism proposed by these authors. Multiconfiguration and relativistic effects lead to fast and efficient thermal equilibration of the excited singlet and triplet populations of this linear gold complex even for coplanar orientations of the ligands. The calculations predict $S_1 \leftrightarrow T_1$ intersystem crossing outcompetes the submicrosecond fluorescence by 2 orders of magnitude, thus quenching prompt fluorescence. The significant time- and environment-dependent shifts of the CMA1 luminescence, observed in experiment, are attributed to effects of (hindered) solvent reorganization.



In a recently published article,¹ Di et al. postulated a rotationally assisted spin-state inversion (RASI) mechanism to explain the luminescence properties of linear carbene–metal–amide (CMA) complexes. According to this mechanism, the S_1 state of the cyclic alkyl amino carbene–gold–carbazolate complex CMA1 (Chart 1) dives below the T_1 state upon

Chart 1. Chemical Structure of CMA1^a

^aAtomic labels displayed in green define the dihedral angle of the torsion potentials.

intramolecular rotation of the carbazolate (Cz) ligand about the N–Au–C axis. The intersection of the T_1 and S_1 potential energy surfaces (PESs) is supposed to enable fast and efficient triplet–singlet reverse intersystem crossing (RISC), thus enhancing the performance of the emitter in OLEDs. Attracted by this spectacular result—singlet–triplet energy splittings ΔE_{ST} are generally positive, not negative—we repeated the quantum chemical calculations on which Di et al. had based their interpretation, only to find that these authors had treated the T_1 state at the level of unrestricted density functional theory (UDFT), whereas the energy of the S_1 state energy had been

determined by time-dependent density functional theory (TDDFT).² The RASI mechanism is therefore highly debatable. Moreover, solvent–solute interactions which are known to be essential for the photophysical properties of CT states^{3–5} had not been included in this theoretical study.

In this Letter we will present evidence that a consistent quantum chemical treatment of the singlet and triplet excitations at the same level of theory places S_1 energetically above T_1 at all considered nuclear arrangements. Hence, the RASI described by Di et al.¹ is considered an artifact of the unbalanced quantum chemical treatment of these states. We offer alternative explanations for the experimentally observed efficient RISC and the large time- and environment-dependent shifts of the luminescence of CMA compounds. To this end, we set out for a comprehensive quantum chemical investigation of the photophysical properties of the gold complex CMA1 including spin–orbit coupling and solvent–solute interactions. Because closed-shell doubly excited configurations, which can contribute only to singlet states, have the ability to invert the singlet–triplet energy gap in principle, we go beyond linear response TDDFT and include higher excitations by means of a multireference configuration interaction (MRCI) expansion. We employ here a combined DFT/MRCI approach that had been designed particularly for a consistent treatment of singlet and triplet states in dimers and multichromophore systems.⁶

Received: October 12, 2017

Accepted: November 6, 2017

Potential Energy Surfaces of Isolated Molecules. The T_1 and S_1 states of CMA1 originate predominately from highest occupied molecular orbital–lowest unoccupied molecular orbital (HOMO–LUMO) excitations. The HOMO is a π -type orbital located mainly on the Cz ligand, whereas the LUMO is a π -type orbital centered on the cyclic alkyl amino carbene (CAAC) and containing additional contributions from the Au d_π orbital. In coplanar orientations of the CAAC and Cz ligands, also the nitrogen center of the Cz ligand contributes to the LUMO, whereas this is not the case for perpendicular orientations of the ligands (see the [Supporting Information](#)).

Compared to TDDFT, the DFT/MRCI treatment leads to an increase of the singlet and triplet excitation energies. This blue shift is not the only change, however. Analysis of the wave functions reveals that the S_1 expansion contains about 7.6% doubly excited configurations in the coplanar arrangement of the ligands, while the percentage of double excitations is about 6% for the T_1 wave function. For this reason, the ΔE_{ST} value of 0.11 eV, obtained from the DFT/MRCI calculations, is significantly smaller than the value of 0.27 eV, deduced from TDDFT energies. Moreover, the coplanar conformation becomes a true minimum of the S_1 PES at the DFT/MRCI level, whereas it constitutes a first-order saddle-point at the TDDFT level (see the [Supporting Information](#)). A second minimum well on the S_1 PES is found for an interligand dihedral angle of approximately 60° in vacuo. All-in-all, the DFT/MRCI torsion potential of the S_1 state is seen to be very flat so that the Cz ligand can rotate almost freely in the gas phase. The T_1 state is less affected by the MRCI treatment. In agreement with the UDFT results of Di et al.,¹ a shallow minimum is found for a coplanar orientation of the CAAC and Cz ligands. (Energy profiles of the T_1 and S_1 states for a torsion of the Cz ligand are displayed in the [Supporting Information](#).) We refrain from comparing our theoretical results for the isolated molecules with experimental findings because all measurements have been conducted either in solution or in the solid state.

Environment Effects on Absorption and Emission Properties. CMA1 is a very polar molecule in the electronic ground state S_0 with a static electric dipole moment of ~ 15 D (see [Figure 1a](#)

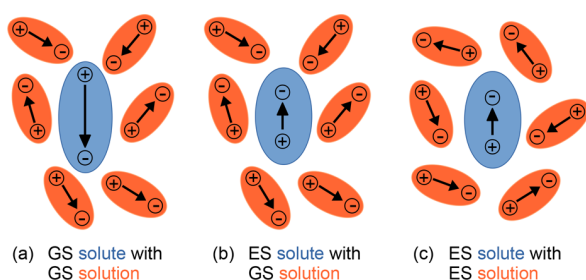


Figure 1. Schematic of the solute–solvent interactions between CMA1 and a polar environment with and without solvent reorientation.

for a schematic representation of the interaction of the dipole with a polar environment). Excitation of the molecule to S_1 or T_1 moves electronic charge density from the Cz ligand to the gold atom and the CAAC ligand. As a consequence, the direction of the electric dipole moment vector is reversed and its magnitude is reduced to ~ 5 D. This remarkable change of the dipole moment by about 20 D has tremendous impact on the absorption and emission properties.

Electronic excitation is an ultrafast process, much too fast for the solvent to reorganize instantaneously. At a time delay close to zero, the solute–solvent interaction, incorporated in the calculations through the PCM⁷ approximations, is adapted to the highly dipolar charge distribution in the electronic ground state of CMA1 ([Figure 1b](#)). Even moderately polar environments such as chlorobenzene (relative permittivity $\epsilon = 5.62$) or tetrahydrofuran ($\epsilon = 7.58$) lead to strong blue shifts of the vertical excitation energy with respect to the gas-phase value because of the unfavorable solvent–solute interactions of the much less polar S_1 state. Di et al. do not explicitly report the values of the absorption maxima in various environments. From the absorption spectrum shown in [Figure 1B](#) of their paper which was measured in solid tetrahydrofuran (THF), a value of approximately 365 nm for the maximum of the first absorption peak can be estimated. Our theoretically determined excitation wavelengths for $S_0 \rightarrow S_1$ absorption of 364 nm in chlorobenzene and 358 nm in THF match the experimental value very well.

Emission of a photon is accompanied by geometry relaxation in the excited state as well as solvent reorganization. Both processes contribute to the Stokes shift but occur on different time scales. Relaxation of the nuclear arrangement of the solute typically takes place at the subpicosecond time scale. Therefore, emission wavelengths measured in femtosecond time-resolved experiments at short delays after electronic excitation mainly reflect the solvent orientation adapted to the ground-state electron distribution ([Figure 1b](#)). The emission maximum (470 nm) reported by Di et al. for prompt fluorescence in chlorobenzene solution for a time delay of 0.5 ps is therefore best compared with the emission wavelength of 454 nm computed with the PCM for the same solvent. The vertical emission energy is blue-shifted with respect to the gas-phase value (2.03 eV) by 0.70 eV. To model the emission at longer time delays (nanosecond to microsecond time scale) in liquid solution, solvent reorganization has been taken into account in the calculations by employing the corrected linear response polarizable continuum model (cLR-PCM).⁸ In this approach, the relaxed density matrix of the excited state is used to calculate the solvent reaction field (for details, see the [Supporting Information](#)). Solvent reorganization ([Figure 1c](#)) leads to a red shift of the computed emission wavelength from 454 to 556 nm. The latter value is in excellent agreement with the wavelength of 550 nm, reported by Di et al. for delayed fluorescence in chlorobenzene solution at room temperature. The time required to fully achieve solvent reorganization depends on various parameters such as the viscosity and the temperature of the medium. In the solid state (frozen solutions, films, or crystalline environment), solvent reorientation is sterically hindered. For this reason, delayed luminescence in the solid state is expected to be blue-shifted with respect to luminescence in liquid solution, in agreement with the experimental findings.

[Figure 2](#) shows the dependence of the calculated radiative rate constants on the type of solvation model and on the interplanar angle of the ligands. Different solvent environments lead to changes of the fluorescence rate constant k_F by a factor of 2 at most. This solvent effect can be traced back mainly to the change in the emission energy which enters the expression for transition probability cubically. The variation of k_F with the interplanar angle is much more pronounced. Fluorescence is found to occur preferably for a coplanar orientation of the ligands ($k_F \sim 4 \times 10^7$ s⁻¹ without solvent reorganization, $\sim 2 \times 10^7$ s⁻¹ when solvent reorganization is included), with the rate

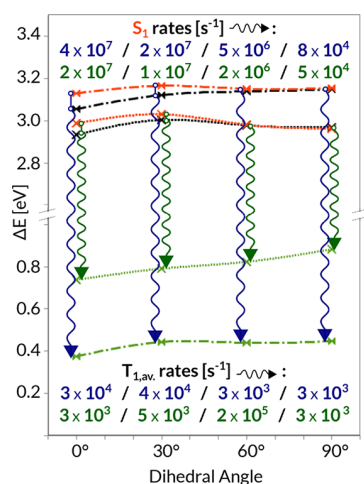


Figure 2. Rate constants for the S_1 and T_1 luminescence in chlorobenzene for the polarizable continuum model (PCM, blue) and for the corrected linear response approach (cLR, green). The T_1 rates are averages over the phosphorescence rates of the three triplet components. Dash-dotted lines correspond to potentials for a rotation of the Cz ligand in the PCM environment; dotted lines represent torsion potentials in the cLR model. S_1 potentials are shown in red, T_1 potentials in black, and S_0 potentials in green.

constants decreasing by almost 3 orders of magnitude when the ligands are oriented perpendicularly. The decrease of k_F upon internal rotation of the Cz ligand can be explained by the progressive electronic decoupling of the donor and acceptor moieties.

In contrast to k_F , the phosphorescence rate constant k_P does not vary significantly with increasing torsion angle if the solvent is not allowed to reorganize (which appears to be the appropriate model for the cryogenic temperature regime). Inspection of the DFT/MRSOCI wave functions reveals that the phosphorescence borrows its intensity mainly from the spin-allowed $S_2 \rightarrow S_0$ transition. The S_2 state interacts strongly with the T_1 state by virtue of the $\langle d_\sigma | \hat{H}_{SO} | d_\pi \rangle$ integral. Di et al. report phosphorescence to have a lifetime of $\sim 10 \mu\text{s}$ below 100 K (peak maximum $\sim 510 \text{ nm}$) in solid film. Our computed phosphorescence lifetime is $\sim 30 \mu\text{s}$. It should be noted, however, that the theoretical value is a pure radiative lifetime where nonradiative decay processes have not been taken into account.

In relaxed solution (cLR-PCM), k_P is seen to be generally 1 order of magnitude smaller, which is mainly caused by the larger energetic splitting between the T_1 state and the state arising from the $d_\sigma \rightarrow \text{LUMO}$ excitation (S_3 here). There is one exception, however. At a torsion angle of 60° , k_P reaches a value as high as $2 \times 10^5 \text{ s}^{-1}$. Here, T_1 and S_1 approach degeneracy

while exhibiting a small, but nonvanishing spin-orbit interaction. The S_1 and T_1 wave functions are therefore strongly mixed, and the phosphorescence borrows its intensity predominantly from the $S_1 \rightarrow S_0$ transition. Because the torsion potential is so flat, this point is easily reached under thermal conditions. At a torsion angle of 90° , the S_1 and T_1 wave functions are still strongly mixed, but the transition dipole moment of the spin-allowed emission is much smaller. Di et al. estimate phosphorescence to contribute to emission in solution at a rate of $3 \times 10^6 \text{ s}^{-1}$ at 300 K. Note again that the calculated values do not contain contributions from nonradiative decay processes.

Intersystem Crossing and Reverse Intersystem Crossing. For CMA1 to be an efficient OLED emitter, all bound electron-hole pairs (excitons) created in the OLED by electrical excitation need to be harvested. Because these excitons feature singlet or triplet total spin, it is mandatory that, in addition to S_1 , also the T_1 state of CMA1 contributes to the luminescence. As we have seen, phosphorescence occurs on the 10–100 μs time scale and is therefore mainly observed at cryogenic temperatures. At room temperature, RISC from T_1 to S_1 can be activated thermally and eventually leads to delayed fluorescence if the equilibration of the excited triplet and singlet populations is sufficiently fast.

The quantities that mainly determine the rate constants for ISC and RISC between S_1 and T_1 are their mutual electronic spin-orbit coupling matrix elements (SOCMEs), the overlaps of their vibrational wave functions, and their populations, which in turn depend on the temperature.⁹ Rate constants were determined for temperatures of 77 and 298 K, respectively. For the computation of the Franck-Condon factors, the imaginary frequency of the torsion potential ($6i \text{ cm}^{-1}$) in the S_1 state, obtained at the TDDFT level, was changed to a real positive value of 6 cm^{-1} because distortions of the nuclear frame along the corresponding normal coordinate yield a minimum for the coplanar arrangement of the ligands at the DFT/MRCI level (see Figure S5). The normal frequency of the T_1 torsion potential is of similar magnitude (9 cm^{-1}).

The calculated rate constants are collected in Table 1. The small adiabatic singlet-triplet energy splittings lead to very similar rate constants for ISC and RISC at room temperature. For conformations with coplanar orientation of the ligands [$\Delta E_{ST\text{adia}} = 793 \text{ cm}^{-1}$ (PCM) and $\Delta E_{ST\text{adia}} = 727 \text{ cm}^{-1}$ (cLR-PCM)], rate constants of the order of $1\text{--}2 \times 10^9 \text{ s}^{-1}$ are obtained. Spin-orbit interaction between T_1 and S_1 is brought about by many configurations with smaller coefficients in the wave function expansions. The sum over squared SOCMEs ranges here between 10 and 60 cm^{-2} , depending on the solvent environment and whether the S_1 minimum (ISC) or T_1 minimum geometry (RISC) has been employed. Irrespective of the particular solvent environment, ISC and RISC are seen

Table 1. Spin-Orbit Coupling Matrix Elements and Nonradiative Rate Constants Computed at the Coplanar S_1 (ISC from S_1 to T_1) and T_1 Minima (RISC from T_1 to S_1)

process	$\langle T_1 \hat{H}_{SO} S_1 \rangle$ [cm^{-1}]			$\Sigma(\text{SOCMEs})^2$	rate constant [s^{-1}]	
	x	y	z		298 K	77 K
ISC@ S_1 min	x	y	z		298 K	77 K
PCM	2.45	0.27	-1.81	9.4	1.3×10^9	3.3×10^9
cLR	-1.22	-3.58	0.17	14.3	2.0×10^9	5.4×10^9
RISC@ T_1 min	x	y	z		298 K	77 K
PCM	7.40	-1.95	-1.33	60.4	7.2×10^8	6.9×10^4
cLR	4.26	0.02	0.96	19.1	3.1×10^8	8.1×10^4

to proceed with time constants about 2 orders of magnitude greater than fluorescence (see also Figure 3). While the ISC

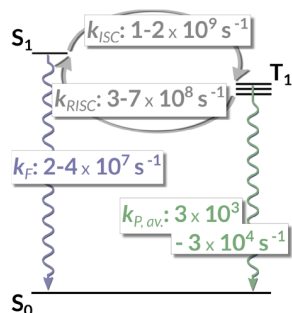


Figure 3. Radiative and nonradiative rates at the coplanar S_1 geometry at 298 K.

rate constants, computed by us for a coplanar orientation of the ligands, are smaller than the value of $2.5 \times 10^{11} \text{ s}^{-1}$, inferred from the experimental observations by Di et al.,¹ our results qualitatively support the statement of these authors, namely, that prompt fluorescence is outcompeted by ISC to triplets.

In the perpendicular orientation of the CAAC and Cz ligands, the S_1 and T_1 electronic states are almost degenerate [$\Delta E_{ST}^{adia} = 372 \text{ cm}^{-1}$ (PCM) and $\Delta E_{ST}^{adia} = 269 \text{ cm}^{-1}$ (cLR-PCM)] while the SOCMEs are of similar size as before. In contrast to ISC and RISC, fluorescence is very slow for a perpendicular arrangement of the ligands because of the nearly vanishing $\langle S_1 | \mu | S_0 \rangle$ transition dipole moment at this point. Delayed fluorescence will rather be emitted in nuclear arrangements close to the coplanar minimum configuration of the excited singlet state.

In summary, the results of our computational study offer an explanation of the experimental findings by Di et al.¹ without resorting to the rotationally assisted spin-state inversion mechanism postulated by these authors. In all nuclear arrangements investigated, the singlet–triplet splitting of the linear carbene–metal–amide CMA1 is positive, i.e., the S_1 PES does not intersect the T_1 PES upon internal rotation of the ligands. The significant time- and environment-dependent shifts of the CMA1 luminescence, observed in experiment, are attributed to effects of (hindered) solvent reorganization instead.

Upon electronic excitation of CMA1, electron density is transferred from the carbazolate ligand to the metal center and the CAAC ligand (mixed LMCT and LLCT transition). CMA1 therefore experiences a huge change of charge distribution when going from the very polar electronic ground state to the much less polar S_1 and T_1 states with reversed orientation of the electric dipole moment vector. At very short time delays after electronic excitation (subpicosecond regime), the environment is still adapted to the charge distribution of the solute in the electronic ground state which is unfavorable for the excited state. At longer time scales, a liquid polar solvent can stabilize the charge distribution in the excited state of the solute by reorientation, thus causing a red shift of the luminescence. In the solid state, the reorientation of the environment is hindered. A particularly large blue shift of the luminescence is expected for a (poly)crystalline sample because of the unfavorable interactions of the excited CMA1 molecules with the very polar neighboring ground-state molecules.

In agreement with the conclusions drawn by Di et al.,¹ our calculations find the equilibration of excited singlet and triplet populations of CMA1 to be very fast under thermal conditions, outcompeting prompt fluorescence. Fluorescence is therefore the time-determining step at room temperature. Depending on the environment, it proceeds with time constants varying between 300 and 500 ns, in excellent agreement with experimental observations. On the basis of our DFT/MRCI results, we predict fluorescence to be emitted primarily from molecular conformations with nearly coplanar orientations of the ligands while ISC and RISC are efficient at all interplanar angles. This explains why thermally activated delayed fluorescence (TADF) of CMA1 is efficient even in the solid state where internal rotation of the carbazolate ligand is hindered.

THEORETICAL METHODS

Geometry optimizations were performed using DFT (ground state) or TDDFT (excited states) employing the PBE0 hybrid functional^{10,11} and a scalar relativistic effective core potential¹² for the gold atom. Throughout, the def-SV(P) basis set¹³ was utilized on all nonmetal atoms and the def2-TZVP basis¹⁴ on gold. Two implicit solvent models were employed to mimic the experimental conditions, the polarizable continuum model (PCM)⁷ and the corrected linear response (cLR)⁸ approach. In TDDFT PCM optimizations, the solvent is adapted to the ground-state density and hence represents a polarizable but rigid environment, whereas the cLR approach yields emission energies and properties for a fully reorganized solvent environment.

Electronic excitation energies and fluorescence rate constants were determined at the DFT/MRCI level of theory employing the Hamiltonian parametrized for multichromophore systems.⁶ To take account of solvation effects in the DFT/MRCI treatment, the apparent charges obtained in the PCM and cLR calculations were introduced as point charges. Rate constants for spin-forbidden nonradiative transitions were computed in Condon approximation according to Fermi's golden rule.⁹ The electronic spin–orbit coupling matrix elements (SOCMEs) of the DFT/MRCI wave functions were evaluated using the SOC def2-ECP for gold and an atomic mean-field approximation of the Breit–Pauli spin–orbit operator on all other centers.^{15,16} The vibrational contributions to the intersystem crossing (ISC) and reverse intersystem crossing (RISC) rates were obtained by a time-correlation function approach.¹⁷ Multireference spin–orbit configuration interaction (MRSOCI)¹⁸ treats electron correlation and spin–orbit coupling on the same footing and implicitly includes SOC between all molecular singlet and triplet states. Phosphorescence rate constants of the individual triplet components can therefore be determined directly by evaluating the transition dipole moments of the multiplicity-mixed DFT/MRSOCI wave functions at the T_1 minimum.¹⁸ To gain more insight, the DFT/MRSOCI wave functions are subsequently projected onto the spin–orbit free DFT/MRCI wave functions.

ASSOCIATED CONTENT

Supporting Information

The Supporting Information is available free of charge on the ACS Publications website at DOI: 10.1021/acs.jpcllett.7b02701.

Further computational details, frontier molecular orbitals, space-filling representation of the crystal packing,

constrained minimum energy paths for internal rotation in varying environments, UDFT and TDDFT excitation energies, and Cartesian coordinates of all stationary points (PDF)

AUTHOR INFORMATION

Corresponding Author

*E-mail: Christel.Marian@hhu.de.

ORCID

Christel M. Marian: 0000-0001-7148-0900

Notes

The authors declare no competing financial interest.

ACKNOWLEDGMENTS

The authors thank Prof. Benedetta Mennucci and Dr. Stefano Caprasecca (Pisa) for valuable discussions. Financial support by the Deutsche Forschungsgemeinschaft through MA 1051/17-1 and INST 208/704-1 FUGG is gratefully acknowledged.

REFERENCES

- (1) Di, D.; Romanov, A. S.; Yang, L.; Richter, J. M.; Rivett, J. P. H.; Jones, S.; Thomas, T. H.; Abdi Jalebi, M.; Friend, R. H.; Linnolahti, M.; Bochmann, M.; Credgington, D. High-Performance Light-Emitting Diodes Based on Carbene-Metal-Amides. *Science* **2017**, *356*, 159–163.
- (2) Föller, J.; Marian, C. M. Re: High-Performance Light-Emitting Diodes Based on Carbene-Metal-Amides. <http://science.sciencemag.org/content/356/6334/159/tab-e-letters>.
- (3) Maroncelli, M. The Dynamics of Solvation in Polar Liquids. *J. Mol. Liq.* **1993**, *57*, 1–37.
- (4) Bagchi, B.; Jana, B. Solvation Dynamics in Dipolar Liquids. *Chem. Soc. Rev.* **2010**, *39*, 1936–1954.
- (5) Etherington, M. K.; Gibson, J.; Higginbotham, H. F.; Penfold, T. J.; Monkman, A. P. Revealing the Spin-Vibronic Coupling Mechanism of Thermally Activated Delayed Fluorescence. *Nat. Commun.* **2016**, *7*, 13680.
- (6) Lyskov, I.; Kleinschmidt, M.; Marian, C. M. Redesign of the DFT/MRCI Hamiltonian. *J. Chem. Phys.* **2016**, *144*, 034104.
- (7) Miertuš, S.; Scrocco, E.; Tomasi, J. Electrostatic Interaction of a Solute with a Continuum. A Direct Utilization of Ab Initio Molecular Potentials for the Prevision of Solvent Effects. *Chem. Phys.* **1981**, *55*, 117–129.
- (8) Caricato, M.; Mennucci, B.; Tomasi, J.; Ingrosso, F.; Cammi, R.; Corni, S.; Scalmani, G. Formation and Relaxation of Excited States in Solution: A New Time Dependent Polarizable Continuum Model Based on Time Dependent Density Functional Theory. *J. Chem. Phys.* **2006**, *124*, 124520.
- (9) Marian, C. M. Spin–Orbit Coupling and Intersystem Crossing in Molecules. *Wiley Interdisciplinary Reviews: Computational Molecular Science* **2012**, *2*, 187–203.
- (10) Perdew, J. P.; Burke, K.; Ernzerhof, M. Generalized Gradient Approximation Made Simple. *Phys. Rev. Lett.* **1996**, *77*, 3865–3868.
- (11) Adamo, C.; Barone, V. Toward Reliable Density Functional Methods without Adjustable Parameters: The PBE0Model. *J. Chem. Phys.* **1999**, *110*, 6158–6170.
- (12) Andrae, D.; Häußermann, U.; Dolg, M.; Stoll, H.; Preuß, H. Energy-Adjusted Ab Initio Pseudopotentials for the Second and Third Row Transition Elements. *Theor. Chim. Acta* **1990**, *77*, 123–141.
- (13) Schäfer, A.; Horn, H.; Ahlrichs, R. Fully Optimized Contracted Gaussian Basis Sets for Atoms Li to Kr. *J. Chem. Phys.* **1992**, *97*, 2571–2577.
- (14) Weigend, F.; Ahlrichs, R. Balanced Basis Sets of Split Valence, Triple Zeta Valence and Quadruple Zeta Valence Quality for H to Rn: Design and Assessment of Accuracy. *Phys. Chem. Chem. Phys.* **2005**, *7*, 3297–3305.
- (15) Kleinschmidt, M.; Tatchen, J.; Marian, C. M. Spin-Orbit Coupling of DFT/MRCI Wavefunctions: Method, Test Calculations, and Application to Thiophene. *J. Comput. Chem.* **2002**, *23*, 824–833.
- (16) Mitin, A. V.; van Wüllen, C. Two-Component Relativistic Density-Functional Calculations of the Dimers of the Halogens from Bromine through Element 117 Using Effective Core Potential and All-Electron Methods. *J. Chem. Phys.* **2006**, *124*, 064305.
- (17) Etinski, M.; Tatchen, J.; Marian, C. M. Thermal and Solvent Effects on the Triplet Formation in Cinnoline. *Phys. Chem. Chem. Phys.* **2014**, *16*, 4740–4751.
- (18) Kleinschmidt, M.; Tatchen, J.; Marian, C. M. SPOCK.CI: A Multireference Spin–Orbit Configuration Interaction Method for Large Molecules. *J. Chem. Phys.* **2006**, *124*, 124101.

Rotationally Assisted Spin-State Inversion in Carbene-Metal-Amides Is an Artifact

Supporting Information

Jelena Föller and Christel M. Marian*

*Institute of Theoretical and Computational Chemistry, Heinrich Heine University
Düsseldorf, Universitätsstr. 1, D-40225 Düsseldorf, Germany*

E-mail: Christel.Marian@hhu.de

November 3, 2017

Computational Details

DFT and TDDFT calculations *in vacuo*

DFT and TDDFT calculations *in vacuo* were performed with the TURBOMOLE program package version 7.0.¹ The ground state equilibrium geometry was optimized with DFT² and the S₁ and T₁ state equilibrium and constrained geometries were optimized with TDDFT.^{3,4} The PBE0 functional^{5,6} was employed using the def-SV(P) basis set⁷ for all non-metal atoms and the def2-TZVP⁸ basis together with the corresponding scalar relativistic def2-ECP⁹ for gold. For the constrained geometry optimizations the dihedral angle between the CAAC and the carbazole ligand was kept fixed. For the T₁ geometry with a 90° dihedral an additional optimization with UDFT was carried out (see Figure S6). Frequency analyses were carried out with SNF.¹⁰ Since the numerical SNF frequency analysis gave no imaginary frequencies

for the perpendicular T_1 geometry, which however looks like a saddle point on the torsional path, a second frequency analysis was carried out with Gaussian16.¹¹ Gaussian16 features analytical frequency calculations for TDDFT. The frequency analysis with Gaussian16 characterizes the perpendicular T_1 geometry as a saddle point (see Table S3).

DFT and TDDFT calculations in solution

For a more realistic representation of the experimental conditions, calculations employing the polarizable continuum model (PCM)¹² were performed with Gaussian16.¹¹ All structures optimized *in vacuo* were subsequently optimized with PCM chlorobenzene (and tetrahydrofuran, but only the ground state). The same functional and basis sets were used as *in vacuo*. In standard TDDFT PCM optimizations the solvent is adapted to the ground state density and not to the excited state density.¹³ The results obtained with this approach might be seen as corresponding to a polar but rigid environment where reorientation of the solvent is hindered. In order to obtain energies and properties for a fully reorganized solvent environment, the corrected linear response (cLR) approach by Mennucci et al. was employed.¹⁴ In this approach, the TDDFT equations are solved twice. In a first step, the explicit solvent contribution is left out. In a second step, the TDDFT equations are solved again. The relaxed density matrix is computed and used to calculate the free energies of the excited state in the presence of the reaction field determined by the relaxed density matrix. For the de-excitation energy, i.e. the emission energy, the energy of the ground state is calculated with the fixed inertial charges of the excited state, while the dynamic part adapts to the ground state.

DFT/MRCI calculations

DFT/MRCI calculations were performed on top of the DFT and TDDFT optimizations. DFT/MRCI is a semi-empirical multi-reference configuration interaction ansatz based on Kohn-Sham orbitals and orbital energies of a closed -shell BH-LYP functional^{15,16} determi-

nant.^{17,18} The reparametrized Hamiltonian by Lyskov et al. which is the standard Hamiltonian for multi-chromophore systems was employed.¹⁹ All orbitals with energies of less than $-3.0 E_h$ and more than $+3.0 E_h$ were frozen. At all geometries, 30 singlet and 30 triplet roots were calculated. In order to include the solvation effects into the DFT/MRCI calculations the apparent charges obtained in the PCM and cLR calculations were introduced as point charges in the subsequent DFT/MRCI calculations. The apparent charges are those point charges that are placed in the center of each cavity element. The output of these charges can be requested by setting the IOP(5/33=3) flag for the PCM and by setting the IOP(10/33=3) flag for the cLR calculations.

Spin–Orbit calculations

Since gold shows strong spin–orbit coupling effects, additional spin–orbit calculations were carried out. The spin–orbit coupling kit SPOCK developed in our laboratory^{20,21} was employed to calculate the spin–orbit coupling matrix elements (SOCMEs) of the spin-free DFT/MRCI wave functions. Herein, we employed the SOC def2-ECP for gold and an atomic mean-field approximation of the Breit-Pauli spin–orbit operator on all other centers.^{22–24} Multi-reference spin–orbit configuration interaction (MRSOCI)²⁵ wave functions were calculated in order to obtain the phosphorescence and fluorescence rates. Five roots, one for the ground state, three for the three components of the first triplet and one for the first excited singlet, were calculated at the T_1 and the S_1 geometries.

The vibrational contributions to the intersystem crossing (ISC) and reverse intersystem crossing (RISC) rates were calculated for 77 K and 298 K with the time-dependent branch of the VIBES program.^{26,27} The time correlation function was integrated over a time interval of 0.3 ps (298 K) or 4 ps (77 K) and grid of 95536 (298 K) or 90000 (77 K) points was chosen. The correlation function was damped with a Gaussian function of width 1 cm^{-1} . The electronic part of the rates, that is the SOCMEs and adiabatic energy gaps, were taken from the DFT/MRCI calculations in solution. The imaginary frequency of the planar S_1 geometry

was changed to a positive real value, since the DFT/MRCI calculations suggest that the structure actually represents a minimum on the potential surface (see Figure S5).

The results obtained for the T_1 and the S_1 geometries with MRCI and MRSOCI are very similar, which is why all figures showing results of these calculations, i.e. Figure 2, Figure 3 and Figure S4, are based on the results for the S_1 geometry.

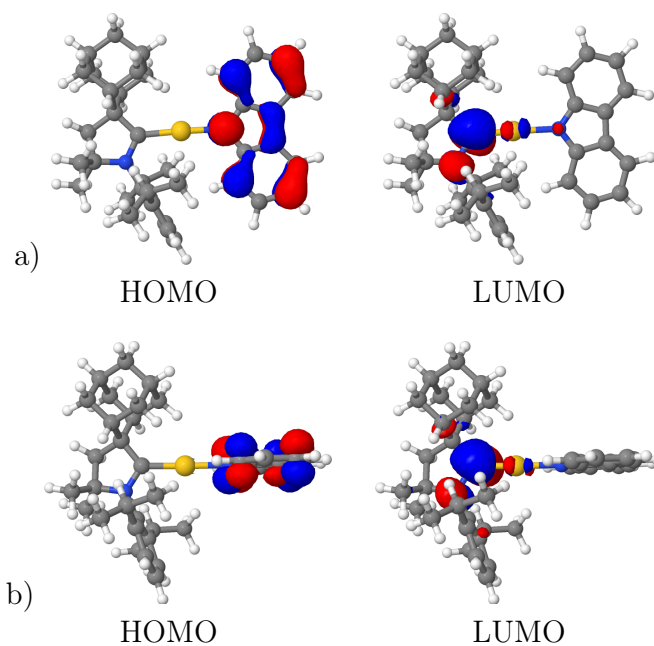


Figure S1: HOMO and LUMO orbitals of the a) planar and b) perpendicular S_1 geometry.

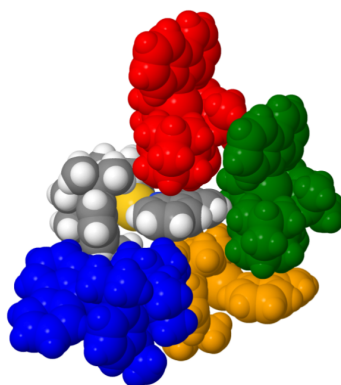


Figure S2: Five CMA1 molecules taken from the crystal structure (spacefill is 90% of the van der Waals radii). The carbazole ring is held in place by the adamantyl and isobutyl moieties of the surrounding molecules.

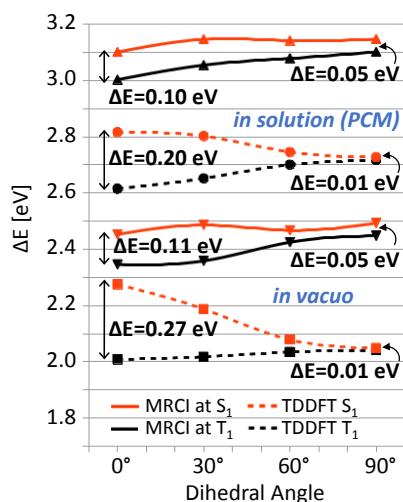


Figure S3: Constrained minimum energy torsion paths for the dihedral angle between the CAAC and the carbazole ligands of CMA1 *in vacuo* (bottom) and in solution (top). The dashed curves correspond to the energies of the TDDFT optimized geometries of the S_1 (red) and T_1 (black) states and the solid lines correspond to the DFT/MRCI energies of the S_1 and T_1 at their respective geometries.

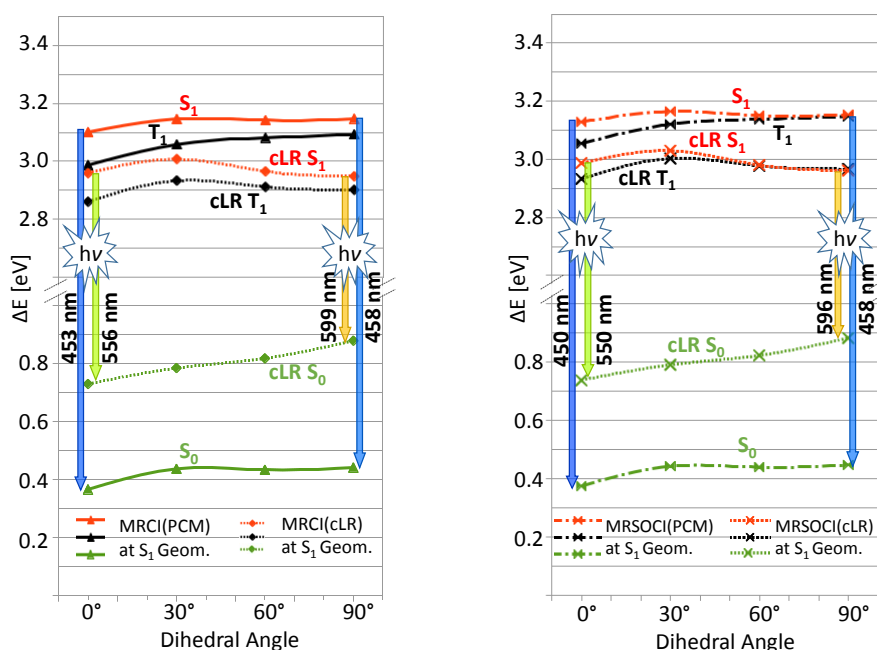


Figure S4: MR(SO)CI energies of the S_0 (green), T_1 (black) and S_1 (red) states at the optimized S_1 geometries for the PCM and the cLR approach. S_1 emission wavelengths given for the coplanar and the perpendicular orientation of the ligands demonstrate that there is a strong red shift of the energies due to solvation effects, whereas the effect of the rotation on the emission energies is comparatively small.

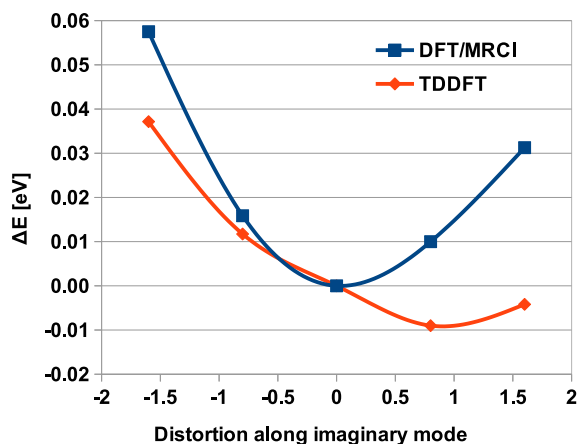


Figure S5: Distortion along the dimensionless normal coordinate with the imaginary frequency of the planar S_1 geometry. The imaginary frequency corresponds to a rotation of the carbazole ligand. The distortion profile verifies that the structure with a coplanar orientation of the ligands is a minimum structure at the DFT/MRCI level whereas the TDDFT calculations suggest a saddle point.

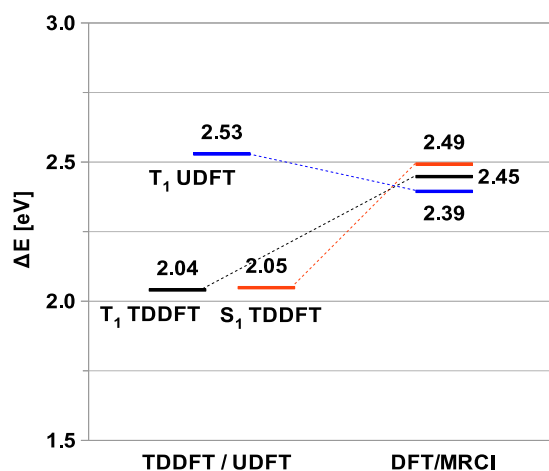


Figure S6: On the left, energies of the perpendicular geometries of the T_1 and S_1 optimized with TDDFT and of the T_1 optimized with UDFT. On the right, the DFT/MRCI energies of these geometries. While the UDFT energy lies about 0.5 eV above the TDDFT T_1 and S_1 , the DFT/MRCI energy of the UDFT geometry is quite close to the energies of the TDDFT calculations and lies even below the energy of the TDDFT T_1 geometry. This demonstrates that the energies obtained with different methods, i.e. UDFT and TDDFT, are not comparable, while calculations with the same method (DFT/MRCI) give reasonable results.

Table S1: DFT absolute energies, stability characterization and Cartesian coordinates of the optimized ground state geometries

S_0 in <i>vacuo</i>				S_0 in chlorobenzene				S_0 in THF			
-1756.627618 E_h				-1756.640833 E_h				-1756.641996 E_h			
Minimum				Minimum				Minimum			
Cartesian coordinates:				Cartesian coordinates:				Cartesian coordinates:			
Au	0.869	0.661	-0.183	Au	0.872	0.663	-0.167	Au	0.872	0.663	-0.167
N	4.662	1.068	-0.107	N	4.695	1.071	-0.097	N	4.697	1.072	-0.097
C	8.678	2.769	-0.042	C	8.717	2.766	-0.012	C	8.720	2.767	-0.011
C	-1.470	-5.316	2.527	C	-1.446	-5.322	2.526	C	-1.446	-5.324	2.520
N	-3.793	-2.188	-0.059	N	-3.795	-2.187	-0.032	N	-3.795	-2.187	-0.036
C	-4.703	4.038	-2.495	C	-4.706	4.008	-2.518	C	-4.707	4.013	-2.512
H	-4.451	3.045	-4.317	H	-4.461	2.992	-4.327	H	-4.462	3.000	-4.322
C	-2.773	7.201	0.467	C	-2.773	7.208	0.404	C	-2.773	7.206	0.416
H	-1.115	8.423	0.806	H	-1.116	8.437	0.725	H	-1.117	8.436	0.740
C	-6.628	-2.368	-0.057	C	-6.637	-2.367	-0.019	C	-6.638	-2.367	-0.023
C	-0.106	-7.579	2.624	C	-0.053	-7.570	2.600	C	-0.050	-7.570	2.592
H	0.508	-8.306	4.459	H	0.570	-8.309	4.427	H	0.571	-8.312	4.418
C	-5.269	3.520	2.166	C	-5.268	3.548	2.152	C	-5.268	3.544	2.158
H	-5.414	2.174	3.755	H	-5.412	2.223	3.757	H	-5.412	2.215	3.760
C	6.929	7.733	-0.010	C	6.968	7.733	0.036	C	6.969	7.734	0.043
H	6.270	9.694	0.006	H	6.308	9.694	0.058	H	6.310	9.695	0.068
C	-2.854	0.113	-0.223	C	-2.864	0.110	-0.206	C	-2.865	0.110	-0.206
C	6.387	-0.889	-0.094	C	6.416	-0.884	-0.086	C	6.418	-0.882	-0.088
C	-2.452	5.803	-2.045	C	-2.457	5.780	-2.093	C	-2.457	5.783	-2.083
H	-2.338	7.169	-3.622	H	-2.349	7.127	-3.686	H	-2.350	7.134	-3.673
H	-0.663	4.727	-2.059	H	-0.666	4.704	-2.096	H	-0.667	4.707	-2.088
C	0.669	-2.822	5.940	C	0.641	-2.844	5.987	C	0.636	-2.848	5.985
H	1.597	-1.623	4.507	H	1.551	-1.604	4.577	H	1.545	-1.604	4.578
H	1.988	-4.364	6.427	H	1.980	-4.376	6.454	H	1.976	-4.378	6.452
H	0.368	-1.671	7.656	H	0.313	-1.729	7.721	H	0.305	-1.736	7.720
C	-1.488	-5.660	-2.123	C	-1.487	-5.635	-2.128	C	-1.486	-5.633	-2.134
C	0.533	-8.893	0.444	C	0.594	-8.858	0.406	C	0.598	-8.856	0.397
H	1.599	-10.660	0.570	H	1.679	-10.614	0.514	H	1.684	-10.612	0.504
C	-2.986	5.261	2.607	C	-2.984	5.294	2.567	C	-2.985	5.289	2.576
H	-3.234	6.237	4.438	H	-3.232	6.293	4.385	H	-3.233	6.284	4.396
H	-1.221	4.155	2.751	H	-1.220	4.188	2.725	H	-1.220	4.183	2.732
C	-5.175	8.813	0.363	C	-5.176	8.818	0.282	C	-5.176	8.817	0.298
H	-5.420	9.870	2.149	H	-5.417	9.895	2.057	H	-5.417	9.891	2.075
H	-5.026	10.229	-1.167	H	-5.028	10.213	-1.267	H	-5.028	10.215	-1.248
C	6.037	3.282	-0.070	C	6.072	3.279	-0.047	C	6.074	3.280	-0.044
C	-2.231	-4.424	0.127	C	-2.223	-4.418	0.136	C	-2.223	-4.418	0.130
C	-5.016	2.019	-0.376	C	-5.021	2.017	-0.373	C	-5.022	2.018	-0.370
C	0.567	-3.618	-5.874	C	0.473	-3.550	-5.908	C	0.470	-3.544	-5.914
H	1.453	-2.185	-4.642	H	1.340	-2.096	-4.688	H	1.335	-2.088	-4.694
H	0.231	-2.752	-7.743	H	0.091	-2.694	-7.773	H	0.086	-2.688	-7.779
H	1.938	-5.171	-6.124	H	1.869	-5.078	-6.176	H	1.868	-5.070	-6.184
C	10.950	-1.624	-0.041	C	10.985	-1.632	-0.020	C	10.988	-1.630	-0.025
H	12.891	-0.907	-0.014	H	12.928	-0.920	0.016	H	12.931	-0.919	0.011
C	5.934	-3.500	-0.109	C	5.958	-3.498	-0.110	C	5.960	-3.497	-0.116
H	4.000	-4.236	-0.132	H	4.023	-4.229	-0.140	H	4.025	-4.228	-0.147
C	-7.111	5.663	-2.593	C	-7.115	5.632	-2.632	C	-7.116	5.637	-2.623

Continued on next page

Cartesian coordinates:			Cartesian coordinates:			Cartesian coordinates:					
H	-6.941	7.028	-4.165	H	-6.946	6.978	-4.221	H	-6.947	6.985	-4.209
H	-8.796	4.501	-3.007	H	-8.798	4.463	-3.028	H	-8.798	4.468	-3.020
C	-1.859	-3.864	4.976	C	-1.865	-3.908	4.993	C	-1.868	-3.913	4.988
H	-3.074	-2.226	4.570	H	-3.101	-2.282	4.608	H	-3.105	-2.288	4.604
C	-1.925	-4.587	-4.754	C	-1.982	-4.566	-4.750	C	-1.983	-4.563	-4.756
H	-3.188	-2.942	-4.582	H	-3.273	-2.945	-4.561	H	-3.276	-2.944	-4.566
C	8.905	0.054	-0.058	C	8.941	0.052	-0.038	C	8.943	0.053	-0.040
C	5.167	5.785	-0.050	C	5.203	5.786	-0.019	C	5.205	5.787	-0.014
H	3.140	6.193	-0.061	H	3.176	6.195	-0.036	H	3.178	6.197	-0.029
C	-7.303	0.293	-0.956	C	-7.311	0.288	-0.933	C	-7.311	0.290	-0.934
H	-9.085	0.935	-0.108	H	-9.089	0.934	-0.080	H	-9.089	0.934	-0.080
H	-7.592	0.254	-3.023	H	-7.608	0.235	-2.997	H	-7.608	0.240	-2.998
C	10.420	4.759	-0.002	C	10.461	4.758	0.042	C	10.464	4.759	0.046
H	12.452	4.369	0.019	H	12.494	4.368	0.069	H	12.496	4.370	0.071
C	-3.138	-5.440	7.039	C	-3.132	-5.532	7.025	C	-3.134	-5.541	7.018
H	-4.936	-6.280	6.403	H	-4.911	-6.390	6.360	H	-4.912	-6.400	6.350
H	-3.536	-4.250	8.706	H	-3.565	-4.369	8.702	H	-3.571	-4.380	8.696
H	-1.908	-6.999	7.680	H	-1.882	-7.080	7.653	H	-1.883	-7.088	7.645
C	7.994	-5.131	-0.090	C	8.015	-5.132	-0.090	C	8.018	-5.130	-0.098
H	7.664	-7.174	-0.100	H	7.681	-7.174	-0.107	H	7.684	-7.173	-0.118
C	-0.119	-7.910	-1.901	C	-0.087	-7.869	-1.930	C	-0.084	-7.866	-1.938
H	0.480	-8.898	-3.614	H	0.505	-8.844	-3.653	H	0.509	-8.840	-3.662
C	9.541	7.235	0.012	C	9.582	7.235	0.065	C	9.584	7.236	0.071
H	10.882	8.809	0.043	H	10.923	8.808	0.108	H	10.925	8.810	0.116
C	-3.164	-6.483	-6.555	C	-3.214	-6.483	-6.533	C	-3.214	-6.480	-6.539
H	-4.919	-7.290	-5.771	H	-4.942	-7.317	-5.718	H	-4.940	-7.316	-5.724
H	-1.883	-8.071	-6.992	H	-1.912	-8.046	-6.994	H	-1.910	-8.042	-7.001
H	-3.628	-5.556	-8.367	H	-3.727	-5.558	-8.332	H	-3.729	-5.555	-8.337
C	-7.646	5.187	2.092	C	-7.644	5.215	2.059	C	-7.644	5.211	2.068
H	-9.386	4.049	1.921	H	-9.382	4.074	1.907	H	-9.382	4.069	1.914
H	-7.799	6.208	3.908	H	-7.793	6.259	3.863	H	-7.793	6.251	3.874
C	-7.639	-2.939	2.589	C	-7.634	-2.916	2.636	C	-7.635	-2.921	2.631
H	-6.974	-4.795	3.257	H	-6.984	-4.774	3.313	H	-6.986	-4.780	3.305
H	-9.722	-3.001	2.515	H	-9.716	-2.963	2.566	H	-9.717	-2.967	2.560
H	-7.093	-1.494	3.982	H	-7.076	-1.464	4.017	H	-7.077	-1.471	4.014
C	-7.455	7.085	-0.089	C	-7.456	7.085	-0.145	C	-7.456	7.084	-0.133
H	-9.201	8.227	-0.172	H	-9.201	8.226	-0.241	H	-9.202	8.225	-0.226
C	10.488	-4.211	-0.058	C	10.516	-4.218	-0.047	C	10.518	-4.217	-0.055
H	12.070	-5.543	-0.045	H	12.094	-5.555	-0.033	H	12.096	-5.554	-0.043
C	-7.601	-4.400	-1.854	C	-7.616	-4.412	-1.796	C	-7.616	-4.409	-1.804
H	-7.028	-4.042	-3.820	H	-7.070	-4.062	-3.770	H	-7.071	-4.056	-3.777
H	-9.685	-4.399	-1.792	H	-9.699	-4.413	-1.709	H	-9.699	-4.410	-1.717
H	-6.945	-6.299	-1.299	H	-6.955	-6.307	-1.233	H	-6.955	-6.305	-1.244

Table S2: TDDFT absolute energies, stability characterization and Cartesian coordinates of the optimized S_1 geometries

$S_{1,\text{plan}}$ in <i>vacuo</i> -1756.544012 E_h Saddle point (i6.05 cm^{-1})				$S_{1,\text{plan}}$ in chlorobenzene -1756.537338 E_h Saddle point (i5.41 cm^{-1})				$S_{1,\text{perp}}$ in <i>vacuo</i> -1756.552324 E_h Minimum				$S_{1,\text{perp}}$ in chlorobenzene -1756.540585 E_h Minimum			
Cartesian coordinates:				Cartesian coordinates:				Cartesian coordinates:				Cartesian coordinates:			
Au	0.769	0.585	0.210	Au	0.772	0.619	0.119	Au	1.106	0.369	-0.226	Au	1.113	0.384	-0.229
N	4.829	0.811	0.449	N	4.753	0.825	0.185	N	5.083	0.508	-0.017	N	5.035	0.492	-0.077
C	8.892	2.357	0.146	C	8.844	2.314	0.006	C	9.283	0.525	-1.215	C	9.206	0.557	-1.366
C	-1.774	-5.574	2.350	C	-1.714	-5.604	2.237	C	-3.008	-4.875	3.017	C	-3.014	-4.787	3.070
N	-4.090	-2.099	0.267	N	-4.075	-2.108	0.248	N	-4.108	-1.839	-0.344	N	-4.078	-1.840	-0.381
C	-4.791	3.930	-2.830	C	-4.794	3.980	-2.725	C	-3.543	4.607	-2.862	C	-3.495	4.654	-2.784
H	-4.619	2.692	-4.504	H	-4.610	2.762	-4.413	H	-3.066	3.617	-4.639	H	-2.965	3.707	-4.570
C	-2.658	7.362	-0.348	C	-2.690	7.397	-0.199	C	-1.831	7.438	0.538	C	-1.896	7.425	0.720
H	-0.943	8.547	-0.203	H	-0.981	8.588	-0.030	H	-0.127	8.424	1.237	H	-0.219	8.406	1.487
C	-6.877	-2.033	0.512	C	-6.856	-2.047	0.505	C	-6.816	-1.483	-0.923	C	-6.771	-1.502	-1.045
C	-0.462	-7.863	2.136	C	-0.362	-7.866	1.966	C	-2.223	-7.305	3.702	C	-2.187	-7.181	3.831
H	0.216	-8.803	3.850	H	0.331	-8.839	3.655	H	-2.161	-7.822	5.704	H	-2.156	-7.650	5.845
C	-5.283	4.060	1.851	C	-5.309	4.054	1.950	C	-5.067	4.102	1.555	C	-5.137	4.048	1.577
H	-5.451	2.952	3.609	H	-5.480	2.925	3.694	H	-5.684	2.766	3.032	H	-5.790	2.680	3.008
C	7.307	7.329	1.002	C	7.255	7.359	0.061	C	8.075	0.019	-6.329	C	7.899	0.301	-6.475
H	6.733	9.288	1.325	H	6.682	9.343	0.078	H	7.649	-0.173	-8.341	H	7.432	0.210	-8.485
C	-3.009	0.223	-0.231	C	-2.994	0.255	-0.138	C	-2.662	0.373	-0.501	C	-2.646	0.383	-0.478
C	6.389	-1.159	-0.059	C	6.333	-1.209	0.106	C	6.528	0.786	2.108	C	6.531	0.667	2.036
C	-2.446	5.617	-2.649	C	-2.463	5.684	-2.521	C	-1.217	6.058	-1.929	C	-1.206	6.102	-1.758
H	-2.272	6.753	-4.396	H	-2.295	6.843	-4.254	H	-0.622	7.430	-3.391	H	-0.585	7.510	-3.175
H	-0.727	4.437	-2.511	H	-0.736	4.514	-2.396	H	0.383	4.743	-1.643	H	0.398	4.794	-1.457
C	0.498	-3.639	6.054	C	0.520	-3.754	6.010	C	-1.114	-2.221	6.437	C	-1.295	-2.055	6.532
H	1.469	-2.291	4.791	H	1.488	-2.364	4.792	H	0.245	-1.474	5.044	H	0.119	-1.302	5.198
H	1.748	-5.289	6.330	H	1.781	-5.402	6.250	H	-0.230	-3.845	7.409	H	-0.435	-3.653	7.566
H	0.246	-2.716	7.910	H	0.246	-2.886	7.890	H	-1.482	-0.739	7.863	H	-1.748	-0.562	7.921
C	-2.107	-5.440	-2.278	C	-2.044	-5.353	-2.384	C	-2.255	-5.975	-1.416	C	-2.141	-5.974	-1.322
C	0.020	-8.950	-0.203	C	0.144	-8.881	-0.401	C	-1.509	-9.072	1.897	C	-1.390	-8.974	2.083
H	1.035	-10.747	-0.330	H	1.196	-10.654	-0.575	H	-0.923	-10.971	2.468	H	-0.768	-10.843	2.712
C	-2.929	5.743	2.037	C	-2.960	5.744	2.164	C	-2.706	5.497	2.502	C	-2.812	5.436	2.617
H	-3.092	6.968	3.724	H	-3.129	6.949	3.866	H	-3.143	6.455	4.309	H	-3.303	6.351	4.432
H	-1.229	4.556	2.302	H	-1.254	4.562	2.412	H	-1.178	4.125	2.880	H	-1.283	4.067	3.007
C	-4.987	9.059	-0.641	C	-5.026	9.085	-0.479	C	-3.940	9.362	0.052	C	-4.003	9.345	0.215
H	-5.146	10.359	0.989	H	-5.199	10.361	1.168	H	-4.391	10.406	1.807	H	-4.511	10.349	1.978
H	-4.804	10.246	-2.353	H	-4.841	10.294	-2.175	H	-3.312	10.777	-1.355	H	-3.345	10.792	-1.145
C	6.277	2.933	0.531	C	6.220	2.944	0.105	C	6.712	0.369	-2.019	C	6.626	0.443	-2.128
C	-2.664	-4.387	0.124	C	-2.627	-4.371	0.044	C	-3.118	-4.225	0.420	C	-3.081	-4.199	0.454
C	-5.086	2.203	-0.456	C	-5.086	2.224	-0.372	C	-4.460	2.592	-0.926	C	-4.453	2.595	-0.916
C	-0.484	-3.080	-6.066	C	-0.458	-2.944	-6.159	C	0.848	-5.148	-4.886	C	1.016	-5.220	-4.770
H	0.505	-1.729	-4.823	H	0.576	-1.638	-4.902	H	1.849	-3.834	-3.615	H	2.000	-3.862	-3.530
H	-1.030	-2.077	-7.815	H	-1.026	-1.889	-7.871	H	1.081	-4.475	-6.851	H	1.272	-4.602	-6.749
H	0.858	-4.593	-6.589	H	0.851	-4.461	-6.750	H	1.769	-7.017	-4.740	H	1.944	-7.080	-4.559
C	10.853	-2.112	-0.700	C	10.818	-2.233	-0.057	C	10.935	1.069	3.417	C	10.965	0.880	3.251
H	12.837	-1.543	-0.831	H	12.810	-1.689	-0.125	H	12.959	1.083	2.999	H	12.978	0.912	2.786
C	5.725	-3.721	-0.359	C	5.661	-3.780	0.119	C	5.693	1.052	4.612	C	5.751	0.813	4.563
H	3.751	-4.315	-0.225	H	3.674	-4.349	0.177	H	3.677	1.045	5.040	H	3.744	0.789	5.039
C	-7.121	5.644	-3.118	C	-7.131	5.685	-3.005	C	-5.648	6.553	-3.354	C	-5.599	6.596	-3.295

Continued on next page

Cartesian coordinates:			Cartesian coordinates:			Cartesian coordinates:			Cartesian coordinates:						
H	-6.929	6.781	-4.863	H	-6.940	6.842	-4.736	H	-5.003	7.914	-4.805	H	-4.925	7.989	-4.702
H	-8.860	4.511	-3.341	H	-8.864	4.545	-3.243	H	-7.355	5.635	-4.127	H	-7.279	5.680	-4.129
C	-2.068	-4.415	4.958	C	-2.032	-4.520	4.875	C	-3.567	-2.989	5.108	C	-3.678	-2.876	5.108
H	-3.179	-2.674	4.739	H	-3.158	-2.784	4.696	H	-4.322	-1.276	4.210	H	-4.419	-1.188	4.152
C	-2.825	-4.163	-4.749	C	-2.787	-4.028	-4.822	C	-1.959	-5.294	-4.190	C	-1.800	-5.364	-4.108
H	-4.055	-2.550	-4.289	H	-4.001	-2.417	-4.313	H	-2.745	-3.385	-4.446	H	-2.602	-3.472	-4.430
C	8.969	-0.356	-0.244	C	8.920	-0.436	0.009	C	9.161	0.804	1.517	C	9.144	0.707	1.382
C	5.480	5.434	0.948	C	5.415	5.473	0.131	C	6.101	0.126	-4.590	C	5.959	0.324	-4.690
H	3.475	5.855	1.206	H	3.401	5.929	0.201	H	4.129	0.032	-5.183	H	3.973	0.262	-5.251
C	-7.450	0.506	-0.765	C	-7.438	0.515	-0.720	C	-6.796	1.206	-2.001	C	-6.743	1.204	-2.081
H	-9.204	1.336	-0.022	H	-9.201	1.319	0.033	H	-8.610	2.157	-1.644	H	-8.576	2.132	-1.765
H	-7.752	0.170	-2.804	H	-7.730	0.216	-2.766	H	-6.566	1.090	-4.073	H	-6.449	1.122	-4.146
C	10.677	4.271	0.207	C	10.643	4.212	-0.063	C	11.219	0.414	-2.966	C	11.110	0.530	-3.158
H	12.685	3.867	-0.077	H	12.661	3.774	-0.136	H	13.199	0.527	-2.383	H	13.100	0.612	-2.610
C	-3.458	-6.166	6.796	C	-3.418	-6.334	6.654	C	-5.498	-3.944	7.039	C	-5.675	-3.828	6.971
H	-5.281	-6.824	6.026	H	-5.235	-6.975	5.857	H	-7.274	-4.550	6.134	H	-7.405	-4.471	6.003
H	-3.836	-5.183	8.598	H	-3.808	-5.406	8.483	H	-5.957	-2.436	8.408	H	-6.210	-2.304	8.294
H	-2.323	-7.861	7.239	H	-2.274	-8.035	7.050	H	-4.762	-5.564	8.131	H	-4.961	-5.419	8.118
C	7.652	-5.448	-0.830	C	7.602	-5.560	0.049	C	7.504	1.321	6.503	C	7.608	0.990	6.426
H	7.184	-7.446	-1.072	H	7.135	-7.573	0.056	H	6.901	1.529	8.468	H	7.050	1.107	8.411
C	-0.777	-7.721	-2.386	C	-0.673	-7.608	-2.553	C	-1.495	-8.385	-0.636	C	-1.341	-8.348	-0.467
H	-0.356	-8.558	-4.230	H	-0.233	-8.389	-4.417	H	-0.854	-9.752	-2.051	H	-0.636	-9.732	-1.833
C	9.868	6.765	0.639	C	9.826	6.744	-0.035	C	10.595	0.154	-5.538	C	10.433	0.397	-5.727
H	11.262	8.290	0.685	H	11.231	8.258	-0.091	H	12.109	0.063	-6.941	H	11.918	0.374	-7.163
C	-4.267	-5.918	-6.543	C	-4.263	-5.746	-6.626	C	-3.323	-7.118	-5.973	C	-3.124	-7.245	-5.864
H	-5.919	-6.797	-5.623	H	-5.915	-6.618	-5.701	H	-5.339	-7.328	-5.492	H	-5.148	-7.448	-5.419
H	-3.055	-7.460	-7.258	H	-3.070	-7.290	-7.367	H	-2.463	-9.020	-5.925	H	-2.256	-9.140	-5.742
H	-4.943	-4.850	-8.205	H	-4.945	-4.650	-8.267	H	-3.198	-6.437	-7.944	H	-2.961	-6.619	-7.850
C	-7.588	5.810	1.585	C	-7.619	5.798	1.697	C	-7.148	6.080	1.112	C	-7.218	6.023	1.116
H	-9.375	4.733	1.569	H	-9.399	4.710	1.659	H	-8.948	5.186	0.553	H	-8.993	5.127	0.486
H	-7.685	7.067	3.254	H	-7.729	7.036	3.379	H	-7.535	7.089	2.903	H	-7.660	6.991	2.916
C	-7.753	-2.041	3.278	C	-7.729	-2.103	3.273	C	-8.516	-1.714	1.417	C	-8.548	-1.787	1.229
H	-7.387	-3.880	4.181	H	-7.369	-3.960	4.142	H	-8.379	-3.627	2.234	H	-8.412	-3.707	2.030
H	-9.811	-1.698	3.358	H	-9.784	-1.752	3.366	H	-10.507	-1.401	0.873	H	-10.522	-1.496	0.619
H	-6.811	-0.560	4.394	H	-6.775	-0.647	4.413	H	-8.038	-0.332	2.894	H	-8.143	-0.417	2.739
C	-7.354	7.400	-0.825	C	-7.383	7.416	-0.694	C	-6.291	7.971	-0.908	C	-6.318	7.961	-0.839
H	-9.045	8.609	-1.034	H	-9.079	8.618	-0.899	H	-7.820	9.347	-1.277	H	-7.845	9.334	-1.222
C	10.178	-4.668	-0.995	C	10.137	-4.807	-0.035	C	10.085	1.326	5.924	C	10.173	1.020	5.786
H	11.654	-6.068	-1.360	H	11.623	-6.243	-0.087	H	11.468	1.536	7.445	H	11.592	1.156	7.281
C	-8.171	-4.231	-0.837	C	-8.156	-4.217	-0.880	C	-7.815	-3.362	-2.879	C	-7.681	-3.358	-3.066
H	-7.730	-4.261	-2.869	H	-7.721	-4.206	-2.914	H	-6.778	-3.221	-4.677	H	-6.576	-3.188	-4.820
H	-10.239	-4.044	-0.634	H	-10.223	-4.035	-0.667	H	-9.824	-2.955	-3.271	H	-9.676	-2.957	-3.530
H	-7.611	-6.065	-0.016	H	-7.595	-6.066	-0.095	H	-7.688	-5.324	-2.184	H	-7.571	-5.329	-2.394

Table S3: TDDFT absolute energies, stability characterization and Cartesian coordinates of the optimized T_1 geometries

$T_{1,\text{plan}}$ <i>in vacuo</i> -1756.553791 E_h Minimum				$T_{1,\text{plan}}$ in chlorobenzene -1756.544714 E_h Minimum				$T_{1,\text{perp}}$ <i>in vacuo</i> -1756.552629 E_h Saddle point (i4.02 cm^{-1})				$T_{1,\text{perp}}$ in chlorobenzene -1756.540991 E_h Saddle point (i9.09 cm^{-1})			
Cartesian coordinates:				Cartesian coordinates:				Cartesian coordinates:				Cartesian coordinates:			
Au	0.925	0.770	-0.202	Au	0.870	0.716	0.330	Au	-0.940	-0.284	-0.200	Au	-0.925	-0.373	-0.180
N	4.854	1.269	0.056	N	4.709	1.263	0.705	N	-4.908	-0.481	0.019	N	-4.838	-0.528	0.016
C	8.857	3.000	0.043	C	8.626	3.111	1.222	C	-8.976	-0.958	1.536	C	-8.926	-0.792	1.525
C	-1.576	-5.338	2.398	C	-1.188	-5.671	2.362	C	3.189	4.864	3.193	C	3.113	4.807	3.198
N	-3.682	-2.365	-0.512	N	-3.707	-2.436	0.138	N	4.263	1.953	-0.285	N	4.239	1.931	-0.293
C	-4.721	4.250	-2.259	C	-4.665	3.519	-2.992	C	3.712	-4.430	-2.973	C	3.737	-4.461	-2.949
H	-4.155	3.578	-4.154	H	-4.190	2.288	-4.612	H	3.218	-3.400	-4.722	H	3.216	-3.437	-4.696
C	-3.433	7.004	1.384	C	-3.157	7.171	-0.369	C	2.039	-7.353	0.368	C	2.126	-7.399	0.410
H	-1.934	8.254	2.130	H	-1.589	8.519	-0.061	H	0.346	-8.367	1.054	H	0.449	-8.428	1.113
C	-6.432	-2.594	-0.928	C	-6.489	-2.612	0.171	C	6.966	1.629	-0.907	C	6.943	1.638	-0.930
C	-0.104	-7.509	2.739	C	0.380	-7.802	2.234	C	2.403	7.265	3.971	C	2.262	7.184	3.989
H	0.254	-8.194	4.658	H	1.032	-8.686	3.987	H	2.362	7.711	5.990	H	2.208	7.620	6.010
C	-5.833	2.969	2.127	C	-5.681	3.649	1.596	C	5.260	-4.022	1.447	C	5.327	-4.035	1.453
H	-6.068	1.381	3.459	H	-5.938	2.548	3.348	H	5.878	-2.718	2.952	H	5.950	-2.726	2.951
C	7.040	7.781	-1.285	C	6.566	7.962	1.584	C	-7.311	-1.505	6.516	C	-7.320	-1.329	6.526
H	6.376	9.667	-1.805	H	5.804	9.877	1.731	H	-6.704	-1.726	8.478	H	-6.734	-1.546	8.495
C	-2.796	0.126	-0.423	C	-2.811	0.040	-0.093	C	2.824	-0.258	-0.504	C	2.829	-0.301	-0.467
C	6.537	-0.597	0.660	C	6.497	-0.614	0.647	C	-6.539	-0.362	-1.985	C	-6.460	-0.376	-2.006
C	-2.692	6.046	-1.243	C	-2.535	5.442	-2.605	C	1.401	-5.918	-2.061	C	1.450	-5.973	-2.014
H	-2.458	7.654	-2.562	H	-2.294	6.576	-4.346	H	0.806	-7.259	-3.553	H	0.856	-7.321	-3.500
H	-0.861	5.043	-1.154	H	-0.728	4.444	-2.270	H	-0.206	-4.622	-1.734	H	-0.170	-4.694	-1.674
C	-0.243	-2.717	6.127	C	0.580	-3.599	6.263	C	1.348	2.085	6.542	C	1.361	2.009	6.582
H	0.793	-1.411	4.872	H	1.530	-2.156	5.092	H	-0.024	1.378	5.141	H	-0.037	1.291	5.212
H	1.095	-4.158	6.829	H	1.945	-5.135	6.642	H	0.470	3.672	7.578	H	0.488	3.582	7.644
H	-0.922	-1.624	7.772	H	0.087	-2.723	8.094	H	1.741	0.559	7.913	H	1.795	0.481	7.939
C	-0.922	-5.722	-2.176	C	-1.202	-5.513	-2.273	C	2.381	6.115	-1.191	C	2.269	6.058	-1.184
C	0.913	-8.810	0.695	C	1.145	-8.799	-0.071	C	1.661	9.091	2.236	C	1.466	8.997	2.262
H	2.030	-10.524	0.999	H	2.363	-10.471	-0.133	H	1.074	10.966	2.880	H	0.824	10.852	2.915
C	-3.764	4.729	3.144	C	-3.526	5.548	2.001	C	2.913	-5.454	2.372	C	3.003	-5.489	2.403
H	-4.285	5.377	5.063	H	-3.973	6.766	3.641	H	3.365	-6.450	4.155	H	3.484	-6.481	4.181
H	-1.965	3.683	3.311	H	-1.760	4.527	2.455	H	1.379	-4.100	2.790	H	1.457	-4.153	2.838
C	-5.921	8.474	1.195	C	-5.591	8.631	-0.943	C	4.156	-9.252	-0.178	C	4.255	-9.277	-0.158
H	-6.472	9.212	3.072	H	-6.054	9.919	0.638	H	4.625	-10.336	1.548	H	4.753	-10.354	1.565
H	-5.687	10.126	-0.066	H	-5.335	9.817	-2.646	H	3.528	-10.634	-1.616	H	3.625	-10.666	-1.588
C	6.216	3.428	-0.322	C	5.969	3.505	1.047	C	-6.346	-0.854	2.134	C	-6.304	-0.795	2.142
C	-2.074	-4.484	-0.095	C	-2.050	-4.556	0.086	C	3.273	4.306	0.573	C	3.209	4.264	0.573
C	-5.065	1.897	-0.530	C	-5.042	1.797	-0.627	C	4.630	-2.457	-0.994	C	4.659	-2.479	-0.981
C	1.501	-3.734	-5.743	C	0.440	-3.009	-5.962	C	-0.757	5.393	-4.654	C	-0.850	5.311	-4.664
H	2.195	-2.235	-4.470	H	1.257	-1.602	-4.656	H	-1.736	4.022	-3.426	H	-1.819	3.919	-3.451
H	1.352	-2.929	-7.665	H	-0.090	-2.027	-7.727	H	-1.008	4.798	-6.641	H	-1.084	4.719	-6.654
H	2.926	-5.260	-5.800	H	1.920	-4.408	-6.430	H	-1.687	7.249	-4.422	H	-1.806	7.153	-4.431
C	11.049	-1.270	1.265	C	11.045	-1.207	0.956	C	-11.038	-0.561	-2.944	C	-10.959	-0.403	-2.972
H	13.002	-0.593	1.303	H	12.964	-0.478	1.190	H	-13.013	-0.763	-2.369	H	-12.940	-0.505	-2.397
C	6.002	-3.142	1.186	C	6.087	-3.215	0.335	C	-5.932	-0.044	-4.548	C	-5.830	-0.147	-4.570
H	4.059	-3.843	1.139	H	4.175	-3.964	0.098	H	-3.963	0.139	-5.133	H	-3.853	-0.067	-5.158
C	-7.212	5.738	-2.444	C	-7.103	4.994	-3.567	C	5.826	-6.350	-3.524	C	5.863	-6.361	-3.524

Continued on next page

Cartesian coordinates:			Cartesian coordinates:			Cartesian coordinates:			Cartesian coordinates:						
H	-6.959	7.348	-3.755	H	-6.835	6.124	-5.307	H	5.181	-7.679	-5.004	H	5.216	-7.696	-4.997
H	-8.733	4.556	-3.250	H	-8.691	3.693	-3.944	H	7.523	-5.402	-4.285	H	7.543	-5.395	-4.299
C	-2.474	-3.929	4.733	C	-1.803	-4.590	4.948	C	3.781	2.908	5.209	C	3.761	2.862	5.207
H	-3.691	-2.377	4.086	H	-3.053	-2.957	4.651	H	4.530	1.231	4.241	H	4.519	1.195	4.229
C	-1.077	-4.721	-4.863	C	-1.876	-4.284	-4.780	C	2.057	5.529	-3.984	C	1.960	5.486	-3.982
H	-2.368	-3.092	-4.842	H	-3.261	-2.783	-4.383	H	2.850	3.635	-4.315	H	2.791	3.611	-4.328
C	9.068	0.336	0.693	C	8.975	0.390	0.958	C	-9.103	-0.631	-1.190	C	-9.028	-0.515	-1.211
C	5.299	5.828	-0.988	C	4.921	5.932	1.226	C	-5.507	-1.133	4.635	C	-5.489	-1.070	4.647
H	3.277	6.129	-1.261	H	2.879	6.206	1.088	H	-3.494	-1.056	5.069	H	-3.475	-1.083	5.094
C	-7.096	0.130	-1.668	C	-7.182	-0.131	-1.160	C	6.952	-1.032	-2.051	C	6.950	-1.027	-2.066
H	-9.047	0.590	-1.116	H	-9.076	0.515	-0.597	H	8.773	-1.982	-1.730	H	8.787	-1.951	-1.765
H	-6.995	0.298	-3.747	H	-7.246	-0.487	-3.217	H	6.706	-0.867	-4.118	H	6.678	-0.868	-4.130
C	10.557	4.962	-0.257	C	10.233	5.144	1.578	C	-10.742	-1.325	3.426	C	-10.721	-1.046	3.410
H	12.586	4.672	0.013	H	12.277	4.883	1.721	H	-12.763	-1.408	3.002	H	-12.741	-1.045	2.974
C	-3.994	-5.596	6.546	C	-3.167	-6.496	6.645	C	5.735	3.801	7.146	C	5.728	3.786	7.115
H	-5.581	-6.551	5.590	H	-4.860	-7.290	5.722	H	7.494	4.453	6.240	H	7.470	4.451	6.185
H	-4.780	-4.444	8.100	H	-3.770	-5.588	8.426	H	6.224	2.244	8.449	H	6.248	2.240	8.419
H	-2.803	-7.074	7.416	H	-1.922	-8.095	7.150	H	5.005	5.372	8.311	H	4.993	5.355	8.280
C	8.023	-4.731	1.758	C	8.196	-4.799	0.339	C	-7.905	0.019	-6.291	C	-7.797	-0.040	-6.323
H	7.658	-6.721	2.174	H	7.936	-6.835	0.101	H	-7.482	0.265	-8.298	H	-7.359	0.138	-8.334
C	0.530	-7.890	-1.734	C	0.377	-7.635	-2.300	C	1.620	8.493	-0.319	C	1.441	8.411	-0.298
H	1.397	-8.869	-3.336	H	1.021	-8.396	-4.112	H	0.957	9.905	-1.677	H	0.737	9.811	-1.648
C	9.627	7.363	-0.926	C	9.176	7.579	1.758	C	-9.888	-1.598	5.930	C	-9.894	-1.312	5.923
H	10.954	8.929	-1.168	H	10.424	9.202	2.038	H	-11.266	-1.890	7.442	H	-11.292	-1.514	7.431
C	-2.080	-6.681	-6.742	C	-3.055	-6.144	-6.660	C	3.393	7.422	-5.717	C	3.268	7.415	-5.697
H	-3.899	-7.494	-6.133	H	-4.688	-7.152	-5.846	H	5.412	7.627	-5.249	H	5.285	7.643	-5.230
H	-0.737	-8.260	-6.990	H	-1.678	-7.582	-7.286	H	2.523	9.316	-5.595	H	2.370	9.294	-5.555
H	-2.357	-5.810	-8.619	H	-3.707	-5.129	-8.364	H	3.253	6.807	-7.708	H	3.133	6.816	-7.693
C	-8.305	4.486	1.987	C	-8.097	5.168	1.051	C	7.350	-5.976	0.944	C	7.430	-5.970	0.928
H	-9.905	3.289	1.384	H	-9.758	3.921	0.861	H	9.142	-5.058	0.398	H	9.205	-5.033	0.360
H	-8.793	5.190	3.895	H	-8.495	6.428	2.672	H	7.753	-7.027	2.708	H	7.860	-7.015	2.688
C	-7.865	-3.463	1.440	C	-7.574	-2.694	2.863	C	8.694	1.813	1.416	C	8.683	1.846	1.381
H	-7.250	-5.370	2.011	H	-7.135	-4.503	3.796	H	8.550	3.701	2.288	H	8.530	3.736	2.247
H	-9.910	-3.555	1.031	H	-9.651	-2.508	2.793	H	10.680	1.533	0.840	H	10.667	1.580	0.792
H	-7.598	-2.176	3.051	H	-6.827	-1.150	4.042	H	8.246	0.386	2.860	H	8.256	0.422	2.834
C	-7.986	6.721	0.172	C	-7.753	6.747	-1.352	C	6.494	-7.823	-1.116	C	6.569	-7.826	-1.122
H	-9.787	7.769	0.023	H	-9.517	7.783	-1.772	H	8.029	-9.179	-1.528	H	8.112	-9.168	-1.549
C	10.505	-3.818	1.801	C	10.632	-3.818	0.643	C	-10.419	-0.229	-5.509	C	-10.320	-0.159	-5.542
H	12.055	-5.107	2.256	H	12.252	-5.102	0.639	H	-11.932	-0.171	-6.915	H	-11.826	-0.069	-6.953
C	-7.110	-4.435	-3.051	C	-7.489	-4.908	-1.259	C	7.926	3.563	-2.829	C	7.868	3.576	-2.865
H	-6.283	-3.856	-4.869	H	-6.899	-4.896	-3.253	H	6.868	3.459	-4.616	H	6.799	3.457	-4.645
H	-9.183	-4.493	-3.287	H	-9.575	-4.902	-1.208	H	9.933	3.183	-3.256	H	9.876	3.215	-3.303
H	-6.468	-6.371	-2.610	H	-6.837	-6.689	-0.389	H	7.793	5.507	-2.084	H	7.721	5.521	-2.125

References

- (1) TURBOMOLE V7.0 2015, a development of University of Karlsruhe and Forschungszentrum Karlsruhe GmbH, 1989-2007, TURBOMOLE GmbH, since 2007; available from <http://www.turbomole.com>.
- (2) von Arnim, M.; Ahlrichs, R. *J. Comput. Chem.* **1998**, *19*, 1746–1757.
- (3) Bauernschmitt, R.; Ahlrichs, R. *Chem. Phys. Lett.* **1996**, *256*, 454–464.
- (4) Furche, F.; Ahlrichs, R. *J. Chem. Phys.* **2002**, *117*, 7433–7447.
- (5) Perdew, J. P.; Burke, K.; Ernzerhof, M. *Phys. Rev. Lett.* **1996**, *77*, 3865–3868.
- (6) Adamo, C.; Barone, V. *J. Chem. Phys.* **1999**, *110*, 6158–6170.
- (7) Schäfer, A.; Horn, H.; Ahlrichs, R. *J. Chem. Phys.* **1992**, *97*, 2571–2577.
- (8) Weigend, F.; Ahlrichs, R. *Phys. Chem. Chem. Phys.* **2005**, *7*, 3297–3305.
- (9) Andrae, D.; Häußermann, U.; Dolg, M.; Stoll, H.; Preuß, H. *Theor. Chim. Acta* **1990**, *77*, 123–141.
- (10) Weymuth, T.; Haag, M. P.; Kiewisch, K.; Lubner, S.; Schenk, S.; Jacob, C. R.; Herrmann, C.; Neugebauer, J.; Reiher, M. *J. Comput. Chem.* **2012**, *33*, 2186–2198.
- (11) Frisch, M. J. et al. Gaussian 16, Revision A.03. 2016; Gaussian Inc. Wallingford CT.
- (12) Miertuš, S.; Scrocco, E.; Tomasi, J. *Chem. Phys.* **1981**, *55*, 117 – 129.
- (13) Scalmani, G.; Frisch, M. J.; Mennucci, B.; Tomasi, J.; Cammi, R.; Barone, V. *J. Chem. Phys.* **2006**, *124*, 094107.
- (14) Caricato, M.; Mennucci, B.; Tomasi, J.; Ingrosso, F.; Cammi, R.; Corni, S.; Scalmani, G. *J. Chem. Phys.* **2006**, *124*, 124520.

- (15) Lee, C.; Yang, W.; Parr, R. G. *Phys. Rev. B* **1988**, *37*, 785–789.
- (16) Becke, A. D. *J. Chem. Phys.* **1993**, *98*, 1372–1377.
- (17) Grimme, S.; Waletzke, M. *J. Chem. Phys.* **1999**, *111*, 5645–5655.
- (18) Kleinschmidt, M.; Marian, C. M.; Waletzke, M.; Grimme, S. *J. Chem. Phys.* **2009**, *130*, 044708.
- (19) Lyskov, I.; Kleinschmidt, M.; Marian, C. M. *J. Chem. Phys.* **2016**, *144*, 034104.
- (20) Kleinschmidt, M.; Tatchen, J.; Marian, C. M. *J. Comput. Chem.* **2002**, *23*, 824–833.
- (21) Kleinschmidt, M.; Marian, C. M. *Chem. Phys.* **2005**, *311*, 71–79.
- (22) Mitin, A. V.; van Wüllen, C. *J. Chem. Phys.* **2006**, *124*, 064305.
- (23) Hess, B. A.; Marian, C. M.; Wahlgren, U.; Gropen, O. *Chem. Phys. Lett.* **1996**, *251*, 365–371.
- (24) AMFI is an atomic spin-orbit integral program written by B. Schimmelpfennig, University of Stockholm, 1996.
- (25) Kleinschmidt, M.; Tatchen, J.; Marian, C. M. *J. Chem. Phys.* **2006**, *124*, 124101.
- (26) Etinski, M.; Tatchen, J.; Marian, C. M. *J. Chem. Phys.* **2011**, *134*, 154105.
- (27) Etinski, M.; Tatchen, J.; Marian, C. M. *Phys. Chem. Chem. Phys.* **2014**, *16*, 4740–4751.

Paper III

Computer-Aided Design of Luminescent Linear NHC Cu(I) Pyridine Complexes

Jelena Föller and Christel M. Marian*

*Institut für Theoretische Chemie und Computerchemie, Heinrich-Heine-Universität
Düsseldorf, Universitätsstr. 1, D-40225 Düsseldorf, Germany*

E-mail: Christel.Marian@hhu.de

Abstract

Multi-reference configuration interaction methods including spin-orbit interactions have been employed to investigate the photophysical properties of various linear NHC-Cu(I)-pyridine complexes with the aim of designing performant thermally activated delayed fluorescence (TADF) emitters for use in organic light emitting diodes (OLEDs). Our theoretical results indicate that this structural motif is very favorable for generating excited triplet states with high quantum yield. The first excited singlet (S_{MLCT}) and the corresponding triplet state (T_{MLCT}) are characterized by $d_{\sigma} \rightarrow \pi_{\text{Py}}$ metal-to-ligand charge-transfer (MLCT) excitations. Efficient intersystem crossing (ISC) and reverse ISC (RISC) between these states is mediated by a near-degenerate second triplet state ($T_{\text{MLCT/LC}}$) with large $d_{\pi} \rightarrow \pi_{\text{Py}}$ contributions. Spin-vibronic coupling is strong and is expected to play a major role in the (R)ISC processes. The calculations reveal, however, that the luminescence is effectively quenched by locally excited triplet states if the NHC ligand carries two diisopropylphenyl (DIPP) substituents. By replacing DIPP with 1-adamantyl residues, this quenching process is suppressed and TADF in the UV spectral regime is predicted to proceed at a rate of about $1/\mu\text{s}$. Introduction of $+I$ substituents on the carbene and $-M$ substituents on the pyridine allows tuning of the emission wavelength from the UV to the blue-green or green spectral region.

Introduction

In the ever-growing field of OLED emitters, Cu(I) complexes have gained increased attention, since they can be considered a cheaper alternative to phosphorescent transition metal complexes with, e.g., iridium or platinum. Besides, several Cu(I) complexes undergo thermally activated delayed fluorescence (TADF), a mechanism where the lowest singlet can be repopulated at higher ambient temperature via reverse intersystem crossing (RISC) from the lowest triplet. This allows for efficient harvesting of all singlet and triplet excitons and short emission lifetimes. The vast majority of Cu(I) complexes investigated in this area are trigonal and tetrahedral complexes, whereas reports of mononuclear, linear copper complexes that show luminescence are scarce.¹⁻⁹ However, a few examples have been presented in literature in the course of last year where one or two of the ligands are either cyclic amino(alkyl) carbenes (CAACs) or diamido carbenes (DACs).¹⁰⁻¹⁴ It seems therefore reasonable to search for luminescent linear N-heterocyclic carbene (NHC) complexes as well.

In this work, the photophysical properties of various linear NHC-Cu(I)-pyridine complexes (Chart 1) have been investigated by means of advanced quantum chemical methods. Experimental results indicate that compounds **1-3**, where the NHC ligand is the widely-used 1,3-bis(2,6-diisopropylphenyl)imidazol-2-ylidene (IPr) ligand, are only very weakly luminescent in the solid state and not luminescent at all in solution.[?] The aim of the present work is to (1) find the source of the problem and (2) to fathom out the possibilities to solve it by systematically modifying the chemical composition of the complexes while retaining the linear NHC-Cu-pyridine coordination.

Methods and Computational Details

For all calculations, the counter ion was omitted. The same methods, basis sets and effective core potentials as in a recently published theoretical article on a trigonal coordinated cationic NHC-copper(I)-phenantroline-complex¹⁵ were employed. The TURBOMOLE program pack-

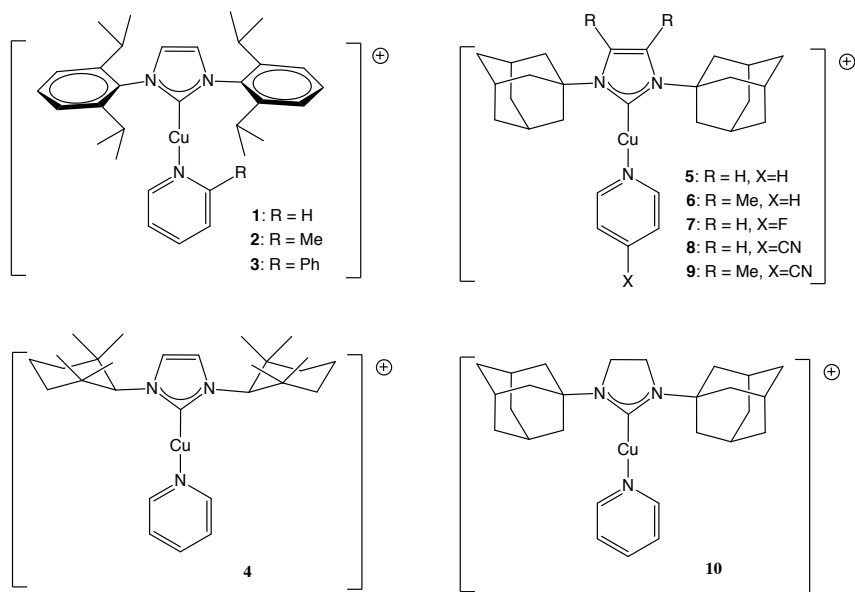


Chart 1: Chemical structures of copper (I) complexes studied in this work.

age was used for all geometry optimizations.^{16,17} All calculations were done *in vacuo*. The equilibrium geometries of the electronic ground states were determined with Kohn Sham density functional theory (DFT)¹⁸ employing the PBE0 functional.^{19,20} For the excited state geometries, time dependent DFT (TDDFT)²¹ calculations were performed. Some excited states, in particular low-lying triplet states, are prone to instabilities of the full linear response TDDFT.²² In these cases, the Tamm-Dancoff approximation (TDA) to TDDFT²³ was employed for the geometry optimization. All nonmetal atoms were represented by the def-SV(P) basis set²⁴ from the Turbomole basis set library, whereas for the Cu ion a relativistic ECP²⁵ and the associated cc-pVDZ-PP basis set²⁶ were employed. The obtained geometries were verified as equilibrium geometries by employing either the AOFORCE module of the TURBOMOLE package^{27,28} or the SNF program.²⁹ Spin-free electronic excitation energies and oscillator strengths were calculated with the DFT/MRCI method,^{30,31} a semi-empirical multireference configuration interaction ansatz based on Kohn-Sham orbitals and orbital energies of a closed shell BH-LYP functional^{32,33} determinant. For the construction of the two-electron integrals, the auxiliary basis sets from the Turbomole library^{34,35} were used in the resolution-of-the-identity approximation. All orbitals with energies of less than

-3.0 hartree and more than +2.0 hartree were frozen. At all geometries, 21 singlet and 20 triplet roots were calculated. Electronic spin-orbit coupling matrix elements (SOCMEs) and phosphorescence lifetimes were obtained with the SPOCK program developed in our laboratory.³⁶⁻³⁸ Because zero-field splitting is small for these complexes, the individual phosphorescence rates of the three triplet components were averaged. Intersystem crossing (ISC) rate constants at room temperature (298 K) were obtained in the Condon approximation. The Franck-Condon weighted density of states needed — in addition to the SOCMEs — for the computation of the ISC rate constants was calculated via a Fourier transformation ansatz employing the VIBES program developed in our laboratory.^{39,40} The time correlation function was damped with a Gaussian function of 10 cm^{-1} width at half maximum.

Results and Discussion

IPr-Cu(I)-pyridine

Optimized geometries

According to DFT/MRCI calculations at the optimized ground-state minimum, the S_1 state of compound **1** has MLCT character where Cu d_σ electron density is transferred to the pyridine ligand. Below the S_1 state, four triplet states are located. The T_1 and T_2 states are local excitations on the diisopropylphenyl (DIPP) moieties of the IPr ligand ($T_{LC,DIPP}$). The T_3 state has the same MLCT character as the S_1 state. The T_4 state has MLCT (coming from a Cu d_π orbital) and LC (mainly localized on the pyridine ligand) contributions which is why it is denominated $T_{MLCT/LC}$. In addition, inter-ligand charge transfer (ILCT) character is mixed in (see Figure 1).

Starting from the S_0 geometry TDDFT optimization of the T_1 state yields a $T_{LC,DIPP}$ minimum that is localized on one of the DIPP phenyl rings. The $T_{MLCT/LC}$ minimum could be optimized starting from the S_1 geometry, optimizing the T_1 at the S_1 geometry. The

$T_{\text{MLCT/LC}}$ has stronger local contributions and less ILCT character at its minimum structure than at the S_0 geometry. Besides, the Cu d_π contributions are slightly decreased, while the d_σ contributions are increased (see Figure 2). TDDFT/TDA optimization of the T_1 state leads to the T_{MLCT} minimum structure. All minimum nuclear arrangements show a coplanar orientation of the NHC core and the pyridine ring.

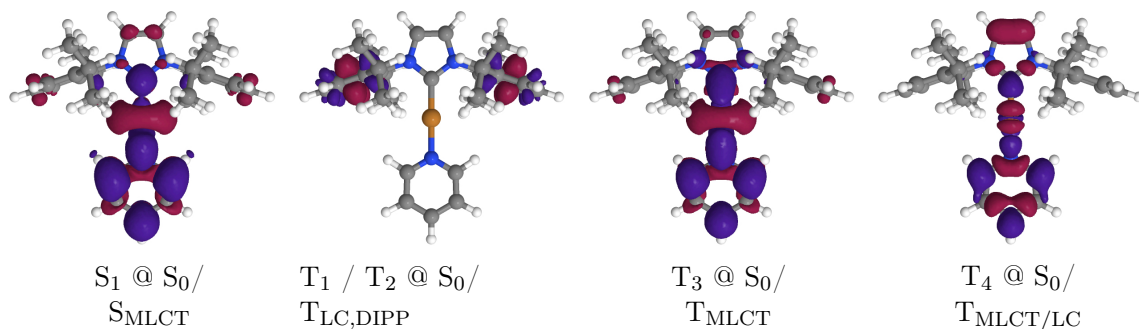


Figure 1: DFT/MRCI difference densities for S_1 and T_1 to T_4 at the IPr-Cu(I)-pyridine S_0 geometry. Areas losing electron density upon electronic excitation from the ground state are shown in red, areas gaining electron density in blue.

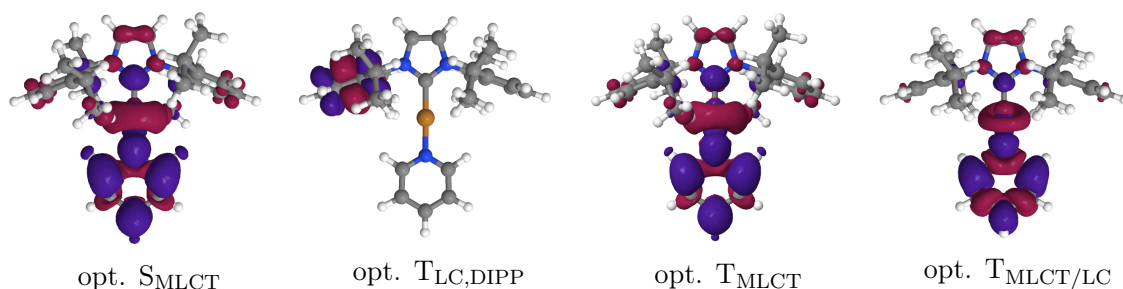


Figure 2: DFT/MRCI difference densities for the optimized excited states of IPr-Cu(I)-pyridine. For color codes, see Fig. 1.

LIP between the S_0 and S_1 minimum

Linearly interpolated paths (LIPs) between the S_0 and S_1 minimum were calculated in order to gain insight into the relaxation paths after photoexcitation (see Figure 3). Because the ordering of states changes between the S_0 and the S_1 minimum, several crossings and avoided crossings may occur. The reaction coordinate $\text{RC}=0.0$ corresponds to the DFT optimized S_0 and the $\text{RC}=1.0$ to the TDDFT optimized S_1 minimum. At each of the points DFT/MRCI

calculations were carried out and the energies relative to the S_0 energy at the S_0 minimum were plotted. After photoexcitation into one of the bright singlets (e.g. the S_4) internal conversion into the S_1 is assumed to be fast. Since the S_1 state is an MLCT state, the geometry relaxation is supposedly faster than the fluorescence and the S_1 will therefore start to relax toward its minimum structure. As can be seen from Figure 3, the S_1 surface (blue squares) crosses at about $RC=0.2$ with the $T_{MLCT/LC}$ (red triangles) surface. Since both the S_1 and the $T_{MLCT/LC}$ have notable Cu d contributions, but from different spatial orbitals, spin-orbit coupling between these two states is expected to be large. And indeed, the largest SOCME at the intersection between the S_1 and the triplet amounts to 235 cm^{-1} . This strikingly large spin-orbit coupling allows for efficient ISC into the $T_{MLCT/LC}$ and is one of the attractive features of this complex. A second crossing occurs at $RC=0.6$ with the $T_{LC,DIPP}$ (orange triangles) states. The SOCMEs for these triplets are significantly smaller, but still large enough to enable ISC into these states, too.

Assuming that the S_1 does not lose all its population on its relaxation path, intersystem crossing rates at the S_1 minimum as well as the LIPs between the S_1 minimum and the triplet minima have to be considered too. Since the S_1 geometry and the T_{MLCT} geometry are virtually the same, no LIP was calculated between the two.

ISC and LIPs between the S_1 minimum and the triplet minima

All the ISC processes are faster than the fluorescence of the S_{MLCT} , which has a rate constant of $k_F = 5.3 \times 10^6\text{ s}^{-1}$ (see also Table 1). The fluorescence is therefore outcompeted by the ISC into the triplets. The $S_{MLCT} \rightsquigarrow T_{MLCT/LC}$ ISC is the fastest with $k_{ISC} = 6.2 \times 10^{10}\text{ s}^{-1}$, because of the large SOCMEs between the S_{MLCT} and the $T_{MLCT/LC}$. The rate between the S_{MLCT} and the T_{MLCT} is $k_{ISC} = 3.2 \times 10^8\text{ s}^{-1}$ and hence one order of magnitude larger than the rate between the S_{MLCT} and the $T_{LC,DIPP}$ ($k_{ISC} = 1.5 \times 10^7\text{ s}^{-1}$). Judging only from the ISC rates, population of the $T_{MLCT/LC}$ seems most likely, however crossings between the singlet and the triplets can also lead to an efficient population of the triplets. The

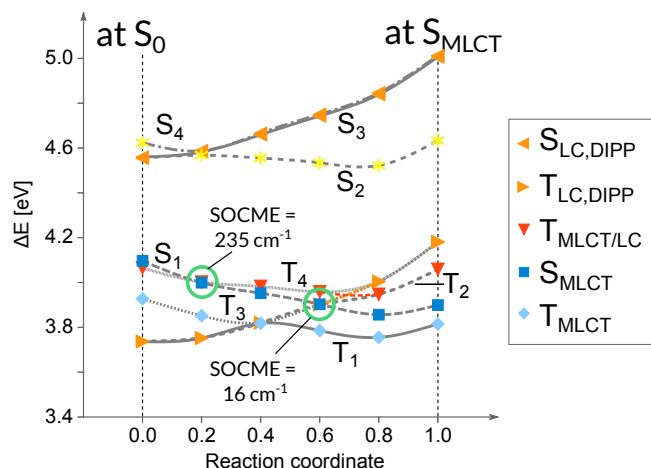


Figure 3: LIP between the S_0 and S_{MLCT} minima of compound **1**, calculated *in vacuo*. The plotted energies are DFT/MRCI energies relative to the S_0 energy at the S_0 minimum. The yellow stars indicate the optically bright singlet. SOCMEs are given for intersections between the S_1 curve and the triplet curves. The colored, dotted lines indicate the course of the corresponding diabatic states.

$T_{MLCT/LC}$ and the $T_{LC,DIPP}$ state both lie above the S_{MLCT} state at the S_{MLCT} geometry, but at their optimized geometries, they lie below the S_{MLCT} . In order to investigate the supposed crossings of the two triplet surfaces with the singlet and the other triplet surfaces as well as the barrier height for the transition into the other states, LIPs between the S_{MLCT} and each of the triplets were calculated. The results are depicted in Figure 4. Figure 4 a) shows the LIP between the S_{MLCT} and the $T_{LC,DIPP}$ minimum and Figure 4 b) the LIP between the S_{MLCT} and the $T_{MLCT/LC}$ minimum. The $T_{LC,DIPP}$ LIP reveals that one of the $T_{LC,DIPP}$ states goes through two avoided crossings with the T_{MLCT} and the $T_{MLCT/LC}$. The $T_{LC,DIPP}$ states are again labeled with orange triangles. If one follows the course of the diabatic state (which is indicated by a dotted orange line) from the S_{MLCT} to the $T_{LC,DIPP}$ minimum, one can see that the first avoided crossing occurs between $RC=0.0$ and $RC=0.2$ between the $T_{LC,DIPP}$ and the $T_{MLCT/LC}$ (red) and the second crossing shortly after $RC=0.2$ between the $T_{LC,DIPP}$ and the T_{MLCT} (light blue). That means that the T_1 state changes its character along the reaction coordinate. While it has MLCT character at the S_{MLCT} minimum, it eventually evolves changes into the $T_{LC,DIPP}$ electronic structure. From Figure 4 b) we can

learn that the S_1 , the T_1 and the T_2 are strongly coupled. Their potential curves are very close in energy and run almost in parallel. As for the $T_{LC,DIPP}$ LIP, we observe that the T_1 state changes its character, starting as the T_{MLCT} at the S_{MLCT} minimum and becoming the $T_{MLCT/LC}$ on its way to the $T_{MLCT/LC}$ minimum. Both minima, i.e. the $T_{MLCT/LC}$ and the $T_{LC,DIPP}$ minimum, can be reached from the T_{MLCT} almost barrier-free. This implies that the T_{MLCT} population will be depleted either by conversion into the $T_{LC,DIPP}$ or the $T_{MLCT/LC}$ and thus that the T_{MLCT} will probably not emit.

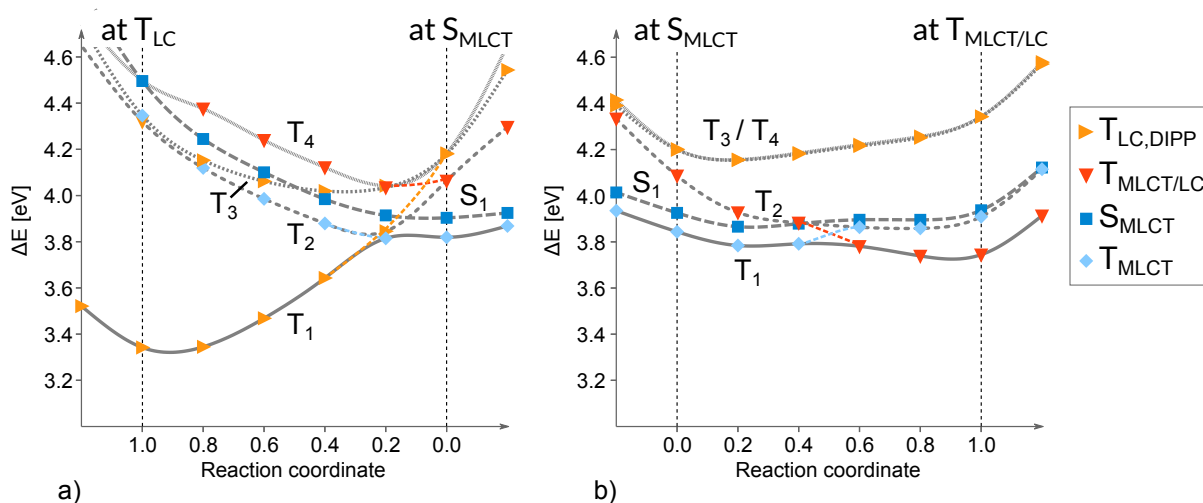


Figure 4: LIPs between a) the optimized geometry of the S_{MLCT} (RC=0.0) and the $T_{LC,DIPP}$ (RC=1.0) and b) the optimized geometry of the S_{MLCT} (RC=0.0) and the $T_{MLCT/LC}$ (RC=1.0) of compound **1** plotted with DFT/MRCI energies. The colored, dotted lines indicate the course of the corresponding diabatic states.

The $T_{MLCT/LC}$ minimum is quite shallow, the T_1 energy at the $T_{MLCT/LC}$ minimum lies only 0.1 eV below the T_1 energy at S_1 minimum. Although the reaction coordinates of $T_{MLCT/LC}$ and the $T_{LC,DIPP}$ state involve different normal coordinates and hence cannot be seen as one coordinate, the S_1 minimum may still be seen as a connecting point. It can thus be suggested that if (at room temperature) the energy difference of 0.1 eV can be overcome it is possible to transfer the $T_{MLCT/LC}$ population via the T_{MLCT} to the $T_{LC,DIPP}$ minimum. The T_1 at the $T_{LC,DIPP}$ minimum, on the other hand, lies almost 0.5 eV below the T_1 at S_1 minimum and a back transfer seems unlikely in this case. With an averaged lifetime of 5.1 s^{-1}

the phosphorescence of the $T_{LC,DIPP}$ state cannot compete with non-radiative deactivation processes and the emission is quenched at room temperature. Population of the $T_{LC,DIPP}$ is therefore disadvantageous, at least for application in OLEDs. The T_{MLCT} and the $T_{MLCT/LC}$, on the other hand, exhibit rather short lifetimes of $6.5 \mu s$ and $24 \mu s$, respectively. So if it were not for the $T_{LC,DIPP}$ state, the complex would probably be a good phosphorescence (or TADF) emitter. In conclusion, that means that one has to either modify the aromatic groups in such a way, that the $T_{LC,DIPP}$ states are pushed to higher energies or the MLCT states to lower energies or to completely remove the $T_{LC,DIPP}$ states by using aliphatic groups. The aim is to get rid of the low-lying $T_{LC,DIPP}$ state that quenches the emission, while preserving the benefits of the T_{MLCT} and the $T_{MLCT/LC}$ states, i.e. strong spin-orbit coupling which guarantees fast ISC and short emission lifetimes. The influence of the modification of the pyridine ligand will be discussed in the next section.

Table 1: Radiative rates for the singlet and triplets of compounds **1-3** at their minima and ISC rates between the S_{MLCT} and the respective triplet minimum.

compound	singlet	k_F [s^{-1}]	triplet	k_P [s^{-1}]	τ_P	k_{ISC} [s^{-1}]
1	S_{MLCT}	4.7×10^6	$T_{LC,DIPP}$	2.0×10^{-1}	5.1 s	1.5×10^7
			T_{MLCT}	1.5×10^5	$6.5 \mu s$	3.2×10^8
			$T_{MLCT/LC}$	4.2×10^4	$24 \mu s$	6.2×10^{10}
2	S_{MLCT}	5.3×10^6	$T_{LC,DIPP}$	1.6×10^{-1}	6.2 s	1.1×10^8
			T_{MLCT}	2.0×10^5	$5.1 \mu s$	5.9×10^7
			$T_{LC/MLCT}$	2.0×10^2	5.1 ms	1.9×10^{12}
3	S_{MLCT}	5.3×10^6	$T_{LC,Phpy}$	6.8×10^1	15 ms	6.0×10^{10}
			T_{MLCT}	2.4×10^2	4.1 ms	2.1×10^{10}

Variation of the pyridine ligand

Methylation in *ortho* position

Replacing the pyridine with a 2-methyl-pyridine (compound **2**) has only a minor effect on the photophysical properties of the complex. The electronic structures of the S_1 and the

triplets are almost identical to the corresponding states of the pyridine complex. Since the second MLCT triplet has stronger local contributions than the $T_{\text{MLCT/LC}}$ of the pyridine complex, it is denoted $T_{\text{LC/MLCT}}$. All states are about 0.1-0.2 eV lower in energy than the corresponding states of the pyridine complex. The LIP between the S_0 and S_1 minimum and the LIP between the S_1 minimum and the triplet minima differ only slightly. Spin-orbit coupling between the S_1 and $T_{\text{LC/MLCT}}$ is a bit smaller and, judging from the S_1 , T_1 and T_2 curves of the $T_{\text{LC/MLCT}}$ LIP, the states are less strongly coupled, which is probably due to the stronger LC character of the $T_{\text{LC/MLCT}}$. The T_1 energy at the $T_{\text{LC/MLCT}}$ minimum lies in this case 0.2 eV below the T_1 energy at the S_1 minimum (Fig. 5) and makes a back conversion to the T_{MLCT} less likely. Although that means a smaller loss of quantum yield due to smaller transfer from $T_{\text{LC/MLCT}}$ population to the $T_{\text{LC,DIPP}}$, it comes at the cost of a longer lifetime of the $T_{\text{LC/MLCT}}$ ($\tau_P = 5.1$ ms) compared to the lifetime of the $T_{\text{MLCT/LC}}$ ($\tau_P = 24$ μs), again due to the stronger LC character of the $T_{\text{LC/MLCT}}$.

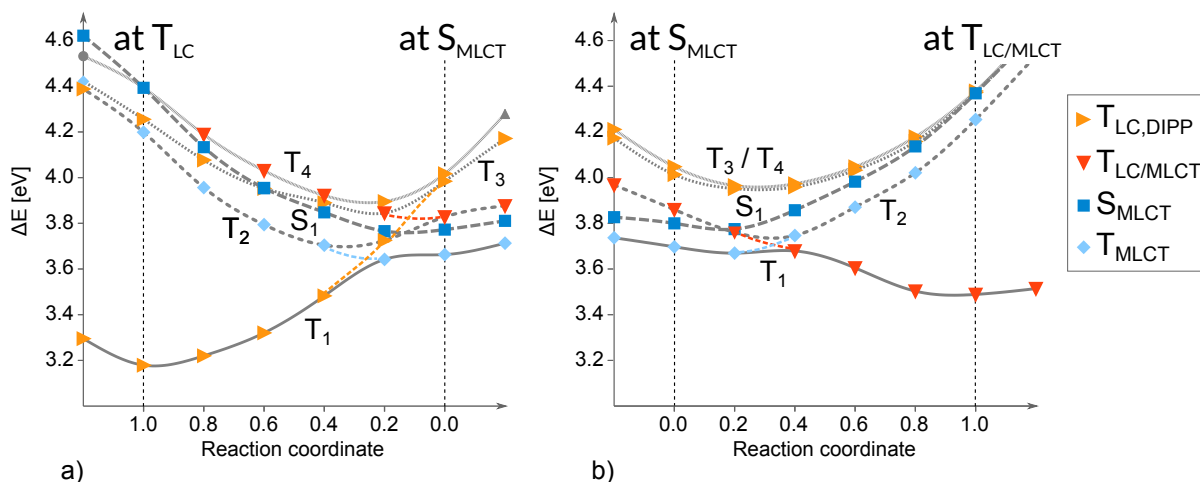


Figure 5: LIPs between a) the optimized geometry of the S_{MLCT} (RC=0.0) and the $T_{\text{LC,DIPP}}$ (RC=1.0) and b) the optimized geometry of the S_{MLCT} (RC=0.0) and the $T_{\text{MLCT/LC}}$ (RC=1.0) of compound **2** plotted with DFT/MRCI energies. The colored, dotted lines indicate the course of the corresponding diabatic states.

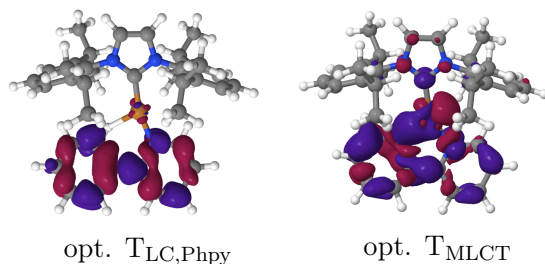


Figure 6: DFT/MRCI difference densities for the optimized excited states of IPr-Cu(I)-2-phenyl-pyridine. For color codes, see Fig. 1.

Phenyl Substitution

Using a 2-phenyl-pyridine instead of the pyridine ligand (compound **3**), on the other hand, has the unfortunate effect that the $T_{MLCT/LC}$ state is replaced by a triplet that stems mainly from a local excitation on phenyl-pyridine ligand ($T_{LC,Phpy}$, see Fig. 6). This $T_{LC,Phpy}$ state now indeed constitutes the global triplet minimum. Barrierless paths exist from the S_{MLCT} minimum to both the T_{MLCT} and $T_{LC,Phpy}$ minima on the T_1 potential energy surface (Fig. 7). The branching ratio will depend strongly on the dynamics of the nonradiative decay process. However, due to vibronic interaction of the triplet states, eventually all triplet population will accumulate in the $T_{LC,Phpy}$ minimum. With a lifetime of $\tau_P = 15$ ms, phosphorescence is too slow to compete against nonradiative decay at room temperature. Hence, the luminescence properties of the Ipr-Cu-2-phenyl-pyridine complex do not really represent an improvement over those of the unsubstituted pyridine compound.

Variation of the NHC Ligand

The results obtained so far indicate that linear coordination of a Cu(I) ion with NHC and pyridine is a very favorable structural motif for generating excited triplet states with high quantum yield. The reason for the efficient triplet formation is the presence of a low-lying triplet state ($T_{MLCT/LC}$) with large $d_\pi \rightarrow \pi_{Py}$ contributions which mediates the ISC between the $d_\sigma \rightarrow \pi_{Py}$ dominated S_{MLCT} and T_{MLCT} states. Unfortunately, the luminescence is effectively quenched if the imidazol-2-ylidene ligand carries two DIPP substituents because

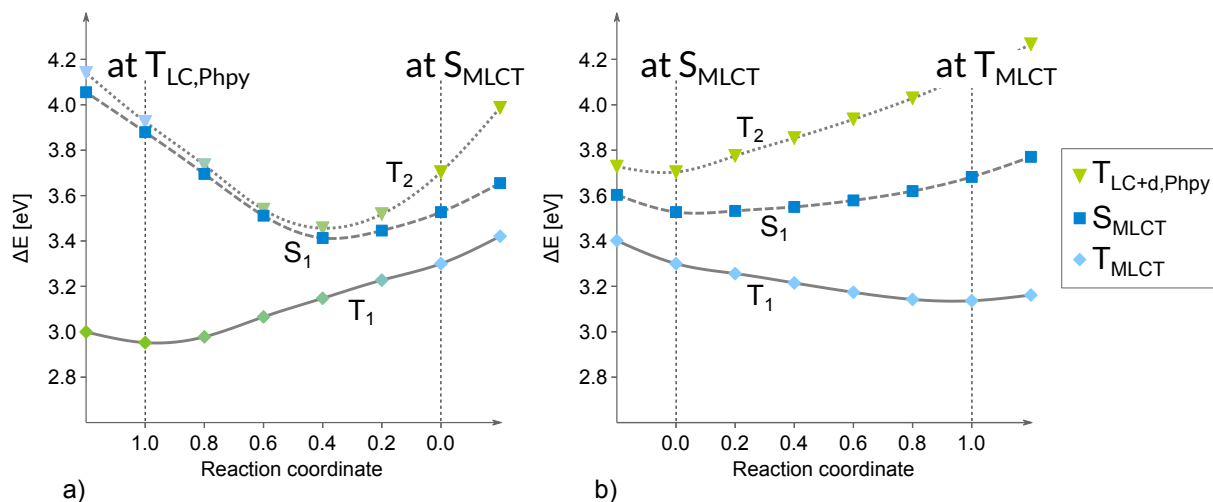


Figure 7: LIPs between a) the optimized geometry of the S_{MLCT} (RC=0.0) and the $T_{LC,Phpy}$ (RC=1.0) and b) the optimized geometry of the S_{MLCT} (RC=0.0) and the T_{MLCT} (RC=1.0) of compound **3** plotted with DFT/MRCI energies.

a local excitation on DIPP ($T_{LC,DIPP}$) with very low radiative rate constants forms the global T_1 minimum. This minimum can be reached from the T_{MLCT} and $T_{MLCT/LC}$ minima without surpassing a significant barrier. If the formation of a dark locally excited triplet state could be suppressed, linear NHC-Cu(I)-pyridine complexes should be excellent phosphorescence or TADF emitters. In the following, we pursue the strategy of replacing the DIPP substituents by bulky aliphatic residues in the hope that this replacement does not destroy the favorable energetic proximity of the S_{MLCT} and $T_{MLCT/LC}$ states.

Modification of the NHC substituents

The NHC substituents appear to have a significant impact on the energy of the MLCT excitation. Trying to get rid of the undesired $T_{LC,DIPP}$ states, we first replaced DIPP by a bulky cyclohexane derivative (Chart 1, compound **4**). This replacement leads to a marked blue shift of the $d_\sigma \rightarrow \pi_{Py}$ excitations by approximately 0.25 eV. The excitation energy of the mixed $T_{MLCT/LC}$ state rises, too, but to a lesser extent. As a consequence, it forms the T_1 state at the ground-state geometry which exhibits an almost coplanar orientation of the imidazol and pyridine rings. While the energy of the $d_\sigma \rightarrow \pi_{Py}$ excited S_{MLCT} and

T_{MLCT} states is nearly unaffected by the torsion of the pyridine ligand, this is not the case for the $T_{\text{MLCT/LC}}$ state which has its minimum for a coplanar structure ($\Delta E_{\text{adia}} = 3.85$ eV). Because of the $d_{\pi} \rightarrow \pi_{\text{Py}}$ contributions to the wavefunction, this state is destabilized upon rotation about the Cu-N bond. When the imidazol and pyridine rings take a perpendicular orientation, the $T_{\text{MLCT/LC}}$ and T_{MLCT} become degenerate ($\Delta E_{\text{adia}} = 3.97$ eV) and are located energetically close to the S_{MLCT} minimum ($\Delta E_{\text{adia}} = 4.09$ eV). $\langle T_{\text{MLCT/LC}} | \hat{\mathcal{H}}_{\text{SO}} | S_{\text{MLCT}} \rangle$ is very large at the S_{MLCT} (sum over squared components ≈ 71490 cm^{-2}) as may be expected for singly states with a change in orbital angular momentum ($d_{\sigma} \leftrightarrow d_{\pi}$) in the copper $3d$ shell. ISC will therefore effectively quench the prompt fluorescence. Phosphorescence rate constants have not been determined for this compound because its emission wavelength (345 nm) lies too far in the UV region for making this complex an interesting OLED emitter.

If instead 1-adamantyl (Ad) residues are attached to the NHC nitrogen atoms (Chart 1, compound **5**), the electronic structure and the excitation energy of the S_1 state remains nearly unchanged compared to the IPr-Cu-pyridine complex. The same is true for the T_{MLCT} and $T_{\text{MLCT/LC}}$ states which represent the T_1 and T_2 electronic states, respectively, in the FC region. Local excitations on the NHC substituents are absent among the low-lying triplet states. Geometry relaxation of the S_{MLCT} state yields a minimum with nearly coplanar orientation of the NHC and pyridine rings. The d^9 configuration on copper is stabilized through contacts with neighboring carbon and hydrogen atoms from the bulky Ad substituents. A similar nuclear arrangement is found for the corresponding T_{MLCT} state. The T_1 - S_1 splitting amounts to 0.14 eV at these geometries, with the T_2 state lying only 0.05 eV above S_1 . Although SOC between S_{MLCT} and T_{MLCT} is rather weak due to the similarity of the electronic structures (sum over squared SOCMEs ≈ 4 cm^{-2}), the small singlet–triplet energy gap and the good overlap of the vibrational wavefunctions make $S_{\text{MLCT}} \rightsquigarrow T_{\text{MLCT}}$ ISC approximately 300 times faster than fluorescence. T_1 borrows electric dipole transition intensity from the bright S_2 state resulting in a high-temperature averaged phosphorescence lifetime of about 10 μs . However, the presence of the $T_{\text{MLCT/LC}}$ in close energetic proximity

changes the picture: Eventually all excited-state population will be transferred to this state. Upon geometry relaxation of the T_2 potential, its electronic structure acquires more and more interligand (IL) charge-transfer character, but the contributions of the $d_\pi \rightarrow \pi_{Py}$ excitation, which are so important for the efficient SOC to the MLCT states with $d_\sigma \rightarrow \pi_{Py}$ character, are preserved. Along this relaxation path, the T_1 and T_2 state go through an avoided crossing with the $T_{IL/MLCT/LC}$ configuration eventually dominating the electronic structure at the global T_1 minimum. The computed rate constants for radiative and non-radiative transitions clearly show that $S_{MLCT} \rightsquigarrow T_{IL/MLCT/LC}$ ISC is 5 orders of magnitude faster than fluorescence (Tab. 2 and Fig. 8). It may therefore safely be assumed that prompt fluorescence is quenched in this compound. The $T_{IL/MLCT/LC}$ minimum exhibits a nearly coplanar orientation of the NHC and pyridine rings. Despite the adiabatic energy gap of $\Delta E_{ST} \approx 2300 \text{ cm}^{-1}$, RISC proceeds very fast at 298 K ($k_{RISC} = 1.0 \times 10^{11} \text{ s}^{-1}$ in Condon approximation). Phosphorescence with a high-temperature averaged lifetime of about 70 μs from this minimum or 10 μs from T_{MLCT} is therefore outcompeted by TADF. The rate determining step in this process is the radiative rate constant of the S_{MLCT} state ($k_F = 2.3 \times 10^6 \text{ s}^{-1}$). We note, however, that this complex emits TADF with maximum around 380 nm in the UV spectral region. It is thus not well suited to act as OLED emitter.

Table 2: Emission wavelengths λ_{max} (nm) and rate constants k (s^{-1}) for radiative decay of the singlet and triplets of compounds **5**, **6**, **8** and **9** at their minima and rate constants for ISC and RISC between the S_{MLCT} and the respective triplet minimum.

compound	singlet	λ_F	k_F	triplet	λ_P	k_P	k_{ISC}	k_{RISC}
5	S_{MLCT}	378	2.4×10^6	T_{MLCT}	395	1.0×10^5	9.0×10^8	
				$T_{IL/MLCT/LC}$	393	1.4×10^4	2.9×10^{11}	1.0×10^{11}
6	S_{MLCT}	398	1.7×10^6	T_{MLCT}	417	4.6×10^4	not calc.	
				$T_{IL/MLCT/LC}$	397	2.1×10^4	not calc.	not calc.
8	S_{MLCT}	452	1.0×10^6	T_{MLCT}	470	7.8×10^4	4.1×10^8	
				$T_{IL/MLCT/LC}$	450	1.3×10^4	1.3×10^{11}	8.0×10^{10}
9	S_{MLCT}	496	8.6×10^5	T_{MLCT}	513	4.6×10^4	7.0×10^7	9.7×10^5
				$T_{IL/MLCT/LC}$	484	5.8×10^3	2.1×10^{11}	3.6×10^{11}

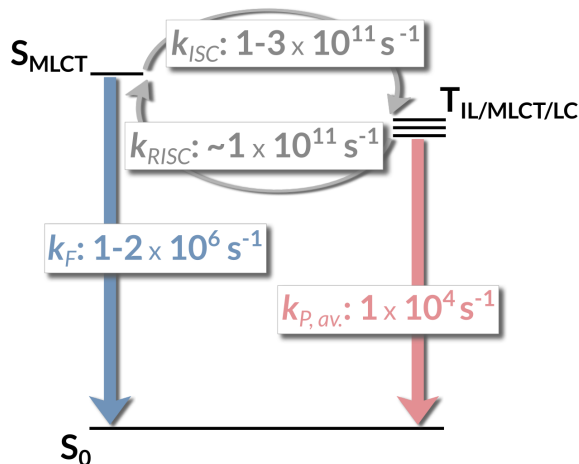


Figure 8: Radiative rates and rates for ISC and RISC between the S_{MLCT} and the $T_{\text{IL/MLCT/LC}}$ minimum for compounds **5** and **8**

There are several ways to tackle this problem. The Ad-NHC-Cu-pyridine complex could be used for triplet harvesting with a subsequent excitation energy transfer (EET) to a strongly fluorescent co-dopant. Such strategy has been pursued, for example, for enhancing the internal quantum efficiency of phosphorescent OLEDs based on iridium complexes.⁴¹ It creates, however, the complication that the donor and acceptor dopants must be introduced into the emitting layer with a specific intermolecular distance and relative orientation as the EET efficiency critically depends on these parameters. Alternatively, the ligands could be modified with the aim of stabilizing the emitting states while retaining the high ISC efficiency. In the following, we investigate substitution effects on the pyridine ligand as well as effects brought about by modification of the NHC core.

Modification of the NHC core

To increase the electron releasing properties of the NHC ligand, we introduced methyl groups in the 4- and 5-positions of the imidazol-2-ylidene (Chart 1, compound **6**). Indeed, the adiabatic excitation energies of the S_{MLCT} and T_{MLCT} states are lowered by about 0.17 eV while their electronic structures are largely preserved. The $T_{\text{IL/MLCT/LC}}$ state is also stabilized compared to the unmethylated compound, but not to the same extent. The reason for

this unexpected behavior is its more pronounced $\pi_{\text{NHC}} \rightarrow \pi_{\text{Py}}$ ILCT character and the concomitant reduced exchange interaction of the open shells. The calculations still indicate an avoided crossing of the two adiabatic triplet potentials, but the respective minimum energies are almost degenerate: In compound **6** we find the $T_{\text{IL/MLCT/LC}}$ minimum adiabatically 3.44 eV above the ground state minimum (3.52 eV in the corresponding unmethylated complex) compared to 3.48 eV (3.65 eV) for the T_{MLCT} state. SOC between the S_{MLCT} or T_{MLCT} on one side and $T_{\text{IL/MLCT/LC}}$ on the other side remains very large so that triplet formation is expected to proceed very fast and with high quantum yield. Calculated phosphorescence lifetimes are of the order several tens of microseconds, 47 μs at the $T_{\text{IL/MLCT/LC}}$ minimum and 22 μs at the T_{MLCT} minimum. Chances to observe TADF are high in the dimethylated compound because the energy gap between the global triplet minimum and the S_1 minimum ($\Delta E_{S-T} = 0.17$ eV) is quite small in relation to a SOCME of several hundred cm^{-1} . Moreover, spin-vibronic coupling is strong and will play a major role in the (R)ISC process.⁴² Coordinates undergoing substantial changes upon this transformation are the interplanar dihedral angle of the pyridine and imidazole-ylidene rings, the Cu-C bond length and the in-plane deformation stretching of the imidazole-ylidene bonds. The emission maximum is expected to lie between 400 and 420 nm, still barely in the visible region.

Alternatively, the C=C double bond of the five-membered ring can be hydrogenated to increase the σ electron donating capacity of the NHC ligand. At the ground state minimum of compound **10**, we find a stabilizing effect of the hydrogenation on the $d_\sigma \rightarrow \pi_{\text{Py}}$ excitation by approximately 0.2 eV. Adiabatically, the effect is less pronounced, 0.06 eV and 0.08 eV for the S_{MLCT} and T_{MLCT} , respectively. Because of the smaller NHC π -system, the π -type ILCT is less favorable in this compound, leading to an increased energy gap between the T_1 and T_2 states at the S_{MLCT} and T_{MLCT} minimum nuclear arrangements. Here, T_2 is dominated by a mixture of $d_\pi \rightarrow \pi_{\text{Py}}$ and local $\pi \rightarrow \pi^*$ excitations on pyridine. All attempts to find the minimum of this electronic state with TDDFT or TDA were unsuccessful as the geometry optimization always lead to crossing with the T_1 state. At the DFT/MRCI level of theory,

we find the lowest excitation energy of the T_2 state (3.79 eV) for a S_2 optimized structure, slightly above the S_1 minimum (3.73 eV). Instead of following this line further, we return to the 1,3-bis(1-adamantyl)imidazol-2-ylidene-Cu(I)-pyridine complex **5** and start modifying the pyridine ligand of this compound.

Tuning the emission wavelength to the visible regime

Electron-withdrawing groups are expected to enhance the electron-acceptor properties of the pyridine ligand, thereby lowering the energies of the $d_\sigma \rightarrow \pi_{\text{Py}}$ and $\pi_{\text{NHC}} \rightarrow \pi_{\text{Py}}$ excitations. The LUMO has large amplitudes on the C_4 (*para*) and C_2 and C_6 (*ortho*) positions of the pyridine moiety. It seems, however, like the inductive ($-I$) effects caused by fluorination of the pyridine ligand in *para* position (compound **7**) are outweighed by its $+M$ effects leading to an increase of these excitation energies. In contrast, mesomeric ($-M$) effects shift the excitation energies in the right direction.

Introducing $-M$ substituents in the pyridine ligand

Adding a cyano group in *para* position of the pyridine ligand (compound **8**) lowers the vertical adiabatic excitation energies of the S_{MLCT} and T_{MLCT} of the 1,3-bis(1-adamantyl)imidazol-2-ylidene-Cu(I)-4-cyano-pyridine by about 0.4-0.5 eV with respect to the unsubstituted complex **5**. Stabilization of the $T_{\text{MLCT/LC}}$ state is slightly less pronounced, but still significant with the result that the T_{MLCT} ($\Delta E_{\text{adia}} = 3.23$ eV) and $T_{\text{IL/MLCT/LC}}$ minima ($\Delta E_{\text{adia}} = 3.18$ eV) are in even closer energetic proximity. Like in the corresponding pyridine complex, the $T_{\text{IL/MLCT/LC}}$ diabatic state intersects the S_{MLCT} and T_{MLCT} diabats. Strong spin-orbit interaction (sum over squared SOCMEs ≈ 74000 cm^{-2}) between S_{MLCT} and $T_{\text{IL/MLCT/LC}}$ causes prompt fluorescence to be quenched on the picosecond time scale ($k_{\text{ISC}} = 1.3 \times 10^{11}$ s^{-1}). With $\Delta E_{\text{ST}} = 1050$ cm^{-1} , $T_{\text{IL/MLCT/LC}} \rightsquigarrow S_{\text{MLCT}}$ RISC is almost equally fast ($k_{\text{ISC}} = 0.8 \times 10^{11}$ s^{-1}) at room temperature (see Fig. 8). Because of the small singlet-triplet energy gap, the pronounced nonadiabatic coupling between the $T_{\text{IL/MLCT/LC}}$

and T_{MLCT} states and the concomitant spin-vibronic coupling between the S_{MLCT} state and the triplet manifold, the singlet and triplet populations will quickly equilibrate before radiative decay. RISC followed by delayed fluorescence ($k_F = 1.0 \times 10^6 \text{ s}^{-1}$) competes with phosphorescence ($k_P = 7.6 \times 10^4 \text{ s}^{-1}$ at the T_{MLCT} , $k_P = 1.3 \times 10^4 \text{ s}^{-1}$ at the $T_{\text{IL/MLCT/LC}}$ minimum) in this compound. TADF and phosphorescence emission are expected to occur in the blue-green spectral region with a maximum around 450-460 nm.

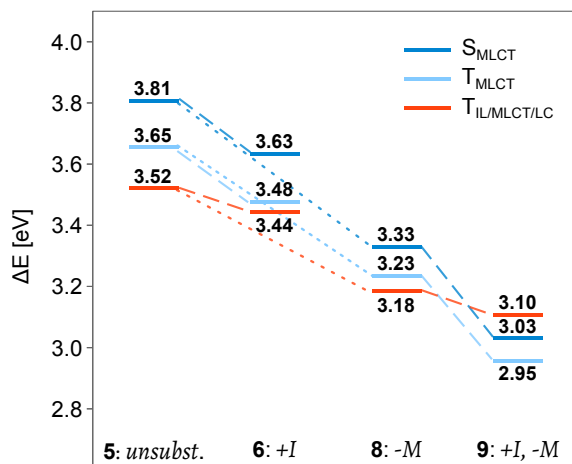


Figure 9: Influence of the $+I$ and $-M$ substituents on the adiabatic energies of the S_{MLCT} , T_{MLCT} and $T_{\text{IL/MLCT/LC}}$ minima of compounds **6**, **8** and **9** compared to the unsubstituted compound **5**.

Combination of $+I$ and $-M$ effects

It turns out that the $+I$ effects, brought about by the methylation of the imidazol-2-ylidene, and the $-M$ effect, caused by attaching a CN substituent to the pyridine ligand, are nearly additive and can be combined to tune the spectral color of the emission (Tab. 2). Figure 9 illustrates the effects of the $+I$ and the $-M$ substituents on the adiabatic energies of the S_{MLCT} , T_{MLCT} and $T_{\text{IL/MLCT/LC}}$ minima of compounds **6**, **8** and **9** compared to the unsubstituted compound **5**.

In the electronic ground state, the pyridine and carbene ligands of 1,3-bis(1-adamantyl)-4,5-dimethylimidazol-2-ylidene-Cu(I)-4-cyano-pyridine (compound **9**) are oriented in a copla-

nar fashion. Upon $d_{\sigma} \rightarrow \pi_{\text{Py}}$ (HOMO-1 \rightarrow LUMO) excitation, additional bonds between the Cu center and neighboring carbon and hydrogen atoms of the Ad residues are formed (Fig. 10) while rotating the 4-CN-pyridine by about 50° . Contrary to all other complexes studied so far, this excitation does not only represent the S_1 state, it also forms the global T_1 minimum, adiabatically located 2.95 eV above the electronic ground state (see also Fig. 9). With a value of roughly 0.08 eV, the S_1 - T_1 energy gap is therefore smaller than in the other compounds. Although the mutual spin-orbit interaction of the states is rather weak (sum over squared SOMCEs $\approx 1 \text{ cm}^{-2}$) due to the nearly identical electronic structures of the S_1 and T_1 , the nested potentials and small energy gap lead to nonradiative rate constants which show that ISC and RISC are competitive with fluorescence and much faster than phosphorescence at room temperature (Tab. 2). So, in this compound, TADF is the dominating process even in the absence of T_2 .

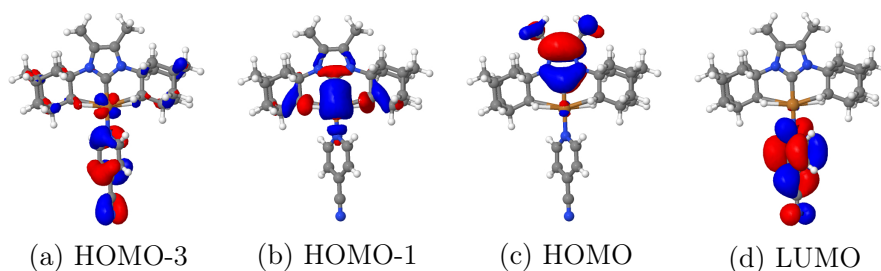


Figure 10: Selected B3LYP MOs engaged in the low-lying singlet and triplet excitations at the T_1 geometry of 1,3-bis(1-adamantyl)-4,5-dimethylimidazol-2-ylidene-Cu(I)-4-cyanopyridine.

Large contributions from $d_{\pi} \rightarrow \pi_{\text{Py}}$ (HOMO-3 \rightarrow LUMO) to the T_2 wavefunction cause the $S_1 \rightsquigarrow T_2$ ISC to be much faster than fluorescence, despite the fact that T_2 is located adiabatically 0.08 eV above the S_1 state. In addition, ILCT excitations contribute to the T_2 wavefunction, favoring a coplanar orientation of the pyridine and carbene rings. At its minimum, the electronic structure of the T_2 state is mainly composed of HOMO \rightarrow LUMO, HOMO-3 \rightarrow LUMO, and HOMO-6 \rightarrow LUMO configurations (Fig. 11). The T_2 PES is found to not only intersect the one of T_1 , but also the S_1 PES. ISC and RISC between S_1 and T_2 are predicted to proceed at the picosecond time scale (Tab. 2). The major excited-state

decay process will therefore be green TADF with a radiative lifetime of about 1 μ s.

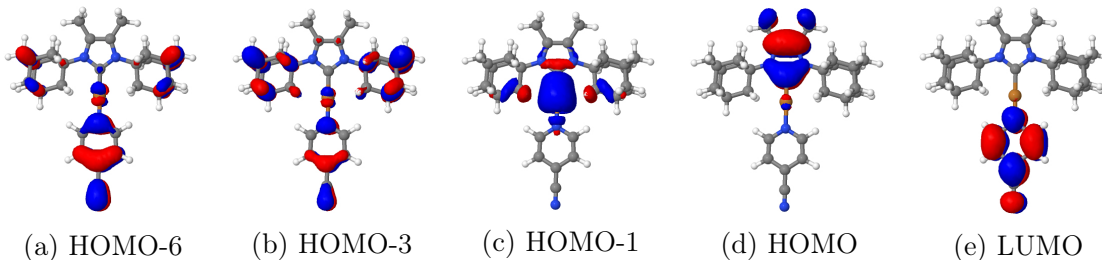


Figure 11: Selected BHLYP MOs engaged in the low-lying singlet and triplet excitations at the T_2 geometry of 1,3-bis(1-adamantyl)-4,5-dimethylimidazol-2-ylidene-Cu(I)-4-cyanopyridine.

Conclusions

The aim of this work was the computer-aided design of an electroluminescent linear NHC-Cu(I)-pyridine complex which emits in the visible spectral regime. To this end, the NHC and pyridine ligands were systematically modified and the photophysical properties of the resulting complexes (vertical and adiabatic excitation energies, fluorescence and phosphorescence rate constants and emission wavelength, spin-orbit couplings and rate constants for (reverse) intersystem crossing) were investigated by multireference quantum chemical methods. The results show that linear coordination of a Cu(I) ion with NHC and pyridine represents an excellent structural motif for generating excited triplet states with high quantum yield. The reason for the efficient triplet formation is presence of a low-lying triplet state ($T_{\text{MLCT/LC}}$) with large $d_\pi \rightarrow \pi_{\text{Py}}$ contributions which mediates the (R)ISC between the $d_\sigma \rightarrow \pi_{\text{Py}}$ dominated S_{MLCT} and T_{MLCT} states. As may be expected for singly states with a change in orbital angular momentum ($d_\sigma \leftrightarrow d_\pi$) in the copper 3d shell, $\langle T_{\text{MLCT/LC}} | \hat{\mathcal{H}}_{\text{SO}} | S_{\text{MLCT}} \rangle$ and $\langle T_{\text{MLCT/LC}} | \hat{\mathcal{H}}_{\text{SO}} | T_{\text{MLCT}} \rangle$ are very large with absolute values between 250 and 300 cm^{-1} . These strong spin-orbit interactions together with narrow singlet-triplet energy gaps and strong nonadiabatic couplings between $T_{\text{MLCT/LC}}$ and T_{MLCT} lead to effective triplet formation and quenching of the prompt fluorescence in all investigated complexes.

The high triplet quantum yield does not automatically lead to strong phosphorescence or even thermally activated delayed fluorescence. Our computational study reveals that a very weakly (if at all) phosphorescent locally excited state forms the global T_1 minimum if the imidazol-2-ylidene ligand carries two diisopropylphenyl (DIPP) substituents and pyridine or 2-methyl-pyridine is used as the other ligand. This minimum can be reached from the T_{MLCT} and $T_{MLCT/LC}$ minima without surpassing a significant barrier. To prevent the formation of these locally excited triplet states, the DIPP substituents were replaced by bulky aliphatic residues in the hope that this replacement does not destroy the favorable energetic proximity of the S_{MLCT} , T_{MLCT} and $T_{MLCT/LC}$ states. And indeed, this strategy paid off: Using tetramethyl-cyclohexyl or 1-adamantyl (Ad) substituents instead of DIPP, resolved the problem of low-lying locally excited triplet states. Unfortunately, however, this substitution shifted the luminescence to the ultraviolet regime. According to our quantum chemical studies, the emission wavelengths can be tuned back to the visible region by attaching $+I$ substituents to the NHC core, i.e. the imidazol-2-ylidene, and/or placing substituents with $-M$ effects in *para* position of the pyridine coordination. As it turned out fluorination of the pyridine ring is not expedient, since the $-I$ effects of fluorine seem to outweighed by its $+M$ effects.

1,3-bis(1-adamantyl)-imidazol-2-ylidene-Cu(I)-4-cyano-pyridine (Chart 1, compound **8**) is predicted to be an efficient blue-green emitter where TADF outcompetes phosphorescence at room temperature. Addition of two methyl groups to the NHC core shifts the emission in 1,3-bis(1-adamantyl)-4,5-dimethylimidazol-2-ylidene-Cu(I)-4-cyano-pyridine (Chart 1, compound **9**) toward the green spectral region while retaining the energetic proximity of the S_{MLCT} , T_{MLCT} and $T_{MLCT/LC}$ states and their strong spin-vibronic coupling. Synthesis of these complexes is on the way and the results of their experimental spectroscopical characterization will be reported in due time.

Acknowledgement

The authors thank Prof. Christian Ganter (Düsseldorf) and Dr. Andreas Steffen (Würzburg) for helpful discussions. Project funds (MA 1051/17-1) provided by the Deutsche Forschungsgemeinschaft as well as funds (INST 208/704-1 FUGG) to purchase the hybrid compute cluster used in this study are gratefully acknowledged.

References

- (1) Osawa, M.; Kawata, I.; Ishii, R.; Igawa, S.; Hashimoto, M.; Hoshino, M. Application of Neutral d10 Coinage Metal Complexes with an Anionic Bidentate Ligand in Delayed Fluorescence-Type Organic Light-Emitting Diodes. *J. Mater. Chem. C* **2013**, *1*, 4375–4383, DOI: 10.1039/C3TC30524D.
- (2) Leitl, M. J.; Krylova, V. A.; Djurovich, P. I.; Thompson, M. E.; Yersin, H. Phosphorescence versus Thermally Activated Delayed Fluorescence. Controlling Singlet–Triplet Splitting in Brightly Emitting and Sublimable Cu(I) Compounds. *J. Am. Chem. Soc.* **2014**, *136*, 16032–16038, DOI: 10.1021/ja508155x.
- (3) Linfoot, C. L.; Leitl, M. J.; Richardson, P.; Rausch, A. F.; Chepelin, O.; White, F. J.; Yersin, H.; Robertson, N. Thermally Activated Delayed Fluorescence (TADF) and Enhancing Photoluminescence Quantum Yields of [Cu^I(diimine)(diphosphine)]⁺ Complexes—Photophysical, Structural, and Computational Studies. *Inorg. Chem.* **2014**, *53*, 10854–10861, DOI: 10.1021/ic500889s.
- (4) Osawa, M.; Hoshino, M.; Hashimoto, M.; Kawata, I.; Igawa, S.; Yashima, M. Application of Three-Coordinate Copper(I) Complexes with Halide Ligands in Organic Light-Emitting Diodes that Exhibit Delayed Fluorescence. *Dalton Trans.* **2015**, *44*, 8369–8378, DOI: 10.1039/C4DT02853H.
- (5) Czerwieńiec, R.; Yersin, H. Diversity of Copper(I) Complexes Showing Thermally Activated Delayed Fluorescence: Basic Photophysical Analysis. *Inorg. Chem.* **2015**, *54*, 4322–4327, DOI: 10.1021/ic503072u.
- (6) Cariati, E.; Lucenti, E.; Botta, C.; Giovanella, U.; Marinotto, D.; Righetto, S. Cu(I) Hybrid Inorganic–Organic Materials with Intriguing Stimuli Sensitive and Optoelectronic Properties. *Coord. Chem. Rev.* **2016**, *306*, 566–614, DOI: <http://dx.doi.org/10.1016/j.ccr.2015.03.004>.

- (7) Czerwieńiec, R.; Leitl, M. J.; Homeier, H. H.; Yersin, H. Cu(I) complexes – Thermally activated delayed fluorescence. Photophysical approach and material design. *Coord. Chem. Rev.* **2016**, *325*, 2 – 28, DOI: <http://dx.doi.org/10.1016/j.ccr.2016.06.016>.
- (8) Bergmann, L.; Hedley, G. J.; Baumann, T.; Bräse, S.; Samuel, I. D. W. Direct observation of intersystem crossing in a thermally activated delayed fluorescence copper complex in the solid state. *Sci. Adv.* **2016**, *2*, DOI: [10.1126/sciadv.1500889](https://doi.org/10.1126/sciadv.1500889).
- (9) Leitl, M. J.; Zink, D. M.; Schinabeck, A.; Baumann, T.; Volz, D.; Yersin, H. Copper(I) Complexes for Thermally Activated Delayed Fluorescence: From Photophysical to Device Properties. *Top. Curr. Chem.* **2016**, *374*, 25, DOI: [10.1007/s41061-016-0019-1](https://doi.org/10.1007/s41061-016-0019-1).
- (10) Gernert, M.; Müller, U.; Haehnel, M.; Pflaum, J.; Steffen, A. A Cyclic Alkyl(amino)carbene as Two-Atom π -Chromophore Leading to the First Phosphorescent Linear CuI Complexes. *Chem. Eur. J.* **2017**, *23*, 2206–2216, DOI: [10.1002/chem.201605412](https://doi.org/10.1002/chem.201605412).
- (11) Shi, S.; Collins, L. R.; Mahon, M. F.; Djurovich, P. I.; Thompson, M. E.; Whittlesey, M. K. Synthesis and characterization of phosphorescent two-coordinate copper(i) complexes bearing diamidocarbene ligands. *Dalton Trans.* **2017**, *46*, 745–752, DOI: [10.1039/C6DT04016K](https://doi.org/10.1039/C6DT04016K).
- (12) Romanov, A. S.; Becker, C. R.; James, C. E.; Di, D.; Credgington, D.; Linnolahti, M.; Bochmann, M. Copper and Gold Cyclic (Alkyl)(amino)carbene Complexes with Sub-Microsecond Photoemissions: Structure and Substituent Effects on Redox and Luminescent Properties. *Chem. Eur. J.* *23*, 4625–4637, DOI: [10.1002/chem.201605891](https://doi.org/10.1002/chem.201605891).
- (13) Di, D.; Romanov, A. S.; Yang, L.; Richter, J. M.; Rivett, J. P. H.; Jones, S.; Thomas, T. H.; Abdi Jalebi, M.; Friend, R. H.; Linnolahti, M.; Bochmann, M.; Credg-

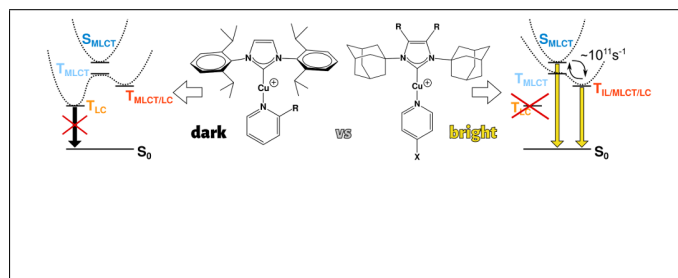
- ington, D. High-performance light-emitting diodes based on carbene-metal-amides. *Science* **2017**, *356*, 159–163, DOI: 10.1126/science.aah4345.
- (14) Föllner, J.; Marian, C. M. Rotationally Assisted Spin-State Inversion in Carbene–Metal–Amides Is an Artifact. *J. Phys. Chem. Lett.* **2017**, *8*, 5643–5647, DOI: 10.1021/acs.jpcclett.7b02701.
- (15) Föllner, J.; Kleinschmidt, M.; Marian, C. M. Phosphorescence or Thermally Activated Delayed Fluorescence? Intersystem Crossing and Radiative Rate Constants of a Three-Coordinate Copper(I) Complex Determined by Quantum-Chemical Methods. *Inorg. Chem.* **2016**, *55*, 7508–7516, DOI: 10.1021/acs.inorgchem.6b00818.
- (16) Ahlrichs, R.; Bär, M.; Häser, M.; Horn, H.; Kölmel, C. Electronic Structure Calculations on Workstation Computers: The Program System Turbomole. *Chem. Phys. Lett.* **1989**, *162*, 165–169, DOI: [http://dx.doi.org/10.1016/0009-2614\(89\)85118-8](http://dx.doi.org/10.1016/0009-2614(89)85118-8).
- (17) TURBOMOLE V6.6 2014, a development of University of Karlsruhe and Forschungszentrum Karlsruhe GmbH, 1989-2007, TURBOMOLE GmbH, since 2007; available from <http://www.turbomole.com>.
- (18) Von Arnim, M.; Ahlrichs, R. Performance of Parallel TURBOMOLE for Density Functional Calculations. *J. Comput. Chem.* **1998**, *19*, 1746–1757, DOI: 10.1002/(SICI)1096-987X(19981130)19:15<1746::AID-JCC7>3.0.CO;2-N.
- (19) Perdew, J. P.; Burke, K.; Ernzerhof, M. Generalized Gradient Approximation Made Simple. *Phys. Rev. Lett.* **1996**, *77*, 3865–3868, DOI: 10.1103/PhysRevLett.77.3865.
- (20) Adamo, C.; Barone, V. Toward Reliable Density Functional Methods without Adjustable Parameters: The PBE0 Model. *J. Chem. Phys.* **1999**, *110*, 6158–6170, DOI: <http://dx.doi.org/10.1063/1.478522>.

- (21) Furche, F.; Ahlrichs, R. Adiabatic Time-Dependent Density Functional Methods for Excited State Properties. *J. Chem. Phys.* **2002**, *117*, 7433–7447, DOI: <http://dx.doi.org/10.1063/1.1508368>.
- (22) Peach, M. J. G.; Williamson, M. J.; Tozer, D. J. Influence of Triplet Instabilities in TDDFT. *J. Chem. Theory Comput.* **2011**, *7*, 3578–3585, DOI: 10.1021/ct200651r.
- (23) Hirata, S.; Head-Gordon, M. Time-dependent density functional theory within the Tamm–Dancoff approximation. *Chem. Phys. Lett.* **1999**, *314*, 291 – 299, DOI: [https://doi.org/10.1016/S0009-2614\(99\)01149-5](https://doi.org/10.1016/S0009-2614(99)01149-5).
- (24) Schäfer, A.; Horn, H.; Ahlrichs, R. Fully Optimized Contracted Gaussian Basis Sets for Atoms Li to Kr. *J. Chem. Phys.* **1992**, *97*, 2571–2577, DOI: <http://dx.doi.org/10.1063/1.463096>.
- (25) Figen, D.; Rauhut, G.; Dolg, M.; Stoll, H. Energy-Consistent Pseudopotentials for Group 11 and 12 Atoms: Adjustment to Multi-Configuration Dirac–Hartree–Fock Data. *Chem. Phys.* **2005**, *311*, 227–244, DOI: <http://dx.doi.org/10.1016/j.chemphys.2004.10.005>.
- (26) Peterson, K. A.; Puzzarini, C. Systematically Convergent Basis Sets for Transition Metals. II. Pseudopotential-Based Correlation Consistent Basis Sets for the Group 11 (Cu, Ag, Au) and 12 (Zn, Cd, Hg) Elements. *Theor. Chem. Acc.* **2005**, *114*, 283–296, DOI: 10.1007/s00214-005-0681-9.
- (27) Deglmann, P.; Furche, F.; Ahlrichs, R. An Efficient Implementation of Second Analytical Derivatives for Density Functional Methods. *Chem. Phys. Lett.* **2002**, *362*, 511–518, DOI: [http://dx.doi.org/10.1016/S0009-2614\(02\)01084-9](http://dx.doi.org/10.1016/S0009-2614(02)01084-9).
- (28) Deglmann, P.; Furche, F. Efficient Characterization of Stationary Points on Potential Energy Surfaces. *J. Chem. Phys.* **2002**, *117*, 9535–9538, DOI: <http://dx.doi.org/10.1063/1.1523393>.

- (29) Weymuth, T.; Haag, M. P.; Kiewisch, K.; Lubner, S.; Schenk, S.; Jacob, C. R.; Herrmann, C.; Neugebauer, J.; Reiher, M. MOVIPAC: Vibrational spectroscopy with a robust meta-program for massively parallel standard and inverse calculations. *J. Comput. Chem.* **2012**, *33*, 2186–2198, DOI: [10.1002/jcc.23036](https://doi.org/10.1002/jcc.23036).
- (30) Grimme, S.; Waletzke, M. A Combination of Kohn–Sham Density Functional Theory and Multi-Reference Configuration Interaction Methods. *J. Chem. Phys.* **1999**, *111*, 5645–5655, DOI: <http://dx.doi.org/10.1063/1.479866>.
- (31) Kleinschmidt, M.; Marian, C. M.; Waletzke, M.; Grimme, S. Parallel Multireference Configuration Interaction Calculations on Mini- β -Carotenes and β -Carotene. *J. Chem. Phys.* **2009**, *130*, 044708, DOI: <http://dx.doi.org/10.1063/1.3062842>.
- (32) Lee, C.; Yang, W.; Parr, R. G. Development of the Colle-Salvetti Correlation-Energy Formula into a Functional of the Electron Density. *Phys. Rev. B* **1988**, *37*, 785–789, DOI: [10.1103/PhysRevB.37.785](https://doi.org/10.1103/PhysRevB.37.785).
- (33) Becke, A. D. A New Mixing of Hartree-Fock and Local Density-Functional Theories. *J. Chem. Phys.* **1993**, *98*, 1372–1377, DOI: <http://dx.doi.org/10.1063/1.464304>.
- (34) Hättig, C.; Hellweg, A. unpublished.
- (35) Weigend, F.; Häser, M.; Patzelt, H.; Ahlrichs, R. RI-MP2: optimized auxiliary basis sets and demonstration of efficiency. *Chem. Phys. Lett.* **1998**, *294*, 143–152, DOI: [https://doi.org/10.1016/S0009-2614\(98\)00862-8](https://doi.org/10.1016/S0009-2614(98)00862-8).
- (36) Kleinschmidt, M.; Tatchen, J.; Marian, C. M. Spin-Orbit Coupling of DFT/MRCI Wavefunctions: Method, Test Calculations, and Application to Thiophene. *J. Comput. Chem.* **2002**, *23*, 824–833, DOI: [10.1002/jcc.10064](https://doi.org/10.1002/jcc.10064).
- (37) Kleinschmidt, M.; Marian, C. M. Efficient Generation of Matrix Elements

- for One-Electron Spin–Orbit Operators. *Chem. Phys.* **2005**, *311*, 71–79, DOI: <http://dx.doi.org/10.1016/j.chemphys.2004.10.025>.
- (38) Kleinschmidt, M.; Tatchen, J.; Marian, C. M. SPOCK.CI: A Multireference Spin-orbit Configuration Interaction Method for Large Molecules. *J. Chem. Phys.* **2006**, *124*, 124101, DOI: <http://dx.doi.org/10.1063/1.2173246>.
- (39) Etinski, M.; Tatchen, J.; Marian, C. M. Time-Dependent Approaches for the Calculation of Intersystem Crossing Rates. *J. Chem. Phys.* **2011**, *134*, 154105, DOI: <http://dx.doi.org/10.1063/1.3575582>.
- (40) Etinski, M.; Tatchen, J.; Marian, C. M. Thermal and Solvent Effects on the Triplet Formation in Cinnoline. *Phys. Chem. Chem. Phys.* **2014**, *16*, 4740–4751, DOI: [10.1039/C3CP53247J](https://doi.org/10.1039/C3CP53247J).
- (41) Baldo, M. A.; Thompson, M. E.; Forrest, S. R. High-efficiency fluorescent organic light-emitting devices using a phosphorescent sensitizer. *Nature* **2000**, *403*, 750, DOI: [10.1038/35001541](https://doi.org/10.1038/35001541).
- (42) Penfold, T. J.; Gindensperger, E.; Daniel, C.; Marian, C. M. Spin-Vibronic Mechanism for Intersystem Crossing. *Chem. Rev.* **Article ASAP**, DOI: [10.1021/acs.chemrev.7b00617](https://doi.org/10.1021/acs.chemrev.7b00617), DOI: [10.1021/acs.chemrev.7b00617](https://doi.org/10.1021/acs.chemrev.7b00617).

Graphical TOC Entry



Book Chapter

Druckfreigabe/approval for printing	
Without corrections/ ohne Korrekturen	<input type="checkbox"/>
After corrections/ nach Ausführung der Korrekturen	<input type="checkbox"/>
Date/Datum:
Signature/Zeichen:

8

Intersystem Crossing Processes in TADF Emitters

Christel M. Marian¹, Jelena Föller¹, Martin Kleinschmidt¹, and Mihajlo Etinski²

¹Heinrich-Heine-University Düsseldorf, Institute of Theoretical and Computational Chemistry, Universitätsstr. 1, 40225 Düsseldorf, Germany

²University of Belgrade, Faculty of Physical Chemistry, Studentski Trg 12-16, 11000 Belgrade, Serbia

8.1 Introduction

This chapter gives a brief overview over quantum chemical methods for computing rate constants of radiative and nonradiative molecular excited-state processes and summarizes our recent theoretical research on the photophysics of thermally activated delayed fluorescence (TADF) emitters.

8.1.1 Electroluminescent Emitters

In the first organic light-emitting diodes (OLEDs), the electroluminescence of fluorescent dyes such as 8-hydroxyquinoline aluminum (Alq₃) was exploited [1]. Dyes of this first generation are highly fluorescent but possess slow intersystem crossing (ISC) and negligible phosphorescence rates. Therefore only the singlet excitons, that means, only about 25% of the generated excitons, can be harvested [2]. The limited internal quantum efficiency appears to be their greatest disadvantage. Advantages are clear colors due to narrow emission bands and good operational stability due to fast radiative decay of the dyes (nanosecond regime) [3, 4].

The second generation of small-molecule OLEDs employs phosphorescent dopants instead of fluorescent ones. Typically, the emitters are organometallic complexes with Ir or Pt cores [5–9]. Their excited singlet states undergo fast ISC to the lowest triplet state. Thus, in addition to the triplet excitons, the singlet excitons can be harvested in phosphorescent organic light-emitting diodes (PHOLEDs), leading to an internal quantum yield of up to 100% [2, 10]. The main limitation of the phosphorescent dyes is their comparatively long radiative lifetime (microsecond regime) that leads to undesirable side effects, namely, quenching processes and bleaching reactions. The latter are particularly pronounced for blue PHOLED emitters. To avoid nonradiative decay via low-lying

Highly Efficient OLEDs: Materials Based on Thermally Activated Delayed Fluorescence,

First Edition. Edited by Hartmut Yersin.

© 2018 Wiley-VCH Verlag GmbH & Co. KGaA. Published 2018 by Wiley-VCH Verlag GmbH & Co. KGaA.

Druckfreigabe/approval for printing	
Without corrections/ ohne Korrekturen	<input type="checkbox"/>
After corrections/ nach Ausführung der Korrekturen	<input type="checkbox"/>
Date/Datum:	
Signature/Zeichen:	

nonemissive metal-centered states, complexes with strongly σ donating and π accepting ligands were devised [11–13], but there is still room for improvement. Because of the very limited operational stability of blue PHOLEDs, hybrid fluorescent–PHOLEDs were employed for generating white light incorporating fluorescent blue and phosphorescent green to red emitters in one device [14].

The third generation of OLED emitters comprises organic donor–acceptor systems [4] as well as transition metal (TM) complexes [15–17] with small singlet–triplet energy gap ΔE_{ST} that lies within the range of thermal energy. Because of the small ΔE_{ST} , reverse intersystem crossing (rISC) from the lowest triplet to the lowest singlet is reasonably fast, and therefore TADF, also called E-type delayed fluorescence (DF) in the older literature [18], is possible in addition to direct fluorescence. Like PHOLEDs, TADF-based OLEDs show an internal quantum efficiency of up to 100% [19]. Furthermore, cheaper first-row TMs such as Cu instead of Ir or Pt can be used. A disadvantage of many presently available TADF OLEDs that they share with the PHOLEDs is the rather low intrinsic radiative transition rate ($k_r = 10^6$ – 10^7 s⁻¹) of the emitters that makes them sensitive to nonradiative decay processes such as triplet–triplet annihilation. Also, the emission from states with charge-transfer (CT) character typically is rather broad, which is not favorable for application in displays [4].

The latest class of OLEDs aims to combine high internal quantum efficiency and long operational stability by using assistant dopants for the harvesting of triplet- and singlet excited states in addition to fluorescence emitters. The assistant dopant transfers its excitation energy nonradiatively to the fluorescent acceptor by Förster resonant energy transfer (FRET). If the donor is sufficiently phosphorescent, it is even possible to induce FRET from triplet to singlet states or vice versa [20, 21]. This mechanism was exploited by Baldo et al. [22] for improving the efficiency of red fluorescence in OLEDs by using the green phosphor Ir(ppy)₃ as sensitizer. Fukagawa et al. [23] utilized singlet-to-triplet FRET from TADF assistant dopants to phosphorescent Ir and Pt complexes. In this way, the amount of phosphorescent emitter could be greatly reduced. Adachi and coworkers combined purely organic, sublimable TADF assistant dopants and fluorescence emitters in one layer, thus uniting the advantages of both [24].

8.1.2 Thermally Activated Delayed Fluorescence

TADF is looked upon as a significant emerging technology for generating highly performant electroluminescent devices for displays and lighting systems [25]. Despite the fact that TADF has been shown to give highly efficient OLEDs, the underlying mechanisms are still not clearly understood. Ideally, thermally stable dyes with small singlet–triplet energy gap, substantial S_1 – T_1 (R)ISC, high fluorescence but minimal nonradiative decay to the electronic ground state are required. However, these conditions for efficient TADF emission are not easily met simultaneously. In addition to the intrinsic emitter properties, emitter–host interactions play an essential role for the luminescence properties of a device [23, 26].

The energy difference between a singlet- and triplet-coupled open-shell configuration depends on the exchange interaction of the unpaired electrons. This

Druckfreigabe/approval for printing	
Without corrections/ ohne Korrekturen	<input type="checkbox"/>
After corrections/ nach Ausführung der Korrekturen	<input type="checkbox"/>
Date/Datum:
Signature/Zeichen:

interaction is small when the density distributions of the orbitals involved in the excitation do not overlap substantially. Typically, this requirement is fulfilled by CT states where the unpaired electrons are far apart. Very small singlet–triplet splittings can also be achieved in molecular systems where the electron clouds in the half-occupied orbitals are not strongly displaced with respect to each other, but where their electron density distributions peak at different atoms and hence are disjunct [27, 28]. Such a situation occurs, for example, in nonalternant hydrocarbons with azulene as a well-known representative. Unfortunately, the overlap of orbital densities between the initial and final states plays also a decisive role for the magnitude of the electronic spin–orbit coupling (SOC) and for the fluorescence rate. Electronic SOC – a further prerequisite for efficient (R)ISC – is a fairly short-ranged interaction. Furthermore, SOC between singlet and triplet configurations with equal occupation of the spatial orbitals vanishes for symmetry reasons. As a consequence, SOC is in general very weak between singlet and triplet CT states. Owing to the near-degeneracy of d orbitals with different magnetic moments, the situation might be more favorable in TM complexes with metal-to-ligand charge-transfer (MLCT) excited states. The interplay of all the factors influencing the probability of TADF is not yet fully understood and needs further investigation. It seems to be clear, however, that a small singlet–triplet energy gap alone is not sufficient for enabling efficient TADF.

8.2 Intersystem Crossing Rate Constants

ISC is a nonradiative transition between states of different electronic spin multiplicity. Hence, a spin-dependent interaction operator is required to mediate the transition. In most cases, electronic SOC will dominate the interaction, but in cases in which this interaction is very weak, electronic spin–spin coupling (SSC) might come into play.

Assuming the coupling of the initial and final states to be small compared with their energy difference (which will be the case in typical TADF emitters), the ISC rate can be evaluated in the framework of perturbation theory (*Fermi's golden rule*). The rate constant for an ISC from a manifold of thermally populated initial vibronic states $|\Psi_a, \{v_{aj}\}\rangle$ to a quasi-continuum of final vibronic states $\langle\Psi_b, \{v_{bk}\}|$, caused by spin–orbit interaction, is then given by

$$k_{\text{ISC}} = \frac{2\pi}{\hbar Z} \sum_{j,k} e^{-\beta E_j} |\langle\Psi_b, \{v_{bk}\} | \hat{H}_{\text{SO}} | \Psi_a, \{v_{aj}\}\rangle|^2 \delta(E_{aj} - E_{bk}) \quad (8.1)$$

where $Z = \sum_j e^{-\beta E_j}$ is a canonical partition function for vibrational motion in the initial electronic state, β is the inverse temperature, and E_j is the energy of the vibrational level in the initial electronic state.

In many articles relating to TADF emitters, the ISC from a singlet to a triplet state colloquially is called a downhill process, whereas the reverse transition, rISC, is called an uphill process. As may be seen from the delta distribution in Eq. (8.1), the energy is strictly conserved during the nonradiative transition, i.e. the initial and final states are isoenergetic. What people have in mind when

Druckfreigabe/approval for printing	
Without corrections/ ohne Korrekturen	<input type="checkbox"/>
After corrections/ nach Ausführung der Korrekturen	<input type="checkbox"/>
Date/Datum:
Signature/Zeichen:

speaking of downhill and uphill processes is the difference between the adiabatic energies of the initial and final electronic states, possibly including zero-point vibrational energy corrections. If that energy difference is positive, the transition is dubbed a downhill process and may occur at any temperature. If that energy difference is negative, thermal energy is required in addition to bridge the gap.

The efficiency of ISC and rISC is controlled by several factors. Intrinsically molecular factors are the magnitude of the spin–orbit coupling matrix element (SOCME), the adiabatic energy difference, and the coordinate displacement of the singlet and triplet potential energy surfaces as well as further factors such as the Duschinsky rotation of the respective vibrational modes. The most important external factor – aside from environment effects – is the temperature.

8.2.1 Condon Approximation

In the Condon approximation, where it is assumed that the electronic and vibrational degrees of freedom can be separated, the ISC rate is given by a product of the electronic and vibrational parts (direct SOC):

$$k_{\text{ISC}}^{\text{dir}} = \frac{2\pi}{\hbar Z} |\langle \Psi_b | \hat{H}_{\text{SO}} | \Psi_a \rangle|_{\mathbf{q}_0}^2 \sum_{j,k} e^{-\beta E_j} |\langle \{v_{bk}\} | \{v_{aj}\} \rangle|^2 \delta(E_{aj} - E_{bk}) \quad (8.2)$$

In principle, the origin of the Taylor expansion, \mathbf{q}_0 , can be chosen at will. It is common practice, however, to choose the minimum geometry of the initial state to determine the electronic SOCME for ISC.

In first-order perturbation theory, each Cartesian component of the spin–orbit Hamiltonian couples the singlet state to one and only one Cartesian triplet sub-level [29]. For this reason, phase factors do not play any role in the calculation of the total ISC rate from a given singlet state to all triplet sublevels in Condon approximation. Furthermore, a common set of vibrational wave functions is chosen for all triplet fine-structure levels. Hence, the squared contributions from all three components can just be summed up yielding

$$k_{\text{ISC}}^{\text{dir}}(S \rightarrow T) = \frac{2\pi}{\hbar Z} \left(\sum_{\kappa} |\langle T_b^{\kappa} | \hat{H}_{\text{SO}} | S_a \rangle|_{\mathbf{q}_0}^2 \right) \times \sum_{j,k} e^{-\beta E_j} |\langle \{v_{bk}\} | \{v_{aj}\} \rangle|^2 \delta(E_{aj} - E_{bk}) \quad (8.3)$$

The situation is slightly more complicated for the reverse transition from a triplet to a singlet state. In general, the fine-structure levels of a triplet state are separated by a zero-field splitting (ZFS). If the ZFS is large in relation to the temperature, individual rISC rate constants would have to be determined for every fine-structure level. Fortunately, ZFSs of TADF emitters are typically very small ($\ll 10 \text{ cm}^{-1}$) compared with thermal energies ($298 \text{ K} \approx 207 \text{ cm}^{-1}$) so that the rISC rate constants can be averaged. Hence, in first-order perturbation theory, the total

Druckfreigabe/approval for printing	
Without corrections/ ohne Korrekturen	<input type="checkbox"/>
After corrections/ nach Ausführung der Korrekturen	<input type="checkbox"/>
Date/Datum:
Signature/Zeichen:

rate constant of rISC for a molecule in the triplet state is given by

$$k_{\text{rISC}}^{\text{dir}}(\text{T} \rightarrow \text{S}) = \frac{2\pi}{3\hbar Z} \left(\sum_{\kappa} |\langle \text{S}_b | \hat{H}_{\text{SO}} | \text{T}_a^{\kappa} \rangle|_{\mathbf{q}_0}^2 \right) \times \sum_{j,k} e^{-\beta E_j} |\langle \{v_{bk}\} | \{v_{aj}\} \rangle|^2 \delta(E_{aj} - E_{bk}) \quad (8.4)$$

where the factor of 3 in the denominator of Eq. (8.4) takes care of the degeneracy of the triplet sublevels.

8.2.1.1 Electronic Spin–Orbit Coupling Matrix Elements

Microscopic spin–orbit Hamiltonians contain vector products between the electronic momentum and the derivatives of the one- and two-electron Coulomb potentials [30, 31]. Because these derivatives drop off like $1/r^3$, SOC is a fairly short-ranged interaction. Denoting the operator for the angular momentum of electron i with respect to nucleus K by $\vec{\ell}_{iK}$ and the corresponding operator for the angular momentum of electron i with respect to electron j by $\vec{\ell}_{ij}$, the Breit–Pauli spin–orbit Hamiltonian is given by

$$\hat{H}_{\text{SO}}^{\text{BP}} = \frac{1}{4} \alpha^2 g_e \sum_i \left\{ \sum_K \frac{Z_K}{r_{iK}^3} \vec{\ell}_{iK} \cdot \vec{s}_i - \sum_{j \neq i} \frac{1}{r_{ij}^3} \vec{\ell}_{ij} \cdot (\vec{s}_i + 2\vec{s}_j) \right\} \quad (8.5)$$

Herein, g_e is the gyromagnetic factor of the electron and α is the fine-structure constant. The two-electron terms of the spin–orbit Hamiltonian contribute roughly 50% to the SOCME in molecules composed of light elements and can therefore not be neglected. They can, however, be combined in good approximation with the true one-electron terms to form an effective one-electron mean-field operator [32]. Whether the mean-field approximation is sufficiently accurate to compute the typically very small SOCMEs of purely organic TADF emitters is not clear at present.

The El-Sayed rules state that ISC in organic molecules is fast between singlet excited states of different orbital types such as $^1(n\pi^*) \rightsquigarrow ^3(\pi\pi^*)$, whereas ISC between states of the same orbital type such as $^1(\pi'\pi^*) \rightsquigarrow ^3(\pi\pi^*)$ is Slow [33]. These qualitative rules are easily understood. To this end, we consider the one-electron spin–orbit Hamiltonian as a compound tensor operator of rank 0:

$$a_{\text{SO}} \vec{\ell} \cdot \vec{s} = a_{\text{SO}} (\hat{\ell}_0 \hat{s}_0 - \hat{\ell}_{+1} \hat{s}_{-1} - \hat{\ell}_{-1} \hat{s}_{+1}) \quad (8.6)$$

where a_{SO} is a system-specific parameter and the subindices $0, \pm 1$ denote the tensor components of the spatial and spin angular momentum operators, respectively. Like the more familiar ladder operators, these tensor operators can shift the magnetic quantum numbers of electrons. (See Ref. [30] for more details.) Consider $\langle ^1(n\pi^*) | \hat{H}_{\text{SO}} | ^3(\pi\pi^*) \rangle$, for example. The two states are related by a single excitation from π to n . While $\hat{\ell}_{-1}$ can be used to transform an

Druckfreigabe/approval for printing	
Without corrections/ ohne Korrekturen	<input type="checkbox"/>
After corrections/ nach Ausführung der Korrekturen	<input type="checkbox"/>
Date/Datum:
Signature/Zeichen:

out-of-plane p_π orbital to an in-plane n orbital, \hat{s}_{+1} shifts the spin state of the electron from β to α . The spin-orbit operator in Eq. (8.6) does not contain any combination that changes the spin magnetic quantum number of the electron, but leaves its spatial angular momentum quantum number untouched. For that reason, $\langle {}^1(\pi'\pi^*) | \hat{H}_{SO} | {}^3(\pi\pi^*) \rangle$ will be small. Moreover, in spatially nondegenerate states (as is the case in organic compounds), angular momentum operators do not have diagonal matrix elements because they are purely imaginary. Therefore, the electronic SOCMEs between a singlet and a triplet state with equal spatial orbital occupation vanish. This means in particular that the electronic SOCMEs between two CT states of similar wave function characteristics, $\langle {}^1CT | \hat{H}_{SO} | {}^3CT \rangle$, which play a prominent role in TADF emitters, will be very small. However, ISC between states of equal orbital type is not always slow. In order to have appreciable SOC between states of the same orbital type, it is necessary to go beyond the Condon approximation (see also Section 8.2.2).

A further obstacle for efficient SOC in TADF emitters is the shortrangedness of the spin-orbit interaction. Because of its r^{-3} dependence, the largest contribution to the SOCME comes from one-center terms. Combining this criterion with the El-Sayed rules, one finds that in Condon approximation appreciable spin-orbit integrals may arise only if the involved molecular orbitals (MOs) exhibit electron densities at the same center and if the atomic orbitals have different magnetic quantum numbers. This excludes the typical pair of 1CT and 3CT states where the unpaired electrons typically are far apart, i.e. their spin densities have little overlap. Consequently, the two-electron exchange integral that largely determines the singlet-triplet energy gap is very small while at the same time also their mutual spin-orbit interaction is tiny. Hypothetically, substantial SOC can be imagined even for CT states, however, namely, if more than two electronic states are involved. Consider, for example, purely organic donor-acceptor systems in which the $(\pi_D\pi_A^*)$ and $(n_D\pi_A^*)$ excitations are energetically near degenerate. Herein, π_D and n_D represent occupied π MO and lone-pair orbitals of the donor, respectively, and π_A^* an unoccupied π MO of the acceptor. Comparing configurations, it is seen that $(\pi_D\pi_A^*)$ and $(n_D\pi_A^*)$ differ from each other by a local ($\pi_D \rightarrow n_D$) replacement at the donor that might in turn yield large SOC. Likewise, in MLCT excited states of Cu(I) complexes, a $(d_\pi\pi^*)$ state might be located energetically close to a $(d_\sigma\pi^*)$ and could make use of the large SOC in the 3d shell.

8.2.1.2 Overlap of Vibrational Wave Functions

When deriving qualitative rules for probabilities of radiationless transitions in large molecules, Jortner and coworkers [34, 35] differentiated between two major cases: the weak and the strong coupling cases (Figure 8.1).

In the weak coupling case (Figure 8.1a), the coordinate displacement for each normal mode is assumed to be relatively small. In this case, the transition probability depends exponentially on the adiabatic energy difference ΔE , i.e. the smaller the energy gap, the larger the transition probability [34]. This relation is commonly called the *energy gap law*. People tend to forget, however, that this qualitative rule applies only for a pair of nested states.

Color Fig: 8.1

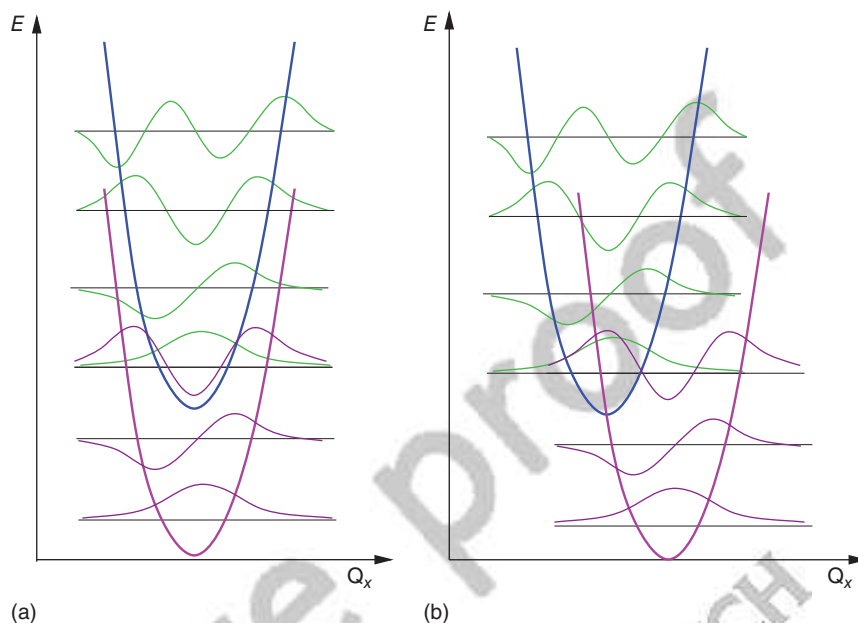


Figure 8.1 Schematic representation of the vibrational overlaps in the (a) weak and (b) strong coupling cases of nonradiative transitions. (a) Nested harmonic oscillators. (b) Displaced harmonic oscillators.

The strong coupling case (Figure 8.1b) is characterized by large relative displacements in some coordinates so that an intersection of the potential energy surfaces can be expected. The probability of the radiationless transition then exhibits a Gaussian dependence on the energy parameter $\Delta E - E_M$ where E_M is the molecular rearrangement energy that corresponds to half the Stokes shift for the two electronic states under consideration [34]. Taking, additionally, temperature effects into account by assuming a Boltzmann distribution resulted in a generalized activated rate equation similar to Marcus theory [35, 36]. In agreement with this model case, occasionally an inverse relationship between the transition probability and ΔE is observed, i.e. there exist cases where the transition probability increases with increasing energy gap [37].

8.2.2 Beyond the Condon Approximation

In order to have appreciable SOC between states of the same orbital type, it is necessary to go beyond the Condon approximation. Henry and Siebrand [38] were the first who discussed various contributions of different couplings to the ISC rate. In addition to the so-called direct spin-orbit interaction, they considered spin-orbit interaction induced by Herzberg-Teller vibronic coupling and spin-orbit interaction induced by Born-Oppenheimer vibronic coupling. In practice, the latter two types are difficult to tell apart. Similar to the Herzberg-Teller expansion of the vibronic interaction, the SOC can be expanded in a Taylor series with respect to the nuclear coordinates about an

Druckfreigabe/approval for printing	
Without corrections/ ohne Korrekturen	<input type="checkbox"/>
After corrections/ nach Ausführung der Korrekturen	<input type="checkbox"/>
Date/Datum:
Signature/Zeichen:

appropriately chosen reference point \mathbf{q}_0 , for example, the equilibrium geometry of the initial state. It is plausible to use normal modes for nuclear coordinates. Then, up to the linear term in normal mode coordinates, the SOCME is [29]

$$\begin{aligned} \langle T_b^k, \{v_{bk}\} | \hat{H}_{SO} | S_a, \{v_{aj}\} \rangle &= \langle T_b^k | \hat{H}_{SO} | S_a \rangle |_{\mathbf{q}_0} \langle \{v_{bk}\} | \{v_{aj}\} \rangle \\ &+ \langle \{v_{bk}\} | \mathbf{b}^\dagger \mathbf{Q}_S | \{v_{aj}\} \rangle \\ &+ \dots \end{aligned} \quad (8.7)$$

where the vector \mathbf{Q}_S contains normal mode coordinates of the singlet electronic state and \mathbf{b}^\dagger is the adjoint of the vector comprising the first-order derivative couplings:

$$b_m = \left. \frac{\partial \langle T_b^k | \hat{H}_{SO} | S_a \rangle}{\partial (\mathbf{Q}_S)_m} \right|_{\mathbf{q}_0} \quad (8.8)$$

If the Taylor expansion is truncated after the linear term, the ISC rate for a singlet–triplet transition is a sum of three contributions due to (i) a direct term k_{ISC}^{dir} , (ii) a mixed direct-vibronic $k_{ISC}^{\text{dir/vib}}$, and (iii) a vibronic coupling term k_{ISC}^{vib} , where the direct term is identical to the expression in Eq. (8.3) and the latter two are given by

$$\begin{aligned} k_{ISC}^{\text{dir/vib},\alpha} &= \frac{4\pi}{\hbar Z} \langle T_b^k | \hat{H}_{SO} | S_a \rangle |_{\mathbf{q}_0} \sum_{j,k} e^{-\beta E_j} \langle \{v_{bk}\} | \{v_{aj}\} \rangle \\ &\times \langle \{v_{bk}\} | \mathbf{b}^\dagger \mathbf{Q}_S | \{v_{aj}\} \rangle \delta(E_{aj} - E_{bk}) \end{aligned} \quad (8.9)$$

$$k_{ISC}^{\text{vib},\alpha} = \frac{2\pi}{\hbar Z} \sum_{j,k} e^{-\beta E_j} |\langle \{v_{bk}\} | \mathbf{b}^\dagger \mathbf{Q}_S | \{v_{aj}\} \rangle|^2 \delta(E_{aj} - E_{bk}) \quad (8.10)$$

Note that all SOCMEs between the singlet state and the Cartesian components of the triplet state are purely imaginary. This is of particular importance when computing the mixed direct-vibronic contributions. Again, due to spin symmetry, there are no cross terms between different Cartesian components in first order. Save for a factor of 1/3 that takes account of the degeneracy of the three triplet fine-structure levels, a similar expression is obtained for the rISC starting from the triplet state.

Numerous examples have been found in heteroaromatic molecules where El-Sayed forbidden $^1(\pi\pi^*) \leftrightarrow ^3(\pi\pi^*)$ ISC processes have rate constants that are nearly as large as those of El-Sayed allowed transitions [39–45]. In most cases, vibronic interaction with an energetically close-lying ($n\pi^*$) excited state through out-of-plane molecular vibrations enhances the transition probability. Even if no n-type orbitals are available, as, e.g. in pure hydrocarbons, pyramidalization of unsaturated carbon centers in the excited state can lead to a substantial increase of electronic SOCMEs [46–48].

8.2.3 Computation of ISC and rISC Rate Constants

ISC and rISC rate constants are highly sensitive with respect to the relative location of the singlet and triplet states. It is, therefore, of utter importance to employ

Druckfreigabe/approval for printing	
Without corrections/ ohne Korrekturen	<input type="checkbox"/>
After corrections/ nach Ausführung der Korrekturen	<input type="checkbox"/>
Date/Datum:
Signature/Zeichen:

reliable electronic structure methods for the computation of the excited-state potentials (see Section 8.3).

8.2.3.1 Classical Approach

In the high-temperature limit, the expression for the singlet–triplet ISC rate constant in Eq. (8.2) reduces to [49]

$$k_{\text{ISC}}^{\text{class.}} = \frac{\sqrt{\pi}}{\hbar\sqrt{\lambda RT}} |\langle \Psi_b | \hat{H}_{\text{SO}} | \Psi_a \rangle|_{q_0}^2 \exp \left[-\frac{(\Delta E_{\text{ab}} - \lambda)^2}{4\lambda RT} \right] \quad (8.11)$$

Herein, ΔE_{ab} is the adiabatic energy difference between the singlet and the triplet state and λ denotes the Marcus reorganization energy that can – to first approximation – be equated with the energy variation in the initial singlet excited state when switching from the singlet equilibrium geometry to the triplet equilibrium geometry [49, 50]. In TADF compounds, the reorganization energy λ can adopt minuscule values because ^1CT and ^3CT states often exhibit similar equilibrium geometries.

8.2.3.2 Static Approaches

The method for computing ISC rate constants, applied in our laboratories, is based on the generating function formalism and the multimode harmonic oscillator approximation [51]. Herein, the triplet state mass-weighted normal modes \mathbf{Q}_{T} with frequencies ω_{T_i} are related to their singlet counterparts by a Duschinsky transformation [52]. The Duschinsky transformation $\mathbf{Q}_{\text{T}} = \mathbf{J}\mathbf{Q}_{\text{S}} + \mathbf{D}$, where \mathbf{J} is the Duschinsky rotation matrix and \mathbf{D} the displacement vector, is particularly important for pairs of states with strongly displaced minimum geometries.

Rates are obtained by numerical integration of the autocorrelation function in the time domain. This approach can even be applied to molecules with a large number of normal modes or to pairs of states that exhibit a large adiabatic energy gap. In these cases, the density of states becomes enormous, and a direct summation over all final vibrational states – even in a small energy interval around the initial state – is prohibitive. The generating function formalism is also applicable to finite-temperature conditions that are essential for uphill processes such as rISC. Herein, a Boltzmann population of vibrational levels in the initial state is assumed [53]. The derivation of the formulas for the direct, mixed direct-vibronic, and vibronic ISC rates in the finite-temperature case can be found in Ref. [29]. A similar correlation function approach for computing rate constants of direct and vibronic ISC has been pursued by Shuai and coworkers [43].

8.2.3.3 Dynamical Approaches

Alternatively, nonadiabatic nuclear dynamics methods have been employed for determining the kinetic constants of ISC and rISC processes [54–56]. Herein, a diabaticization scheme has been used to avoid the explicit calculation of nonadiabatic coupling matrix elements [57], and wavepacket dynamics simulations have been carried out within the framework of the multiconfiguration time-dependent Hartree (MCTDH) method [58]. We refrain from going into details here because these methods are reviewed in Chapter 9.

Druckfreigabe/approval for printing	
Without corrections/ ohne Korrekturen	<input type="checkbox"/>
After corrections/ nach Ausführung der Korrekturen	<input type="checkbox"/>
Date/Datum:	
Signature/Zeichen:	

8.3 Excitation Energies and Radiative Rate Constants

8.3.1 Time-Dependent Density Functional Theory

It is well known that time-dependent density functional theory (TDDFT) yields substantial errors for the excitation energies of CT states, when approximate standard exchange-correlation functionals are used [59]. The balanced description of CT and locally excited (LE) states remains to be a challenge for TDDFT methods, even if used in conjunction with modern hybrid and range-separated density functionals. Huang et al. [60] systematically correlated calculated and experimental singlet- and triplet-transition energies of 17 CT compounds with the aim to find a recipe for the computational prediction of these quantities. They employed TDDFT using density functionals with varying amount of Hartree-Fock (HF) exchange ranging from 0% (BLYP) to 100% (M06-HF). They propose to determine the optimal percentage of HF exchange semiempirically from a comparison of the calculated vertical S_1 energy with the measured absorption maximum and to use this value for scaling the HF contribution to the exchange-correlation functional. Within the chosen set of molecules, optimal HF contributions between approximately 5% and 40% were found. This semiempirical procedure seems to work well, but it becomes very involved if also LE states play a role. In that case, the authors recommend employing distinct HF contributions for the different types of states.

Moral et al. [61] advocate the use of TDDFT in Tamm-Dancoff approximation (TDA) instead of full linear response TDDFT. They tested the performance of these approaches on a small set of organic molecules with experimentally known singlet-triplet splitting. Among them were three typical host materials with moderately high ΔE_{ST} values (0.5–0.7 eV) as well as three TADF emitters with low ΔE_{ST} values (0.1–0.3 eV). In this series, TDDFT-TDA yields a smaller root-mean-square deviation (RMSD) than TDDFT, leading the authors to conclude that TDA is better suited for computing singlet-triplet splittings. It appears questionable, however, whether the unweighted RMSD really represents a good measure for assessing the performance of different methods on this property. Owing to their significantly larger ΔE_{ST} values, the host materials dominate the error analysis. Looking at the raw data of these authors, a different picture emerges. The PBE0 functional is the only one for which both types of calculations have been carried out. Indeed, TDDFT-TDA reproduces the singlet-triplet splittings of the three host materials to a better extent than TDDFT, whereas TDDFT performs better for the three TADF emitters. If the focus is laid on vertical singlet excitation energies, the performance of TDA is very unsatisfactory. In conjunction with the B2-PLYP functional [62], the excitation energies of TADF materials are underestimated by up to 0.7 eV, whereas those of the host materials are somewhat overestimated. TDDFT-TDA performs better for TADF molecules if the B2GP-PLYP functional [63] is employed instead, but then the excitation energies of the host materials are largely overestimated (by up to 0.5 eV). Further investigations are necessary for a sound judgment because the set is too small for being really representative.

Druckfreigabe/approval for printing	
Without corrections/ ohne Korrekturen	<input type="checkbox"/>
After corrections/ nach Ausführung der Korrekturen	<input type="checkbox"/>
Date/Datum:
Signature/Zeichen:

8.3.2 DFT-Based Multireference Configuration Interaction

The combined density functional theory and multireference configuration interaction (DFT/MRCI) method of Grimme and Waletzke is a well-established semiempirical quantum chemical method for efficiently computing excited-state properties [64]. The MRCI expansion is based on MOs from a closed-shell Kohn–Sham DFT calculation employing the BHLYP hybrid functional [65]. In the Hamiltonian, BHLYP orbital energies are utilized to incorporate parts of the dynamical electron correlation. Parameters that scale the Coulomb and exchange integrals and damp off-diagonal matrix elements have been introduced in the Hamiltonian to avoid double counting of the electron correlation. These parameters were fitted to experimental data. Independent benchmark studies on a representative set of organic molecules confirmed that the mean absolute error for DFT/MRCI electronic excitation energies lies below 0.2 eV [66]. A distributed memory parallel code facilitates the calculation of electronic spectra of larger molecules [67]. The average deviation is somewhat larger for first- and second-row TM complexes, but Escudero and Thiel found the DFT/MRCI method to be superior to the tested TDDFT approaches and thus recommended it for exploring the excited-state properties of TM complexes [68]. This even holds true for third-row TM complexes, if spin–orbit interaction is included that cannot be neglected in heavy-element compounds [69, 70]. Furthermore, DFT/MRCI is one of the few electronic structure methods applicable to large systems that gives the correct order of excited states in extended polyenes and polyacenes where doubly excited configurations play an essential role [67, 71].

While the method performs very well in general, it may be problematic when treating the donor–acceptor systems with small orbital density overlap that are key components of metal-free TADF OLEDs. Caution is advised if double excitations with four open shells contribute to the DFT/MRCI wave function with substantial weight or if singlet-coupled CT excitations exhibit lower energies than their triplet counterparts. Recently, an alternative form of correcting the matrix elements of an MRCI Hamiltonian that is built from a Kohn–Sham set of orbitals was devised in our laboratory [72]. The new parameterization is spin invariant and incorporates less empiricism compared with the original formulation while preserving its high computational efficiency. The robustness of the original and redesigned Hamiltonians has been tested on experimentally known vertical excitation energies of organic molecules yielding similar statistics for the two parameterizations [72, 73]. Besides that, the new formulation is free from artifacts related to doubly excited states with four open shells, producing qualitatively correct and consistent results for excimers and covalently linked multichromophoric systems.

Long-range interactions are not well represented by either of the two parameterized Hamiltonians. Asymptotically, DFT/MRCI performs like the underlying BHLYP functional. For charge-separated systems this means that the energy increases with $1/2R$ instead of $1/R$ where R is the distance between the two charged subsystems. Furthermore, dispersion interactions are not properly taken care of by DFT/MRCI. The latter problem may be easily remedied, for example, by adding the semiempirical Grimme D3 dispersion correction [74].

Druckfreigabe/approval for printing	
Without corrections/ ohne Korrekturen	<input type="checkbox"/>
After corrections/ nach Ausführung der Korrekturen	<input type="checkbox"/>
Date/Datum:
Signature/Zeichen:

8.3.3 Fluorescence and Phosphorescence Rates

Similar to ISC and rISC rate constants, also rate constants for radiative transitions can be derived in the framework of time-dependent perturbation theory. Herein, the vector potential for the motion of the electrons in the external electromagnetic radiation field is used as perturbation operator instead of \hat{H}_{SO} . Typically, one proceeds by a multipole expansion of the interaction, with the electric dipole operator as the leading term. The rate constant for spontaneous emission from a manifold of thermally populated initial vibronic states $|\Psi_a, \{v_{aj}\}\rangle$ to a quasi-continuum of final vibronic states $\langle\Psi_b, \{v_{bk}\}|$ due to electric dipole interaction is then given by

$$k_{\text{rad}} = \frac{4\alpha\omega^3}{3c^2Z} \sum_{j,k} e^{-\beta E_j} |\langle\Psi_b, \{v_{bk}\} | \hat{\mu} | \Psi_a, \{v_{aj}\}\rangle|^2 \delta(E_{aj} - E_{bk} - \hbar\omega) \quad (8.12)$$

where ω is the radiation frequency, α is the fine-structure constant, c is the speed of light, and the other symbols have the same meaning as in Eq. (8.1). The procedure for simplifying the expression in Eq. (8.12) further by a Taylor expansion with respect to mass-weighted normal coordinates is similar to that described in Section 8.2. Formulas for radiative transition rates in Franck–Condon (FC) or Herzberg–Teller approximation, respectively, can readily be derived.

Once the electronic wave functions have been obtained, it is straightforward to compute the electric dipole coupling matrix elements for fluorescence emission. If wave functions are not available – which is the case in TDDFT and coupled-cluster approaches – the electronic transition rates can be computed by means of linear response theory [75]. Typical fluorescence rate constants for emission from LE $^1(\pi\pi^*)$ states are of the order of 10^8 – 10^9 s $^{-1}$, whereas they are several orders of magnitude smaller for $^1(n\pi^*)$ states. Because of competing nonradiative processes, the latter states are optically dark in most cases. The fluorescence rates of ^1CT state depend critically on the overlap of the electron density distributions of the orbitals involved in the transition. If that overlap is small, fluorescence rates of 10^5 – 10^6 s $^{-1}$ are expected at most.

In the context of spin-forbidden transitions, the coupling matrix element in Eq. (8.12) requires a bit of attention. In this case, multiplicity-mixed electronic wave functions need to be employed. They are complex-valued in general. The fundamentals regarding selection rules and intensity borrowing from spin-allowed transitions have been worked out in detail in Ref. [30] and need not be repeated here. Nevertheless, it is instructive to compare phosphorescence from a $^3(n\pi^*)$, a $^3(\pi\pi^*)$, and a ^3CT state to the electronic ground state S_0 . According to the El-Sayed rules (see Section 8.2.1.1), the $^3(n\pi^*)$ state exhibits sizeable SOCMs with the electronic ground state and electronically excited $^1(\pi\pi^*)$ states. Large contributions to the electric transition dipole matrix element can originate from two terms: (i) the mutual spin–orbit interaction of $^3(n\pi^*)$ and S_0 multiplied by the difference of the static dipole moments of these states and (ii) the spin–orbit interaction of $^3(n\pi^*)$ with optically bright $^1(\pi\pi^*)$ states from which intensity can be borrowed. In heteroaromatic compounds, thus phosphorescence rates of 10^3 s $^{-1}$ can be achieved. For a $^3(\pi\pi^*)$ state, the direct spin–orbit interaction with S_0 is very small so that term (i) can be neglected. With regard

Druckfreigabe/approval for printing	
Without corrections/ ohne Korrekturen	<input type="checkbox"/>
After corrections/ nach Ausführung der Korrekturen	<input type="checkbox"/>
Date/Datum:
Signature/Zeichen:

AQ1

to term (ii), it is seen that ${}^3(\pi\pi^*)$ exhibits sizeable SOCMEs with ${}^1(n\pi^*)$ states, but the latter are optically dark. Therefore, the probability of a spin-forbidden radiative decay is much smaller for a ${}^3(\pi\pi^*)$ state, with rates typically below 1 s^{-1} . The same applies to ${}^3\text{CT}$ states of purely organic donor–acceptor systems. The shortrangedness of the spin–orbit interaction makes the contributions of type (i) vanish, despite the pronounced static dipole moment difference of the ${}^3\text{CT}$ and S_0 states. In contrast, phosphorescence from ${}^3\text{MLCT}$ states of TM complexes can acquire substantial probability through configuration interaction. The transition dipole moment may adopt sizable values originating from the combination of $\langle S_0|\hat{\mu}|{}^1(d'\pi^*)\rangle$ and $\langle {}^1(d'\pi^*)|\hat{H}_{\text{SO}}|{}^3(d\pi^*)\rangle$ in MLCT transitions. Also the direct, first (i)-type interaction of the ${}^3\text{MLCT}$ state with the electronic ground state can play a role, because the SOCMEs $\langle S_0|\hat{H}_{\text{SO}}|{}^3(d\pi^*)\rangle$ may not be negligible. Depending on the amount of configuration mixing and the size of the SOCMEs, phosphorescence rates of 10^4 – 10^6 s^{-1} can be reached in these complexes.

Although the concept of intensity borrowing from spin-allowed transitions is very transparent if Rayleigh–Schrödinger perturbation theory is applied to expand the multiplicity-mixed wave functions in terms of pure \hat{S}^2 eigenfunctions, this is not the procedure followed in practice. The reason is that the (in principle) infinite perturbation sums converge very slowly with respect to the number of electronic states. In an actual calculation, it is more advantageous to use methods that avoid an explicit summation over states such as multireference spin–orbit configuration interaction (MRSOCI) [76] or quadratic response theory [77, 78].

8.4 Case Studies

In the following, a brief literature survey on the results of quantum chemical studies on TADF emitters will be given before turning to a review of our own recent (and still ongoing) work in more detail. For a few prototypical cases, spin-dependent multiconfigurational electronic structure methods have been employed to describe the electronically excited-state potentials and their couplings. These data are used as input for Fourier transform methods that enable us to determine rate constants of radiative and nonradiative transitions and thus may further the understanding of the photophysical processes in TADF emitters.

8.4.1 Copper(I) Complexes

Various organometallic complexes based upon d^{10} metal ions were found to show TADF, the most abundant ones being Cu(I) complexes [15–17]. Among them are four-coordinated but also three-coordinated bis-phosphine complexes [79–87] and bridged bimetallic Cu(I) complexes of type $\text{Cu}_2\text{X}_2(\text{N}^{\wedge}\text{P})_2$ ($\text{X} = \text{Hal}$) [88, 89]. On the basis of combined DFT and TDDFT calculations, it was concluded that restricted flexibility of four-coordinated Cu(I)–bis-imine–bis-phosphine complexes leads to a reduction of nonradiative deactivation and thus an increase

Druckfreigabe/approval for printing	
Without corrections/ ohne Korrekturen	<input type="checkbox"/>
After corrections/ nach Ausführung der Korrekturen	<input type="checkbox"/>
Date/Datum:
Signature/Zeichen:

of emission quantum yield [83]. In threefold-coordinated Cu(I) complexes with a sterically demanding monodentate N-heterocyclic carbene (NHC) ligand and a heterocyclic bidentate ligand, the relative orientation of the ligands seems to decide whether TADF or phosphorescence is observed [90–93]. In the phosphorescent complexes, the conformational analysis indicates a nearly free rotation about the $C_{\text{NHC}}\text{—Cu}$ bond in solution [91]. Conformational flexibility appears to be also the key to understanding the photophysical properties of three-coordinate thiolate Cu(I) complexes that give bright blue emission at 77 K and orange emission at ambient temperature [94]. Very recently, even highly efficient blue luminescence of two-coordinated Cu(I) complexes has been reported [95].

Most experimental works on these complexes are accompanied by some Kohn–Sham DFT calculations that focus on the nature of the highest occupied molecular orbital (HOMO) and the lowest unoccupied molecular orbital (LUMO). This bears some danger because numerous examples are known in the literature showing that the lowest electronically excited state does not necessarily originate from a HOMO–LUMO transition [44, 71]. Proceeding with due caution, it is preferable to use TDDFT or – even better – approximate coupled-cluster methods or DFT/MRCI to characterize the excited states. In several cases, TDDFT has been employed to determine singlet–triplet energy gaps ΔE_{ST} of Cu(I) complexes [83, 84, 88, 93, 96, 97]. Gneuß et al. found a good correlation between computed triplet emission wavelength, as obtained from TDDFT in conjunction the B3LYP functional, and measured peak maxima in a new class of luminescent mononuclear copper(I) halide complexes with tripodal ligands [96]. Quantum chemical studies of Cu(I) complexes that explicitly take account of spin–orbit interaction are very rare, however. To our knowledge, there is only a series of papers studying the emission properties of four-coordinated Cu(I)–bis-phenanthroline complexes [54, 55, 98, 99] and our own work on luminescent Cu(I)–NHC complexes [100]. In the following, these cases will be analyzed in more detail.

8.4.1.1 Three-Coordinated Cu(I)–NHC–Phenanthroline Complex

Using the methods described in Sections 8.2 and 8.3, recently Föller et al. [100] conducted a thorough quantum chemical study on the photophysical behavior of a luminescent Cu(I) complex comprising an NHC and a phenanthroline ligand (Figure 8.2). This complex had been investigated experimentally by Krylova et al. [90] who also performed DFT calculations and assigned the luminescence to originate from an MLCT state. The bulky isopropylphenyl substituents on the imidazol-2-ylidene ligand are essential for the relative orientation of the NHC and phenanthroline ligands. Substitution by methyl or even phenyl substituents in 1,3-position of the NHC leads to a barrierless torsional relaxation of the excited triplet and singlet states yielding a perpendicular conformation of the two ligands. Dispersion, included in the calculations by means of the semiempirical Grimme D3 correction [74], is seen to have a small but differential effect on the torsion potentials in the ground and excited states. It preferentially lowers the coplanar arrangement of the ligands and increases the barrier between the two minima on the excited-state potential energy surface. Qualitatively, this trend is easily understood. In the coplanar nuclear arrangement, the hydrogen atoms

Color Fig: 8.2

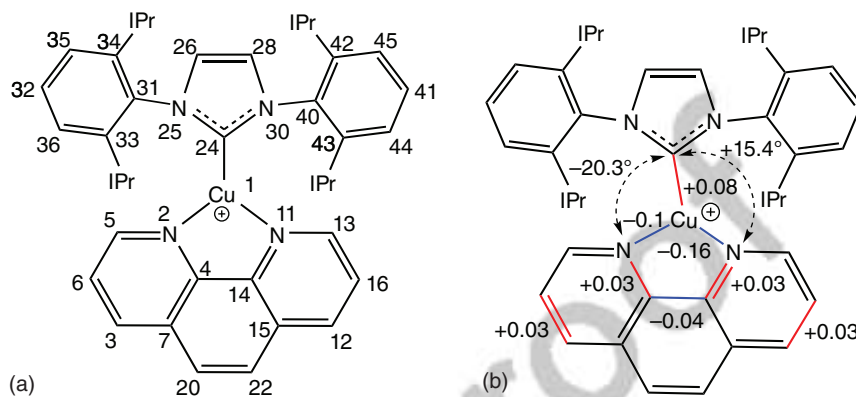


Figure 8.2 (a) Chemical structure of the Cu(I)-NHC-phenanthroline complex and (b) important differences in the coplanar S_0 and T_1 minimum nuclear arrangements according to Ref. [100]. Source: Ref. [100]. Reproduced with permission of American Chemical Society.

AQ2

in positions 5 and 13 of the phenanthroline ligand (Figure 8.2a) directly point toward the aromatic π system of the isopropylphenyl substituents of the NHC ligand, whereas these are far apart when the NHC and phenanthroline ligands are oriented in a perpendicular fashion.

The spin-free vertical excitation spectra were calculated by means of the original DFT/MRCI method [64, 67]. SOC was included in the calculation of absorption spectra at the level of quasi-degenerate perturbation theory (QDPT) using the in-house SPOCK [101, 102]. Fluorescence and phosphorescence rates were obtained at the MRSOCI level [76]. FC emission profiles and temperature-dependent ISC and rISC rates were determined in harmonic approximation by means of a Fourier transform approach [51, 103].

The experimental absorption spectrum [90] and calculated spectra at scalar relativistic level and including SOC effects are displayed in Figure 8.3. They are seen to match perfectly, showing that the applied quantum chemical methods are very well suited for studying these complexes. Very weak bands between 400 nm and 500 nm were assigned to triplet MLCT states. In the calculated FC spectrum, the electronic excitations to the S_1 , T_1 , and T_2 states lie between 400 nm and 420 nm but have small oscillator strengths so that they are barely visible in Figure 8.3. At the ground-state equilibrium geometry, S_1 and T_2 may be characterized as $d/\sigma \rightarrow \pi^*(\text{phen})$ single excitations where d/σ is a linear combination of a d_{xy} -like orbital of copper with in-plane p orbitals of the phenanthroline (phen) nitrogens. At this point, T_1 results from a $d/\pi \rightarrow \pi^*(\text{phen})$ excitation where d/π is a d_{xz} -like orbital with π contributions located at the phenanthroline and NHC ligands. Following the line of arguments in Section 8.2.1.1, substantial spin-orbit interaction is expected between the T_1 and S_1 states because their coupling involves a change of orbital angular momentum. This is the case, indeed, at the FC point. However, a slight geometry distortion is sufficient to reverse the order of the two triplet states. Henceforth, we renumerate the states according to the order of their adiabatic minima. The main configurations of the relaxed S_1 and T_1 states

Color Fig. 8.3

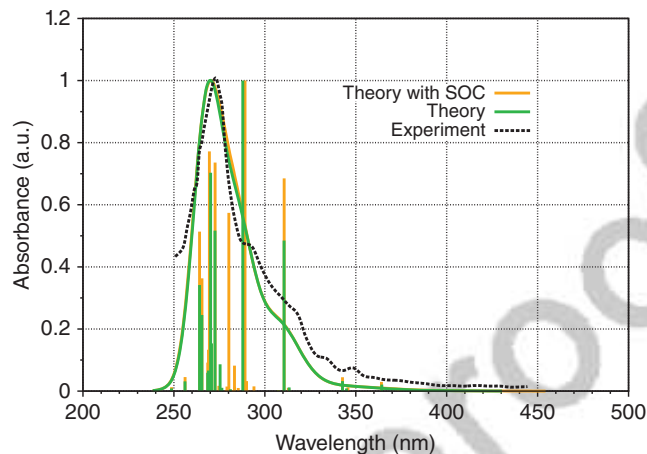


Figure 8.3 Absorption spectrum of the Cu(I)-NHC-phenanthroline complex shown in Figure 1.2a. The experimental data points were read from Ref. [90]. Note that the theoretical spectra have not been shifted but are displayed as calculated.

Color Fig. 8.4

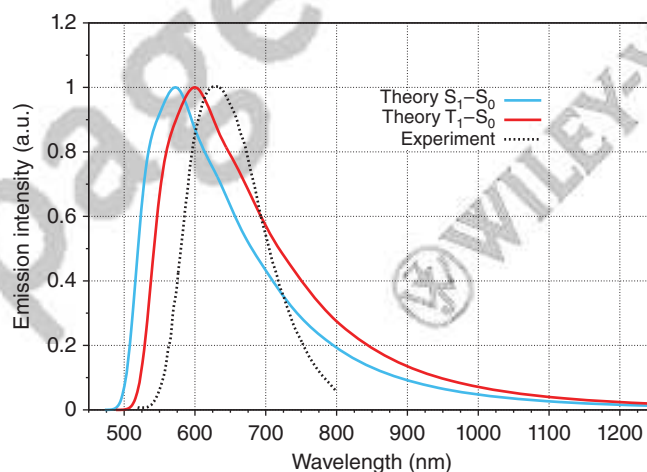


Figure 8.4 Emission spectra of the Cu(I)-NHC-phenanthroline complex shown in Figure 1.2b. The experimental data points were read from Ref. [90].

are $d/\sigma \rightarrow \pi^*(\text{phen})$ excitations. The excited-state minima with torsion angle of 0° show a T-shaped distortion of the three-coordinated Cu(I), as suggested by Krylova et al. [90].

The perpendicular arrangement constitutes a saddle-point on the electronic ground-state potential energy surface located approximately 0.35 eV above the minimum. In the excited states, this arrangement of the ligands yields a local minimum. It is separated from the global minimum with coplanar arrangement of the ligands only by a shallow barrier (c. 0.12 eV) that is easily overcome by thermal activation. However, comparison of the theoretical and experimental

emission spectra (Figure 8.4) clearly shows that the complex emits preferentially in a coplanar arrangement of the NHC and phen ligands.

The singlet–triplet splitting changes only slightly along the path, namely, from 650 cm^{-1} at 0° to 830 cm^{-1} at 90° , in contrast to the observations of Leitl et al. [93] in a related Cu(I)–NHC–dipyridyldimethylborate complex. These authors report an increase from 540 cm^{-1} at 0° to 3700 cm^{-1} at 70° torsion angle. The different behavior of the two complexes can be explained by the different electron density distributions of the frontier orbitals. In the Cu(I)–NHC–phen complex, the density of the HOMO is mainly located at copper and the LUMO at the phen ligand, which does not change so much during the torsion (Figure 8.5). Correspondingly, only a small increase of the energy gap is found. In contrast, the orbital overlaps of the Cu(I)–NHC–dipyridyldimethylborate increases considerably upon torsion [93]. In that case, the LUMO is located at the NHC ligand and the HOMO of the 90° geometry has substantial additional density at the NHC ligand. Adiabatically, the singlet–triplet splitting exhibits a value of merely 0.08 eV in the Cu(I)–NHC–phen complex. As the energy gap between the S_1 and T_1 states is so small, TADF might be possible, and therefore phosphorescence and fluorescence as well as ISC and rISC rates were investigated for both the coplanar (torsion angle 0°) and perpendicular (torsion angle 90°) arrangement of the ligands by Föller et al. [100].

Figure 8.6 provides an overview over the computed rate constants in the coplanar arrangement of the ligands at room temperature. Kirchhoff et al. [104] carefully analyzed the kinetics of a three-level system relating to TADF. They concluded that the steady-state emission properties of the three-level system depend upon the relative values of the various rate constants as well as the relative energies of the levels and considered two limiting cases, the kinetic limit and the equilibrium limit. The basic assumption in the kinetic limit case is that the S_1 state achieves a steady-state concentration that is negligibly affected by the rISC process. Most of the photons would then appear from prompt fluorescence or phosphorescence. The decay of the Cu(I)–NHC–phen complex reaches

Color Fig: 8.5

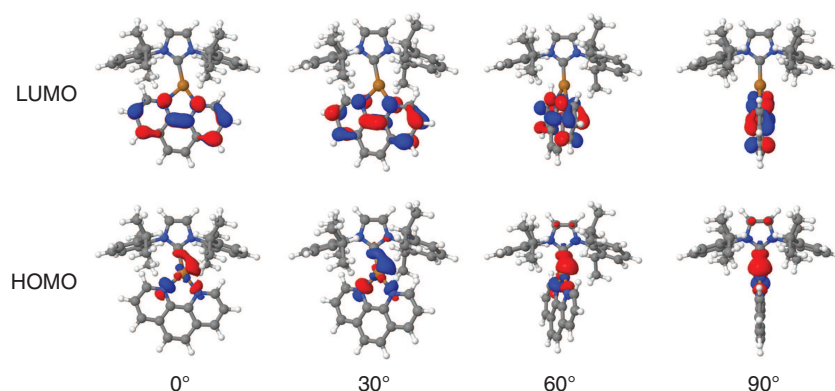


Figure 8.5 Frontier orbital densities of the Cu(I)–NHC–phenanthroline complex for different torsion angles according to Ref. [100]. *Source:* Ref. [100]. Reproduced with permission of American Chemical Society.

Color Fig. 8.6

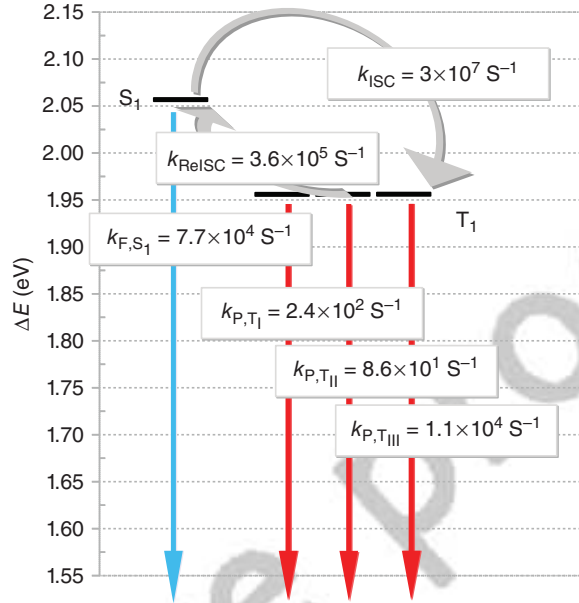


Figure 8.6 Computed rate constants (298 K) of the Cu(I)-NHC-phenanthroline complex in the coplanar T_1 minimum nuclear arrangement according to Ref. [100]. Source: Ref. [100]. Reproduced with permission of American Chemical Society.

nearly the kinetic limit at 77 K, as k_{ISC} are several orders of magnitude smaller than k_{F} and k_{ISC} . In contrast, the equilibrium limit case where the steady-state populations of the S_1 and T_1 states are determined by Boltzmann statistics appears to be more appropriate at room temperature. For this limit case to be adequate, $k_{\text{ISC}} \gg k_{\text{F}} + k_{\text{IC}_0}$ and $k_{\text{ISC}} \gg k_{\text{P}} + k_{\text{ISC}_0}$. We have not calculated the rate constants for the internal conversion (IC) of S_1 to S_0 (k_{IC_0}) and for the ISC from T_1 to S_0 (k_{ISC_0}). Because of the substantial energy gap between the S_1 and T_1 states on the one hand and the electronic ground state on the other hand, these processes are assumed to be much slower than the radiative decay rates and will be neglected in the following. The first condition for the equilibrium limit, namely, $k_{\text{ISC}} \gg k_{\text{F}}$ is certainly fulfilled at all temperatures, but the second condition $k_{\text{ISC}} \gg k_{\text{P}}$ is not (Figure 8.6). In such case, formula

$$\tau(T) = \frac{3 + \exp[-\Delta E(S_1 - T_1)/k_{\text{B}}T]}{\frac{3}{\tau(T_1)} + \frac{1}{\tau(S_1)} \exp[-\Delta E(S_1 - T_1)/k_{\text{B}}T]} \quad (8.13)$$

used by many experimentalists to fit the energy gap between the S_1 and T_1 states $\Delta E(S_1 - T_1)$, and the decay times of the individual states from the temperature dependence of the total emission decay time [84] are not valid at low temperatures.

The respective quantum yields were calculated instead following the kinetic analysis of Hirata et al. [105]. In deriving their expression for the TADF quantum yield Φ_{TADF} in relation to the triplet quantum yield Φ_{T} , the authors assumed that the IC from the S_1 state to the electronic ground-state S_0 can be neglected and that the ISC from S_1 to T_1 is much faster than the reverse process. Neglecting the nonradiative deactivation of the T_1 sublevels, but taking account of their

Druckfreigabe/approval for printing	
Without corrections/ ohne Korrekturen	<input type="checkbox"/>
After corrections/ nach Ausführung der Korrekturen	<input type="checkbox"/>
Date/Datum:
Signature/Zeichen:

phosphorescence decay through the averaged high-temperature limit of the individual rate constants, one arrives at

$$\frac{\Phi_{\text{TADF}}}{\Phi_{\text{P}}} = \frac{1}{\frac{k_{\text{P,av}}}{k_{\text{rISC}}\Phi_{\text{PF}}} + 1} \quad (8.14)$$

For 298 K our calculated quantum yield of prompt fluorescence Φ_{PF} is quite small, only 0.3%. The quantum yield for the deactivation via phosphorescence is 77.7%, and the remaining 22% are the quantum yield for TADF. This may explain why Krylova et al. [90] classify this complex as phosphorescent emitter.

The emission quantum yield Φ_{em} is related to the radiative and nonradiative decay rate constants by

$$\Phi_{\text{em}} = \frac{k_{\text{r}}}{k_{\text{nr}} + k_{\text{r}}} = \frac{\tau_{\text{r}}}{\tau} \quad (8.15)$$

Using this relation, intrinsic radiative lifetimes τ_{r} can be deduced from the knowledge of the experimental emission decay time constant τ and the quantum yield Φ_{em} . The τ_{r} can directly be compared with theoretical values. In the present example, Krylova et al. [90] had determined values of $\tau = 0.08 \mu\text{s}$ with $\Phi_{\text{em}} < 0.001$ in CH_2Cl_2 and of $\tau = 1.2 \mu\text{s}$ with $\Phi_{\text{em}} = 0.026$ in crystals at room temperature. Using Eq. (8.15), intrinsic radiative lifetimes of $>80 \mu\text{s}$ in CH_2Cl_2 at 300 K and of $\approx 46 \mu\text{s}$ in the crystalline state can be derived. These values compare better with the calculated fluorescence lifetime of $\tau_{\text{F}} = 11 \mu\text{s}$ than with the calculated phosphorescence lifetime of $\tau_{\text{p}} = 267 \mu\text{s}$ [100].

Summarizing, it is found that the excited singlet and triplet populations of the three-coordinated Cu(I)-NHC-phen complex have time to equilibrate before they decay radiatively to the electronic ground state. TADF is possible, but it competes with phosphorescence that is the dominating radiative decay channel. As discussed above, torsion of the ligands has only small impact on the singlet-triplet gap. However, the electronic coupling between the S_1 and T_1 states – and hence the probability for (reverse)ISC – is seen to increase substantially when moving from a coplanar to a perpendicular arrangement of the ligands. The quantum chemical analysis by Föller et al. [100] suggests that a perpendicular arrangement of the ligands in a three-coordinate NHC-Cu(I)-(N[^]N) complex is not a hindrance *per se* for observing TADF (in addition to phosphorescence), provided that the electron is transferred to the (N[^]N) ligand in the MLCT transition and not to the NHC ligand.

8.4.1.2 Four-coordinated Cu(I)-bis-Phenanthroline Complexes

In the 1980s, McMillin and coworkers investigated the luminescence of a series of cationic Cu(I)-bis-phen complexes in solution [104]. The emission intensity was found to decrease as the temperature of the solution is lowered, accompanied by a slight redshift in the positions of the emission maxima. The authors interpreted the strong temperature dependence of the solution emission of the cationic bis(2,9-dimethyl-1,10-phenanthroline)copper(I) complex ($\text{Cu}(\text{dmp})_2^+$, Figure 8.7a) in terms of emission from two thermally equilibrated excited states separated by c. 1800 cm^{-1} whereof the lower one was ascribed triplet MLCT

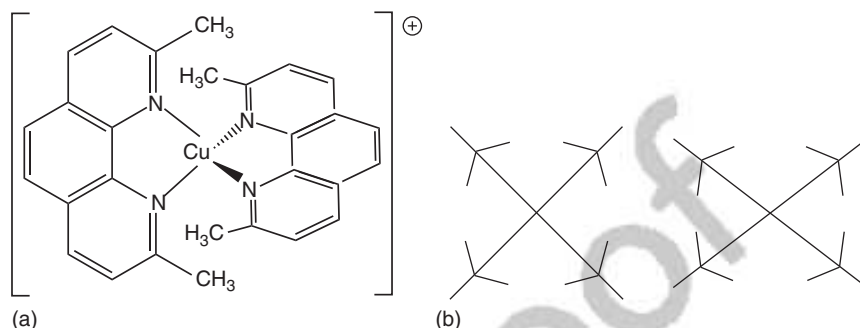


Figure 8.7 (a) Chemical structure of the cationic bis(2,9-dimethyl-1,10-phenanthroline) copper(I) complex and (b) schematic view of the pseudo-Jahn-Teller (PJT) distortion in the MLCT states according to Ref. [98]. *Source:* Ref. [98]. Reproduced with permission of American Chemical Society.

AQ3

and the upper one singlet MLCT character. It was suggested that DF dominates the emission at room temperature.

Owing to a pseudo-Jahn-Teller (PJT) distortion of the copper d^9 electronic configuration, these complexes undergo a fast flattening structural change in the MLCT excited state upon photo excitation (Figure 8.7b). TDDFT calculations revealed that there are four closely spaced triplet states in energetic proximity to the lowest singlet state [106]. Siddique et al. [98] carried out a combined experimental and theoretical study of the $\text{Cu}(\text{dmp})_2^+$ complex including a rough estimate of the spin-forbidden transition probabilities (semiempirical spin-orbit Hamiltonian on Cu only, single-configuration approximation of the wave functions). The dihedral angle of the two ligand planes was found to change from 90° in the electronic ground state to about 75° in the MLCT states. Siddique et al. noticed that the photophysical properties depend strongly on that dihedral angle, the flattening distortion reducing not only the magnitude of the mutual SOCMEs of the lower states but also the transition dipole moment of spin-allowed transition from which the phosphorescence borrows intensity.

In very elaborate theoretical investigations of the photophysics of cationic Cu(I)-bis-phen complexes, Capano et al. [54, 55, 99] used methods for determining the kinetic constants of the excited-state processes differing from those described above. They applied the vibronic coupling Hamiltonian [57] and the quantum dynamics within the framework of the MCTDH method [58] to study the primary excited-state nonadiabatic dynamics following the photoexcitation. To this end, they identified eight important vibrational modes and determined the nonadiabatic coupling coefficients for IC in a linear coupling model [54, 55]. The results of the wavepacket dynamics show that the IC from the initially photoexcited S_3 state to the S_1 state takes place with a time constant of about 100 fs and that ultrafast ISC occurs and competes with structural dynamics associated with the PJT distortion [55]. Approximately 80% of the wave packets are found cross into the triplet state within 1 ps. Further analysis of the MCTDH dynamics results emphasizes the importance of vibronic interactions for the ISC. It suggests that the ISC occurs close to FC point – despite the moderate

Druckfreigabe/approval for printing	
Without corrections/ ohne Korrekturen	<input type="checkbox"/>
After corrections/ nach Ausführung der Korrekturen	<input type="checkbox"/>
Date/Datum:	
Signature/Zeichen:	

size of the SOCMEs – from S_1 to T_2 and T_3 promoted by the motion along a vibrational mode that drives the S_1 state into curve crossings with T_2 and T_3 .

In their latest work, Capano et al. [99] used DFT, TDDFT, as well as classical and quantum mechanics/molecular mechanics (QM/MM) molecular dynamics (MD) simulations to investigate the influence of the geometric and electronic structure, SOC, singlet–triplet gap, and the solvent environment on the emission properties of a series of four-coordinated cationic bis-phen complexes. They systematically varied the parent structure by adding electron-withdrawing or donating substituents. Furthermore, they investigated the influence of long alkyl chains at 2,9-positions of phenanthrolines because they were said [104] to retard the excited-state PJT distortion and to increase the luminescence. In agreement with earlier work by Siddique et al. [98], Capano et al. conclude that the magnitude of the SOC matrix elements depends critically on the dihedral angle between the ligands, thus explaining the bi-phasic ISC observed experimentally to originate from the initially excited and relaxed S_1 structures, respectively. Furthermore, they show that the singlet–triplet gap of the MLCT states is governed by inductive effects of the substituents that also control the oscillator strength of the fluorescence.

It might be interesting to carry out similar theoretical studies for related ($P^{\wedge}P$) complexes in the future. Experimentally, it was shown that the quantum efficiencies of cationic mononuclear copper(I) complexes based on phenanthroline ligands could be increased from about 1% to around 60% when exchanging one of the phenanthrolines by a diphosphineether [108].

8.4.2 Metal-Free TADF Emitters

Electroluminescence from purely organic molecules was detected more than 60 years ago using acridine orange as the emitter [109]. Despite the substantial singlet–triplet splitting of $\approx 2900 \text{ cm}^{-1}$, acridine orange shows relatively strong DF [110]. Most of present-day's metal-free TADF emitters are bi- or multi-chromophoric systems consisting of electronically weakly coupled donor (D) and acceptor (A) subunits that undergo intramolecular charge-transfer (ICT) processes upon electronic excitation. The donor and acceptor subunits are covalently linked in such a way that the respective π systems are (nearly) orthogonal, either by twisted single bonds [19, 105, 111–120] or by a spiro-junction [121–123].

Many TADF molecules exhibit highly twisted structures, because the energetic splitting of a singlet–triplet pair depends on the degree to which the electron density distributions of the involved half-occupied orbitals overlap. However, in an ICT compound also the transition density, and hence the oscillator strength of the emission depends on this quantity. Recognizing that small, but nonnegligible overlap densities between the electronic wave functions of the S_0 and S_1 states may lead to a substantial increase of the fluorescence rate without significantly increasing ΔE_{ST} , Shizu et al. rationally designed highly efficient green and blue TADF emitters [117, 124].

A very instructive experimental investigation of donor–acceptor–donor (D–A–D) and donor–donor–donor (D–D–D) type emitters was carried out

Druckfreigabe/approval for printing	
Without corrections/ ohne Korrekturen	<input type="checkbox"/>
After corrections/ nach Ausführung der Korrekturen	<input type="checkbox"/>
Date/Datum:	
Signature/Zeichen:	

by Dias et al [111]. With one exception, all compounds had a disubstituted heterocyclic core, with the substituents attached either in an angular or linear fashion. In the D–D–D structures, the lowest-lying triplet state is an LE state with $^3(\pi\pi^*)$ characteristics. Nevertheless, all emitters show DF in ethanol solution at room temperature, though with different kinetics. Some exhibit a linear relation of the DF intensity with exciton dose, indicating thermal activation of the DF, whereas others show a quadratic dependence, implicating DF caused by triplet fusion. Particularly striking is the observation of TADF for a compound with a singlet–triplet splitting of 0.84 eV. To explain their observations, Dias et al. [111] postulate an intermediate $^3(n\pi^*)$ state that bridges the gap between the lowest triplet and singlet states in the heteronuclear compounds. Gibson et al. [56] predicted second-order SOC of the singlet and triplet CT states to an intermediate LE $^3(\pi\pi^*)$ state to enhance the ISC and rISC rate constants of a D–A molecule, composed of a phenothiazine (PTZ) donor and a dibenzothiophene-S-S-dioxide DBTO2 acceptor, by several orders of magnitude. The crucial role of vibronic SOC to an energetically close-lying 3LE state for the TADF efficiency of the corresponding D–A–D compound was impressively demonstrated by Etherington et al. [120]. These authors employed host material with temperature-sensitive polarity to tune the LE and CT states of the PTZ-DBTO2-PTZ system in and out of resonance. They could show that the emission intensity goes through a maximum at the zero crossing of the energy difference. The concomitant quantum dynamics studies included spin–orbit interaction between the 3LE and the CT states, vibronic interaction between the two triplet states, and hyperfine interaction between the singlet and triplet CT states as possible coupling terms. The outcome of these studies suggests that hyperfine interaction between the two CT states is by far too small and that the combination of spin–orbit and vibronic interaction is required to effectuate the rISC (compare also Chapter 12).

Also the theoretical study by Chen et al. [125] was motivated by the question why some butterfly-shaped blue D–A–D emitters show TADF properties although their lowest excited triplet state has LE character and the singlet–triplet splitting is substantial. Adachi and coworkers explained this behavior by reverse internal conversion (RIC) from the LE $^3(\pi\pi^*)$ to the 3CT state that then undergoes rISC to the 1CT state [116]. Although the investigated compounds are similar to those studied by Monkman and coworkers [111, 118, 120], Chen et al. [125] come to different conclusions. They computed rISC rates between the T_1 and S_1 states in harmonic oscillator approximation including Duschinsky effects using a Fermi's golden rule expression. Their ansatz is very similar to the one employed in our laboratory, except for the fact that they use two-component TDDFT [126] for computing the electronic coupling matrix elements. Not unexpectedly, the rate of rISC from the T_1 state with LE character to the S_1 state with ICT character is several orders of magnitude too small in Condon approximation. Scanning through the torsional angle between donor and acceptor subunits reveals an intersection of the two lowest triplet potential energy curves at 90° with a maximum for the lowest triplet state. Actually, the authors find a broken-symmetry minimum for T_1 in their D–A–D example. It is argued that the triplet states can approach the intersection by low-frequency motions and that nonadiabatic interactions are

Druckfreigabe/approval for printing	
Without corrections/ ohne Korrekturen	<input type="checkbox"/>
After corrections/ nach Ausführung der Korrekturen	<input type="checkbox"/>
Date/Datum:
Signature/Zeichen:

expected to play a significant role. Rates for vibration-assisted transitions have not been presented, though, in that work [125].

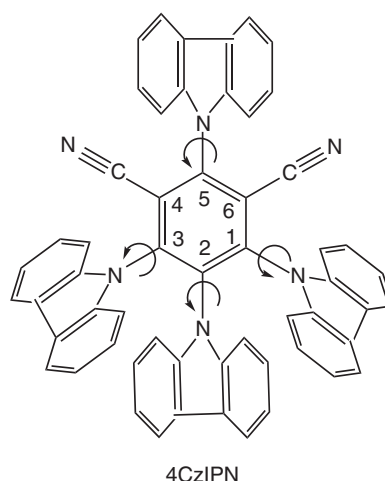
In the following, the photophysics of three metal-free TADF emitters shall be discussed in more detail, namely, of the green TADF emitter 1,2,3,5-tetrakis(carbazol-9-yl)-4,6-dicyanobenzene (4CzIPN) and of the assistant dopants 3-(9,9-dimethylacridin-10(9*H*)-yl)-9*H*-xanthen-9-one (ACRXTN) and 10-phenyl-10*H*,10'*H*-spiro[acridine-9,9'-anthracen]-10'-one (ACRSA). 4CzIPN has very high photoluminescence efficiency in apolar solvents and films [19, 112] and is considered a prototypical donor–acceptor multichromophoric system. ACRXTN, consisting of an acridine donor unit and a xanthone acceptor unit [24], is particularly interesting because of the already very involved photophysical properties of the heteroaromatic xanthone moiety [44]. ACRSA, finally, is one of the few spiro-compounds known to exhibit efficient TADF [122]. These compounds were investigated recently by means of high-level quantum chemical methods in our laboratory with the aim to shine light on some of the underlying mechanisms [127–129]. The (preliminary) results of these studies will be compared with experimental data and – where available – theoretical results from TDDFT calculations.

8.4.2.1 1,2,3,5-Tetrakis(carbazol-9-yl)-4,6-dicyanobenzene (4CzIPN)

Attaching carbazolyl donor units to dicyano-substituted benzene cores as acceptors, Uoyama et al. [19] presented a series of luminescence emitters, their color varying from turquoise to red depending on the number of carbazolyl units and the positions of the cyano substituents. The green emitter 1,2,3,5-tetrakis(carbazol-9-yl)-4,6-dicyanobenzene (4CzIPN, Figure 8.8) turned out to be a TADF emitter with excellent internal quantum efficiency in toluene and in 4,4'-(bis-carbazol-9-yl)biphenyl (CBP) film [19]. OLEDs based on 4CzIPN show high luminance efficiencies and excellent operational stability [130].

4CzIPN is a CT system with small singlet–triplet energy gap, the magnitude of which has been estimated from Arrhenius plots assuming that only T_1 is

Figure 8.8 Chemical structure of the green TADF emitter 1,2,3,5-tetrakis(carbazol-9-yl)-4,6-dicyanobenzene (4CzIPN).



Druckfreigabe/approval for printing
Without corrections/ ohne Korrekturen <input type="checkbox"/>
After corrections/ nach Ausführung der Korrekturen <input type="checkbox"/>
Date/Datum:
Signature/Zeichen:

located energetically below S_1 (see, however, below). The estimates vary slightly depending on the conditions and the solvent. Uoyama et al. [19] report a value of $\Delta E_{ST} = 83$ meV in CBP film, whereas Ishimatsu et al. [112] give a somewhat larger value of 140 ± 19 meV in toluene. Also the measured luminescence lifetimes vary somewhat between the two studies, but the values are in the same ballpark. At room temperature, Uoyama et al. obtain time constants of 17.8 ns for prompt and 5.1 μ s for delayed fluorescence in toluene solution under nitrogen atmosphere, while Ishimatsu et al. report 14.2 ns and 1.82 μ s for these processes, respectively, in the same solvent. Uoyama et al. [19] also carried out quantum chemical calculations. The computed singlet–triplet energy gap depends strongly on the functional used in the TDDFT calculations, ranging from approximately 10 meV for the hybrid functionals B3LYP and PBE0 over 362 meV for M06-2X to 700 meV for the Coulomb attenuated CAM-B3LYP in the gas phase. Likewise, the computed vertical emission wavelengths vary substantially with the functional, ranging from 731 nm (B3LYP) to 430 nm (M06-2X) and 420 nm (ω B97X-D).

The energy gap law [34] states that in the weak coupling regime, that is, for small coordinate displacements, the rate of nonradiative transition between two electronic states decreases exponentially with their increasing energy separation (see also Section 8.2.1.2). This does not necessarily mean, however, that a smaller energy gap automatically leads to improved luminescence properties of a TADF emitter. A detailed experimental and theoretical study investigating the solvent effects on TADF in 4CzIPN revealed a surprising trend with regard to the efficiency of the delayed fluorescence. Ishimatsu et al. [112] observe larger Stokes shifts of the emission in polar solvents compared with toluene suggesting stronger ICT in the excited state. Concomitantly, the activation energy for rISC is lowered. However, despite the smaller magnitude of ΔE_{ST} in polar solvents, the photoluminescence quantum yield decreases from 94% in toluene solution over 54% in dichloromethane and 18% in acetonitrile to 14% in ethanol. Using TDDFT in conjunction with the M06-2X functional and modeling the solvent–solute interaction by a polarizable continuum model [131, 132], they also computed absorption and emission energies for 4CzIPN in these solvents. The authors consistently explain the experimentally observed trends for ΔE_{ST} , the emission wavelength, and the photoluminescence quantum yields by increasing ICT character of the excited states with increasing solvent polarity, leading in turn to weaker electric dipole transitions.

Ishimatsu et al. [112] report torsion angles between donors and acceptor of c. 50–65° for the electronic ground state, with the largest dihedral angle for the carbazolyl donor in 1-position and the smallest one for the donor in 3-position. In the DFT/B3LYP optimized structure obtained for the isolated molecule in our laboratory, the dihedral angles between the carbazolyl donors in 1-, 2-, and 3-positions and the isophthalonitrile core are very similar (+63 and +64°), while the carbazolyl donor in 5-position shows a stronger twist (–71°) [127]. For computing the spin-free properties of the electronically excited states, the parallelized version of the original DFT/MRCI [64, 67] method was employed in the preliminary calculations. The wave function of the first excited singlet state is dominated by the HOMO→LUMO ICT transition but with marked

Color Fig: 8.9

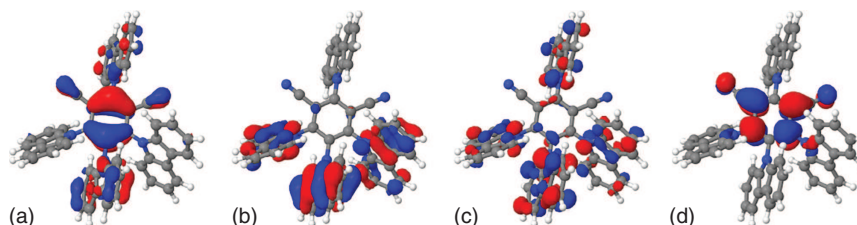


Figure 8.9 BHLYP molecular orbitals of 4CzIPN, important for the characterization of the lowest excited states according to Marian [127]. (a) HOMO-17, (b) HOMO-1, (c) HOMO, (d) LUMO.

contributions from local excitations. In particular, the local HOMO-17→LUMO excitation on the isophthalonitrile core (Figure 8.9) has a coefficient of nearly 0.1 in the S_1 wave function at the ground-state minimum. Local excitations lead to an enhancement of the oscillator strength for $S_0 \rightarrow S_1$. This transition is responsible for the shoulder at c. 450 nm in the absorption spectrum of 4CzIPN [19]. The vertical DFT/MRCI excitation energy of 2.94 eV (422 nm) in the gas phase is expected to be slightly redshifted due to solvent–solute interactions. The TDDFT excitation energy obtained by Ishimatsu et al. [112] for the M06-2X functional in a PCM (3.29 eV, 376 nm) is substantially higher. Interestingly, we find two triplet states below S_1 at the FC point, with the electronic structure of T_1 corresponding to S_2 . The multiconfigurational T_1 wave function has the HOMO-1→LUMO configuration as leading term. T_2 is dominated by the HOMO → LUMO configuration. Both triplet excited states exhibit larger contributions from LE on the isophthalonitrile core than their singlet counterparts.

The T_1 nuclear arrangement was optimized with unrestricted DFT. At the T_1 minimum, the donors in 1-, 2-, and 3-positions exhibit larger torsion angles with respect to the isophthalonitrile core (ranging between +68 and +73°) than in the electronic ground state, whereas the dihedral angle is flatter (−66°) for the donor in 5-position. This trend reflects the fact that electron density was mainly donated by the carbazolyl substituents in 1-, 2-, and 3-positions upon the ICT excitation to the T_1 state. At this point of the coordinate space, S_1 and T_1 result predominantly from the HOMO → LUMO excitation. Still, two triplets are found below the first excited singlet state in the DFT/MRCI calculations. S_1 and T_1 are separated by an energy gap of 86 meV here, in excellent agreement with experimental evidence. The T_2 state is located halfway between the T_1 and S_1 states at this geometry.

The SPOCK [101, 102] program was used to determine SOCMEs of the DFT/MRCI wave functions. The mutual SOCMEs of the three closely spaced electronic states are small. For the S_1 and T_1 DFT/MRCI wave functions, a sum over squared SOCMEs of 10^{-2} cm^{-2} was obtained. The electronic coupling of S_1 and T_2 is slightly larger (sum over squared SOMCEs $4 \times 10^{-2} \text{ cm}^{-2}$). The presence of the intermediate triplet state might therefore accelerate the ISC and rISC processes. The calculation of ISC and rISC rate constants is in progress.

Fluorescence and phosphorescence rates were obtained at the MRSOCI level [76]. The MRSOCI calculations were performed at the (unrestricted density functional theory) UDFT-optimized T_1 minimum. Technically, they are at the

Druckfreigabe/approval for printing	
Without corrections/ ohne Korrekturen	<input type="checkbox"/>
After corrections/ nach Ausführung der Korrekturen	<input type="checkbox"/>
Date/Datum:	
Signature/Zeichen:	

limit of what can be handled by the current version of the SPOCK program. In the Davidson diagonalization of the MRSOCI matrix, 8 complex-valued eigenvectors with expansion lengths of $\approx 5 \times 10^8$ configuration state functions were determined. The sublevels of the T_1 states are degenerate for all practical purposes. Phosphorescence is not a competitive decay mechanism in 4CzIPN. The calculated rate constants for phosphorescence are of the order of merely $10^{-2} - 10^{-1} \text{ s}^{-1}$.

Although the S_1 state wave function is dominated by ICT excitations ($\Delta\mu \approx 7 \text{ D}$), the fluorescence exhibits substantial oscillator strength. The emission from the S_1 state gains intensity from small amounts of local excitations on the isophthalonitrile core. At the T_1 minimum geometry, a vertical emission wavelength of 482 nm is computed for the isolated molecule, in good agreement with the experimental peak maximum at 507 nm [19, 112] measured in toluene. For a comparison of the calculated (pure) radiative lifetime of 44 ns with measured time constants, quantum yields have to be taken into account. Using Eq. (8.15) and the experimentally determined quantum yield of 21.1% for prompt fluorescence at 300 K [19] yields a lifetime of $\tau \approx 9.3 \text{ ns}$ that compares well the experimental values of 17.8 ns [19] and 14.2 ns [112] in toluene solution.

The magnitude of the local contributions to the $S_1 \rightarrow S_0$ transition density depends critically on the dihedral angles between the molecular planes of the carbazolyl and isophthalonitrile moieties. When this angle is constrained to 90° , the oscillator strength drops by four orders of magnitude, thus markedly decreasing the luminescence probability. In this case, only one triplet state of B_1 symmetry is located below the first excited singlet state, and their mutual SOCME vanishes by symmetry selection rules. This shows that the deviation from an orthogonal orientation of the donor and acceptor units is essential for the performance of the 4CzIPN TADF emitter.

8.4.2.2 Mechanism of the Triplet-to-Singlet Upconversion in the Assistant Dopants ACRXTN and ACRSA

Recently, one of us started investigating the photophysics of 3-(9,9-dimethylacridin-10(9H)-yl)-9H-xanthen-9-one (ACRXTN) and 10-phenyl-10H,10'H-spiro[acridine-9,9'-anthracen]-10'-one (ACRSA) (Figure 8.10) by quantum chemical methods [128, 129]. ACRXTN and ACRSA have been utilized as assistant dopants in OLEDs [24]. The idea behind this approach is to use triplet excitons for populating the S_1 state of the assistant dopant by rISC. Instead of radiatively decaying by fluorescence, the S_1 state transfers its excitation energy by FRET to a strongly fluorescent organic emitter. Nakanotani et al. [24] could show that the presence of the assistant dopant substantially improved the external electroluminescence quantum efficiency of the OLED, indicating an internal exciton production efficiency of nearly 100%.

In ACRXTN, acridine and xanthone are covalently linked, with the corresponding molecular planes arranged in a perpendicular fashion (see Figure 8.10). The HOMO of ACRXTN is a π -type orbital on the acridine moiety, whereas its LUMO is a π^* orbital localized on xanthone. Hence, the lowest electronically excited state is expected to have ICT character. For computing electronically excited states, TDDFT [133] in conjunction with the B3LYP density functional,

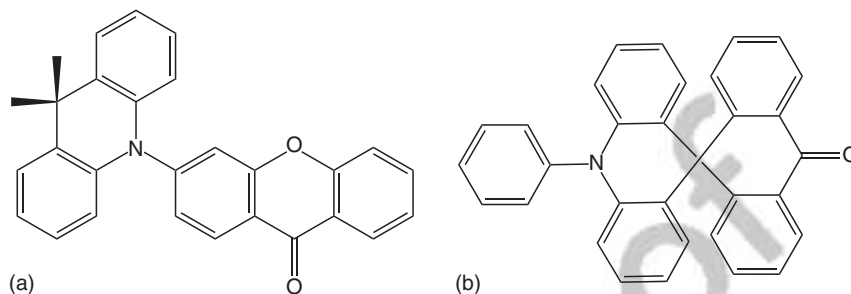


Figure 8.10 Chemical structures of the assistant dopants (a) ACRXTN and (b) ACSRA.

resolution-of-the-identity approximated coupled-cluster response methods (RI-CC2) [134, 135] as well as the redesigned DFT/MRCI-R [72] quantum chemical methods were employed. All theoretical methods agree that the lowest excited triplet and singlet states originate from an ICT excitation from acridine to xanthone [128]. Experimentally, the fluorescence (F) and phosphorescence (P) emissions in dichloromethane peak at 2.53 and 2.47 eV, respectively. The vertical DFT/MRCI-R emission energies in vacuum are only slightly larger (F: 2.77 eV, P: 2.71 eV) in the SV(P) basis, RI-CC2 yields an even higher value of 3.09 eV for both, whereas TDDFT/B3LYP gives 2.19 eV (F) and 2.18 eV (P). While the energetic separation between the LE and ICT states is nearly identical for DFT/MRCI-R and RI-CC2, this is not the case for TDDFT/B3LYP. Hence, it appears that RI-CC2 might be better suited for the optimization of excited-state geometries than TDDFT.

ACRXTN seems to have inherited some of the photophysical properties of the parent monochromophores [44]. In addition to the ICT states, two low-lying triplet states with $^3(n_O\pi_L^*)$ and $^3(\pi\pi^*)$ electronic structure as well as a $^1(n_O\pi_L^*)$ state are found that correspond to local excitations of the xanthone moiety [128]. So far, ISC and rISC rate constants have not been determined for this kind of complex. From the course of the potential energy curves and the knowledge of the coupling matrix elements, the following qualitative picture emerges.

In apolar media, the S_1 potential energy surface of ACRXTN exhibits at least two minima, the global minimum with ICT electronic structure and a local minimum originating from a local $(n_O\pi_L^*)$ excitation on xanthone. Two or three minima are expected on the lowest triplet excited-state surface, with the triplet ICT minimum being the global one. The second minimum on the T_1 surface exhibits $T_{\pi\pi^*}$ electronic structure. It is nearly degenerate with the $T_{n\pi^*}$ minimum in apolar media. In the ICT potential well, the singlet–triplet splitting is small enough (0.06 eV) to enable, at least in principle, the thermally activated rISC from the triplet to the corresponding singlet. However, the direct SOC between the states is too small (sum of squares $\approx 10^{-3} \text{ cm}^{-2}$) to make this process efficient. The carbonyl stretching vibration drives the system through a crossing with the $T_{\pi\pi^*}$ state that mediates the coupling of the ICT states and allows for an equilibration of the singlet and triplet ICT populations. In polar media, the $(n_O\pi^*)$ states are blueshifted, whereas the $T_{\pi\pi^*}$ and ICT states experience slight redshifts. Hence, a double minimum situation on the lowest triplet excited-state surface can be

Druckfreigabe/approval for printing	
Without corrections/ ohne Korrekturen	<input type="checkbox"/>
After corrections/ nach Ausführung der Korrekturen	<input type="checkbox"/>
Date/Datum:
Signature/Zeichen:

foreseen. In contrast, only one minimum with ICT character is expected on the lowest singlet excited-state potential energy surface. The $T_{\pi\pi^*}$ state continues to be the doorway state mediating the R(ISC) of the singlet and triplet ICT states in ARXCTN.

The spiro-compound ACRSA is very similar in that respect. Within an energy interval of 0.3 eV, five electronically excited states are found in the gas phase and in apolar solvents [129]. In ACRSA, the ICT from the phenylacridine to the anthracenone chromophores (HOMO \rightarrow LUMO) is the lowest excitation in the vertical absorption region. Because of its low oscillator strength (4×10^{-5}), the singlet transition at 378 nm is barely visible in the calculated absorption spectrum. This is also true for the $^1(n_O\pi_L^*)$ excitation (346 nm) and the (HOMO-1 \rightarrow LUMO) transition (318 nm). According to our calculations, the shoulder in the absorption spectrum around 310 nm stems from two local acridine transitions. The shoulder is slightly blueshifted with respect to experiment where a shoulder is observed around 320 nm in toluene solution [122]. This is also the case for the band maximum that is found at about 280 nm compared with the experimental value at approximately 300 nm. It arises from acridine to phenyl excitations. The overall shape of the computed absorption spectrum agrees very well with the experimental spectrum in toluene. Test calculations for the isolated system suggest that the computed excitation energies are lowered by about 0.1 eV when a larger basis set of valence triple-zeta plus polarization quality is used, thus improving the agreement with experiment.

With a dielectric constant of $\epsilon = 2.38$, toluene is an apolar solvent. Nevertheless, the solvent-solute interactions, modeled by conductor-like solvent model (COSMO) [136, 137], preferentially stabilize the ICT state by 0.09 eV, whereas the $n_O\pi_L^*$ state is destabilized by 0.10 eV with respect to the gas phase. Adiabatically, the lowest excited state does not stem from the (HOMO \rightarrow LUMO) transition. At the DFT/MRCI-R level of theory, an LE state of the anthracenone moiety, $^3(n_O\pi_L^*)$, constitutes the global minimum on the T_1 potential energy surface. Close by, the 3CT and the lowest $^3\pi\pi^*$ states are located. Likewise, the global minimum of the S_1 state has $^1(n_O\pi_L^*)$ character that is nearly degenerate with the 1CT state. For this reason, strong nonadiabatic coupling is expected in addition to SOC. Similar to ACRXTN, the C=O stretching mode drives the low-lying states toward intersections of the potential energy surfaces (Figure 8.11). And indeed, rate constants for rISC of the order of 10^9 s^{-1} in toluene have been derived from quantum dynamics calculations including vibronic coupling and SOC simultaneously [129]. The efficient rISC in this compound is attributed to the presence of LE $n\pi^*$ and $\pi\pi^*$ states and their strong interaction with the CT states.

Vibronic interactions are also required to make fluorescence electric dipole allowed. The calculated vertical singlet emission energies of 2.93 eV (423 nm) for the ICT state and of 2.89 eV (429 nm) for the $n_O\pi_L^*$ state in toluol are substantially blueshifted with respect to the photoluminescence band maximum that is found at about 500 nm in the same solvent according to Nasu et al. [122]. At present, it is not clear where the discrepancy comes from. Two things are striking, however. Firstly, in DPEPO film the emission maximum is found experimentally at about 480 nm [122]. Due to the polarity of DPEPO, a bathochromic shift of the peak

Color Fig: 8.11

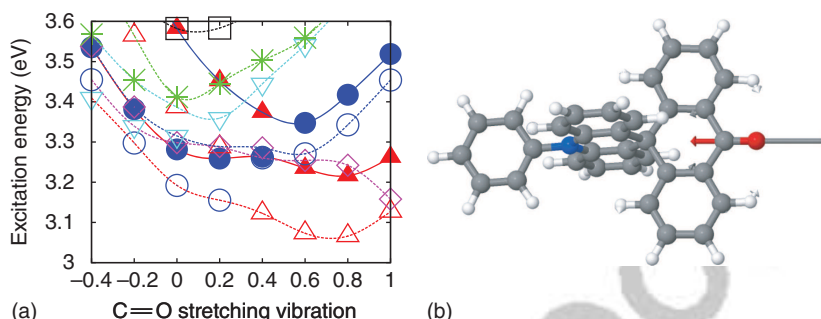


Figure 8.11 DFT/MRCI-R energy profiles of ACRSA along the C=O stretching normal coordinate (mode 138). Zero represents the ground-state equilibrium geometry (C=O bond length 122 pm), positive/negative distortions correspond to an elongation/a shortening of the C=O bond. Solid lines: singlets; dashed lines: triplets; triangles: ICT states with leading $\pi_H\pi_L^*$ configuration; circles: $n_O\pi_L^*$ states; diamonds: $\pi\pi^*$ states with leading $\pi_O\pi_L^*$ configuration; upside down triangles: $\pi\pi^*$ states with leading $\pi_H\pi_{L+1}^*$ configuration; squares: $\pi\pi^*$ states with leading $\pi_{H-1}\pi_L^*$ configuration; stars: $\pi\pi^*$ states with $\pi_{H-5}\pi_L^*$ leading configuration.

maximum with respect to its wavelength in toluene solution would have been expected. Instead, a hypsochromic shift of at least 20 nm is found.

Secondly, ACRSA is used as an assistant dopant for the blue fluorescence emitter tetra-ter-butylperylene (TBPe). Herein, it is assumed that ACRSA transfers its excitation energy by FRET to TBPe. Save for the proper orientation of the transition dipole moments, FRET is only efficient, however, if the emission spectrum of the FRET donor and the absorption spectrum of the FRET acceptor have substantial overlap [138]. As may be seen from Figure 1b of Ref. [24], there is barely any overlap between the emission spectrum ascribed to ACRSA and the absorption spectrum of TBPe that has its origin transition at wavelength shorter than 450 nm. As the enhancement of external quantum efficiency by the assistant dopant is undoubted, the shown emission spectrum can probably not be assigned to ACRSA.

Polar solvents such as acetonitrile ($\epsilon_r \approx 36$) shift the ($n_O\pi_L^*$) states substantially toward higher excitation energies, whereas the lowest ${}^3\pi\pi^*$ state is nearly unaffected by the solvent. In contrast, the ICT states are significantly redshifted. Because of these trends, we expect the electronic states to be turned into and out of resonance depending on the particular environment and the temperature.

8.5 Outlook and Concluding Remarks

Insight into the factors that determine the probability of TADF is a key step toward the design and optimization of third-generation OLED emitters. Despite intensive research on this topic in the latest years, a complete and consistent rationalization of TADF is still missing. As outlined in this chapter, a small singlet–triplet splitting of the electronically excited emitter states is not sufficient for TADF to take place. Rather, the molecular parameters that steer the relative probabilities of excited-state processes such as intramolecular charge

Druckfreigabe/approval for printing	
Without corrections/ ohne Korrekturen	<input type="checkbox"/>
After corrections/ nach Ausführung der Korrekturen	<input type="checkbox"/>
Date/Datum:	
Signature/Zeichen:	

and energy transfer, ISC, rISC, fluorescence, phosphorescence, and nonradiative deactivation have to be understood. Computational chemistry can substantially contribute to this understanding. In particular, it can provide detailed information about spectroscopically dark states and their coupling to the luminescent one, information that is difficult or even impossible to obtain from experimental data alone. Moreover, starting from a lead structure, quantum chemistry can easily assess the effects of chemical substitution.

With regard to internal quantum yields and rate constants, experimental and theoretical information is complimentary. Experimentally, (R)ISC rate constants are often determined indirectly from the quantum yields of the prompt and delayed components. Time-resolved spectra of such complexes, from which ISC rate constants could be retrieved directly, are still scarce. While suffering from uncertainties with regard to the underlying models and quantum chemical methods, theory can, in principle, determine rate constants and use them to derive internal TADF quantum yields that can be compared with experimental data.

The quantum chemical methods employed in our preliminary work are well suited for computing spectroscopic properties of the systems at hand. DFT/MRCI-R is the method of choice for obtaining reliable electronic excitation energies and excited-state properties at reasonable cost in the purely organic donor–acceptor systems. SPOCK is a powerful tool for computing electronic SOCME and phosphorescence rate constants. Less demanding single-reference linear response methods such as RI-CC2 or, where applicable, TDDFT can be used to obtain excited-state minimum geometries and vibrational frequencies. Because of the comparably low nonradiative transition rates, typical for (reverse) ISC in TADF emitters, a static Fourier transform formalism seems appropriate for calculating the rate constants. What is presently missing is an efficient way to compute vibronic SOC rates for larger systems. Vibronic SOC is considered essential in donor–acceptor systems because of the small magnitude of the direct electronic SOCMEs between singlet and triplet CT states.

The latest class of hyperfluorescent OLEDs combines high internal quantum efficiency and long operational stability by using assistant dopants for the harvesting of triplet and singlet excitons in addition to fluorescence emitters. So far, quantum chemical research in that direction is missing. Modeling the excitation energy transfer from the assistant dopant to the fluorescent acceptor beyond the ideal dipole approximation is a challenging task that could be worth considering.

References

- 1 Tang, C.W. and VanSlyke, S.A. (1987). Organic electroluminescent diodes. *Appl. Phys. Lett.* 51: 913–915.
- 2 Baldo, M.A., O'Brien, D.F., You, Y., Shoustikov, A., Sibley, S., Thompson, M.E., and Forrest, S.R. (1998). Highly efficient phosphorescent emission from organic electroluminescent devices. *Nature* 395: 151–154.
- 3 Adachi, C. (2014). Third-generation organic electroluminescence materials. *Jpn. J. Appl. Phys.* 53: 060101.

Druckfreigabe/approval for printing	
Without corrections/ ohne Korrekturen	<input type="checkbox"/>
After corrections/ nach Ausführung der Korrekturen	<input type="checkbox"/>
Date/Datum:	
Signature/Zeichen:	

- 4 Adachi, C. and Adachi, J. (2015). High performance TADF for OLEDs. *Presentation at the 2015 SSL R&D WORKSHOP in San Francisco, CA*. http://energy.gov/sites/prod/files/2015/02/f19/adachi_oled-tadf_sanfrancisco2015.pdf (accessed 10 March 2018).
- 5 Thompson, M. (2007). The evolution of organometallic complexes in organic light-emitting devices. *MRS Bull.* 32: 694–701.
- 6 Kappaun, S., Slugovc, C., and List, E.J.W. (2008). Phosphorescent organic light-emitting devices: working principle and iridium based emitter materials. *Int. J. Mol. Sci.* 9: 1527–1547.
- 7 Yersin, H., Rausch, A.F., Czerwieniec, R., Hofbeck, T., and Fischer, T. (2011). The triplet state of organo-transition metal compounds. Triplet harvesting and singlet harvesting for efficient OLEDs. *Coord. Chem. Rev.* 255: 2622–2652.
- 8 Wagenknecht, P.S. and Ford, P.C. (2011). Metal centered ligand field excited states: their roles in the design and performance of transition metal based photochemical molecular devices. *Coord. Chem. Rev.* 255: 591–616.
- 9 Choy, W.C.H., Chan, W.K., and Yuan, Y. (2014). Recent advances in transition metal complexes and light-management engineering in organic optoelectronic devices. *Adv. Mater.* 26: 5368–5399.
- 10 Baldo, M.A., Lamansky, S., Burrows, P.E., Thompson, M.E., and Forrest, S.R. (1999). Very high-efficiency green organic light-emitting devices based on electrophosphorescence. *Appl. Phys. Lett.* 75: 4–6.
- 11 Sajoto, T., Djurovich, P.I., Tamayo, A.B., Oxgaard, J., Goddard, W.A. (2009). Temperature dependence of blue phosphorescent cyclometalated Ir(III) complexes. *J. Am. Chem. Soc.* 131: 9813–9822.
- 12 Hudson, Z.M., Sun, C., Helander, M.G., Chang, Y.L., Lu, Z.H., and Wang, S. (2012). Highly efficient blue phosphorescence from triarylboron-functionalized platinum(II) complexes of N-heterocyclic carbenes. *J. Am. Chem. Soc.* 134: 13930–13933.
- 13 Darmawan, N., Yang, C.H., Mauro, M., Raynal, M., Heun, S., Pan, J., Buchholz, H., Braunstein, P., and Cola, L.D. (2013). Efficient near-UV emitters based on cationic bis-pincer iridium(III) carbene complexes. *Inorg. Chem.* 52: 10756–10765.
- 14 Reineke, S., Thomschke, M., Lüssem, B., and Leo, K. (2013). White organic light-emitting diodes: status and perspective. *Rev. Mod. Phys.* 85: 1245–1293.
- 15 Cariati, E., Lucenti, E., Botta, C., Giovanella, U., Marinotto, D., and Righetto, S. (2016). Cu(I) hybrid inorganic-organic materials with intriguing stimuli responsive and optoelectronic properties. *Coord. Chem. Rev.* 306: 566–614.
- 16 Czerwieniec, R., Leitl, M.J., Homeier, H.H., and Yersin, H. (2016). Cu(I) complexes - thermally activated delayed fluorescence. Photophysical approach and material design. *Coord. Chem. Rev.* 325: 2–28.
- 17 Leitl, M.J., Zink, D.M., Schinabeck, A., Baumann, T., Volz, D., and Yersin, H. (2016). Copper(I) complexes for thermally activated delayed fluorescence: from photophysical to device properties. *Top. Curr. Chem.* 374: 25.
- 18 Parker, C.A. and Hatchard, C.G. (1961). Triplet-singlet emission in fluid solutions. phosphorescence of eosin. *Trans. Faraday Soc.* 57: 1894–1904.

Druckfreigabe/approval for printing	
Without corrections/ ohne Korrekturen	<input type="checkbox"/>
After corrections/ nach Ausführung der Korrekturen	<input type="checkbox"/>
Date/Datum:	
Signature/Zeichen:	

- 19 Uoyoma, H., Goushi, K., Shizu, K., Nomura, H., and Adachi, C. (2012). Highly efficient organic light-emitting diodes from delayed fluorescence. *Nature* 492: 234–238.
- 20 Förster, T. (1959). 10th spiels memorial lecture. Transfer mechanisms of electronic excitation. *Discuss. Faraday Soc.* 27: 7–17.
- 21 Ermolaev, V.L. and Sveshnikova, E.B. (1963). Inductive-resonance transfer of energy from aromatic molecules in the triplet state. *Dokl. Akad. Nauk* 149: 1295–1298.
- 22 Baldo, M.A., Thompson, M.E., and Forrest, S.R. (2000). High-efficiency fluorescent organic light-emitting devices using a phosphorescent sensitizer. *Nature* 403: 750–753.
- 23 Fukagawa, H., Shimizu, T., Kamada, T., Yui, S., Hasegawa, M., Morii, K., and Yamamoto, T. (2015). Highly efficient and stable organic light-emitting diodes with a greatly reduced amount of phosphorescent emitter. *Sci. Rep.* 5: 9855/1–7.
- 24 Nakanotani, H., Higuchi, T., Furukawa, T., Masui, K., Morimoto, K., Numata, M., Tanaka, H., Sagara, Y., Yasuda, T., and Adachi, C. (2014). High-efficiency organic light-emitting diodes with fluorescent emitters. *Nat. Commun.* 5: 4016–4022.
- 25 Jou, J.H., Kumar, S., Agrawal, A., Li, T.H., and Sahoo, S. (2015). Approaches for fabricating high efficiency organic light emitting diodes. *J. Mater. Chem. C* 3: 2974–3002.
- 26 Jankus, V., Data, P., Graves, D., McGuinness, C., Santos, J., Bryce, M.R., Dias, F.B., and Monkman, A.P. (2014). Highly efficient TADF OLEDs: how the emitter-host interaction controls both the excited state species and electrical properties of the devices to achieve near 100% triplet harvesting and high efficiency. *Adv. Funct. Mater.* 24: 6178–6186.
- 27 Klán, P. and Wirz, J. (2009). *Photochemistry of Organic Compounds: From Concepts to Practice*. Wiley.
- 28 Vosskötter, S., Konieczny, P., Marian, C.M., and Weinkauff, R. (2015). Towards an understanding of the singlet-triplet splittings in conjugated hydrocarbons: azulene investigated by anion photoelectron spectroscopy and theoretical calculations. *Phys. Chem. Chem. Phys.* 17: 23573–23581.
- 29 Etinski, M., Petković, M., Ristić, M.M., and Marian, C.M. (2015). Electron-vibrational coupling and fluorescence spectra of tetra-, penta-, and hexacoordinated chlorophylls c_1 and c_2 . *J. Phys. Chem. B* 119: 10156–10169.
- 30 Marian, C. (2001). Spin-orbit coupling in molecules. In: *Reviews in Computational Chemistry*, vol.17 (ed. K. Lipkowitz and D. Boyd), 99–204. Weinheim: Wiley-VCH.
- 31 Marian, C.M. (2012). Spin-orbit coupling and intersystem crossing in molecules. *WIREs Comput. Mol. Sci.* 2: 187–203.
- 32 Heß, B.A., Marian, C.M., Wahlgren, U., and Gropen, O. (1996). A mean-field spin-orbit method applicable to correlated wavefunctions. *Chem. Phys. Lett.* 251: 365–371.
- 33 El-Sayed, M.A. (1968). The triplet state: its radiative and nonradiative properties. *Acc. Chem. Res.* 1: 8–16.

Druckfreigabe/approval for printing	
Without corrections/ ohne Korrekturen	<input type="checkbox"/>
After corrections/ nach Ausführung der Korrekturen	<input type="checkbox"/>
Date/Datum:	
Signature/Zeichen:	

- 34 Englman, R. and Jortner, J. (1970). Energy gap law for radiationless transitions in large molecules. *Mol. Phys.* 18: 145–164.
- 35 Freed, K.F. and Jortner, J. (1970). Multiphonon processes in the nonradiative decay of large molecules. *J. Chem. Phys.* 52: 6272–6291.
- 36 Marcus, R.A. (1984). Nonadiabatic processes involving quantum-like and classical-like coordinates with applications to nonadiabatic electron transfers. *J. Chem. Phys.* 81: 4494–4500.
- 37 Etinski, M. and Marian, C.M. (2010). Overruling the energy gap law: fast triplet formation in 6-azauracil. *Phys. Chem. Chem. Phys.* 12: 15665–15671.
- 38 Henry, B.R. and Siebrand, W. (1971). Spin–orbit coupling in aromatic hydrocarbons. Analysis of nonradiative transitions between singlet and triplet states in benzene and naphthalene. *J. Chem. Phys.* 54: 1072–1085.
- 39 Tatchen, J., Gilka, N., and Marian, C.M. (2007). Intersystem crossing driven by vibronic spin–orbit coupling: a case study on psoralen. *Phys. Chem. Chem. Phys.* 9: 5209–5221.
- 40 Perun, S., Tatchen, J., and Marian, C.M. (2008). Singlet and triplet excited states and intersystem crossing in free-base porphyrin: TDDFT and DFT/MRCI study. *ChemPhysChem* 9: 282–292.
- 41 Salzmann, S., Tatchen, J., and Marian, C.M. (2008). The photophysics of flavins: what makes the difference between gas phase and aqueous solution. *J. Photochem. Photobiol., A* 198: 221–231.
- 42 Rai-Constapel, V., Salzmann, S., and Marian, C.M. (2011). Isolated and solvated thioxanthone: a photophysical study. *J. Phys. Chem. A* 115: 8589–8596.
- 43 Peng, Q., Niu, Y., Shi, Q., Gao, X., and Shuai, Z. (2013). Correlation function formalism for triplet excited state decay: Combined spin–orbit and nonadiabatic couplings. *J. Chem. Theory Comput.* 9: 1132–1143.
- 44 Rai-Constapel, V., Etinski, M., and Marian, C.M. (2013). Photophysics of xanthone: a quantum chemical perusal. *J. Phys. Chem. A* 117: 3935–3944.
- 45 Rai-Constapel, V. and Marian, C.M. (2016). Solvent tunable photophysics of acridone: a quantum chemical perspective. *RSC Adv.* 6: 18530–18537.
- 46 Danovich, D., Marian, C.M., Neuheuser, T., Peyerimhoff, S.D., and Shaik, S. (1998). Spin–orbit coupling patterns induced by twist and pyramidalization modes in C_2H_4 : a quantitative study and a qualitative analysis. *J. Phys. Chem. A* 102: 5923–5936.
- 47 Cogan, S., Haas, Y., and Zilberg, S. (2007). Intersystem crossing at singlet conical intersections. *J. Photochem. Photobiol., A* 190: 200–206.
- 48 Penfold, T.J. and Worth, G.A. (2010). The effect of molecular distortions on spin–orbit coupling in simple hydrocarbons. *Chem. Phys.* 375: 58–66.
- 49 Beljonne, D., Shuai, Z., Pourtois, G., and Bredas, J.L. (2001). Spin–orbit coupling and intersystem crossing in conjugated polymers: a configuration interaction description. *J. Phys. Chem. A* 105: 3899–3907.
- 50 Burin, A.L. and Ratner, M.A. (1998). Spin effects on the luminescence yield of organic light emitting diodes. *J. Chem. Phys.* 109: 6092–6102.
- 51 Etinski, M., Tatchen, J., and Marian, C.M. (2011). Time-dependent approaches for the calculation of intersystem crossing rates. *J. Chem. Phys.* 134: 154105.

Druckfreigabe/approval for printing	
Without corrections/ ohne Korrekturen	<input type="checkbox"/>
After corrections/ nach Ausführung der Korrekturen	<input type="checkbox"/>
Date/Datum:	
Signature/Zeichen:	

- 52 Duschinsky, F. (1937). The importance of the electron spectrum in multi atomic molecules concerning the Franck-Condon principle. *Acta Physicochim.* 7: 551–566.
- 53 Etinski, M., Rai-Constapel, V., and Marian, C.M. (2014). Time-dependent approach to spin-vibronic coupling: implementation and assessment. *J. Chem. Phys.* 140 (11): 114104.
- 54 Capano, G., Penfold, T.J., Röthlisberger, U., and Tavernelli, I. (2014). A vibronic coupling Hamiltonian to describe the ultrafast excited state dynamics of a Cu(I)-phenanthroline complex. *Chimia* 68: 227–230.
- 55 Capano, G., Chergui, M., Röthlisberger, U., Tavernelli, I., and Penfold, T.J. (2014). A quantum dynamics study of the ultrafast relaxation in a prototypical Cu(I) phenanthroline. *J. Phys. Chem. A* 118: 9861–9869.
- 56 Gibson, J., Monkman, A.P., and Penfold, T.J. (2016). The importance of vibronic coupling for efficient reverse intersystem crossing in thermally activated delayed fluorescence molecules. *ChemPhysChem* 17: 2956–2961.
- 57 Köppel, H., Domcke, W., and Cederbaum, L.S. (1984). Multi-mode molecular dynamics beyond the Born–Oppenheimer approximation. *Adv. Chem. Phys.* 57: 59–246.
- 58 Beck, M.H., Jäckle, A., Worth, G.A., and Meyer, H.D. (2000). The multiconfiguration time-dependent Hartree method: a highly efficient algorithm for propagating wavepackets. *Phys. Rep.* 324: 1–105.
- 59 Dreuw, A. and Head-Gordon, M. (2004). Failure of time-dependent density functional theory for long-range charge-transfer excited states: the zincbacteriochlorin–bacteriochlorin and bacteriochlorophyll–spheroidene complexes. *J. Am. Chem. Soc.* 126: 4007–4016.
- 60 Huang, S., Zhang, Q., Shiota, Y., Nakagawa, T., Kuwabara, K., Yoshizawa, K., and Adachi, C. (2013). Computational prediction for singlet- and triplet-transition energies of charge-transfer compounds. *J. Chem. Theory Comput.* 9: 3872–3877.
- 61 Moral, M., Muccioli, L., Son, W.J., Olivier, Y., and Sancho-García, J.C. (2015). Theoretical rationalization of the singlet-triplet gap in OLEDs materials: impact of charge-transfer character. *J. Chem. Theory Comput.* 11: 168–177.
- 62 Grimme, S. (2006). Semiempirical hybrid density functional with perturbative second-order correlation. *J. Chem. Phys.* 124: 034108.
- 63 Karton, A., Tarnopolsky, A., Lamère, J.F., Schatz, G.C., and Martin, J.M.L. (2008). Highly accurate first-principles benchmark data sets for the parametrization and validation of density functional and other approximate methods. Derivation of a robust, generally applicable, double-hybrid functional for thermochemistry and thermochemical kinetics. *J. Phys. Chem. A* 112: 12868–12886.
- 64 Grimme, S. and Waletzke, M. (1999). A combination of Kohn-Sham density functional theory and multi-reference configuration interaction methods. *J. Chem. Phys.* 111 (13): 5645–5655.
- 65 Becke, A.D. (1993). A new mixing of Hartree-Fock and local density-functional theories. *J. Chem. Phys.* 98: 1372–1377.
- 66 Silva-Junior, M.R., Schreiber, M., Sauer, S.P.A., and Thiel, W. (2008). Benchmarks for electronically excited states: time-dependent density functional

Druckfreigabe/approval for printing	
Without corrections/ ohne Korrekturen	<input type="checkbox"/>
After corrections/ nach Ausführung der Korrekturen	<input type="checkbox"/>
Date/Datum:	
Signature/Zeichen:	

- theory and density functional theory based multireference configuration interaction. *J. Chem. Phys.* 129: 104103.
- 67 Kleinschmidt, M., Marian, C.M., Waletzke, M., and Grimme, S. (2009). Parallel multireference configuration interaction calculations on mini- β -carotenes and β -carotene. *J. Chem. Phys.* 130: 044708.
- 68 Escudero, D. and Thiel, W. (2014). Assessing the density functional theory-based multireference configuration interaction (DFT/MRCI) method for transition metal complexes. *J. Chem. Phys.* 140: 194105/1–8.
- 69 Kleinschmidt, M., van Wüllen, C., and Marian, C.M. (2015). Intersystem-crossing and phosphorescence rates in facIr^{III}(ppy)₃: a theoretical study involving multi-reference configuration interaction wavefunctions. *J. Chem. Phys.* 142: 094301.
- 70 Heil, A., Gollnisch, K., Kleinschmidt, M., and Marian, C.M. (2016). On the photophysics of four heteroleptic iridium(III) phenylpyridyl complexes investigated by relativistic multi-configuration methods. *Mol. Phys.* 114: 407–422.
- 71 Marian, C.M. and Gilka, N. (2008). Performance of the DFT/MRCI method on electronic excitation of extended π -systems. *J. Chem. Theory Comput.* 4: 1501–1515.
- 72 Lyskov, I., Kleinschmidt, M., and Marian, C.M. (2016). Redesign of the DFT/MRCI Hamiltonian. *J. Chem. Phys.* 144: 034104.
- 73 Jovanović, V., Lyskov, I., Kleinschmidt, M., and Marian, C.M. (2017). On the performance of DFT/MRCI-R and MR-MP2 in spin-orbit coupling calculations. *Mol. Phys.* 115: 109–137.
- 74 Grimme, S., Antony, J., Ehrlich, S., and Krieg, H. (2010). A consistent and accurate ab initio parametrization of density functional dispersion correction (DFT-D) for the 94 elements H-Pu. *J. Chem. Phys.* 132: 154104.
- 75 Helgaker, T., Jørgensen, P., and Olsen, J. (2000). *Molecular Electronic-Structure Theory*. Wiley.
- 76 Kleinschmidt, M., Tatchen, J., and Marian, C.M. (2006). SPOCK.CI: a multireference spin-orbit configuration interaction method for large molecules. *J. Chem. Phys.* 124: 124101.
- 77 Ågren, H., Vahtras, O., and Minaev, B. (1996). Response theory and calculations of spin-orbit coupling phenomena in molecules. *Adv. Quantum Chem.* 27: 71–162.
- 78 Christiansen, O., Gauss, J., and Schimmelpfennig, B. (2000). Spin-orbit coupling constants from coupled-cluster response theory. *Phys. Chem. Chem. Phys.* 2: 965–971.
- 79 Deaton, J.C., Switalski, S.C., Kondakov, D.Y., Young, R.H., Pawlik, T.D., Giesen, D.J., Harkins, S.B., Miller, A.J.M., Mickenberg, S.F., and Peters, J.C. (2010). E-type delayed fluorescence of a phosphine-supported Cu₂(μ -NAr₂)₂ diamond core: harvesting singlet and triplet excitons in OLEDs. *J. Am. Chem. Soc.* 132: 9499–9508.
- 80 Czerwieniec, R., Kowalski, K., and Yersin, H. (2013). Highly efficient thermally activated fluorescence of a new rigid Cu(I) complex [Cu(dmp)(phanephos)]⁺. *Dalton Trans.* 42: 9826–9830.
- 81 Chen, X.L., Yu, R., Zhang, Q.K., Zhou, L.J., Wu, X.Y., Zhang, Q., and Lu, C.Z. (2013). Rational design of strongly blue-emitting cuprous

Druckfreigabe/approval for printing	
Without corrections/ ohne Korrekturen	<input type="checkbox"/>
After corrections/ nach Ausführung der Korrekturen	<input type="checkbox"/>
Date/Datum:	
Signature/Zeichen:	

- complexes with thermally activated delayed fluorescence and application in solution-processed OLEDs. *Chem. Mater.* 25: 3910–3920.
- 82 Osawa, M., Kawata, I., Ishii, R., Igawa, S., Hashimoto, M., and Hoshino, M. (2013). Application of neutral d¹⁰ coinage metal complexes with an anionic bidentate ligand in delayed fluorescence-type organic light-emitting diodes. *J. Mater. Chem. C* 1: 4375–4383.
- 83 Linfoot, C.L., Leitzl, M.J., Richardson, P., Rausch, A.F., Chepelin, O., White, F.J., Yersin, H., and Robertson, N. (2014). Thermally activated delayed fluorescence (TADF) and enhancing photoluminescence quantum yields of [Cu^I(diimine)(diphosphine)]⁺ complexes—photophysical, structural, and computational studies. *Inorg. Chem.* 53: 10854–10861.
- 84 Czerwieniec, R. and Yersin, H. (2015). Diversity of copper(I) complexes showing thermally activated delayed fluorescence: basic photophysical analysis. *Inorg. Chem.* 54: 4322–4327.
- 85 Osawa, M., Hoshino, M., Hashimoto, M., Kawata, I., Igawa, S., and Yashima, M. (2015). Application of three-coordinate copper(I) complexes with halide ligands in organic light-emitting diodes that exhibit delayed fluorescence. *Dalton Trans.* 44: 8369–8378.
- 86 Zhang, Q., Chen, J., Wu, X.Y., Chen, X.L., Yu, R., and Lu, C.Z. (2015). Outstanding blue delayed fluorescence and significant processing stability of cuprous complexes with functional pyridine–pyrazolate diimine ligands. *Dalton Trans.* 44: 6706–6710.
- 87 Bergmann, L., Hedley, G.J., Baumann, T., Bräse, S., and Samuel, I.D.W. (2016). Direct observation of intersystem crossing in a thermally activated delayed fluorescence copper complex in the solid state. *Sci. Adv.* 2: e1500889.
- 88 Leitzl, M.J., Küchle, F.R., Mayer, H.A., Wesemann, L., and Yersin, H. (2013). Brightly blue and green emitting Cu(I) dimers for singlet harvesting in OLEDs. *J. Phys. Chem. A* 117: 11823–11836.
- 89 Hofbeck, T., Monkowius, U., and Yersin, H. (2015). Highly efficient luminescence of Cu(I) compounds: thermally activated delayed fluorescence combined with short-lived phosphorescence. *J. Am. Chem. Soc.* 137: 399–404.
- 90 Krylova, V.A., Djurovich, P.I., Whited, M.T., and Thompson, M.E. (2010). Synthesis and characterization of phosphorescent three-coordinate Cu(I)–NHC complexes. *Chem. Commun.* 46: 6696–6698.
- 91 Krylova, V.A., Djurovich, P.I., Aronson, J.W., Haiges, R., Whited, M.T., and Thompson, M.E. (2012). Structural and photophysical studies of phosphorescent three-coordinate copper(I) complexes supported by an N-heterocyclic carbene ligand. *Organometallics* 31: 7983–7993.
- 92 Krylova, V.A., Djurovich, P.I., Conley, B.L., Haiges, R., Whited, M.T., Williams, T.J., and Thompson, M.E. (2014). Control of emission colour with N-heterocyclic carbene (NHC) ligands in phosphorescent three-coordinate Cu(I) complexes. *Chem. Commun.* 50: 7176–7179.
- 93 Leitzl, M.J., Krylova, V.A., Djurovich, P.I., Thompson, M.E., and Yersin, H. (2014). Phosphorescence versus thermally activated delayed fluorescence. Controlling singlet–triplet splitting in brightly emitting and sublimable Cu(I) compounds. *J. Am. Chem. Soc.* 136: 16032–16038.

Druckfreigabe/approval for printing	
Without corrections/ ohne Korrekturen	<input type="checkbox"/>
After corrections/ nach Ausführung der Korrekturen	<input type="checkbox"/>
Date/Datum:	
Signature/Zeichen:	

- 94 Osawa, M. (2014). Highly efficient blue-green delayed fluorescence from copper(I) thiolate complexes: luminescence color alteration by orientation change of the aryl ring. *Chem. Commun.* 50: 1801–1803.
- 95 Gernert, M., Müller, U., Haehnel, M., Pflaum, J., and Steffen A. (2017). A cyclic alkyl(amino)carbene as two-atom- π -chromophore leading to the first phosphorescent linear Cu(I) complexes. *Chem. Eur. J.* 23: 2206–2216.
- 96 Gneuß, T., Leitl, M.J., Finger, L.H., Rau, N., Yersin, H., and Sundermeyer, J. (2015). A new class of luminescent Cu(I) complexes with tripodal ligands - TADF emitters for the yellow to red color range. *Dalton Trans.* 44: 8506–8520.
- 97 Cheng, G., So, G.K.M., To, W.P., Chen, Y., Kwok, C.C., Ma, C., Guan, X., Chang, X., Kwok, W.M., and Che, C.M. (2015). Luminescent zinc(II) and copper(I) complexes for high-performance solution-processed monochromic and white organic light-emitting devices. *Chem. Sci.* 6: 4623–4635.
- 98 Siddique, Z.A., Yamamoto, Y., Ohno, T., and Nozaki, K. (2003). Structure-dependent photophysical properties of singlet and triplet metal-to-ligand charge transfer states in copper(I) bis(diimine) compounds. *Inorg. Chem.* 42: 6366–6378.
- 99 Capano, G., Röthlisberger, R.U., Tavernelli, I., and Penfold, T.J. (2015). Theoretical rationalization of the emission properties of prototypical Cu(I)-phenanthroline complexes. *J. Phys. Chem. A* 119: 7026–7037.
- 100 Föllner, J., Kleinschmidt, M., and Marian, C.M. (2016). Phosphorescence or thermally activated delayed fluorescence? Intersystem crossing and radiative rate constants of a three-coordinate Cu(I) complex determined by quantum chemical methods. *Inorg. Chem.* 55: 7508–7516.
- 101 Kleinschmidt, M., Tatchen, J., and Marian, C.M. (2002). Spin-orbit coupling of DFT/MRCI wavefunctions: method, test calculations, and application to thiophene. *J. Comput. Chem.* 23: 824–833.
- 102 Kleinschmidt, M. and Marian, C.M. (2005). Efficient generation of matrix elements of one-electron spin-orbit operators. *Chem. Phys.* 311: 71–79.
- 103 Etinski, M., Tatchen, J., and Marian, C.M. (2014). Thermal and solvent effects on the triplet formation in cinnoline. *Phys. Chem. Chem. Phys.* 16: 4740–4751.
- 104 Kirchhoff, J.R., Gamache, R.E., Blaskie, M.W., Paggio, A.A.D., Lengel, R.K., and McMillin, D.R. (1983). Temperature dependence of luminescence from Cu(NN)²⁺ systems in fluid solution. Evidence for the participation of two excited states. *Inorg. Chem.* 22: 2380–2384.
- 105 Hirata, S., Sakai, Y., Masui, K., Tanaka, H., Lee, S.Y., Nomura, H., Nakamura, N., Yasumatsu, M., Nakanotani, H., Zhang, Q., Shizu, K., Miyazaki, H., and Adachi, C. (2015). Highly efficient blue electroluminescence based on thermally activated delayed fluorescence. *Nat. Mater.* 14: 330–336.
- 106 Zgierski, M.Z. (2003). Cu(I)-2,9-dimethyl-1,10-phenanthroline: density functional study of the structure, vibrational force-field, and excited electronic states. *J. Chem. Phys.* 118: 4045–4051.
- 107 Wang, F. and Ziegler, T. (2005). A simplified relativistic time-dependent density-functional theory formalism for the calculations of excitation energies including spin-orbit coupling effect. *J. Chem. Phys.* 123 (15): 154102.

Druckfreigabe/approval for printing	
Without corrections/ ohne Korrekturen	<input type="checkbox"/>
After corrections/ nach Ausführung der Korrekturen	<input type="checkbox"/>
Date/Datum:	
Signature/Zeichen:	

- 108 Bergmann, L. (2016). *New Emitters for OLEDs: The Coordination- and Photo-Chemistry of Mononuclear Neutral Copper(I) Complexes (Beiträge zur Organischen Synthese)*. Logos Verlag Berlin.
- 109 Bernanose, A., Comte, M., and Vouaux, P. (1953). A new method of light emission by certain organic compounds. *J. Chim. Phys.* 50: 64–68.
- 110 Yersin, H., Czerwieniec, R., and Hupfer, A. (2012). Singlet harvesting with brightly emitting Cu(I) and metal-free organic compounds. Proceedings of SPIE, Volume 8435, p. 843508.
- 111 Dias, F.B., Bourdakos, K.N., Jankus, V., Moss, K.C., Kamtekar, K.T., Bhalla, V., Santos, J., Bryce, M.R. (2013). Triplet harvesting with 100% efficiency by way of thermally activated delayed fluorescence in charge transfer oled emitters. *Adv. Mater.* 25: 3707–3714.
- 112 Ishimatsu, R., Matsunami, S., Shizu, K., Adachi, C., Nakano, K., and Imato, T. (2013). Solvent effect on thermally activated delayed fluorescence by 1,2,3,5-tetrakis(carbazol-9-yl)-4,6-dicyanobenzene. *J. Phys. Chem. A* 117: 5607–5612.
- 113 Wu, S., Aonuma, M., Zhang, Q., Huang, S., Nakagawa, T., Kuwabara, K., and Adachi, C. (2014). High-efficiency deep-blue organic light-emitting diodes based on a thermally activated delayed fluorescence emitter. *J. Mater. Chem. C* 2: 421–424.
- 114 Tanaka, H., Shizu, K., Nakanotani, H., and Adachi, C. (2014). Dual intramolecular charge-transfer fluorescence derived from a phenothiazine-triphenyltriazine derivative. *J. Phys. Chem. C* 118: 15985–15994.
- 115 Wang, H., Xie, L., Peng, Q., Meng, L., Wang, Y., Yi, Y., and Wang, P. (2014). Novel thermally activated delayed fluorescence materials-thioxanthone derivatives and their applications for highly efficient OLEDs. *Adv. Mater.* 26: 5198–5204.
- 116 Zhang, Q., Li, B., Huang, S., Nomura, H., Tanaka, H., and Adachi, C. (2014). Efficient blue organic light-emitting diodes employing thermally activated delayed fluorescence. *Nat. Photonics* 8: 326–332.
- 117 Shizu, K., Tanaka, H., Uejima, M., Sato, T., Tanaka, K., Kaji, H., and Adachi, C. (2015). Strategy for designing electron donors for thermally activated delayed fluorescence emitters. *J. Phys. Chem. C* 119: 1291–1297.
- 118 Dias, F.B., Santos, J., Graves, D.R., Data, P., Nobuyasu, R.S., Fox, M.A., Batsanov, A.S., Palmeira, T., Berberan-Santos, M.N., Bryce, M.R., and Monkman, A.P. (2016). The role of local triplet excited states and D-A relative orientation in thermally activated delayed fluorescence: photophysics and devices. *Adv. Sci.* 3 (12): 1600080.
- 119 Data, P., Pander, P., Okazaki, M., Takeda, Y., Minakata, S., and Monkman, A.P. (2016). Dibenzo[a,j]phenazine-cored donor-acceptor-donor compounds as green-to-red/NIR thermally activated delayed fluorescence organic light emitters. *Angew. Chem.* 128: 5833–5838.
- 120 Etherington, M., Gibson, J., Higginbotham, H.F., Penfold, T.J., and Monkman, A.P. (2016). Second-order spin-vibronic coupling mediates triplet harvesting and thermally-activated delayed fluorescence in charge transfer molecules. *Nat. Commun.* 7: 13680.

Druckfreigabe/approval for printing	
Without corrections/ ohne Korrekturen	<input type="checkbox"/>
After corrections/ nach Ausführung der Korrekturen	<input type="checkbox"/>
Date/Datum:	
Signature/Zeichen:	

- 121 Méhes, G., Nomura, H., Zhang, Q., Nakagawa, T., and Adachi, C. (2012). Enhanced electroluminescence efficiency in a spiro-acridine derivative through thermally activated delayed fluorescence. *Angew. Chem. Int. Ed.* 51: 11311–11315.
- 122 Nasu, K., Nakagawa, T., Nomura, H., Lin, C.J., Cheng, C.H., Tseng, M.R., Yasuda, T., and Adachi, C. (2013). A highly luminescent spiro-anthracenone-based organic light-emitting diode exhibiting thermally activated delayed fluorescence. *Chem. Commun.* 49: 10385–10387.
- 123 Lu, J., Zheng, Y., and Zhang, J. (2015). Tuning the color of thermally activated delayed fluorescent properties for spiro-acridine derivatives by structural modification of the acceptor fragment: a DFT study. *RSC Adv.* 5: 18588–18592.
- 124 Shizu, K., Noda, H., Tanaka, H., Taneda, M., Uejima, M., Sato, T., Tanaka, K., Kaji, H., and Adachi, C. (2015). Highly efficient blue electroluminescence using delayed-fluorescence emitters with large overlap density between luminescent and ground states. *J. Phys. Chem. C* 119: 26283–26289.
- 125 Chen, X.K., Zhang, S.F., Fan, J.X., and Ren, A.M. (2015). Nature of highly efficient thermally activated delayed fluorescence in organic light-emitting diode emitters: nonadiabatic effect between excited states. *J. Phys. Chem. C* 119: 9728–9733.
- 126 Li, Z.D., Suo, B.B., Zhang, Y., Xiao, Y.L., and Liu, W.J. (2013). Combining spin-adapted open-shell TD-DFT with spin-orbit coupling. *Mol. Phys.* 111: 3741–3755.
- 127 Lyskov, I. and Marian, C.M. (2017). Climbing up the ladder: intermediate triplet states promote the reverse intersystem crossing in the efficient TADF emitter ACRSA. *J. Phys. Chem. C* 121: 21145–21153.
- 128 Marian, C.M. (2016). Mechanism of the triplet-to-singlet upconversion in the assistant dopant ACRXTN. *J. Phys. Chem. C* 120: 3715–3721.
- 129 Lyskov, I. and Marian, C.M. (2017). Climbing up the ladder: intermediate triplet states promote the reverse intersystem crossing in the efficient TADF emitter ACRSA. *J. Phys. Chem. C* 121: 21145–21153.
- 130 Nakanotani, H., Masui, K., Nishide, J., Shibata, T., and Adachi, C. (2013). Promising operational stability of high-efficiency organic light-emitting diodes based on thermally activated delayed fluorescence. *Sci. Rep.* 3: 2127.
- 131 Improta, R., Barone, V., Scalmani, G., and Frisch, M.J. (2006). A state-specific polarizable continuum model time dependent density functional theory method for excited state calculations in solution. *J. Chem. Phys.* 125: 054103.
- 132 Improta, R., Scalmani, G., Frisch, M.J., and Barone, V. (2007). Toward effective and reliable fluorescence energies in solution by a new state specific polarizable continuum model time dependent density functional theory approach. *J. Chem. Phys.* 127: 074504.
- 133 Furche, F. and Ahlrichs, R. (2002). Adiabatic time-dependent density functional methods for excited state properties. *J. Chem. Phys.* 117: 7433–7447.
- 134 Hättig, C. and Weigend, F. (2000). CC2 excitation energy calculations on large molecules using the resolution of the identity approximation. *J. Chem. Phys.* 113: 5154–5161.

Druckfreigabe/approval for printing	
Without corrections/ ohne Korrekturen	<input type="checkbox"/>
After corrections/ nach Ausführung der Korrekturen	<input type="checkbox"/>
Date/Datum:
Signature/Zeichen:

- 135 Hättig, C., Hellweg, A., and Köhn, A. (2006). Distributed memory parallel implementation of energies and gradients for second-order Møller-Plesset perturbation theory with the resolution-of-the-identity approximation. *Phys. Chem. Chem. Phys.* 8: 1159–1169.
- 136 Klamt, A. and Schüürmann, G. (1993). COSMO: a new approach to dielectric screening in solvents with explicit expressions for the screening energy and its gradient. *J. Chem. Soc., Perkin Trans. 2* 5: 799–805.
- 137 Schäfer, A., Klamt, A., Sattel, D., Lohrenz, J.C.W., and Eckert, F. (2000). COSMO implementation in turbomole: extension of an efficient quantum chemical code towards liquid systems. *Phys. Chem. Chem. Phys.* 2: 2187–2193.
- 138 May, V. and Kühn, O. (2004). *Charge and Energy Transfer Dynamics in Molecular Systems*. Wiley-VCH.

Page Proof
WILEY-VCH

Druckfreigabe/approval for printing	
Without corrections/ ohne Korrekturen	<input type="checkbox"/>
After corrections/ nach Ausführung der Korrekturen	<input type="checkbox"/>
Date/Datum:	
Signature/Zeichen:	

“keywords/abstract

Dear Author,

Keywords and abstracts will normally not be included in the print version of your chapter but only in the online version (if not decided differently by Wiley-VCH).

Thank you!”

Abstract

Keywords

Page proof
WILEY-VCH

Druckfreigabe/approval for printing	
Without corrections/ ohne Korrekturen	<input type="checkbox"/>
After corrections/ nach Ausführung der Korrekturen	<input type="checkbox"/>
Date/Datum:
Signature/Zeichen:

Author Queries

AQ1	Alphabetical listing is not allowed as per style. Hence, we have changed to roman numeral in the following sentences: The shortrangedness of the spin-orbit....Also the direct, first (i)-type.... Please check and amend if necessary.
AQ2	Please check and confirm the insertion of part labels "a" and "b" in Figure 8.2.
AQ3	Please check and confirm the insertion of part labels "a" and "b" in Figure 8.7.

Page Proof
WILEY-VCH